

Department of Civil Engineering

**Dynamic Response of Silo Supporting Structure under Pulsating
Loads**

Phung Tu

**This thesis is presented for the Degree of
Doctor of Philosophy
of
Curtin University**

September 2017

Declaration

To the best of my knowledge and belief, this thesis contains no material previously published by any other person except where due acknowledgement has been made. This thesis contains no material which has been accepted for the award of any other degree or diploma in any university.

Signed:



Name: Phung TU

Date: 3 November 2018

ACKNOWLEDGEMENT

I would like to thank my wife and children for their support.

I would like to thank my supervisor, Dr Vanissorn Vimonsatit, for her assistance, support and encouragement throughout my doctoral degree.

I also acknowledge Mr Simon Robson, my former Lead Structural Engineer, for his trust in my design of the Train Load Out (TLO) Silo in 2008.

I also would like to thank the former chief executive officers of Rio Tinto for preserving the engineering fundamentals behind the 2500 tonnes iron ore TLO silo.

I also thank the following people for their assistance and encouragement throughout my doctoral degree:

- Prof Hamid Nikraz
- Prof Ian Howard
- Prof Andrew Whyte
- Dr Arne Bredin
- Dr Jun Li
- Dr Pinghe Ni
- Mr Mick Elliss
- Mr Mark Whittaker
- Mr Darren Isaac
- Mr Ashley Hughes
- Mr Jonathan Kwan
- Mr Luke English
- Mr Craig Gwyther
- Mr Rob Walker

ABSTRACT

Expanded flow bins are commonly used in the material handling industry to store and load train wagons. These bins are known in the industry as Train Load Out (TLO) bins. It has been reported that some iron ore TLO bins suffer a dynamic condition during discharge known as silo quaking. Silo quaking is a very complex industrial phenomena and is often occurred in silo structures during discharge. There are three types of silo quakes such as silo honking, silo shock and silo pulsation.

A scaled model of the actual TLO bin was designed and fabricated to investigate this phenomenon. The proposed numerical model supports the theory that pulsation loads occur in almost all bins and whether the induced dynamic loads cause any quaking problems are dependent on the severity of the loads, natural frequencies of the bin and its supporting structure.

The results confirmed that silo quaking is a time varying mass structural dynamic problem and the existence of a silo quake spectrum. The outcomes of the research, equation of silo quaking and equation of silo quake response spectrum, lay solid foundations for further research into the silo quaking phenomena and structural design methods to mitigate the effects of silo quaking on the silo structure.

LIST OF FIGURES

Figure 2-1: Typical TLO bin dimensions (Tu and Vimonsatit 2013).....	13
Figure 3-1: Mass flow bin with load cells (Roberts and Wensrich 2002).	19
Figure 3-2: Velocity profiles in mass flow silo (Roberts and Wensrich 2002).	19
Figure 3-3: Normal pressures and shear stresses at location 5 (Roberts and Wensrich 2002).	20
Figure 3-4: Normal pressures and shear stresses at location 14 (Roberts and Wensrich 2002).	20
Figure 3-5: Two static pressure profiles from successive runs using rice grains (Bennett and Kmita 1996).....	21
Figure 3-6: Two dynamic pressure profiles from successive runs using rice grains (Bennett and Kmita 1996).....	22
Figure 3-7: Pressure vs time traces for wheat (Bennett and Kmita 1996).	23
Figure 3-8: Pressure vs time traces for corn (Bennett and Kmita 1996).....	23
Figure 3-9: Pressure vs time traces for rice (Bennett and Kmita 1996).....	24
Figure 3-10: Pressure vs time traces for unrestricted rice flow (Bennett and Kmita 1996).	24
Figure 3-11: Pressure vs time traces for restricted rice flow (Bennett and Kmita 1996).	25
Figure 3-12: Pressure vs time traces for slow filling (Bennett and Kmita 1996)..	26
Figure 3-13: Pressure vs time traces for fast filling (Bennett and Kmita 1996). ..	26
Figure 3-14: Analytical dynamic load model for calculating dynamic pressures due to shock (Roberts 1996).	27
Figure 3-15: Shock waves at location z (Roberts 2003).	28
Figure 3-16: Comparison between measured and calculated normal and shear stress amplitudes for experimental wheat silo (Roberts and Wensrich 2002). ..	30
Figure 3-17: Arch forms across the hopper opening (To 2005).....	31
Figure 3-18: Symbols for the hopper (Shinohara et al. 1968).....	33
Figure 3-19: 2D Pascal's triangle.....	40
Figure 3-20: 3D stress block.	42

Figure 3-21: Contact between particle and silo wall as per Equation 3-110 (Nassauer and Kuna 2013).	58
Figure 3-22: Contact between particle and particle as per Equation 3-111 (Nassauer and Kuna 2013).	59
Figure 3-23: Example of response spectrum – acceleration vs frequency.	63
Figure 3-24: Kobe (Kobe 1995) earthquake time history generated by software SeismoSignal 2016.	65
Figure 3-25: Kobe acceleration spectrum generated by software SeismoSignal 2016.	66
Figure 3-26: Kobe velocity spectrum generated by software SeismoSignal 2016...	66
Figure 3-27: Kobe displacement spectrum generated by software SeismoSignal 2016.	67
Figure 3-28: Typical earthquake design spectrum for different soil type (AS/NZS1170.4 2007).	68
Figure 3-29: Solution procedure for Newmark equations.	74
Figure 3-30: Salt dispenser.	85
Figure 4-1: Silo and supporting frame.	90
Figure 4-2: 3D isometric view of the silo support structure.	91
Figure 4-3: Silo support structure – bottom view.	92
Figure 4-4: Silo support structure – top view.	92
Figure 4-5: Silo support structure – Section A.	93
Figure 4-6: Silo support structure – Section B.	93
Figure 4-7: Silo support structure – Section C.	94
Figure 4-8: Silo support structure – Section D.	94
Figure 4-9: 200 mm hopper opening with swing gate in locked position.	95
Figure 4-10: 200 mm hopper opening with swing gate open.	96
Figure 4-11: Data analysis using parallel computing.	97
Figure 4-12: Dimensions of test silo (swing gate not shown).	101
Figure 4-13: Accelerometer locations – Silo.	102
Figure 4-14: Accelerometer locations – platform top view.	103
Figure 4-15: Accelerometer locations – Section A.	104
Figure 4-16: Accelerometer locations – Section B.	104
Figure 4-17: NI-9234 data logger.	105

Figure 4-18:	Filling test silo with iron ore.	107
Figure 4-19:	Bulk bags inside the tray filled with iron ore after silo discharge..	108
Figure 4-20:	Silo support frame modified to carry 4 x load cells – Top View. ..	110
Figure 4-21:	Silo supported on 4 x load cells – Bottom View.	110
Figure 4-22:	Accelerometer locations – Section A.	111
Figure 4-23:	Accelerometer locations – Section B.	112
Figure 4-24:	Accelerometer locations – Silo.	113
Figure 4-25:	HBM QuantumX MX840A universal data amplifier.	114
Figure 4-26:	Drums carrying iron ore.	116
Figure 4-27:	Automatic direct shear tester.	117
Figure 4-28:	Apparatus to test soil liquid limit.	118
Figure 4-29:	Plastic limit test.	119
Figure 4-30:	Water bath used for testing soil density.	120
Figure 4-31:	Volumetric flasks used in density measurement.	121
Figure 4-32:	Vacuum used for testing soil density.	121
Figure 4-33:	Sieve shaker.	122
Figure 4-34:	Oven used for moisture content tests.	123
Figure 5-1:	Measured flow rates for silo with 400mm hopper opening.	128
Figure 5-2:	Measured flow rates for silo with 200mm hopper opening.	129
Figure 5-3:	Measured flow rates for silo with 250mm hopper opening.	130
Figure 5-4:	Measured flow rates for silo with 300mm hopper opening.	131
Figure 5-5:	Total mass of iron ore remaining inside the silo vs time for 400mm hopper opening.	132
Figure 5-6:	Total mass of iron ore remaining inside the silo vs time for 250mm hopper opening.	132
Figure 5-7:	Total mass of iron ore remaining inside the silo vs time for 200mm hopper opening.	133
Figure 5-8:	Total mass of iron ore remaining inside the silo vs time for 300mm hopper opening.	134
Figure 5-9:	Acceleration vs Time for Experiment 1 - 400mm Hopper.	136
Figure 5-10:	Acceleration vs Time for Experiment 10 - 200mm Hopper.	137
Figure 5-11:	Acceleration vs Time for Experiment 21 - 250mm Hopper.	138
Figure 5-12:	Acceleration vs Time for Experiment 29 - 300mm Hopper.	139
Figure 5-13:	Silo Quake Response Spectrum - 200mm Hopper.	141

Figure 5-14:	Silo Quake Response Spectrum - 250mm Hopper.....	142
Figure 5-15:	Silo Quake Response Spectrum - 300mm Hopper.....	143
Figure 5-16:	Silo Quake Response Spectrum - 400mm Hopper.....	144
Figure 5-17:	Damage to test silo support structure due to silo quaking.....	149
Figure 6-1:	A simplified dynamic model of TLO bin (Tu and Vimonsatit 2013).	152
Figure 6-2:	Single Degree Of Freedom (SDOF) dynamic model.....	153
Figure 6-3:	Weight of iron ore remaining inside the silo vs time Experiment 1..	159
Figure 6-4:	Weight of iron ore remaining inside the silo vs time Experiment 2..	159
Figure 6-5:	Weight of iron ore remaining inside the silo vs time Experiment 3..	160
Figure 6-6:	Instantaneous dynamic loads for Experiment 1.....	161
Figure 6-7:	Instantaneous dynamic loads for Experiment 2.....	161
Figure 6-8:	Instantaneous dynamic loads for Experiment 3.....	162
Figure 6-9:	Flow rates for Experiment 1.....	164
Figure 6-10:	Computed accelerations vs time for Experiment 1 – 400mm hopper opening.....	164
Figure 6-11:	Measured accelerations vs time for Experiment 1.....	165
Figure 6-12:	Flow rates for Experiment 2.....	165
Figure 6-13:	Computed accelerations vs time for Experiment 2 – 350mm hopper opening.....	166
Figure 6-14:	Measured accelerations vs time for Experiment 2.....	166
Figure 6-15:	Flow rates for Experiment 3.....	167
Figure 6-16:	Computed accelerations vs time for Experiment 3 – 300mm hopper..	167
Figure 6-17:	Measured accelerations vs time for Experiment 3.....	168
Figure 6-18:	Acceleration vs time calculated by Equation 6-7 with forces and masses obtained from Rocky DEM – 400mm hopper opening.....	170
Figure 6-19:	Acceleration vs time calculated by Equation 6-7 with forces and masses obtained from Rocky DEM and added stiffness damping– 400mm hopper opening.....	171
Figure 6-20:	Acceleration vs time calculated by Equation 6 7 with forces and masses obtained from Rocky DEM and added mass damping– 400mm hopper opening.....	171

Figure 6-21: Acceleration vs time calculated by Equation 6 7 with forces and masses obtained from Rocky DEM and added critical damping – 400mm hopper opening.	172
Figure 6-22: Iron ore TLO silo (Roberts 2008).....	173
Figure 6-23: 2000 tonne iron ore TLO Silo (Roberts 2008).	174
Figure 6-24: Flow rates for 2000 tonne iron ore TLO (Roberts 2008).	175
Figure 6-25: Dynamic response of TLO supporting structure with 1000 tonnes of iron ore inside.....	176
Figure 6-26: Dynamic response of TLO supporting structure with 1250 tonnes of iron ore inside.....	177
Figure 6-27: Dynamic response of TLO supporting structure with 1500 tonnes of iron ore inside.....	178
Figure 6-28: Experiment 1 with modified structural stiffness.	180
Figure 6-29: Experiment 2 with modified structural stiffness.	180
Figure 6-30: Experiment 3 with modified structural stiffness.	181
Figure 6-31: Experiment 1 with modified critical damping ratio.	181
Figure 6-32: Experiment 2 with modified critical damping ratio.	182
Figure 6-33: Experiment 3 with modified critical damping ratio.	182
Figure 6-34: Experiment 1 with modified stationary mass.	183
Figure 6-35: Experiment 2 with modified stationary mass.	183
Figure 6-36: Experiment 3 with modified stationary mass.	184
Figure 7-1: Shear experiment at 0% moisture content.....	188
Figure 7-2: Shear experiment at 2% moisture content.....	188
Figure 7-3: Shear experiment at 7.5% moisture content.....	189
Figure 7-4: Wall friction experiments at 0% moisture content.....	190
Figure 7-5: Wall friction experiments at 2% moisture content.....	191
Figure 7-6: Wall friction experiments at 7.5% moisture content.....	191
Figure 7-7: Line of best fit for Liquid Limit tests.....	195
Figure 7-8: A graph of sieve analysis results of raw iron ore sample.....	197
Figure 7-9: A graph of sieve analysis results of washed iron ore sample.....	198
Figure 8-1: Deflected shapes of silo during discharge (Wilde, Rucka and Tejchman 2008).	200
Figure 8-2: Mechanism of silo honking according to (Niedostatkiewicz, Wójcik and Tejchman 2014).....	201

Figure 8-3: Sound waves arrive at the eardrum (Cutnell and Johnson 2012)..... 202

LIST OF TABLES

Table 4-1:	Computer specifications.....	98
Table 4-2:	Experiments – Silo Quake Response Spectrum.....	99
Table 4-3:	Experiments – Equation of Silo Quaking.	114
Table 5-1:	Moisture content variations for Silo Quake Response Spectrum Experiments.....	127
Table 5-2:	Calibration factors for Equation of Silo Quaking Response Spectrum.	146
Table 6-1:	Moisture content variations.....	158
Table 6-2:	Stationary mass, critical damping ratio and stiffness for Experiment 1, 2 and 3.	168
Table 6-3:	Parameters used for Rocky DEM analysis.....	169
Table 6-4:	Stationary mass, critical damping ratio and stiffness for DEM analyses.	172
Table 6-5:	Estimated structural properties of the 2000 tonnes TLO.	175
Table 6-6:	Stationary mass, critical damping ratio and stiffness for Experiment 1, 2 and 3.	184
Table 7-1:	Angle of Internal Friction vs Moisture Content.....	189
Table 7-2:	Angle of Wall Friction vs Moisture Content.	192
Table 7-3:	Bulk density at various moisture content.	192
Table 7-4:	Density of iron ore.	193
Table 7-5:	Liquid Limit of iron ore.	194
Table 7-6:	Plastic Limit of iron ore.	194
Table 7-7:	Plasticity Index of iron ore.....	195
Table 7-8:	Sieve Analysis Results of Raw Sample of Iron Ore.	196
Table 7-9:	Sieve Analysis Results of Washed Sample of Iron Ore.....	196
Table 8-1:	Typical sound intensities and intensity levels relative to the threshold of hearing (Cutnell and Johnson 2012)	204
Table A-1:	PCB 393B04 performance specifications (Pcb Piezotronics 2017)..	234
Table A-2:	PCB 393B04 environmental specifications (Pcb Piezotronics 2017).....	234

Table A-3:	PCB 393B04 electrical specifications (Pcb Piezotronics 2017).	235
Table A-4:	PCB 393B04 physical specifications (Pcb Piezotronics 2017).....	235

TABLE OF CONTENTS

Acknowledgement.....	i
Abstract	ii
List of Figures	iii
List of Tables.....	ix
1 Introduction	4
1.1 Objectives	6
1.2 Scope	8
1.3 Research Significance	9
1.4 Organisation of Thesis.....	9
1.5 Publications	11
2 Structural Design of Silos – A Review	12
3 Literature Review	16
3.1 Introduction	16
3.2 Mechanism of Silo Quaking and Silo Music.....	17
3.3 Analytical Modelling of Silo Quaking	27
3.3.1 Slip-Stick.....	27
3.3.2 Dynamic Arches at Hopper Opening	30
3.4 Numerical Modelling of Silo Quaking	35
3.4.1 Finite Element Method.....	37
3.4.1.1 Micro-polar Elasto-Plastic Constitutive Model	43
3.4.1.2 Hypoplasticity Constitutive Model	46
3.4.1.3 Micro-Polar Hypoplasticity Constitutive Model	49
3.4.2 Discrete Element Method.....	55
3.5 Structural Dynamics	61
3.5.1 Response Spectrum	63
3.5.2 Modal Superposition Method.....	68
3.5.3 Newmark β	71
3.5.4 Wilson θ	75
3.6 Signal Processing	76
3.6.1 Empirical Mode Decomposition	77

3.6.2	Hilbert Transform and Hilbert Marginal Spectrum	82
3.7	Fundamental Issues with Current Granular Flow Theories.....	83
3.8	Hazards Associated With Silo Inserts	86
3.9	Conclusion.....	87
4	Research Methodology.....	89
4.1	Introduction	89
4.2	Model TLO Silo	89
4.3	Computing Facilities for Data Analyses.....	97
4.4	Silo Quake Response Spectrum – Experimental Setup.....	98
4.5	Silo Quaking – Experimental Setup	109
4.6	Material Classification	116
4.7	Conclusion.....	124
5	Silo Quake Response Spectrum	125
5.1	Introduction	125
5.2	Flow Rates and Accelerograms	125
5.2.1	Flow Rates.....	127
5.2.2	Accelerograms.....	135
5.3	Silo Quake Response Spectrum	140
5.4	Structural Connection Failure.....	149
5.5	Conclusion.....	150
6	Equation of Silo Quaking.....	151
6.1	Introduction	151
6.2	Equation of Silo Quaking	151
6.3	Computation of Dynamic Forces	158
6.4	Computed Accelerations vs Measure Accelerations	163
6.5	Equation of Silo Quaking Coupled with Discrete Element Method	169
6.6	Equation of Silo Quaking Coupled with Forces from Analytical Formulae	172
6.7	Reduction of Amplitude of Vibration using Equation of Silo Quaking	178
6.8	Conclusion.....	185
7	Material Classification	187
7.1	Introduction	187
7.2	Direct Shear Test Results to ASTM D6128-16.....	187
7.3	Density To AS1289.3.5.1 (2006)	193

7.4	Plastic Limit To AS1289.3.2.1 (2009) and Liquid Limit To AS1289.3.1.1 (2009).....	194
7.5	Sieve Analysis To AS1289.3.6.1 (2009).....	196
7.6	Conclusion.....	198
8	Relevance of Equation of Silo Quaking to The Silo Honking Phenomenon ...	199
8.1	Introduction	199
8.2	Background to Silo Honking	199
8.3	Background to Acoustics.....	201
8.4	Silo Honking a Vibro-Acoustics Problem.....	206
8.5	Conclusion.....	207
9	Conclusion and Recommendation.....	209
9.1	Concluding Remarks	209
9.2	Silo Quake Response Spectrum	210
9.3	Equation of Silo Quaking	211
9.4	Recommendations for Future Research	212
	References	214
	Appendix A – Accelerometer Specifications.....	234
	Appendix B – Marginal Spectrum (MS) – Silo Quake Response Spectrum	237
	Appendix C – Accelerograms	238
	Appendix D – IMFS.....	239
	Appendix E – Attribution of Research Outputs	240

1 INTRODUCTION

The silo quake terminology is often used to describe the dynamic phenomena created during silo emptying process that has been occurring ever since the first silo was built. The phenomena were first documented by during experiments and subsequently by other researchers. Phillips (1910) observed the motion through a tube with glass face filled with sand. The tube had an orifice at one end which can be opened or closed. As soon as the orifice was opened, the sand in the upper part of the tube moved downward intermittently in jerks which accompanied by a rattling sound which later changed to a distinct musical note. Furthermore, Gorenc et al. (1984) observed that the flow of the granules caused the wall of the tube to vibrate.

These phenomena have been recorded during tall mass flow (Wensrich 2002b), intermediate flow (Wensrich 2002b), funnel flow (Roberts 2003) or expanded flow regardless whether the discharge is controlled or free outlet (Wilde et al. 2010) and in multi-outlet bins (Roberts 2003). These phenomena can occur for both cohesionless and cohesive soils (Wilde et al. 2010) and appear mainly in steel or aluminium silos as compared to concrete silos (Wilde, Rucka and Tejchman 2008). The pulsation loads only occur in non-cohesive materials while pulsations, and shock loads appear in cohesive materials (Tejchman 1996). Another variant of silo quake is called silo music or silo honking which can occur in tall mass flow silos during discharge.

Silo music can cause noise pollution to the neighbourhood surrounding the industrial plants and hearing damage to plant operators (Wilde, Rucka and Tejchman 2008). Similarly, an earthquake like dynamic loads resulted from silo quaking can cause damage to surrounding structures, fatigue failure of structural connections and silo failure (Wilde, Rucka and Tejchman 2008).

Despite a number of researches have been done silo quaking is still not well understood (Wilde, Rucka and Tejchman 2008). It must be noted that in a few of these silos, the problems can be mitigated by simple methods (Tejchman 1999). However, straight forward solutions that can systematically reduce silo vibration

without expensive modifications do not exist (Wilde, Rucka and Tejchman 2008) and cure all method is far from reality (Wensrich 2002b).

For many years, researchers and design engineers are still struggling to explain the following observations:

1. Aluminium silos quake more often compared to steel and concrete silos (Tejchman and Wojcik 2011).
2. Silo quake often occurs during discharge but not during filling (Herrald 2012).
3. Silo honking often occurs with nanomaterials but not with others (Bates 2013).
4. Silo quake is more pronounced when there is less granular material in the silo (Herrald 2012; Roberts 2008).

The reader needs to appreciate that it is a common practice in structural engineering to provide sufficient resistance in the design of structure so that the structure can resist the imposed forces without having to displace, sway, or vibrate excessively. Such practice is employed herein to provide the structural engineer with methods of providing extra resistance in the design of the silo structure to prevent the silo quaking phenomenon.

Earthquake response spectrum is an established structural design method to predict dynamic response of structures subjected to ground motions. The earthquake response spectrum analysis method provides an excellent vehicle to firstly develop such “engineering feel” and then being able to carry it across different projects (Hart and Wong 2000). The major advantage of the response spectrum analysis method is that it combines important components of structural dynamics and design (Hart and Wong 2000).

However, there is insufficient knowledge in the literature regarding the existence of a similar response spectrum applicable to silos apart from it being hypothesised recently (Tu and Vimonsatit 2013). The establishment of a silo quake response

spectrum would revolutionise the way structural engineers analyse and design silos to resist the effects of dynamic loads generated during silo discharge.

Furthermore, principles of structural dynamics were selected to generalise the silo quaking phenomena because during silo quake the silo supporting structures have been found to be adversely affected. Additionally, existing structural dynamic analysis procedures applicable to analysing the response of the silo structure subjected to dynamic forces generated during silo flow are not documented in the literature nor international design codes compared to structural dynamic analysis procedures for an earthquake. As such, the structural engineers have to use unsuitable analysis procedures to analyse and design the silo structures that are known to quake during discharge.

1.1 Objectives

The aims of this thesis are to firstly prove the hypothesis that the natural frequencies of the silo and its supporting structure determine whether silo quake will occur (Roberts 1996), and secondly to demonstrate that silo quaking is a process in which the silo supporting structure restores its dynamic equilibrium by vibrating excessively. Its equilibrium is disturbed by the pulsating loads and mass losses during discharge. It will also be demonstrated that silo quaking can be prevented by providing sufficient stiffness, mass and damping in the supporting structure to counterbalance the pulsating forces and mass losses occur during silo discharge. This balance restoring process can be readily observed in nature.

The process of providing extra mass, damping and stiffness in the silo supporting structure to prevent silo quaking was implemented successfully in an industrial size, 2500 tonnes iron ore Train Load Out (TLO) bin by the author in 2008. The silo has been in operation since 2010 without silo quaking issues.

Roberts' (1996) hypothesis and the balance or dynamic equilibrium restoring process taken by silo supporting structure during granular discharge will be demonstrated by (i) proving the existence of a silo quake response spectrum similar to earthquake response spectrum, which is essential to the structural design of silos, and (ii) generalising the silo quaking phenomena using principles of time varying mass structural dynamics and transient structural dynamics.

In dealing with silo quaking, it is necessary to observe and appreciate this balance restoring process, which is a process that nature takes to restore its balance once its balance is disturbed. Furthermore, it is highly recommended that the reader of this thesis familiarises themselves with the concepts of time varying mass structural dynamics and transient structural dynamic analysis because such concepts are employed in this thesis to explain the process that the silo supporting structure takes to restore its balance disturbed by pulsating loads and mass losses and effectively prevent silo quaking.

The time varying mass structural dynamics concepts presented in this thesis may be better understood with reference to literature on rocket science that can be readily found on National Aeronautics and Space Administration (NASA) website or similar. Similarly, the transient dynamic analysis can be better understood with reference to literature on earthquake engineering.

Furthermore, concepts of nonlinear and nonstationary signal processing technique, Hilbert Huang Transform (HHT) presented in this thesis was originally invented by a mathematician at NASA to analyse nonlinear and nonstationary signals. It is recommended that the reader of the thesis familiarise themselves with HHT before reading this thesis.

In particular, the objectives of the research are:

1. Determine the nature of the dynamic response, linear and stationary or nonlinear stationary, of the silo structure during granular discharge.

2. Determine the appropriate signal processing techniques based on the nature of the captured dynamic response of the silo structure during flow.
3. Identify the existence of the silo quake response spectrum using the appropriate signal processing techniques.
4. Graphically present the silo quake response spectrum in a manner that can assist the structural design engineer in making design decisions.
5. Generalise the silo quake response spectrum by formulating a mathematical model to represent the graph of the silo quake response spectrum.
6. Identify the relationship between the dynamic response of the silo supporting structure and the flow of granules from the silo during material discharge from the silo.
7. Generalise the silo quaking phenomena by formulating a mathematical model to describe the dynamic response of the silo structure during the discharge process or another word the balance restoring process that the silo supporting structure undertake to restore its balance that has been disturbed by the pulsating loads and mass losses.

1.2 Scope

The research is carried out on a physical model of a 2500 tonnes iron ore TLO silo of 1 to 10 scale. The iron ore used in all the experiments is donated by Rio Tinto's which is a representative sample of the ore in the TLO silo that the author had structurally designed in 2008 and successfully avoided the silo quaking phenomena by modifying the silo supporting structure's overall stiffness and mass. This research is limited to determining the dynamic response of the silo supporting structure during granular discharge. The dynamic response of the silo are captured by the accelerometers, and the masses are captured by weighing beams and load cells.

1.3 Research Significance

Currently, there is a lack of guidance on how to analyse, design and construct silo supporting structure to avoid silo quaking. The findings in this research give the practising structural engineers the understandings and engineering fundamentals to analyse, design and method to construct silo structures to prevent silo quaking. Furthermore, this research lays the foundation for future researches into the silo quaking phenomena.

1.4 Organisation of Thesis

This thesis addresses the shortcomings in the understanding of silo quaking, current dynamic structural analyses and designs. It will do so in 9 chapters, which are outlined below:

Chapter 1 introduces the concept of silo quaking, the variants of silo quake and lack of guidance for the structural engineer to analyse and design silos to prevent silo quaking.

Chapter 2 reviews the current structural analysis and design method for silo structures.

Chapter 3 reviews the current literature on silo quaking, structural dynamics and signal processing techniques.

Chapter 4 presents the experimental setups to determine the silo quake response spectrum, the equation of silo quaking and material characterisations.

Chapter 5 presents the results of the experiments that identify the silo quake response spectrum.

Chapter 6 presents the results of the experiments that are used to derive the equation describing the dynamic response of the silo supporting structure or equation of silo quaking.

Chapter 7 presents the results of the experiments that are used to classify the iron ore material.

Chapter 8 presents the relevance of the equation of silo quaking to the silo honking phenomenon.

Chapter 9 concludes the research findings and presents recommendations for future researches into the silo quaking phenomena.

References presents the list of references that are used in this research.

Appendix A lists the specifications of the accelerometer and data logger used in the experiments related to the Silo Quake Response Spectrum.

Appendix B displays all the Silo Quake Marginal Spectra.

Appendix C displays all the accelerograms.

Appendix D displays all the IMFs.

1.5 Publications

It is important to note that some parts of this thesis have been published or pending publication in relevant journals before the submission of this thesis.

Tu, P, and V Vimonsatit. 2013. "The Effect of Structural Stiffness on Iron Ore Train Load out Bin." In 11th International Conference on Bulk Materials Storage, Handling and Transportation, Newcastle NSW Australia, edited by Jan-Dirk Prigge and Mark Jones. University of Newcastle.

Tu, P and Vimonsatit, V. 2013. Structural Design of Iron Ore Train Load Out Bin. Australian Bulk Handling Review. 18 (6): pp. 24-28.

Tu, P and Vimonsatit, V. 2017. Silo Quaking of Iron Ore Train Load Out Bin - A Time-Varying Mass Structural Dynamic Problem. Advanced Powder Technology. 2017;28(11):3014-25.

Tu, P, Vimonsatit, V and Li, J. 2018. Silo Quake Response Spectrum of Iron Ore Train Load Out Bin. Advanced Powder Technology. 2018, 29(11): 2775-2784.

2 STRUCTURAL DESIGN OF SILOS – A REVIEW

The inclusion of a TLO bin in the Mine Process has proven to be a more efficient way for loading the train wagons, and it is also more cost-effective when compared to the traditional TLO Vault and Stockpile. These iron ore TLO bins quite often have a storage capacity of 2000 tonnes. In recent years, iron ore TLO bins have been designed to have a storage capacity of 2500 tonnes. TLO bins often are designed using expanded flow regime. Expanded flow is a bulk solid flow regime where the ore at the upper portion of the bin is designed for funnel flow, and the lower portion of the bin is designed for mass flow. The advantage of the expanded flow regime is the ability to store a large amount of ore in a squat bin while still maintaining mass flow without the need for a much taller bin.

Roberts (2008) suggested that tall bins require conveying the ore to the top of the bin where the filling process occurred impractical at mine sites. These TLO bins are often made from structural steel and are circular rather than square or rectangular. Square or rectangular bins carry the pressure loads of the stored iron ore on the bin walls in bending and shear stresses whereas circular bins carry such loads in hoop stresses. Consequently, large TLO bins that utilise hoop stresses to carry the pressure loads acting on the walls will require less steel compared to square or rectangular bins. However, there have been some reports from various mine sites that these iron ore TLO bins suffer excessive vibrations during ore discharge.

The vibration starts as soon as the clamshell gate at the bottom of the TLO bin opens to discharge the ore into the wagon passing underneath it. The motion quickly intensifies and dissipates as the clamshell gate closes and the motion repeats itself as the clamshell gate opens to load another wagon passing under. These types of vibrations are commonly known in the research literature as Silo Quaking. The quaking causes several problems such as; structural connections failure, reduced fatigue life of structural members, computer data corruption, personnel discomfort, loss of production and increase in maintenance costs.

The TLO bin pressures are calculated in three parts which are an upper cylindrical section, middle hopper section and lower hopper section in accordance with guidance given in AS3774 (1996). Based on the geometries shown in Figure 2, the upper cylindrical section and middle hopper section are designed for funnel flow while the lower hopper section is designed for mass flow. The ore properties used in all pressure calculations are obtained directly from data provided in AS3774 (1996). Thus, such flow regime is called expanded flow.

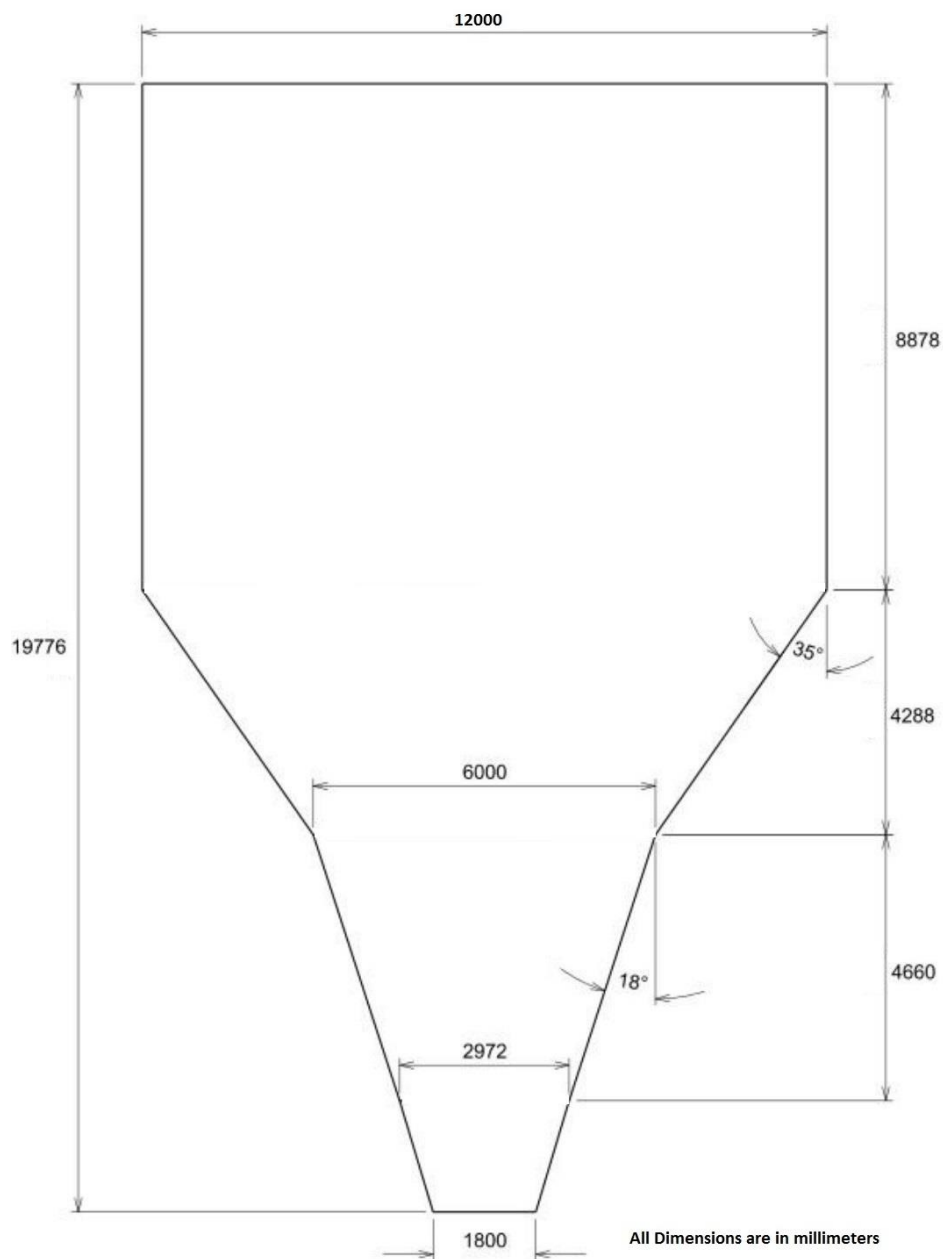


Figure 2-1: Typical TLO bin dimensions (Tu and Vimonsatit 2013).

As pointed out by Tu (2008), Australian Standards (AS) AS4100 (1998) and AS3990 (1993), which are the ultimate limit state and working stress steel design codes respectively, do not provide guidelines for steel bin shell design. These design codes were written to provide design engineers with guidance on acceptable design standards applicable to structural elements such as beams, columns and braces but not thin plates and shells applicable to bins or silos. It has been well documented in research literature that thin plates and shells suffer from buckling modes dissimilar to other structural elements. In particular, AS4100 (1998), BS7604 (2015) and EN1993-1-9 (2005) give the design engineers guidance on fatigue analysis and design of steel structures.

Design guidance on buckling modes applicable to thin plates can be found in DIN18800-3 (2008) and EN1993-1-5 (2006) while design guidance on buckling modes applicable to thin shells has been documented in DIN18800-4 (2008) and EN1993-1-6 (2007). It is important to note that EN1993-1-6 (2007) is an extension of DIN18800-4 (2008), it incorporates guidance on numerical shell analyses and fatigue design where DIN18800-4 (2008) only covers traditional manual membrane buckling design.

Furthermore, AS3774 (1996) only gives guidance on how to calculate bin pressures unlike its Eurocode counterpart EN1993-4-1 (2007). EN1993-4-1 (2007) gives the design engineers guidance on the structural design of silos. It refers to EN1993-1-6 (2007) for guidance on the design of thin shells and EN1993-1-5 (2006) for guidance on the design of plates.

It is important to note that neither of the silo loading codes such as AS3774 (1996) and EN1993-4-1 (2007) mention anything on the silo quaking phenomena. The phenomena can only be learnt by reading literature and textbooks. Additionally, neither design codes such as AS3774 (1996), EN1993-4-1 (2007), EN1993-1-5 (2006) and EN1993-1-5 (2006) give any guidance on analysis and design methodologies to counter the effects of silo quaking despite that silo structures have the highest rate of failure amongst all structures according to research undertaken by Tu (2008).

The author had proven through an industrial application that such dynamic phenomena could be effectively dampened by designing the supporting structure of the TLO bin sufficiently stiff. Based on the author's design experiences, it is found that the frequencies of silo quake in TLO silos are less than 2 Hz and most importantly can be dampened by modifying the stiffness of the supporting structure.

3 LITERATURE REVIEW

3.1 Introduction

Silo quaking is a term used to describe the vibration characteristics of silos and their supporting structures during discharge. According to Roberts (2003), silo quake occurs during discharge of tall mass flow, squat funnel flow, intermediate flow and expanded flow silos. Wensrich (2002b) concluded that silo quake is a dynamic behaviour that occurs within bulk storage vessels and is a recurring problem in gravity flow bins and silos according to Roberts (2003). During discharge, it has been observed by various researchers such as Firewicz (1988), Bennett and Kmita (1996) and Buick et al. (2004) that the flow is intermittent and pulsating. This is evident when inspecting Figure 3-6. The phenomena are characterised by strong vibrations in the upstream material separated by periods of no movement (Wensrich 2002b) and accompanied by booming sound commonly named as silo honking or silo music) (Wilde et al. 2010).

Tejchman (1996) concluded that there are three types of silo quakes such as silo honking, silo shock and silo pulsation. The quaking causes several problems such as; structural connections failure, reduced fatigue life of structural members, computer data corruption, personnel discomfort and health-related issues, loss of production, increase in maintenance costs and catastrophic failure as noted by Chou et al. (2002). Roberts (1996) believed that pulsation loads occur in most bins. However, whether the induced pulsating loads cause silo quake depends on the severity of the load, natural frequencies of the silo structure (Roberts 1996).

There have been some experimental, numerical studies to determine the causes of silo quaking and attempts have been made to predict and control the dynamic behaviours that occur while discharging silos to date. Through experimental studies, it was found that the pressure fluctuations obtained are very sensitive to changes in the silo granular material system (Bennett and Kmita 1996).

This chapter focuses on the literature of the physical mechanism of silo quaking and silo music, experimental findings, proposed numerical methods aimed to predict the dynamic behaviours of silos during discharge, analytical methods currently used for design purposes, current structural dynamic analyses and signal processing algorithm suitable for analysing nonlinear and nonstationary signals. This chapter also outlines shortcomings in current literature on silo quaking.

3.2 Mechanism of Silo Quaking and Silo Music

Since silo quaking was first recorded by Phillips (1910) and subsequently by McCabe (1974), the phenomena have been studied extensively at several universities around the world. As the result of extensive researches several causes of dynamic effects have been proposed:

- a. Collapsing arches (Firewicz 1988)
- b. Slip-stick interaction between the solids and silo walls (Wensrich 2002b)
- c. Grain collisions of the bulk solid (Wilde, Rucka and Tejchman 2008)
- d. Insufficient flowability of the silo fill (Wilde, Rucka and Tejchman 2008)
- e. Energy release by the fall of the bulk solid from the region of mass flow into the region of channel flow (Wilde, Rucka and Tejchman 2008)
- f. Propagating longitudinal stress waves due granular structure interactions (Wilde, Rucka and Tejchman 2008)
- g. Alternating flow patterns during flow (Wilde, Rucka and Tejchman 2008)
- h. Nonlinear change of the wall friction with flow velocity (Wilde, Rucka and Tejchman 2008)
- i. Acceleration and deceleration of the granular material at the silo transitions (Wilde, Rucka and Tejchman 2008)
- j. Internal slip–stick (Wilde, Rucka and Tejchman 2008)
- k. Solid dilation during flow (Wilde, Rucka and Tejchman 2008)

However, in recent years the slip-stick model has gained more acceptance than other models (Wilde, Rucka and Tejchman 2008).

Silo quaking can be found in tall mass flow, squat or funnel flow silos as noted by Roberts (1996) and Wensrich (2002a). Tejchman (1996) suggested that silo quaking occurs in silos where the fill's height is above the critical height H_{cr} (Figure 3-2). Furthermore, Tejchman (1996) identified that the H_{cr} is approximately equal to the diameter D of the cylinder portion of the silo measured above the transition in full-scale silos. However, Tejchman (1996) did not give any explanation why H_{cr} is a particular multiple of diameter D in model silos. The location of critical height H_{cr} was later confirmed by Roberts and Wensrich (2002).

It was reported by Roberts and Wensrich (2002) that plug type flow occurs with uniform velocity profile above the critical height H_{cr} across the cross section. The flow, below the critical height H_{cr} , in the transition region, converges due to the influence of the hopper and the velocity profile is found to be non-uniform (Roberts and Wensrich 2002). Roberts (2003) observed the formation of the flow pressures together with the dilation of the bulk solid. During dilation, it is possible that the vertical pressures are supporting the plug of bulk solid decrease slightly thus causing the plug of bulk solid to drop momentarily (Roberts 2003). This cycle repeats itself giving rise to pulsation loads (Roberts 2003).

The severity of the pulse increases with the silo height, and negligible pulsing occurs near the transition (Roberts and Wensrich 2002). A model silo was constructed and fitted with load cells at various locations around the model silo shown in Figure 3-1. During granular discharge, the pulsations were negligible at location 5 (Figure 3-3) as compared to location 14 (Figure 3-4). Limited data was made available about location 1, 2 and 3. It can be seen from the positions of the load cells shown in Figure 2-1 that Roberts and Wensrich (2002) concentrated their effort on the shock loads in the cylinder portion of the silo compared to the research undertaken by Bennett and Kmita (1996).

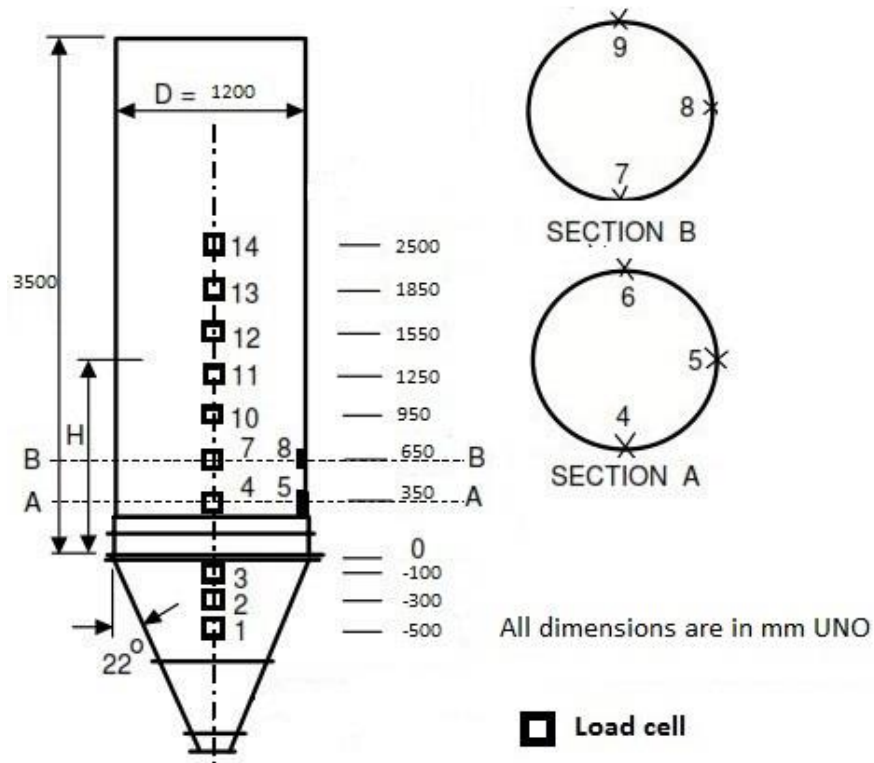


Figure 3-1: Mass flow bin with load cells (Roberts and Wensrich 2002).

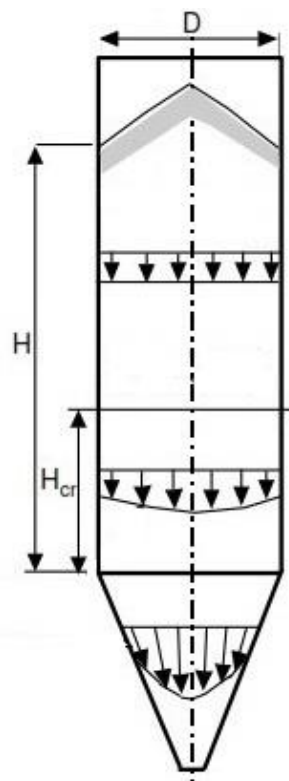


Figure 3-2: Velocity profiles in mass flow silo (Roberts and Wensrich 2002).

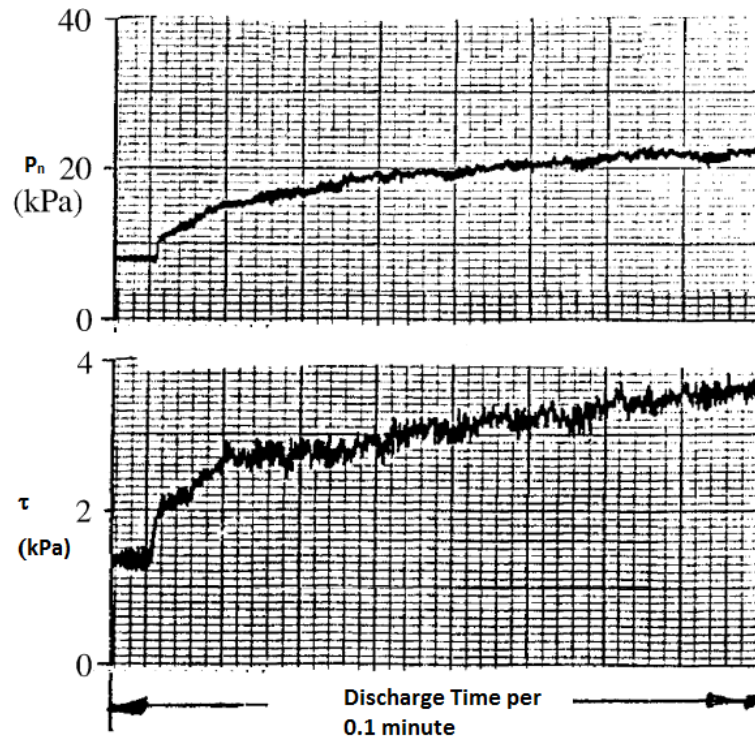


Figure 3-3: Normal pressures and shear stresses at location 5 (Roberts and Wensrich 2002).

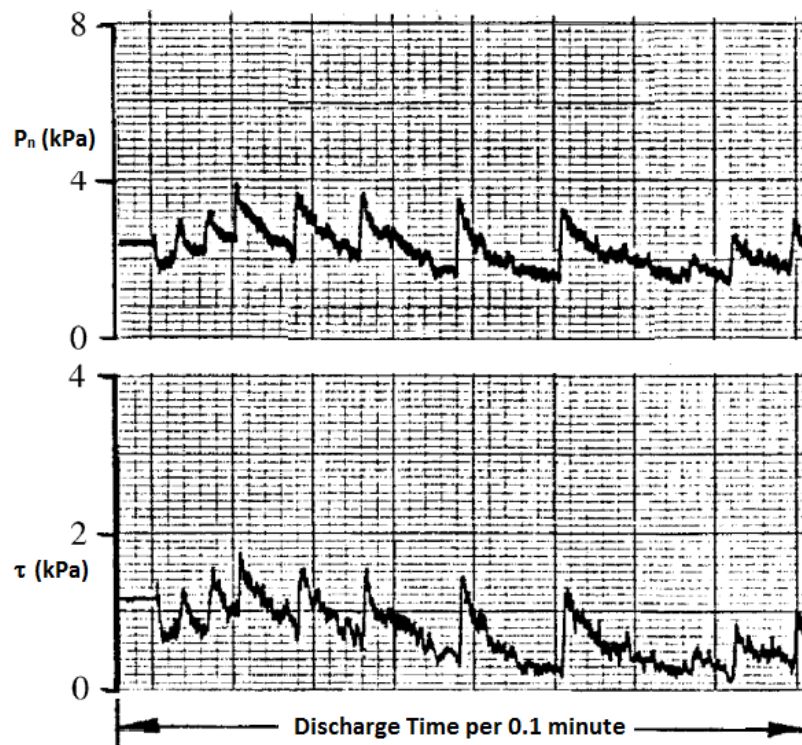


Figure 3-4: Normal pressures and shear stresses at location 14 (Roberts and Wensrich 2002).

In a separate research undertaken by Bennett and Kmita (1996) at the University of Swinburne in Melbourne Australia a number of load cells and displacement transducers were mounted on the transition and hopper parts of the silo, the test silo was filled with corn, rice and wheat and where static and dynamic pressures and frequencies were recorded.

It was reported that Bennett and Kmita (1996) were unable to reproduce static and dynamic pressure results in successive experiments despite every effort was made to fill at the same rate, fill with same material, to the same level and with the same gravity door opening procedure. This is evident in Figure 3-5 and Figure 3-6 shown below.

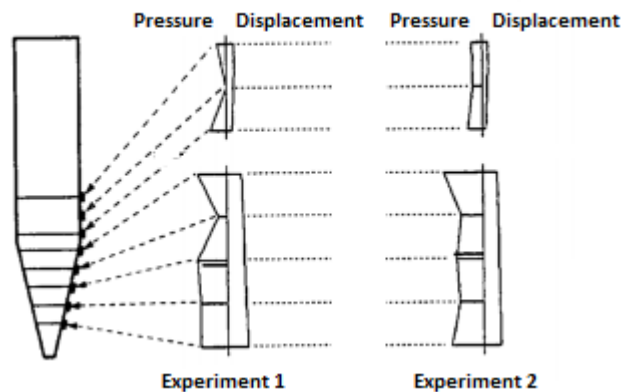


Figure 3-5: Two static pressure profiles from successive runs using rice grains (Bennett and Kmita 1996).

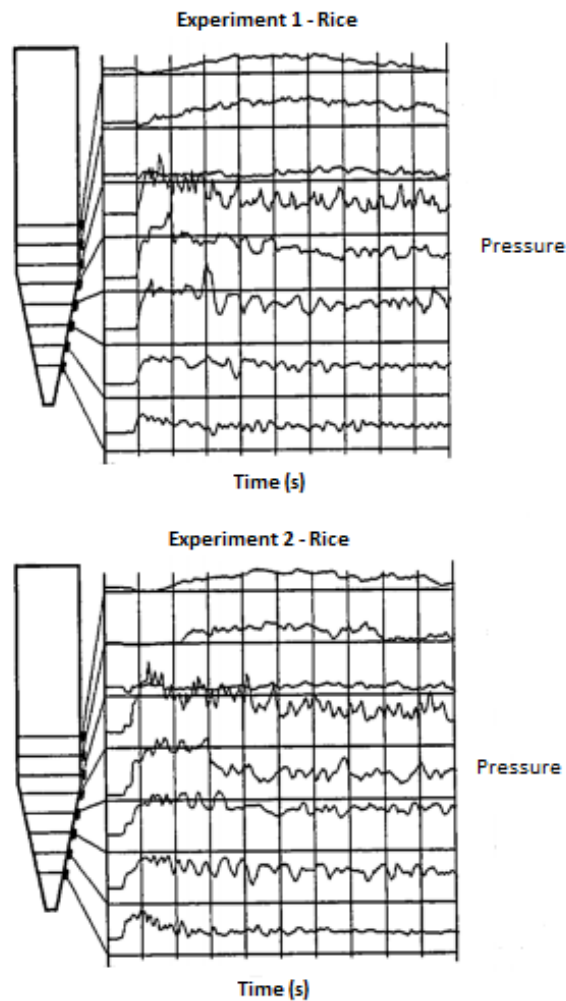


Figure 3-6: Two dynamic pressure profiles from successive runs using rice grains (Bennett and Kmita 1996).

Bennett and Kmita (1996) did not give clear explanations regarding the variations in both static and dynamic pressure profiles. However, the rice grain is elliptical and varies in shapes. Therefore it is reasonable to suspect that the alignment and position of each rice grain after each fill will be different. Hence the rice grain to rice grain interactions and silo walls to rice grain interactions will be different after each fill thus causing variations in both static and dynamic pressure profiles (Figure 3-5 and Figure 3-6).

Experiments conducted by Bennett and Kmita (1996) also concluded that the magnitude of pulsation loads and frequencies vary with the flowability of the granular material. This is evident when comparing the data shown in Figure 3-7, Figure 3-8 and Figure 3-9. Closer examinations of Figure 3-7, Figure 3-8 and Figure

3-9 reveal that pressures and pressure variations increased with a decrease in material flowability. However, the average pressure magnitudes are similar in all three materials in the hopper region (Bennett and Kmita 1996). Bennett and Kmita (1996) investigated the effects of changing discharge rates and filling rates on pressures and pressure variations.

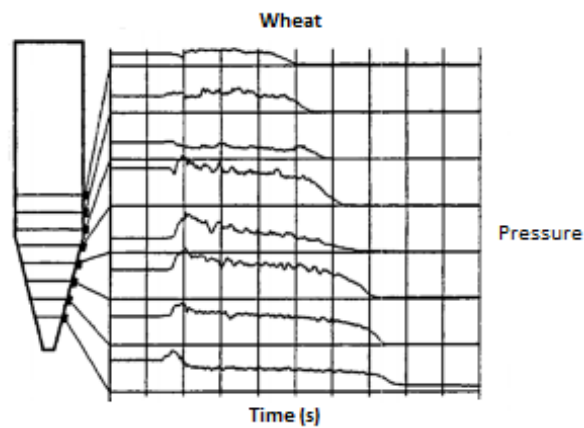


Figure 3-7: Pressure vs time traces for wheat (Bennett and Kmita 1996).

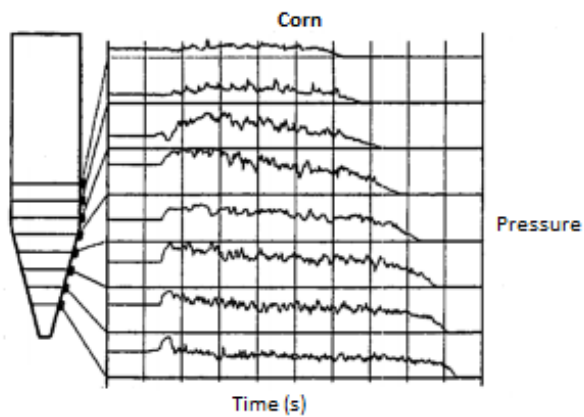


Figure 3-8: Pressure vs time traces for corn (Bennett and Kmita 1996).

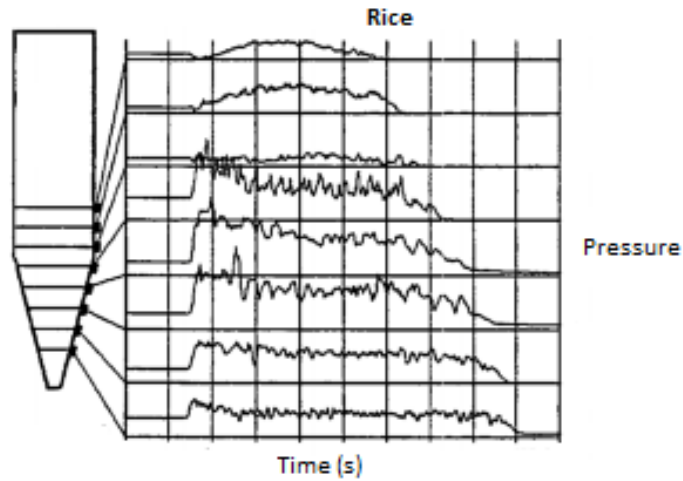


Figure 3-9: Pressure vs time traces for rice (Bennett and Kmita 1996).

Bennett and Kmita (1996) varied the discharge rates by fixing a 25mm outside diameter tube inside the hopper just above the outlet. The flow restriction and consequently reduced flow rate caused an increase in pressure pulsing magnitude, a decrease in pulsing frequency with minor variations in average pressure levels (Figure 3-10 and Figure 3-11 below). However, such variations were not so obvious at the lowest load cell (Bennett and Kmita 1996).

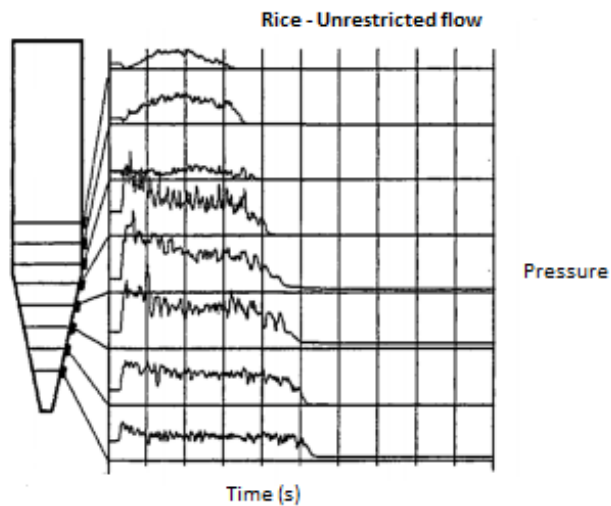


Figure 3-10: Pressure vs time traces for unrestricted rice flow (Bennett and Kmita 1996).

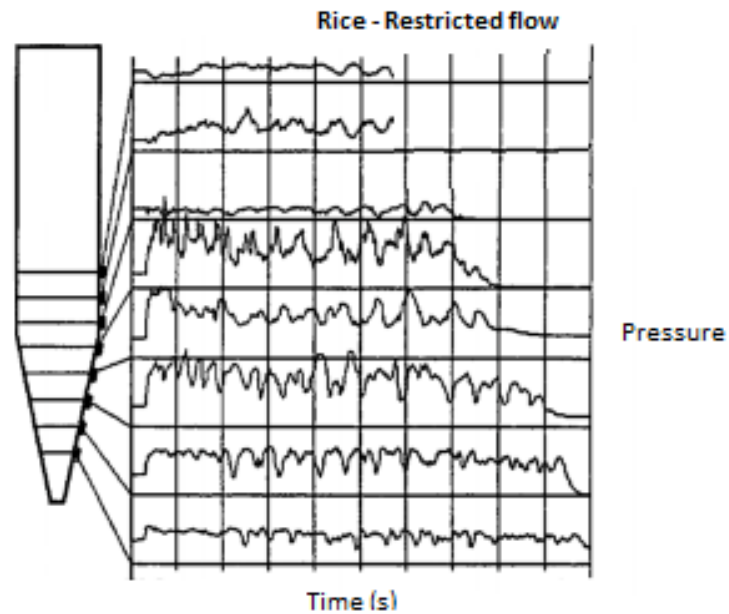


Figure 3-11: Pressure vs time traces for restricted rice flow (Bennett and Kmita 1996).

It was also found by Bennett and Kmita (1996) that the filling rate influences the pressure pulsations. This phenomenon is evident when comparing data shown in Figure 3-12 and Figure 3-13. The material in Figure 3-12 was feed through a narrow bin slot in a sprinkling manner compared to the fast filling of material in Figure 3-13. Bennett and Kmita (1996) concluded that fast filling resulted in unstable stress state in the material consequently produced more pronounced pulsing effects and that pressure fluctuations inside the silo are very sensitive to introduced changes within the silo.

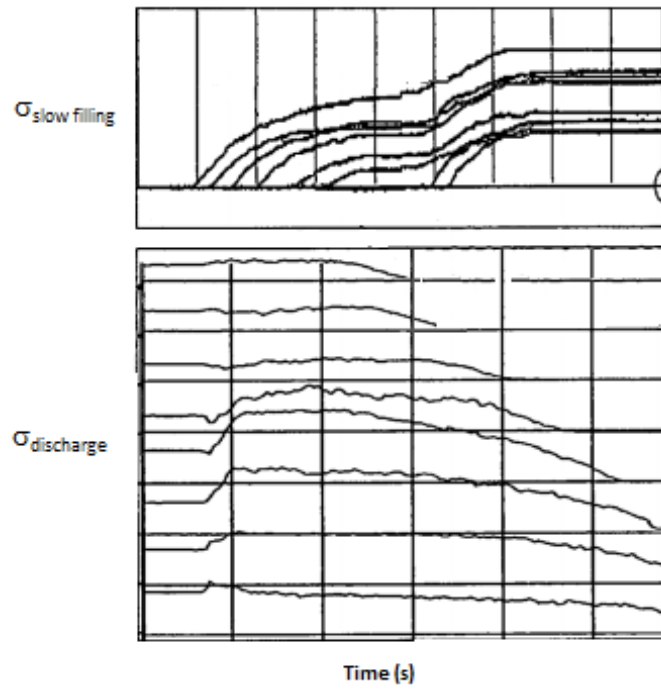


Figure 3-12: Pressure vs time traces for slow filling (Bennett and Kmita 1996).

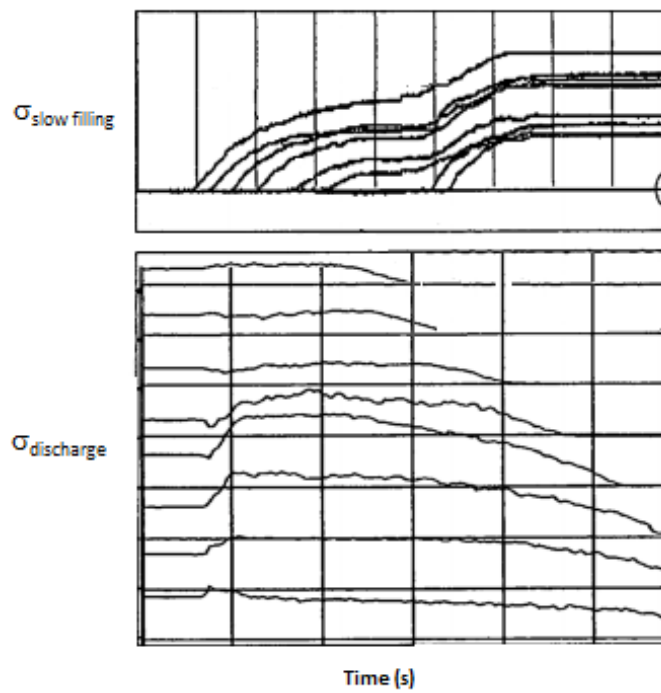


Figure 3-13: Pressure vs time traces for fast filling (Bennett and Kmita 1996).

3.3 Analytical Modelling of Silo Quaking

At present, there are analytical methods in the research literature to predicting pulsation loads and frequencies during silo discharge. These analytical methods are founded around the slip-stick and collapsing arch phenomena at the hopper opening. Slip-stick phenomenon is often found in tall silos whereas the collapsing arches phenomena is often found near the hopper opening.

3.3.1 Slip-Stick

After many years of research, Roberts (1996) proposed analytical formulae to predict shock loads and frequencies in tall silos. These formulae are based on a slip-stick phenomenon which is often found in tall silos. Roberts (1996) assumed a single shock plane dynamic load model (Figure 3-14) to predict shock loads in industrial silos experiencing quaking problems with reasonable accuracy. Although these formulae apply to tall silos, they can also be used in squat silos as well (Roberts 2008).

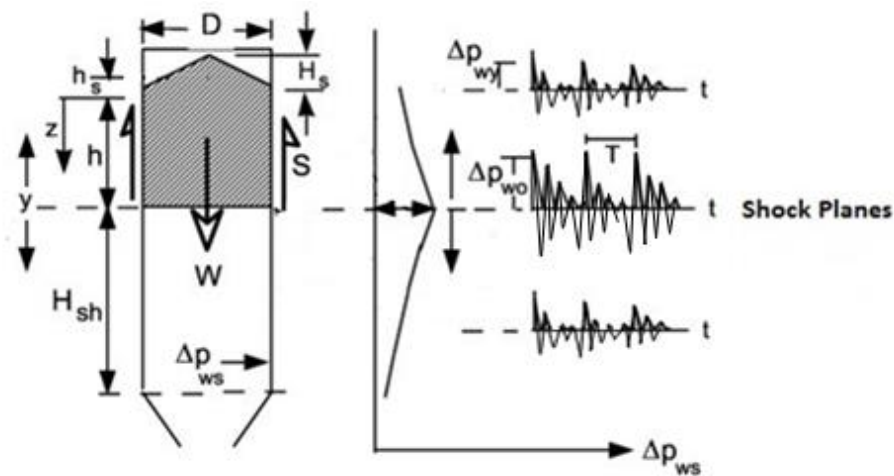


Figure 3-14: Analytical dynamic load model for calculating dynamic pressures due to shock (Roberts 1996).

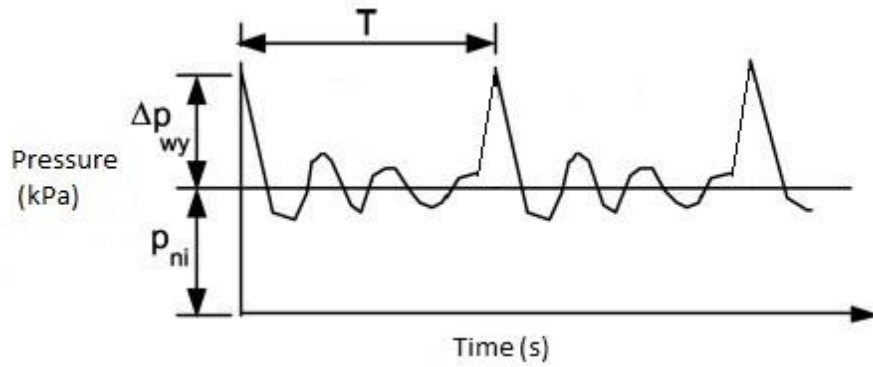


Figure 3-15: Shock waves at location z (Roberts 2003).

Roberts (1996) proposed that the following analytical formulae, to estimate the pulsation load and period in silos during discharge. It must be noted that the average shock plane H_s is located between $1.5D$ and $2D$.

$$\Delta p_{v0} = k_d \gamma \left[(1 - e^{-\mu K h / R}) \left(\frac{R}{\mu K} - h_s \right) + h_s \right] \quad \text{Equation 3-1}$$

$$\Delta p_{w0} = K \Delta p_{v0} \quad \text{Equation 3-2}$$

$$R = \frac{D}{2(I + m)} \quad \text{Equation 3-3}$$

$$h_s = \frac{H_s}{m + 2} \quad \text{Equation 3-4}$$

$$\Delta p_{wy} = \Delta p_{w0} e^{-\mu K \gamma / R} \quad \text{Equation 3-5}$$

$$T = \left(t_0 + \frac{v}{a} \right) + \sqrt{\frac{v}{a} \left(2t_0 + \frac{v}{a} \right)} \quad \text{Equation 3-6}$$

$$a = \frac{\Delta p_{v0}}{\gamma(h + h_s)} \quad \text{Equation 3-7}$$

$$v = \frac{Q}{\rho A} \quad \text{Equation 3-8}$$

$$t_0 = \frac{\Delta \varepsilon_y}{v} \quad \text{Equation 3-9}$$

The definitions for the variables in the above equations are as follow:

- $\gamma = \rho g$ = the bulk specific weight
- ρ = the bulk density
- h = the head
- K = the ratio of lateral to vertical pressure
- H_s = the actual surcharge head
- D = the diameter or width of flow channel
- m = silo shape factor i.e. 0 for rectangular and 1 for circular
- $\mu = \tan \phi$ = coefficient of wall friction
- ϕ = wall friction angle
- Δp_{v0} = maximum increment in the average vertical pressure due to the shock load
- Δp_{w0} = maximum increment in the average lateral pressure due to the shock load
- R = effective radius
- h_s = effective surcharge head
- Δp_{wy} = additional pulsation wall pressure applied to the initial or static pressure on each side of the shock surface
- k_r = ratio of shear to normal stress amplitude
- a = acceleration of upper mass during pulse motion
- v = average velocity of bulk solid in the cylinder during discharge
- Q = discharge rate
- t_0 = the time for motion of upper mass to be initiated
- $\Delta \varepsilon_y$ = dynamic displacement of consolidated mass in the vertical direction
- A = area of outlet

The formulae proposed by Roberts (1996) were compared against experimental results for a wheat silo, and it can be seen in Figure 3-16 that there exist strong correlations between measured and computed normal stress amplitude, similarly for measured and computed shear stress amplitude. However it must be noted that flow characteristics for wheat are different to that of other granular materials such as rice

and corn, and pressure fluctuations obtained are very sensitive to changes in the silo granular material system (Bennett and Kmita 1996). Furthermore, the formulae are more applicable to tall silos as it does not take into account of the convergence of the silo wall at the hopper.

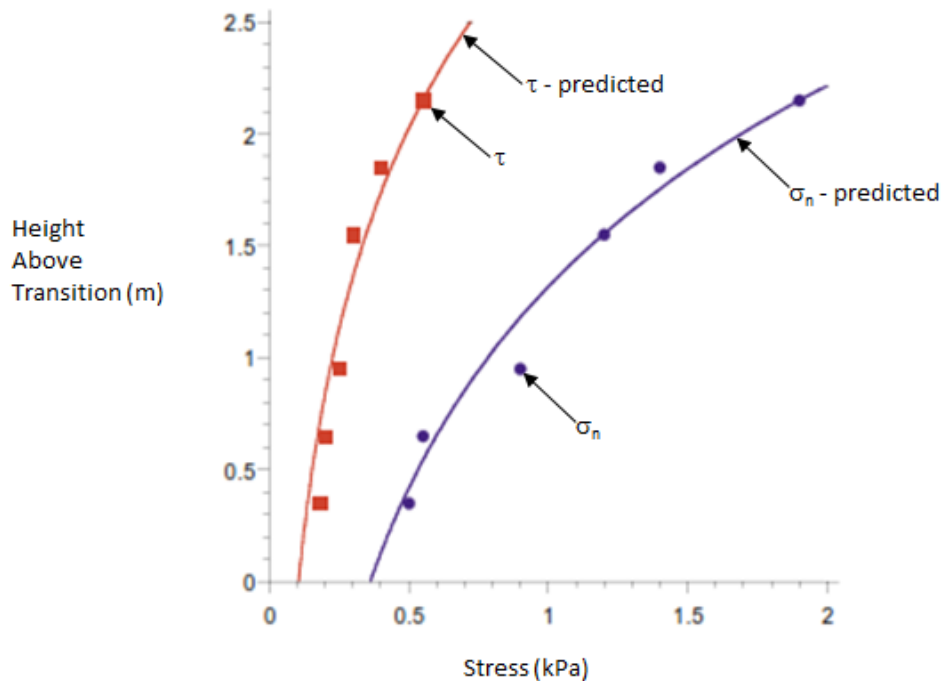


Figure 3-16: Comparison between measured and calculated normal and shear stress amplitudes for experimental wheat silo (Roberts and Wensrich 2002).

3.3.2 Dynamic Arches at Hopper Opening

It was pointed out by Brown and Richards (1959) that the flow of particles in nature is accompanied by the periodic collapsing phenomenon. The periodic collapsing phenomenon of solids flow inside the hopper was described by Shinohara et al. (1968) using the dynamic arch theory and was later investigated by Firewicz (1988). According to Shinohara et al. (1968), dynamic arch is the terminology used to describe the behaviour of falling particles inside the hopper where the falling

granules lose their velocities, form blocks and then drop freely down at the dynamic arch.

According to Shinohara et al. (1968), the arching phenomena can be classified as static and dynamic arches. The term static arch or sometimes called dome or bridge is a condition where the material forms an arch across the hopper opening thus stopping the material flow completely as shown in Figure 3-17 (Shinohara et al. 1968). Whereas, according to Shinohara et al. (1968), the dynamic arch describes the instantaneous formation and collapses of the arch which does not block the flow.

DYNAMIC ARCHING ACROSS HOPPER OPENING

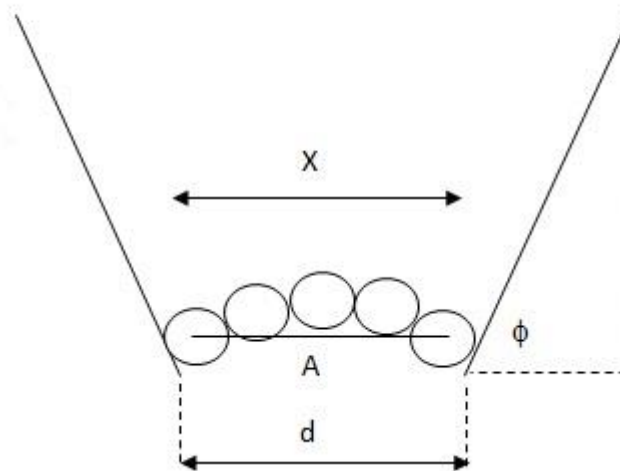


Figure 3-17: Arch forms across the hopper opening (To 2005).

Shinohara et al. (1968) suggested Equation 3-10 to calculate the flow rate F from hoppers where the solids make a discoidal block of similar diameter to the conical hopper outlet as illustrated in Figure 3-18.

$$F = n \left(\frac{\pi}{4} D_o^2 l \right) p_b \quad \text{Equation 3-10}$$

$$l = \frac{\left(\frac{\tau_T}{\tau_S} D_o \right)}{\left(\frac{D_o \rho_b}{\tau_S} - 4 \right)} \quad \text{Equation 3-11}$$

$$n = \frac{\sqrt{2gS_A}}{l} \left(\frac{1 - \epsilon_0}{1 - \epsilon_A} \right) \quad \text{Equation 3-12}$$

$$S_A = \sqrt[3]{\frac{f^2}{16} D_o^{4/3} k^{-4/3}} \quad \text{Equation 3-13}$$

$$f = \frac{\sqrt{2g}}{\mu_A} \left(\frac{1 - \epsilon_0}{1 - \epsilon_A} \right) \quad \text{Equation 3-14}$$

$$k = \tan \frac{\theta}{2} \quad \text{Equation 3-15}$$

The definitions for the variables in the equations shown above are as follow:

- n is the collapsing frequency as shown in Equation 3-12
- l is the thickness of the falling particle layer Equation 3-11
- ρ_b is the bulk density of the disk
- D_o is the size of the opening as shown in Figure 3-18
- ϵ_0 is the void fraction of the material at the opening
- ϵ_A is the overall void fraction of the material at the section
- g is the gravity 9.81m/s^2
- S_A is the location of the dynamic arch
- τ_T is the shear strength of the horizontal plane of rupture of the disk
- τ_S is the shear strength of the vertical yield plane
- f is the flow constant

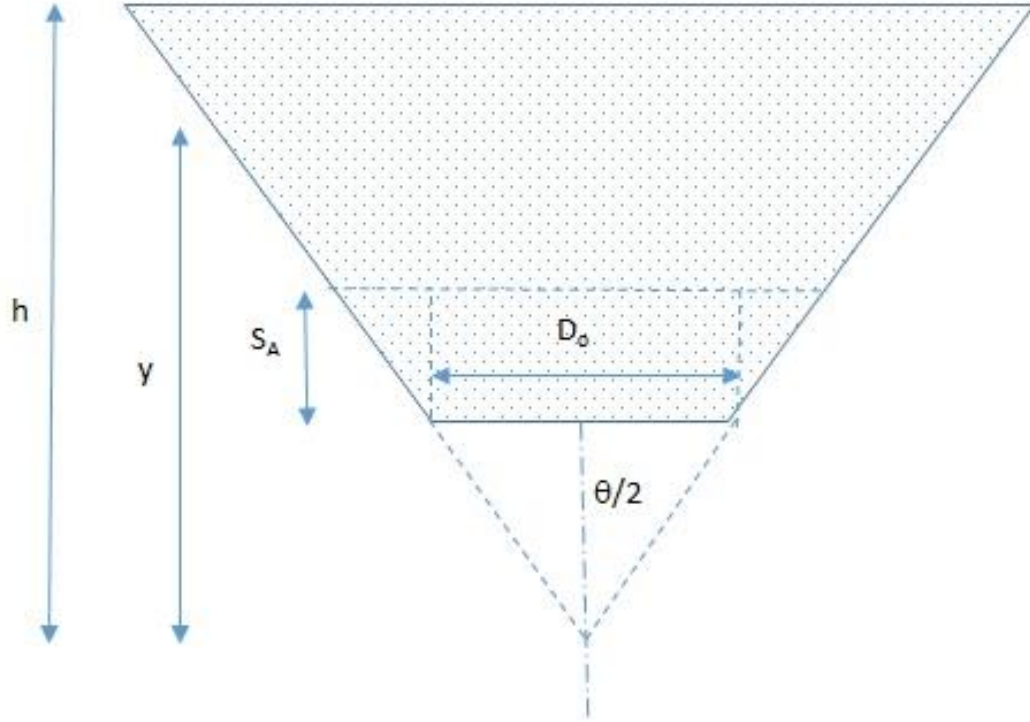


Figure 3-18: Symbols for the hopper (Shinohara et al. 1968).

Firewicz (1988) investigated the equations proposed by Shinohara et al. (1968) and proposed the following refined equations to estimate the flow rates, the height of the dynamic arch above the orifice and the average velocity of the particles:

$$S_{A_{\text{mino}}} = \left(\frac{D_o \sqrt{f_{\text{mino}}}}{8k} \right)^{4/3} \quad \text{Equation 3-16}$$

$$f_{\text{mino}} = \left(\frac{8}{3} \right)^{3/2} \left(\frac{k}{D_o} \right)^{1/2} \quad \text{Equation 3-17}$$

$$\frac{F_o}{\varphi_b \sqrt{g} d_p^{2.5}} = 0.453 \left(\tan \frac{\theta}{2} \right)^{-0.5} \left(\frac{D_o}{d_p} \right)^{2.5} \quad \text{Equation 3-18}$$

$$f = 0.325 \sqrt{g} \left(\frac{D_o}{k} \right)^{0.5} \left(\frac{1 - \epsilon_0}{1 - \epsilon_A} \right) \quad \text{Equation 3-19}$$

$$n = \frac{1}{\sqrt{3}} \sqrt{\frac{g D_o}{k}} \frac{1}{l} \left(\frac{1 - \epsilon_0}{1 - \epsilon_A} \right) \quad \text{Equation 3-20}$$

$$k = \tan \frac{\theta}{2} \quad \text{Equation 3-21}$$

$$Y = g(S_A) \quad \text{Equation 3-22}$$

The definitions for the variables in the equations shown above are as follow:

- $S_{A_{\text{mino}}}$ is the height of the dynamic arch at which function Y in Equation 3-22 reaches minimum or zero
- S_A is the height of the dynamic arch above the opening
- θ is the hopper half angle
- ε_0 is the void fraction of the material at the opening
- ε_A is the overall void fraction of the material at the section
- l is the thickness of the falling particle layer
- f_{mino} is the expression at which function Y shown in Equation 3-22 reaches minimum and zero
- g is the gravitational acceleration
- D_o is the size of the opening
- d_p is the average particle diameter
- φ_p is the bulk density of the solids

Firewicz (1988) compared the results obtained from the proposed equations and found that the collapsing frequency was similar to values observed by other researchers. It was also confirmed by Firewicz (1988) that discharge of particulate solids from silos is pulsating rather than continuous and the existence of the dynamic arch. This dynamic arch is formed for a short period and collapses.

The formulae presented by Shinohara et al. (1968) and Firewicz (1988) describe the pulsating flow at the hopper opening due to the formation and collapse of the dynamic arch above the opening thus can be applied to many types of silos. It is evident when inspecting Figure 3-11 to Figure 3-12 where the pulsations were recorded in the hopper region of the experimental silo.

3.4 Numerical Modelling of Silo Quaking

As described by Jaeger, Nagel, and Behringer (1996) there are three types of granular flows; rapid flow, quasi-static flow and transitional flow. During rapid flow, the particles collide with each other and collide with the silo wall material which in turn develop the internal stresses (Tejchman and Wojcik 2011). In quasi-static and transitional flows, the stresses arise due to friction between the particles and the materials (Tejchman and Wojcik 2011). Currently, there are two theoretical models, continuum and dis-continuum mechanics, commonly employed to model the flow of granules from silos and associated dynamic effects called silo quaking. According to Tejchman and Wojcik (2011), the continuum mechanic models are well suited for flow with low deformation rates and discontinuum mechanic models are more suitable for rapid flow.

Continuum mechanics was first formulated by a French mathematician named Augustin Louis Cauchy in the 19th century and is still an active research topic (Quinn 2012). Irgens (2008) described it as a special branch of Physics in which matter is treated by the same theory irrespective of phase or structure for example solids, liquids and gases and its macroscopic properties are described by constitutive equations. The finite element method (FEM) in recent years has gained much attention, developed and currently is a popular numerical method used to model continuum mechanical problems (Sarhosis et al. 2016).

As postulated by Tejchman (1998a), the existing continuum theories do not realistically describe the material behaviour during silo flow because these theories were derived from methods of plasticity and elasticity. The numerical methods founded on the theory of plasticity, total plastification of the fill in the silo is assumed, which is not realistic. Whereas, the numerical methods founded on the theory of elasticity, are not thoroughly verified by experiments. Furthermore, it is assumed that wall friction angle along the silo wall, determined by wall shear tests, remains constant (Tejchman 1998a). However, it was found by Tejchman (1989),

that the wall friction angle changes during shearing and was affected by the boundary conditions of the entire silo.

According to Tejchman (1998a), the numerical methods proposed by Häussler and Eibl (1984) and Tano, Godoy, and Diez (1994) were more realistic than analytical formulae. However, improvements needed to be made to the proposed numerical models to realistically simulate the silo quaking phenomena such as:

- mesh size independence,
- inertial forces,
- cohesive characteristics of granules,
- material softening at shear zones, and
- wall roughness.

The discontinuum concept, unlike the continuum concept, emphasises the microstructure of certain length scale (Mohammadi 2004). The field of discontinuum mechanics is a relatively new discipline and is becoming popular due to the availability of powerful computing hardware (Zhao 2015). Mechanics of Discontinua have been used to solve problems such as packing of particles, particle flow, particle consolidation, fracture, fragmentation and progressive collapse of structures. According to Mohammadi (2004), the concepts of continuum mechanics which are often described using differential equations, whereas the concepts of discontinuum mechanics are described by interactions between individual particles and behaviour of these particles. A popular numerical tool to model discontinuum problems is the Discrete Element Method (DEM).

3.4.1 Finite Element Method

The Finite Element Method (FEM) is a numerical method commonly employed to solve field problems represented by partial differential equations (Smith 2004; Cook 1995; Cook et al. 2002). According to Moaveni (2008) and Rao (2011), the concept of finite element dates back several centuries. Courant (1940) used a piecewise polynomial interpolation technique to investigate the torsion and was subsequently credited for being the first person to develop the finite element method. It was not until the 1950s that the aerospace industry began to develop the concept to analyse weight-critical framed structures (Khennane 2013). Since it was conceptualised by Clough (1960), the FEM has been developed for use in civil engineering structures, aircraft structures, geotechnical engineering, hydrodynamics, nuclear engineering, biomedical engineering, mechanical engineering and electrical engineering. In modern days, the structural design of a complex structure is often performed by FEM.

According to Rao (2011), the basic fundamental behind the FEM is to find the solution to a complex problem by simplifying the problem. Given that the actual problem is simplified, the solution to such problem will always be approximate rather than exact and is limited by the existing mathematical tools (Rao 2011). As stated by Rao (2011), in the FEM, the continuum of the complicated problem is represented by an assemblage of finite elements. As such, those elements are interconnected at their shared nodal points, and the nodes are usually on the element's boundary.

Furthermore, it is assumed that the actual field variables inside the continuum such as displacement, stress, strain, temperature, acceleration, velocity and pressure can be approximated by summing the field variables of the finite elements representing the continuum. The field variables inside the element are determined by a simple approximation function. The approximation function defines the field values of the element at their nodes. As such, these field equations are assembled into matrix notations and solved accordingly.

The finite elements are often used to idealise the real structure and often found in commercial codes are bar element, 2D beam element, 3D beam element, constant strain and linear strain triangle, bilinear and quadratic rectangle, four nodes and ten nodes tetrahedral, eight node and 20 node brick. Equation 3-23 represents the equilibrium condition for the individual finite element where the elemental stiffness matrix $[k]$ for such elements is formed by using Equation 3-24. Finally, the finite elements are assembled at the common nodes thus forming the global stiffness matrix $[K]$, global displacement matrix $[D]$ and global load matrix $[R]$ as shown in Equation 3-25.

$$[k][d] = [r_e] \quad \text{Equation 3-23}$$

$$[k] = \int [B^T][E][B]dV \quad \text{Equation 3-24}$$

$$[K][D] = [R] \quad \text{Equation 3-25}$$

Where:

- $[B]$ is the strain-displacement matrix.
- $[E]$ is the constitutive matrix.
- dV is the increment of the element volume V .
- $[k]$ is the elemental stiffness matrix determined from element shape function.
- $[d]$ is the elemental displacement matrix.
- $[r_e]$ is the elemental nodal load matrix determined from element shape function.

As described by Liu (2013), the displacements within the finite element are calculated by interpolation using the elemental nodal displacements and are illustrated in Equation 3-26, Equation 3-27, Equation 3-28, Equation 3-29 and Equation 3-30.

$$U^h(x, y, z) = \sum_{i=1}^{n_d} N_i(x, y, z) d_i = N(x, y, z) d_e \quad \text{Equation 3-26}$$

$$d_i = \begin{Bmatrix} d_1 \\ d_2 \\ \vdots \\ d_{n_f} \end{Bmatrix} \quad \text{Equation 3-27}$$

$$d_e = \begin{Bmatrix} d_1 \\ d_2 \\ \vdots \\ d_{n_d} \end{Bmatrix} \quad \text{Equation 3-28}$$

$$N(x, y, z) = [N_1(x, y, z) \ N_2(x, y, z) \ \dots \ N_{n_d}(x, y, z)] \quad \text{Equation 3-29}$$

$$N_i = \begin{bmatrix} N_{i1} & 0 & 0 & 0 \\ 0 & N_{i2} & 0 & 0 \\ 0 & 0 & \ddots & 0 \\ 0 & 0 & 0 & N_{in_f} \end{bmatrix} \quad \text{Equation 3-30}$$

Where:

- U^h is the approximation for the displacement component in the x, y and z direction of the finite element.
- n_d is the number of nodes in the element.
- d_i is the nodal displacement at the i^{th} node.
- d_e is the nodal displacement for the whole element.
- n_f is the number of degrees of freedom at a node.
- N is the matrix of shape functions for the nodes in the element.
- N_i is the sub-matrix of shape functions for displacement components.
- N_{ik} shown in Equation 3-30 is the shape function of the k^{th} displacement component at the i^{th} node.

The displacement component of an element at a node can be estimated by a linear combination of n_d linear and independent basis functions $p_i(x)$ as shown in the equation below.

$$u^h(x) = \sum_{i=1}^{n_d} p_i(x) \alpha_i = p^T(x) \alpha^T \quad \text{Equation 3-31}$$

$$\alpha^T = \{ \alpha_1, \alpha_2, \dots, \alpha_{n_d} \} \quad \text{Equation 3-32}$$

$$p^T(x) = \{ 1, x, x^2, x^3, \dots, x^p \} \quad \text{Equation 3-33}$$

Where:

- u^h is the approximated value of the displacement component x .
- $p_i(x)$ is the basis function of monomials in the space coordinates x derived from the Pascal's triangle illustrated in Figure 3-19.
- α_i is the coefficient for the monomial $p_i(x)$.

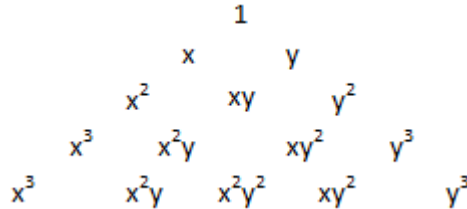


Figure 3-19: 2D Pascal's triangle.

The coefficient α can be determined by Equation 3-37.

$$d_i = p^T(x_i) \alpha \quad \text{Equation 3-34}$$

$$d_e = P \alpha \quad \text{Equation 3-35}$$

$$P = \begin{bmatrix} p_1(x_1) & p_1(x_1) & \dots & p_1(x_1) \\ p_1(x_1) & p_1(x_1) & \dots & p_1(x_1) \\ \vdots & \vdots & \ddots & \vdots \\ p_1(x_1) & p_1(x_1) & \dots & p_1(x_1) \end{bmatrix} \quad \text{Equation 3-36}$$

$$\alpha = P^{-1} d_e \quad \text{Equation 3-37}$$

$$u^h(x) = \sum_{i=1}^{n_d} N_i(x) d_i \quad \text{Equation 3-38}$$

Where:

- P is the moment matrix consisting of monomials derived from the Pascal's triangle shown in Figure 3-19.

Once the nodal forces have been determined, the stresses and strains in the element can be calculated by the material's constitutive equations. As such, the constitutive equation, according to Liu (2013), specifies the stress-strain relationship in the material of concern.

According to Hooke's law, the stress tensor is related to the strain tensor as shown in Equation 3-39 where σ and ε are the stress tensor and strain tensor respectively and c is the matrix of material constants illustrated in Equation 3-40 are often determined in experiments. The matrix notations of the typical generalised Hooke's law are illustrated in Equation 3-40. Furthermore, the directions of normal and shear components of stress in three dimensions are illustrated in Figure 3-20.

$$\sigma = c\varepsilon \quad \text{Equation 3-39}$$

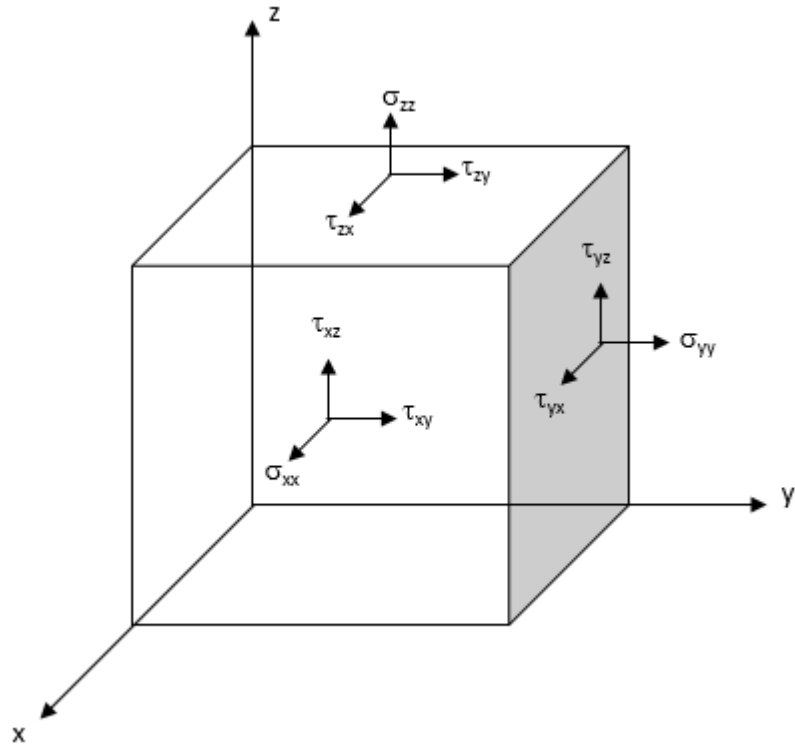


Figure 3-20: 3D stress block.

$$\begin{Bmatrix} \sigma_{xx} \\ \sigma_{yy} \\ \sigma_{zz} \\ \tau_{yz} \\ \tau_{xz} \\ \tau_{xy} \end{Bmatrix} = \begin{bmatrix} c_{11} & c_{12} & c_{13} & c_{14} & c_{15} & c_{16} \\ c_{21} & c_{22} & c_{23} & c_{24} & c_{25} & c_{26} \\ c_{31} & c_{32} & c_{33} & c_{34} & c_{35} & c_{36} \\ c_{41} & c_{42} & c_{43} & c_{44} & c_{45} & c_{46} \\ c_{51} & c_{52} & c_{53} & c_{54} & c_{55} & c_{56} \\ c_{61} & c_{62} & c_{63} & c_{64} & c_{65} & c_{66} \end{bmatrix} \begin{Bmatrix} \epsilon_{xx} \\ \epsilon_{yy} \\ \epsilon_{zz} \\ \epsilon_{yz} \\ \epsilon_{xz} \\ \epsilon_{xy} \end{Bmatrix} \quad \text{Equation 3-40}$$

The strain matrix ϵ can be written as follows:

$$\epsilon = LU \quad \text{Equation 3-41}$$

$$U = \begin{Bmatrix} u \\ v \\ w \end{Bmatrix} \quad \text{Equation 3-42}$$

$$L = \begin{bmatrix} \partial/\partial x & 0 & 0 \\ 0 & \partial/\partial y & 0 \\ 0 & 0 & \partial/\partial z \\ 0 & \partial/\partial z & \partial/\partial y \\ \partial/\partial z & 0 & \partial/\partial x \\ \partial/\partial y & \partial/\partial x & 0 \end{bmatrix} \quad \text{Equation 3-43}$$

Where:

- u, v, w are displacements in the x, y, z directions respectively.
- U is the displacement vector.
- L is a matrix of partial differential operators.

The finite element method coupled with various constitutive models such as Polar Elasto-Plastic, Hypoplastic and Polar Hypoplastic have been developed and adopted by various researchers such as Tejchman and Gudehus (1993b), Tejchman (1995), Tejchman (1998a), Tejchman (1998b), Roberts and Wensrich (2002), Wensrich (2003), Wilde, Rucka, and Tejchman (2008), Wilde et al. (2010) and Tejchman and Wojcik (2011) to estimate the dynamic characteristics of silos during discharge commonly known as silo quaking.

3.4.1.1 Micro-polar Elasto-Plastic Constitutive Model

Mühlhaus (1989) combined the Cosserat (micro-polar continuum) theory with a conventional elastoplastic constitutive model to analyse limit load problems in blocky materials and subsequently the formulation was named micro-polar elastoplastic constitutive model. As such, the inclusion of the micro-polar continuum mechanics allows for independent rotations in the kinematics as described by Mindlin (1963). The model proposed by Mühlhaus (1989), which uses the mean grain diameter as a characteristic length, also allows for isotropic hardening, isotropic softening and couple stresses (Tejchman 2013). As such, the constitutive model according to Tejchman (2013) is summarised as follows:

$$\dot{\varepsilon}_{ij} = \dot{\varepsilon}_{ij}^e + \dot{\varepsilon}_{ij}^p \quad \text{Equation 3-44}$$

$$\dot{\kappa}_i = \dot{\kappa}_i^e + \dot{\kappa}_i^p \quad \text{Equation 3-45}$$

$$\varepsilon_{ij} = \frac{1}{E} [(1 + \nu)\sigma_{ij} - \nu\sigma_{kk}], \quad i = k \quad \text{Equation 3-46}$$

$$\varepsilon_{ij}^e = \frac{1}{2G} \frac{\partial \tau^2}{\partial \sigma_{ij}}, \quad \kappa_i^e = \frac{1}{2G} \frac{\partial \tau^2}{\partial m_i} \quad i \neq j \quad \text{Equation 3-47}$$

$$\varepsilon_{ij}^p = \lambda \frac{\partial g}{\partial \sigma_{ij}}, \quad \kappa_i^p = \lambda \frac{\partial g}{\partial m_i} \quad \text{Equation 3-48}$$

$$\tau = \left(a_1 s_{ij} s_{ji} + a_2 s_{ij} s_{ji} + \frac{a_3}{d_{50}^2} m_i m_i \right)^{0.5} \quad \text{Equation 3-49}$$

$$f = \tau + \mu(e_0, \gamma^p) p - c \quad \text{Equation 3-50}$$

$$g = \tau + \alpha(e_0, \gamma^p) p \quad \text{Equation 3-51}$$

$$s_{ij} = \sigma_{ij} - p \delta_{ij} \quad \text{Equation 3-52}$$

$$a_1 = 3/8 \quad \text{Equation 3-53}$$

$$a_2 = 1/8 \quad \text{Equation 3-54}$$

$$a_3 = 1 \quad \text{Equation 3-55}$$

$$\mu = \sin \phi \quad \text{Equation 3-56}$$

$$\alpha = \sin \beta \quad \text{Equation 3-57}$$

Where:

- τ is the second invariant of the deviatoric stress tensor.
- s_{ij} is the non-symmetric deviatoric stress tensor.
- p is the mean stress.
- σ_{ij} is the stress tensor.
- m_i is the couple stress vector.

- a_1, a_2, a_3 are coefficients.
- d_{50} is the mean grain diameter.
- f is the yield function.
- g is the potential function.
- μ is the mobilised friction factor.
- α is the mobilised dilatancy factor.
- ϕ is the angle of internal friction.
- β is the angle of dilatancy.
- c is the cohesion factor.
- e_0 is the initial void ratio.
- γ^p is the plastic shear deformation.
- ε_{ij} is the deformation tensor.
- $\dot{\varepsilon}_{ij}$ is the rate of deformation tensor.
- κ_i is the curvature vector.
- $\dot{\kappa}_i$ is the rate of curvature vector.
- λ is the proportionality factor.
- E is the elastic modulus.
- G is the shear modulus.
- ν is the Poisson ratio.
- δ_{ij} is the Kronecker delta.
- ^e denotes elastic strain or curvature.
- ^p denotes plastic strain or curvature.

According to Tejchman (2013), it was found by various researchers that micro-polar elastoplastic constitutive formulation gave comparable results to experimental values and also that the numerical results were independent of the finite element mesh.

3.4.1.2 Hypoplasticity Constitutive Model

Rate dependent formulation which later became hypoplasticity constitutive formulation, an alternative to elastoplastic constitutive model, was introduced by Kolymbas (1977) and developed by various authors such as Wu, Bauer, and Kolymbas (1996) for analysis of granular materials. According to Tejchman (2013), the hypoplasticity constitutive model considers the necessary mechanical properties of the granules observed during homogeneous deformations. Furthermore, according to Kolymbas (1999), the hypoplasticity formulation is much simpler than elastoplasticity formulation owing to the fact that it avoids notions such as yield surface and plastic potential which appear in elastoplasticity. The other important fact is that the unique equation that describes hypoplasticity holds true for both loading and unloading states because the failure surface and flow rule, rather than prescribed, emerge as by-products (Wu and Niemunis 1996, 1997). Thus, the hypoplasticity formulation is simpler to implement into numerical algorithms. Gudehus (1996) and Bauer (1996) introduced a general hypoplastic constitutive formulation and calibration parameters respectively for granular materials as shown in Equation 3-58.

$$\dot{\hat{T}}_s = f_s \left[L(\hat{T}_s, D_s) + f_d N(\hat{T}_s) \|D_s\| \right] \quad \text{Equation 3-58}$$

$$\hat{T}_s = \frac{T_s}{tr T_s} \quad \text{Equation 3-59}$$

$$\|D_s\| = \sqrt{tr D_s^2} \quad \text{Equation 3-60}$$

$$f_d = \left(\frac{e - e_d}{e_c - e_d} \right)^\alpha \quad \text{Equation 3-61}$$

$$f_b = \frac{h_s}{nh_i} \left(\frac{1+e_i}{e_i} \right) \left(\frac{3p_s}{h_s} \right)^{1-n}$$

Equation 3-62

$$f_s = \frac{h_s}{nh_i} \left(\frac{1+e_i}{e_i} \right) \left(\frac{e_i}{e} \right)^\beta \left(\frac{3p_s}{h_s} \right)^{1-n}$$

Equation 3-63

$$p_s = \frac{-trT_s}{3}$$

Equation 3-64

$$h_i = \frac{1}{c_1^2} + \frac{1}{3} - \left(\frac{e_{i0} - e_{d0}}{e_{c0} - e_{d0}} \right)^\alpha \frac{1}{c_1 \sqrt{3}}$$

Equation 3-65

$$L(\hat{T}_s, D_s) = a_1^2 D_s + \hat{T}_s tr(\hat{T}_s, D_s)$$

Equation 3-66

$$N(\hat{T}_s) = a_1 (\hat{T}_s + \hat{T}_s^*)$$

Equation 3-67

$$\hat{T}_s^* = \hat{T}_s - \frac{1}{3} \delta$$

Equation 3-68

$$a_1^{-1} = c_1 + c_2 \left\| \hat{T}_s^* \right\| [1 + \cos(3\theta)]$$

Equation 3-69

$$c_1 = \sqrt{\frac{3}{8}} \frac{(3 - \sin \phi_c)}{\sin \phi_c}$$

Equation 3-70

$$c_2 = \frac{3}{8} \frac{(3 + \sin \phi_c)}{\sin \phi_c}$$

Equation 3-71

Where:

- \hat{T}_s denotes the granulate stress ratio tensor and it has the same principal axes as T_s .
- $\|D_s\|$ is the Euclidean norm of D_s .
- T_s is the Cauchy granulate stress tensor.
- D_s is the stretching tensor of the granulate skeleton D_s .
- f_d is the density factor.
- e is the void ratio.
- e_c is the critical void ratio.
- e_d is the void ratio of maximum densification.
- α is a material constant ($0 < \alpha < 1$) which can be found from a triaxial test with a compacted specimen (Tejchman 2005).
- β is a material constant which can be found from a triaxial test with a compacted specimen (Tejchman 2005).
- f_b is the pressure dependent factor.
- p_s is the mean pressure.
- h_i is the constant for the pressure dependent factor f_b .
- a_l is the dimensionless scalar factor.
- L is the tensorial function.
- N is the tensorial function.
- δ is the Kronecker delta.
- e_i is the maximum void ratio.
- e_{i0} is the maximum void ratio when mean pressure (p_s) is 0.
- e_{c0} is the critical void ratio when mean pressure (p_s) is 0.
- e_{d0} is the minimum void ratio when mean pressure (p_s) is 0.
- h_s is the granulate hardness (the slope of the graph) estimated from the oedometric compression test with an initially uncompact specimen (Tejchman 2005).
- n is the curvature of the semi-logarithmic representation of the oedometric compression test (Tejchman 2005).
- θ is the Lode angle which is the angle on the deviatoric plane between the stress vector and the axis of the principle stress (Tejchman 2013).
- ϕ_c is the critical friction angle (Tejchman 2005).

- c_1 is the dimensionless constant.
- c_2 is the dimensionless constant.

As outlined by Tejchman (2013), the hypoplastic constitutive model requires material parameters such as α , β , ϕ_c , e_{i0} , e_{c0} , e_{d0} , h_s and n . Comprehensive calibration tests to determine these parameters are outlined by Herle and Gudehus (1999), Bauer (1996) and Tejchman (2005).

3.4.1.3 Micro-Polar Hypoplasticity Constitutive Model

As previously mentioned, the inclusion of the micro-polar continuum allows for independent rotations in the kinematics described by Mindlin (1963). According to Tejchman (2005), each material point for a plane strain element has a total of three degrees of freedom, where u_1 and u_2 are translational degrees of freedom and ω is the rotational degrees of freedom. As such, ω is related to the micro-rotation of the micro-element. The micro-polar continuum model considers both the micro and macro deformations.

As described by Tejchman and Bauer (2005) the gradients of the rotation are connected to the curvatures associated with coupled stresses. Consequently, leading to a non-symmetrical stress tensor and a characteristic length related to the mean grain diameter (Tejchman and Bauer 2005). The micro-polar hypoplasticity constitutive formation described below has proven to be an effective numerical method for simulating various kinematics of granular materials by Tejchman (1998c), Tejchman and Ummenhofer (2000), Tejchman and Gudehus (2001), Huang, Nübel, and Bauer (2002), Tejchman (2002), Huang and Bauer (2003), Tejchman (2004), Tejchman and Bauer (2005), Tejchman and Wu (2007) and Tejchman and Górski (2008).

$$\hat{\sigma}_{ij} = f_s \left[\begin{array}{l} L_{ij} \left(\hat{\sigma}_{kl}, \hat{m}_k \cdot d_{kl}^c, k_k, d_{50} \right) + \\ f_d N_{ij} \left(\hat{\sigma}_{ij} \right) \sqrt{d_{kl}^c d_{kl}^c + k_k k_k d_{50}^2} \end{array} \right] \quad \text{Equation 3-72}$$

$$\frac{\circ m_i}{d_{50}} = f_s \left[\begin{array}{l} L_{ij}^c \left(\hat{\sigma}_{kl}, \hat{m}_k \cdot d_{kl}^c, k_k, d_{50} \right) + \\ f_d N_i^c \left(\hat{m}_i \right) \sqrt{d_{kl}^c d_{kl}^c + k_k k_k d_{50}^2} \end{array} \right] \quad \text{Equation 3-73}$$

$$\dot{\sigma}_{ij} = \dot{\sigma}_{ij} - w_{ik} \sigma_{kj} + \sigma_{ik} w_{kj} \quad \text{Equation 3-74}$$

$$\dot{m}_i = \dot{m}_i - 0.5 w_{ik} m_k + 0.5 m_k w_{ik} \quad \text{Equation 3-75}$$

$$\dot{e} = (1+e) d_{kk} \quad \text{Equation 3-76}$$

$$d_{ij}^c = d_{ij} + w_{ij} - w_{ij}^c \quad \text{Equation 3-77}$$

$$k_i = w_{j,i}^c \quad \text{Equation 3-78}$$

$$w_{kk}^c = 0 \quad \text{Equation 3-79}$$

$$w_{21}^c = -w_{21}^c = w^c \quad \text{Equation 3-80}$$

$$d_{ij} = \frac{(v_{i,j} + v_{j,i})}{2} \quad \text{Equation 3-81}$$

$$w_{ij} = \frac{(v_{i,j} - v_{j,i})}{2}$$

Equation 3-82

$$\hat{\sigma}_{ij} = \frac{\sigma_{ij}}{\sigma_{kk}}$$

Equation 3-83

$$\hat{m}_k = \frac{m_k}{\sigma_{kk} d_{50}}$$

Equation 3-84

$$f_d = \left(\frac{e - e_d}{e_c - e_d} \right)^\alpha$$

Equation 3-85

$$f_s = \frac{h_s}{nh_i} \left(\frac{1+e_i}{e_i} \right) \left(\frac{e_i}{e} \right)^\beta \left(-\frac{\sigma_{kk}}{h_s} \right)^{1-n}$$

Equation 3-86

$$h_i = \frac{1}{c_1^2} + \frac{1}{3} - \left(\frac{e_{i0} - e_{d0}}{e_{c0} - e_{d0}} \right)^\alpha \frac{1}{c_1 \sqrt{3}}$$

Equation 3-87

$$e_i = e_{i0} \exp \left[- \left(-\frac{\sigma_{kk}}{h_s} \right)^n \right]$$

Equation 3-88

$$e_d = e_{d0} \exp \left[- \left(-\frac{\sigma_{kk}}{h_s} \right)^n \right]$$

Equation 3-89

$$e_c = e_{c0} \exp \left[- \left(-\frac{\sigma_{kk}}{h_s} \right)^n \right]$$

Equation 3-90

$$L_{ij} = a_1^2 d_{ij}^c + \hat{\sigma}_{ij} \left(\hat{\sigma}_{kl} d_{kl}^c + \hat{m}_k k_k d_{50} \right) \quad \text{Equation 3-91}$$

$$L_i^c = a_1^2 \left[k_i d_{50} + \hat{m}_i \left(\hat{\sigma}_{kl} d_{kl}^c + \hat{m}_k k_k d_{50} \right) \right] \quad \text{Equation 3-92}$$

$$N_{ij} = a_1 \left(\hat{\sigma}_{ij} + \hat{\sigma}_{ij}^* \right) \quad \text{Equation 3-93}$$

$$N_i^c = a_1^2 a_c \hat{m}_i \quad \text{Equation 3-94}$$

$$\hat{\sigma}_{ij}^* = \hat{\sigma}_{ij} - \frac{1}{3} \delta_{ij} \quad \text{Equation 3-95}$$

$$a_1^{-1} = c_1 + c_2 \sqrt{\hat{\sigma}_{kl}^* \hat{\sigma}_{lk}^*} [1 + \cos(3\theta)] \quad \text{Equation 3-96}$$

$$\cos(3\theta) = - \frac{\sqrt{6}}{\left[\hat{\sigma}_{kl}^* \hat{\sigma}_{kl}^* \right]^{1.5}} \left(\hat{\sigma}_{kl}^* \hat{\sigma}_{lm}^* \hat{\sigma}_{mk}^* \right) \quad \text{Equation 3-97}$$

$$c_1 = \sqrt{\frac{3}{8}} \frac{(3 - \sin \phi_c)}{\sin \phi_c} \quad \text{Equation 3-98}$$

$$c_2 = \frac{3}{8} \frac{(3 + \sin \phi_c)}{\sin \phi_c} \quad \text{Equation 3-99}$$

Where (some notations are repeated for completeness):

- σ_{ij} denotes Cauchy skeleton (effective) stress tensor.
- d_{kl} is the rate of deformation tensor.

- $\|d_{kl}\|$ is the Euclidian norm $\sqrt{d_{kl}d_{kl}}$.
- $\hat{\sigma}_{ij}$ is the normalised stress tensor.
- $\hat{\sigma}_{ij}^*$ is the deviatoric part of the normalised stress tensor
- \hat{m}_k is the normalised couple stress tensor
- m_k is the couple stress tensor.
- m_i is the Cauchy couple stress vector.
- $\overset{\circ}{m}_i$ is the Jaumann couple stress rate vector.
- $\overset{\circ}{d}_{ij}^c$ is the polar rate of deformation tensor.
- w^c is the rate of Cosserat rotation.
- k_i is the rate of the curvature vector
- a_c is the micro-polar constant.
- d_{50} is the mean grain diameter.
- L is the tensorial function.
- N is the tensorial function.
- d_{ij} is the deformation tensor.
- w_{ij} is the spin tensor.
- $v_{i,j}$ is the material velocity
- $v_{j,i}$ is the material velocity.
- \dot{e} is the rate of the void ratio
- d_{kk} is the rate of deformation.
- σ_{kk} is the applied stress.
- k_k is the rate curvature tensor.
- f_d is the density factor.
- e is the void ratio.
- e_c is the critical void ratio.
- e_d is the void ratio of maximum densification.
- α is a material constant ($0 < \alpha < 1$) which can be found from a triaxial test with a dense specimen (Tejchman 2005).

- β is a material constant which can be found from a triaxial test with a compacted specimen (Tejchman 2005).
- f_b is the pressure dependent factor.
- h_i is the constant for the pressure dependent factor f_b .
- a_I is the dimensionless scalar factor.
- δ_{ij} is the Kronecker delta.
- e_i is the maximum void ratio.
- e_{i0} is the maximum void ratio when σ_{kk} is 0.
- e_{c0} is the critical void ratio when σ_{kk} is 0.
- e_{d0} is the minimum void ratio when σ_{kk} is 0.
- h_s is the granulate hardness (the slope of the graph) estimated from oedometric compression test with an initially uncompact specimen (Tejchman 2005).
- n is the curvature of the semi-logarithmic representation of the oedometric compression test (Tejchman 2005).
- θ is the Lode angle which is the angle on the deviatoric plane between the stress vector and the axis of the principle stress (Tejchman 2013).
- ϕ_c is the critical friction angle (Tejchman 2005).
- c_1 is the dimensionless constant.
- c_2 is the dimensionless constant.

Lin and Wu (2016) conducted numerical studies of a simple shear test and biaxial shear test to compare the Discrete Element Method (DEM) and FEM coupled with the micro-polar hypoplastic constitutive model. The presence of the characteristic length in micro-polar hypoplastic model enabled it to predict the width of the shear band. It was concluded that the micro-polar hypoplastic model could reproduce the microscopic material behaviour similar to DEM. However, the FEM coupled with the micro-polar hypoplastic constitutive model was found to be much less computing intensive.

3.4.2 Discrete Element Method

The Discrete Element Method (DEM), a numerical method, was first introduced by Cundall (1971) to simulate progressive movements of rock. In 1979, Cundall and Strack (1979) used a computer program created by Cundall (1978) to analyse circular disks and spheres. The method was developed further as to take advantage of the availability of faster computer hardware to solve real physics and industrial size problems.

The granular material in a silo is considered to be made up of many discrete particles that interact as they flow out of the silo. The linear and angular momentum of each particle are governed by the differential equation of motions Equation 3-100 and Equation 3-101 (Remias 1998). At each time step, the total forces acting on individual particles, total forces acting on the silo wall, velocities and positions for each particle are obtained and input into the calculation process in the next time step (Remias 1998). The two most time-consuming aspects of DEM simulation are the contact search and contact force calculations.

$$M \ddot{x}_i(t) + \lambda M \dot{x}_i(t) = F_i(t) \quad \text{Equation 3-100}$$

$$I \ddot{\omega}_i(t) + \lambda I \dot{\omega}_i(t) = M_i(t) \quad \text{Equation 3-101}$$

Where:

- M is the mass of the particle.
- I is the moment of inertia of the particle.
- λ is a damping coefficient.
- $\ddot{x}_i(t)$ is the acceleration of the particle at time step i .
- $\dot{x}_i(t)$ is the velocity of the particle at time step i .

- $\ddot{\omega}_i(t)$ is the angular acceleration of the particle at time step i .
- $\dot{\omega}_i(t)$ is the angular velocity of the particle at time step i .

The damping coefficient λ can be calculated by the formula (Equation 3-102) given by Matuttis (2014) or alternatively by formulae proposed by Hu et al. (2010).

$$\lambda = -D \sqrt{\left(\frac{A}{l}\right)} m^* v_{1,2}^\perp \quad \text{Equation 3-102}$$

$$m^* = \frac{m_1 m_2}{m_1 + m_2} \quad \text{Equation 3-103}$$

$$v_{1,2} = v_1 - v_2 - (\omega_1 r_1 - \omega_2 r_2) \quad \text{Equation 3-104}$$

Where:

- D is the damping coefficient.
- A is the area.
- l is the characteristic length.
- m^* is the reduced mass.
- m_1 is the mass of particle 1.
- m_2 is the mass of particle 2.
- r_1 is the contact vector for particle 1.
- r_2 is the contact vector for particle 2.
- ω_1 is the angular velocity of particle 1.
- ω_2 is the angular velocity of particle 2.
- $v_{1,2}$ is the relative velocity between particle 1 and 2.
- $v_{1,2}^\perp$ is the relative normal velocity between particle 1 and 2.

In DEM, the contact interactions which ultimately result in forces between particle to particle and particle to the wall are expressed by Equation 3-105:

$$f = \sum_{i=1}^N \sum_{j=1}^N f_{ij}$$

Equation 3-105

Where:

- f is the total force.
- N is the number of elements
- i and j are the target and contactor elements.
- f_{ij} is the contact force between the target and contactor element.

The simple contact algorithm shown in Equation 3-105, is very computing intensive because the number of operations is proportional to N^2 as demonstrated by Munjiza (2004). Therefore it is important to find an efficient contact search algorithm in DEM to reduce the associated computing costs. In recent years Nezami et al. (2004), John, Raju, and Robert (2009), Kodam et al. (2010), Walizer and Peters (2011), Boon, Houlsby, and Utili (2013) and Chen et al. (2015) proposed more advanced contact search algorithms which require less computing time.

Furthermore, there are numerous contact models developed for DEM in literature such as Poisson's model, Newton's model, Stronge's model, Spring-dashpot model, Hertz's model, Non-linear damping model, friction model and least squares methods as outlined by Gilardi and Sharf (2002), Machado et al. (2012) and O'Sullivan (2014). A different model is more suited to a particular element shape, and different DEM software uses different contact models. The calculation time in DEM is an important factor because a significant amount of the total time is used to calculate the contact forces according to Nassauer and Kuna (2013). Nassauer and Kuna (2013) proposed a contact force model based on Hertz's model for arbitrarily shaped particles and is shown in Equation 3-106 below.

$$F = E^* \frac{4}{3\sqrt{\pi}} \sqrt{Vd} \quad \text{Equation 3-106}$$

$$r = \sqrt{d_1(2R_1 - d_1)} = \sqrt{d_2(2R_2 - d_2)} \quad \text{Equation 3-107}$$

$$\frac{1}{E^*} = \frac{1-\nu_1^2}{E_1} + \frac{1-\nu_2^2}{E_2} \quad \text{Equation 3-108}$$

$$\frac{1}{R} = \frac{1}{R_1} + \frac{1}{R_2} \quad \text{Equation 3-109}$$

Where:

- F is the contact force between particle to wall or particle to particle.
- ν_i is the Poisson's ratio of the particle.
- E_i is Young's modulus of the particle.
- R_i is the radius of the particle.
- d is the overlapping distance between particle to the wall (Figure 3-21) or particle to particle (Figure 3-22).
- V is the overlapping volume between particle to the wall (Figure 3-21) or particle to particle (Figure 3-22).

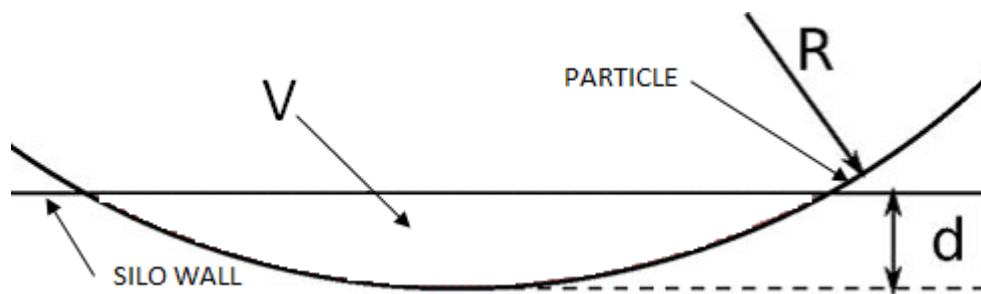


Figure 3-21: Contact between particle and silo wall as per Equation 3-110 (Nassauer and Kuna 2013).

$$V = \frac{1}{3} \pi d_1^2 (3R - d)$$

Equation 3-110

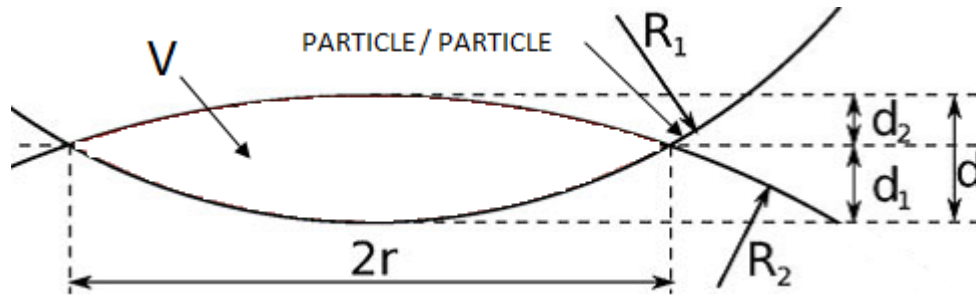


Figure 3-22: Contact between particle and particle as per Equation 3-111 (Nassauer and Kuna 2013).

$$V = \frac{1}{3} \pi (d_1^2 (3R_1 - d_1) + d_2^2 (3R_2 - d_2))$$

Equation 3-111

According to Remias (1998), the pressures acting on the silo wall can be calculated by

$$p_n = \frac{1}{l} \sum_{i=1}^m (F_c^i n_i)$$

Equation 3-112

$$p_t = \frac{1}{l} \sum_{i=1}^m (F_c^i t_i)$$

Equation 3-113

Where:

- n_i is the unit vector normal to the wall along the direction of the force F_i^c .
- t_i is the unit vector parallel to the wall along the direction of the force F_i^c .
- F_i^c is the force acting on the wall from particle to wall interaction.
- m is the number of contact points along the wall.
- l is the length of the contact on the wall.

- p_n pressure acting normal to the wall.
- p_t pressure acting parallel to the wall.

The cohesive forces for a particle to particle and particle to the wall can be determined by multiply the coefficient of cohesion with the contact length as per Equation 3-114 (Matuttis 2014).

$$|F^{coh}| = c_{cohesion} l_{contact}$$

Equation 3-114

Where:

- $|F^{coh}|$ is the cohesive force.
- $c_{cohesion}$ coefficient of particle cohesion.
- $L_{contact}$ is the contact length.

The stresses according to Matuttis (2014) acting on the particles can be calculated by

$$\sigma_{ij} = \frac{1}{V} \sum_k I_i^{(k)} f_j^{(k)}$$

Equation 3-115

$$f^k = \begin{pmatrix} f_x^{(k)} \\ f_y^{(k)} \\ f_z^{(k)} \end{pmatrix}$$

Equation 3-116

Where:

- V is the volume of the particle.
- k denotes the particle.

- $l^{(k)}$ is the vector connecting the centre of mass (COG) of the particle to the force points x , y and z .
- $f_x^{(k)}$ is the force of particle k in the x direction.
- $f_y^{(k)}$ is the force of particle k in the y direction.
- $f_z^{(k)}$ is the force of particle k in the z direction.
- $\sigma_{i,j}$ is the stresses of the particle.

DEM has been used by some researchers such as Donohue TJ et al. (2012), Donohue, Wensrich, and Roberts (2016) to simulate the silo quaking phenomena. However, it was concluded that much more research is required to accurately predict the silo quaking phenomena.

3.5 Structural Dynamics

The advance of modern computers has allowed the practising engineers the ability to implement numerical methods formulated to predict the response of the structure due to dynamic loadings. As described by Hart and Wong (2000), the stiffness matrix method (refer to Equation 3-117) have been developed and implemented in computer codes to predict the dynamic response of the structure based on the equations below:

$$M\ddot{X}(t) + C\dot{X}(t) + KX(t) = F_e(t) \quad \text{Equation 3-117}$$

Where:

$$M = \begin{bmatrix} m_{11} & \cdots & m_{1n} \\ \vdots & \ddots & \vdots \\ m_{n1} & \cdots & m_{nn} \end{bmatrix} \quad \text{Equation 3-118}$$

$$C = \begin{bmatrix} c_{11} & \cdots & c_{1n} \\ \vdots & \ddots & \vdots \\ c_{n1} & \cdots & c_{nn} \end{bmatrix} \quad \text{Equation 3-119}$$

$$K = \begin{bmatrix} k_{11} & \cdots & k_{1n} \\ \vdots & \ddots & \vdots \\ k_{n1} & \cdots & k_{nn} \end{bmatrix} \quad \text{Equation 3-120}$$

$$X(t) = \begin{Bmatrix} x_1(t) \\ \vdots \\ x_n(t) \end{Bmatrix} \quad \text{Equation 3-121}$$

$$F_e(t) = \begin{Bmatrix} F_1(t) \\ \vdots \\ F_n(t) \end{Bmatrix} \quad \text{Equation 3-122}$$

In Equation 3-118 to Equation 3-122, the term n represents the total number of degrees of freedom. According to Hart and Wong (2000), the terms M , C and K are symmetric positive definitive matrices and are described as:

1. M is the mass matrix of the entire structure lumped to the appropriate degrees of freedom.
2. C is the damping matrix of the entire structure. Currently, there is no method to accurately computing the damping of each structural member. Therefore it is generally assumed to be a linear combination of the mass (M) and stiffness (K) matrices commonly referred to as proportional damping.
3. K is the stiffness matrix of the structure. This matrix includes all the properties of each structural member, including the length, cross-sectional area, a moment of inertia, elastic constants, torsional rigidity and modulus of elasticity.
4. $X(t)$ is the displacement vector that includes translations in the x , y and z directions and rotations in the x , y and z directions.
5. $F_e(t)$ is the force vector that includes forces in the x , y , and z directions and rotational moments in the x , y and z directions.

Various solution schemes such as Response Spectrum, Mode Superposition, Newmark β and Wilson θ have been developed to solve Equation 3-117. According to Paz (2004), the choice of the solution method depends on the linearity of the differential equation that are often expressed by the matrices K , M and C and the complexity of the load vector as a function of time. The modal superposition method is applicable

when Equation 3-117 is linear. Whereas, if the structure exhibits nonlinearity, other numerical methods such as Newmark β and Wilson θ are more applicable.

3.5.1 Response Spectrum

As stated by Gupta (1992), Kappos (2002), Paz (2004) and Clough (2010) the response spectrum analysis method, is a graphical illustration of the maximum response such as displacement, acceleration and velocity to a specified load function. The load function can be derived by analysing a series of single degree of freedom (SDOF) dynamic systems. As such, it has gained considerable acceptance in recent years in structural dynamics practices and especially in earthquake engineering according to Paz (2004). The response spectrum analysis method only requires the natural frequency and the ordinate of maximum response, for example, displacement, acceleration and velocity as shown in Figure 3-23 below.

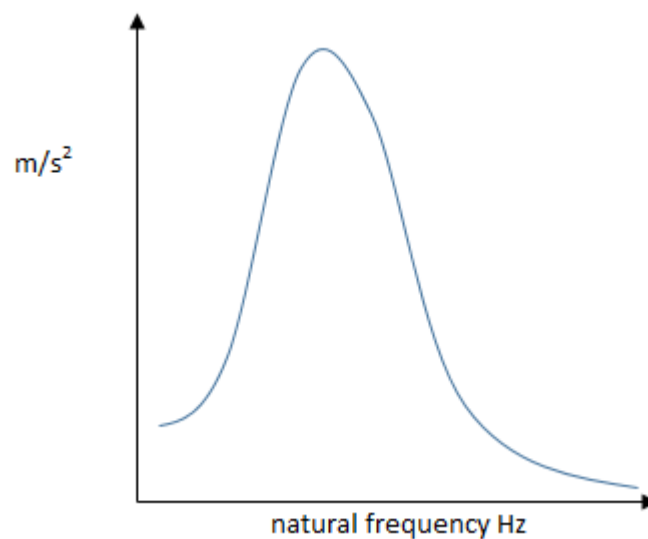


Figure 3-23: Example of response spectrum – acceleration vs frequency.

As noted by Hart and Wong (2000), in the field of structural dynamics, it is difficult for the structural engineers to develop an “engineering feel” that can be carried to

other projects. The response spectrum analysis method, on the other hand, provides an excellent vehicle to firstly develop such “engineering feel” and then being able to carry it across different projects. The major advantage of the response spectrum analysis method is that it combines important components of structural dynamics and design such as (Hart and Wong 2000):

1. The mode shapes and natural frequencies of vibration are included in this analysis because those two factors are critical to estimating the dynamic response of the structure.
2. It is very simple to represent damping in the response spectrum analysis where only one value of damping for each response mode is retained in the solution.
3. In this method, the estimation of earthquake design values for the site can be obtained independently from the process of calculating the natural frequencies and mode shapes, thus, allow the works to be conducted simultaneously.
4. Calculated natural frequencies and mode shapes can be reused for different earthquake ground motions and different damping values.

As described by Hart and Wong (2000), to mathematically change the problem from a dynamic analysis due to external force to a dynamic analysis due to an earthquake, the externally applied force $f_e(t)$ shown in Equation 2.5-1 is replaced by $m\ddot{u}_g(t)$ thus Equation 2.5-1 can be written as:

$$m\ddot{x}(t) + c\dot{x}(t) + kx(t) = -m\ddot{u}_g(t) \quad \text{Equation 3-123}$$

$$\ddot{x}(t) + 2\zeta\omega_n\dot{x}(t) + \omega_n^2x(t) = -\ddot{u}_g(t) \quad \text{Equation 3-124}$$

$$\omega_n^2 = \frac{k}{m} \quad \text{Equation 3-125}$$

$$2\zeta\omega_n = \frac{c}{m} \quad \text{Equation 3-126}$$

Where:

- $\ddot{u}_g(t)$ is the ground acceleration at time t .
- ω_n is the natural frequency of the structure.
- ζ is the critical damping ratio.
- m is the mass of the structure.
- k is the stiffness of the structure.
- c is the damping of the structure.
- $\ddot{x}(t)$ is the acceleration of the structure at time t .
- $\dot{x}(t)$ is the velocity of the structure at time t .
- $x(t)$ is the displacement of the structure at time t .

The spectral displacement (Figure 3-27), spectral velocities (Figure 3-26) and spectral acceleration (Figure 3-25) can be obtained by computing and scanning the obtained accelerograms (Figure 3-24).

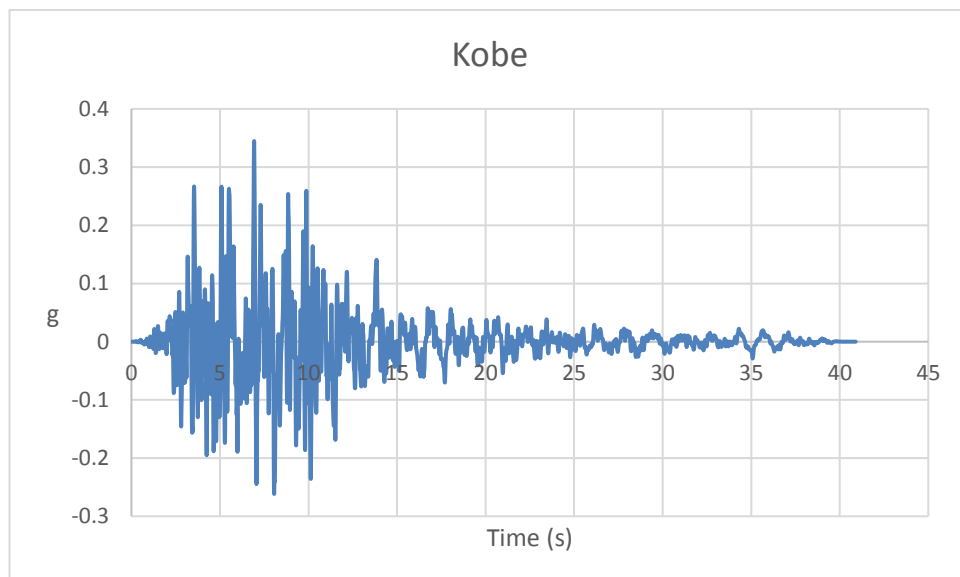


Figure 3-24: Kobe (Kobe 1995) earthquake time history generated by software SeismoSignal 2016.

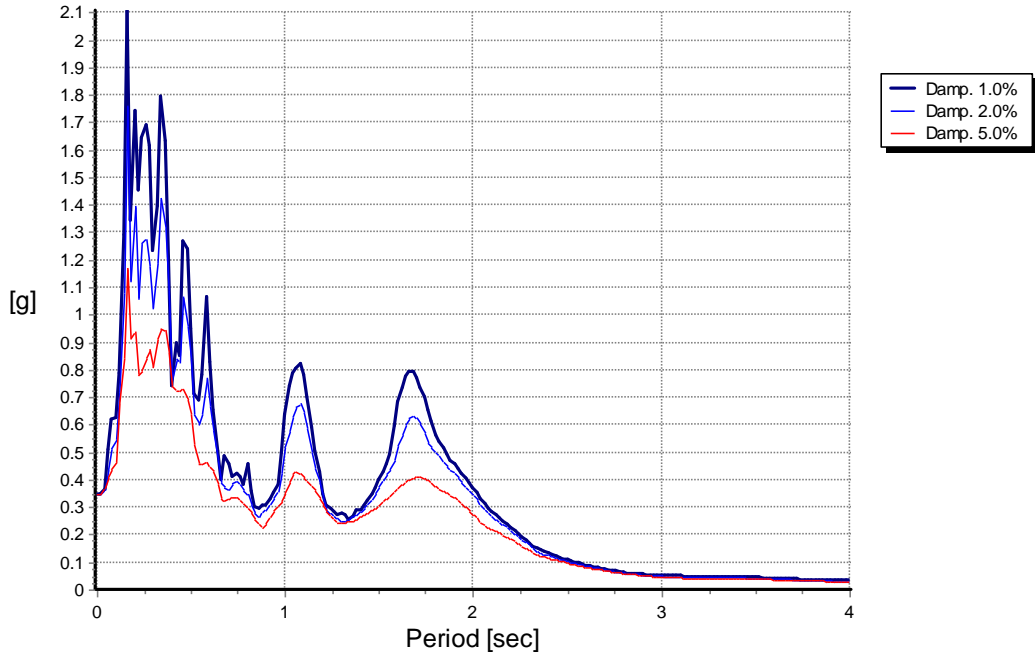


Figure 3-25: Kobe acceleration spectrum generated by software SeismoSignal 2016.

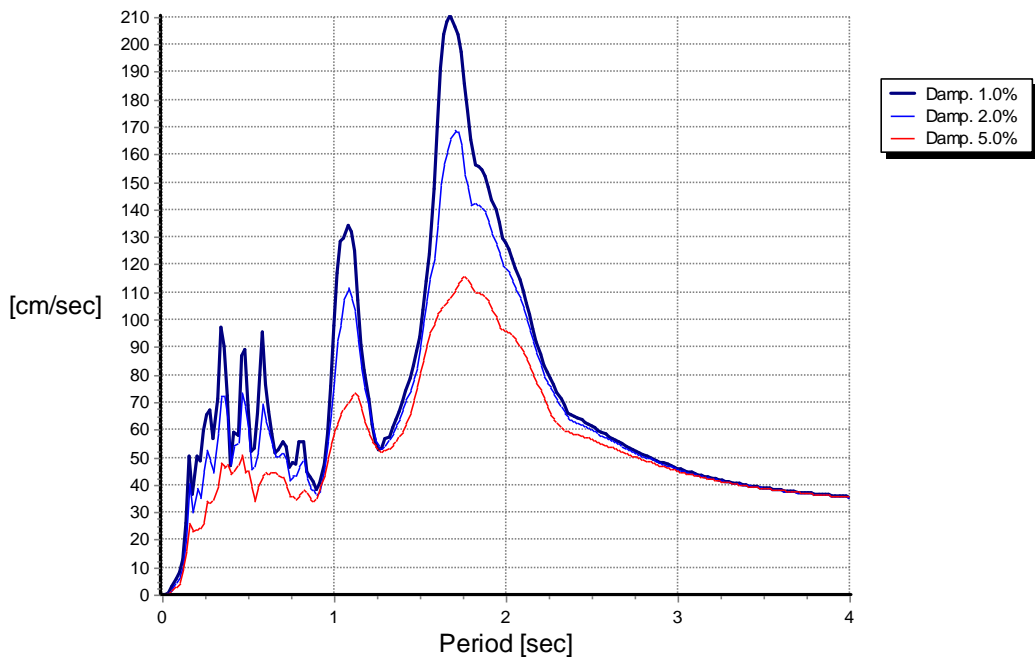


Figure 3-26: Kobe velocity spectrum generated by software SeismoSignal 2016.

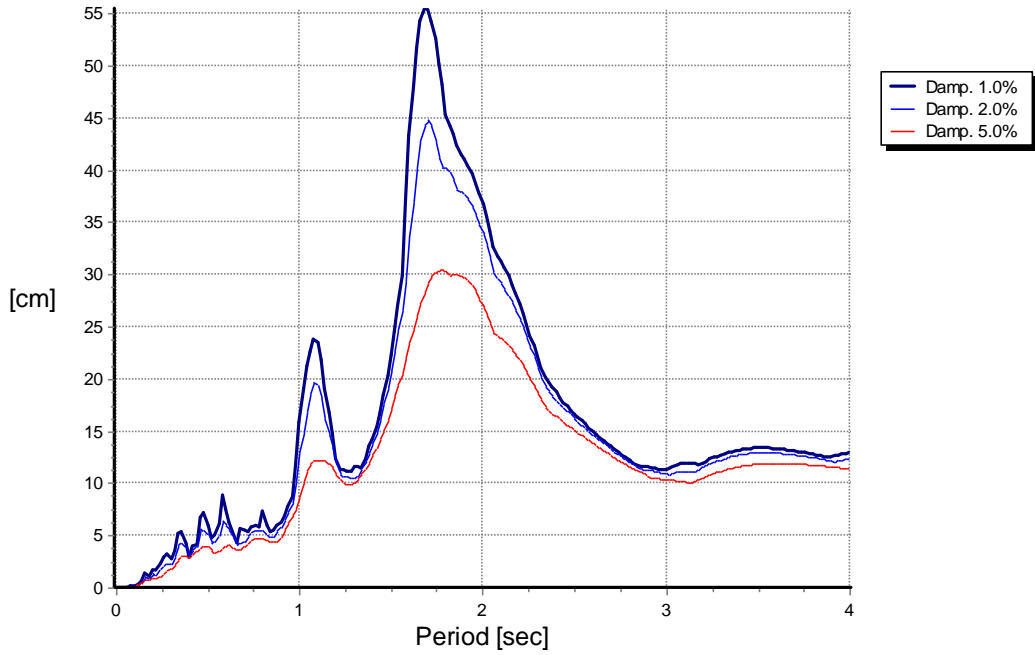


Figure 3-27: Kobe displacement spectrum generated by software SeismoSignal 2016.

The mathematical representation of the spectral displacement, spectral acceleration and spectral velocity respectively are:

$$S_d(\omega_n, \zeta) = |x(t)|_{max} \quad \text{Equation 3-127}$$

$$S_v(\omega_n, \zeta) = |\dot{x}(t)|_{max} \quad \text{Equation 3-128}$$

$$S_a(\omega_n, \zeta) = |\ddot{x}(t)|_{max} \quad \text{Equation 3-129}$$

According to Biot (1941), (Housner 1959) and Gupta (1992) were the first to recognise the potential of the response spectrum as a tool to design earthquake. Biot (1941) investigated the response spectrum by creating a single degree of freedom mechanical analyser and subjected it recorded earthquake acceleration time histories. Housner (1959) produced the smoothened response spectra by averaging recorded

acceleration time history of El Centro (1934), El Centro (1940), Olympia (1949) and Tehachapi (1952). Various researchers such as Newmark and Hall (1982), Housner and Jennings (1982), Kim and D'Amore (1999), Aschheim and Black (2000), Lopez et al. (2006) and Clough (2010) investigated the response spectra further and formulated methodologies to generate the response spectra (elastic and inelastic) and design the structures to resist the earthquake motions. The results of such researches have been incorporated into design codes such as AS/NZS 1170.4, Eurocode 8 and Uniform Building Code.

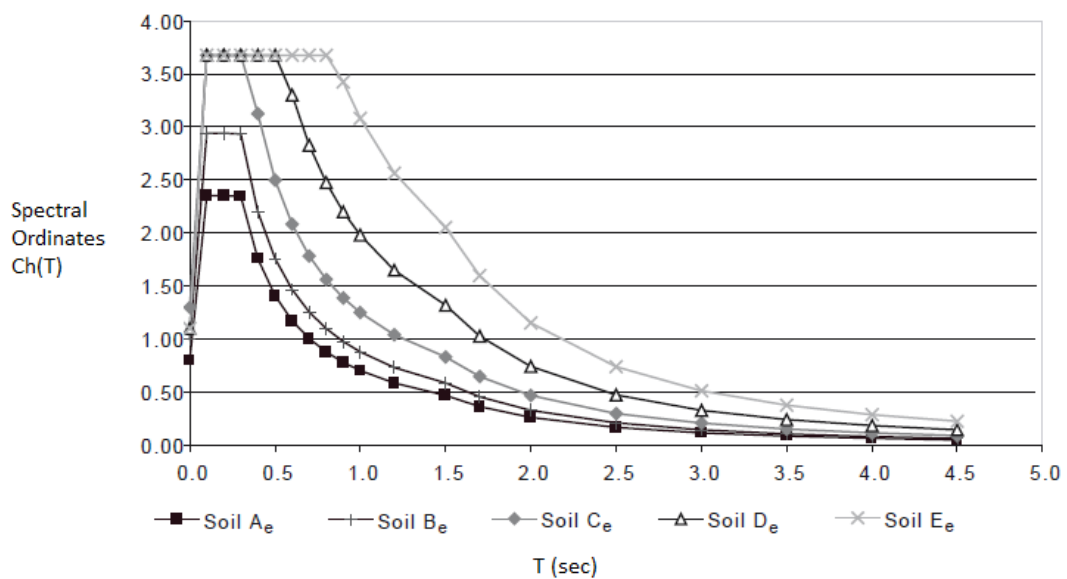


Figure 3-28: Typical earthquake design spectrum for different soil type (AS/NZS1170.4 2007).

3.5.2 Modal Superposition Method

One of the most effective and common approach for analysing linear structural systems subjected to time dependent forces such as an earthquake is the mode superposition method. According to Wilson (2002), after a set of orthogonal vectors have been determined, the global equilibrium equations can be simplified to a set of uncoupled

second order differential equations. As such, the method requires that Equation 3-117 to be rewritten as a set of 2nd ordinary differential equations (ODEs) (Wilson 2002).

$$M\ddot{u}(t) + C\dot{u}(t) + Ku(t) = \sum_{j=1}^J f_j g(t)_j \quad \text{Equation 3-130}$$

Where:

- $f_j(t)$ is space vector.
- $g(t)_j$ is the time function.
- M is the mass matrix of the structure.
- K is the stiffness matrix of the structure.
- C is the damping matrix of the structure.
- $\ddot{u}(t)$ is the acceleration of the structure at time t .
- $\dot{u}(t)$ is the velocity of the structure at time t .
- $u(t)$ is the displacement of the structure at time t .

As described in Equation 3-130 by Wilson (2002), all types of loadings can be represented by a sum of J space vectors f_j . According to Wilson (2002), the space vectors f_j are not a function of time and J time functions $g(t)_j$. From principles of calculus, Equation 3-130 can be solved by separating the variables as follows:

$$u(t) = \Phi Y(t) \quad \text{Equation 3-131}$$

$$\dot{u}(t) = \Phi \dot{Y}(t) \quad \text{Equation 3-132}$$

$$\ddot{u}(t) = \Phi \ddot{Y}(t) \quad \text{Equation 3-133}$$

Where:

- Φ is the spatial vector.
- $Y(t)$ is the displacement vector containing N functions of time.

- $\dot{Y}(t)$ is the velocity vector containing N functions of time.
- $\ddot{Y}(t)$ is the acceleration vector containing N functions of time.

The term Φ in the preceding equations represent a N_d by N matrix containing N spatial vectors (Wilson 2002). Those spatial vectors are not a function of time t , whereas, $Y(t)$ is a vector containing N functions of time (Wilson 2002). However according to Wilson (2002), the space functions must satisfy the following mass and stiffness orthogonality conditions:

$$I = \Phi^T M \Phi \quad \text{Equation 3-134}$$

$$\Omega^2 = \Phi^T K \Phi \quad \text{Equation 3-135}$$

Where:

- The term I is a diagonal matrix.
- Ω^2 is a diagonal matrix with the ω_n^2 as the diagonal terms.
- ω_n^2 is the eigenvalue of mode n^{th} .

According to Wilson (2002), the term ω_n has the unit of radians per second but may not be the natural frequencies of the structure. Upon substitution Equation 3-131 through to Equation 3-135 the following Equation 3-136 is produced:

$$I\ddot{Y}(t) + d\dot{Y}(t) + \Omega^2 Y(t) = \sum_{j=1}^J p_{nj} g(t)_j \quad \text{Equation 3-136}$$

$$p_j = \Phi^T f_j \quad \text{Equation 3-137}$$

$$d_{nn} = 2\zeta_n \omega_n \quad \text{Equation 3-138}$$

Where:

- p_j is the modal participation factors for load function f_j .
- p_{nj} is the modal participation factors associated with n^{th} mode.
- d_{nn} is the modal damping of mode n^{th} .
- ω_n is the natural frequency of mode n^{th} .
- ζ_n is the ratio of the damping in mode n^{th} to the critical damping of the mode.

Classical damping is often assumed to uncouple the modal equations as shown in Equation 3-138. Therefore, the resulting typical uncoupled modal equation for linear structural systems is as follow:

$$\ddot{y}(t)_n + 2\zeta_n \omega_n \dot{y}(t)_n + \omega_n^2 y(t)_n = \sum_{j=1}^J p_{nj} g(t)_j \quad \text{Equation 3-139}$$

3.5.3 Newmark β

In 1959, Professor Newmark introduced a method to solve structural dynamic problems for seismic and blast loadings. This method has been adopted extensively and has been modified and improved over the last four decades according to Wilson (2002). The Newmark's method was derived from Taylor's series expansions as:

$$u_t = u_{t-\Delta t} + \Delta t \dot{u}_{t-\Delta t} + \frac{\Delta t^2}{2} \ddot{u}_{t-\Delta t} + \frac{\Delta t^3}{6} \dddot{u}_{t-\Delta t} + \dots \quad \text{Equation 3-140}$$

$$\dot{u}_t = \dot{u}_{t-\Delta t} + \Delta t \ddot{u}_{t-\Delta t} + \frac{\Delta t^2}{2} \dddot{u}_{t-\Delta t} + \dots \quad \text{Equation 3-141}$$

Newmark combined Equation 3-140 and Equation 3-141 and simplified them by introducing integration constants, β and γ , to replace the remaining terms of Taylor's series as follow:

$$u_t = u_{t-\Delta t} + \Delta t \dot{u}_{t-\Delta t} + \frac{\Delta t^2}{2} \ddot{u}_{t-\Delta t} + \beta \Delta t^3 \ddot{u}_t \quad \text{Equation 3-142}$$

$$\dot{u}_t = \dot{u}_{t-\Delta t} + \Delta t \ddot{u}_{t-\Delta t} + \gamma \Delta t^2 \ddot{u}_t \quad \text{Equation 3-143}$$

The Newmark method assumes that the acceleration is linear within the time step Δt , therefore, the term \ddot{u} can be written as:

$$\ddot{u} = \frac{\ddot{u}_t + \ddot{u}_{t-\Delta t}}{\Delta t} \quad \text{Equation 3-144}$$

which produces the Newmark's equations in the following form:

$$u_t = u_{t-\Delta t} + \Delta t \dot{u}_{t-\Delta t} + \left(\frac{1}{2} - \beta\right) \Delta t^2 \ddot{u}_{t-\Delta t} + \beta \Delta t^2 \ddot{u}_t \quad \text{Equation 3-145}$$

$$\dot{u}_t = \dot{u}_{t-\Delta t} + (1 - \gamma) \Delta t \ddot{u}_{t-\Delta t} + \gamma \Delta t \ddot{u}_t \quad \text{Equation 3-146}$$

Wilson in 1962, developed Newmark's sets of equations into a matrix notation together with added mass proportional damping and stiffness. Wilson introduced a set of equations to obtain a direct solution of the equations at each time step (Wilson 2002).

$$\ddot{u}_t = b_1(u_t - u_{t-\Delta t}) + b_2\dot{u}_{t-\Delta t} + b_3\ddot{u}_{t-\Delta t} \quad \text{Equation 3-147}$$

$$\dot{u}_t = b_4(u_t - u_{t-\Delta t}) + b_5\dot{u}_{t-\Delta t} + b_6\ddot{u}_{t-\Delta t} \quad \text{Equation 3-148}$$

Where

$$b_1 = \frac{1}{\beta\Delta t^2} \quad \text{Equation 3-149}$$

$$b_2 = \frac{1}{\beta\Delta t} \quad \text{Equation 3-150}$$

$$b_3 = \beta - \frac{1}{2} \quad \text{Equation 3-151}$$

$$b_4 = \gamma\Delta t b_1 \quad \text{Equation 3-152}$$

$$b_5 = 1 + \gamma\Delta t b_2 \quad \text{Equation 3-153}$$

$$b_6 = \frac{1}{\beta\Delta t} \quad \text{Equation 3-154}$$

Substituting Equation 3-147 and Equation 3-148 gives:

$$\begin{aligned} & (b_1M + b_4C + K)u_t \\ & = F_t + M(b_1u_{t-\Delta t} - b_2\dot{u}_{t-\Delta t} - b_3\ddot{u}_{t-\Delta t}) \\ & + C(b_4u_{t-\Delta t} - b_5\dot{u}_{t-\Delta t} - b_6\ddot{u}_{t-\Delta t}) \end{aligned} \quad \text{Equation 3-155}$$

The solution of the Newmark method in matrix notation is demonstrated in Figure 3-29.

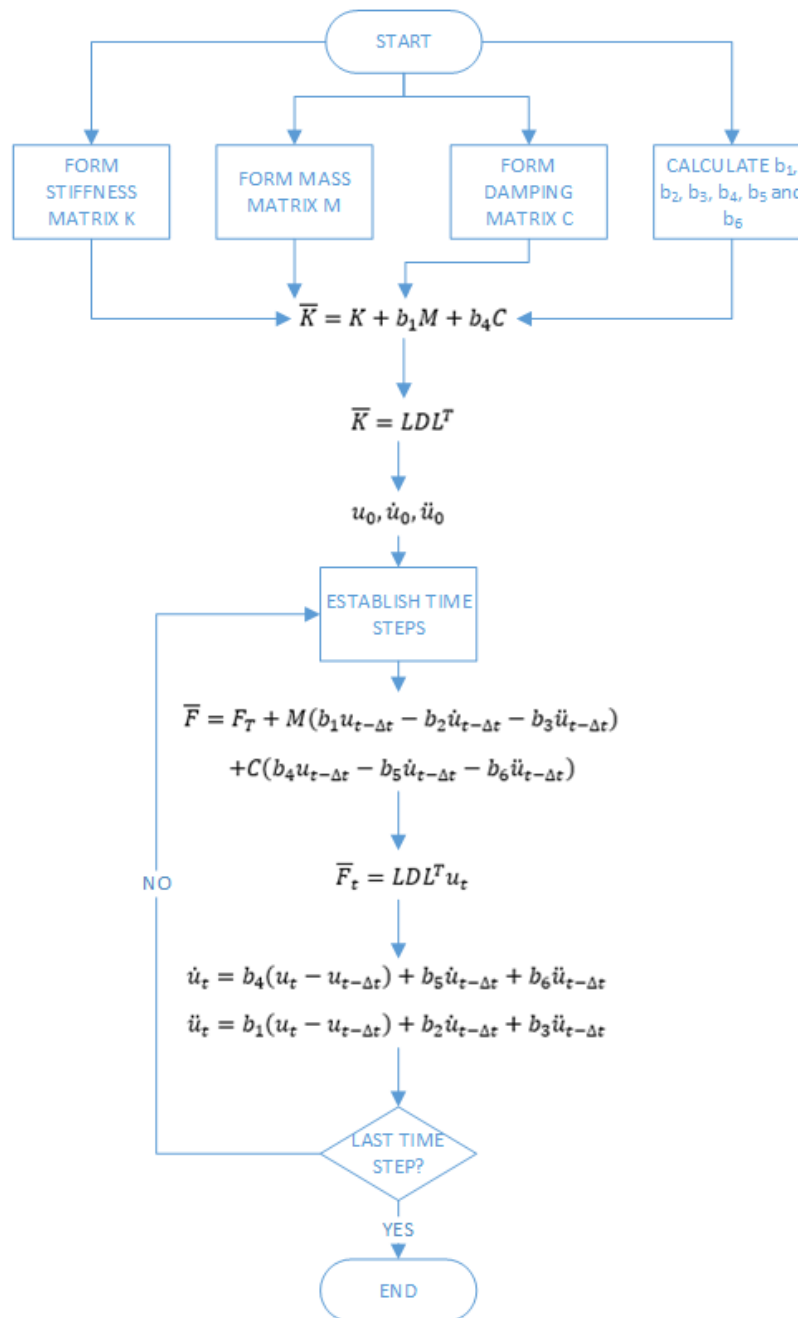


Figure 3-29: Solution procedure for Newmark equations.

The procedure described in Figure 3-29 demonstrates that the mass, stiffness and damping matrices remain constant throughout the solution time steps. However, this is not true for a silo structure, where the total mass of the structure, during discharge, changes with respect to time. The change in the total mass of the structure consequently causes the damping and stiffness matrices to change accordingly. Therefore such analysis procedures are not suitable for silo structures.

3.5.4 Wilson θ

Wilson (1973), observed that the typical unstable solution tends to oscillate about the true solution and introduced the factor θ to make the Newmark method unconditionally stable (Wilson 2002). To minimise the spurious oscillations, Wilson (1973) proposed that the numerical solution needed to be evaluated within the solution time step. To accomplish this, Wilson modified the Newmark method using the time step defined by Equation 3-156 and a load defined by Equation 3-157, respectively, as shown in the following equations, where $\theta \geq 1.0$:

$$\Delta t' = \theta \Delta t \quad \text{Equation 3-156}$$

$$R_{t'} = R_{t-\Delta t} + \theta(R_T - R_{t-\Delta t}) \quad \text{Equation 3-157}$$

As proposed by Wilson (1973), once the acceleration \ddot{u} vector has been determined by Newmark's equations at the integration time step $\theta \Delta t$, the values of nodal accelerations, displacements and velocities shall be determined using the following equations:

$$\ddot{u}_t = \ddot{u}_{t-\Delta t} + \frac{1}{\theta}(\ddot{u}_{t'} - \ddot{u}_{t-\Delta t}) \quad \text{Equation 3-158}$$

$$\dot{u}_t = \dot{u}_{t-\Delta t} + (1 - \gamma)\Delta t \ddot{u}_{t-\Delta t} + \gamma \Delta t \ddot{u}_t \quad \text{Equation 3-159}$$

$$u_t = u_{t-\Delta t} + \Delta t \dot{u}_{t-\Delta t} + \frac{\Delta t^2(1 - 2\beta)}{2} \ddot{u}_{t-\Delta t} + \beta \Delta t^2 \ddot{u}_t \quad \text{Equation 3-160}$$

3.6 Signal Processing

Accelerometers are devices designed to measure the accelerations of a moving or vibrating body. Such devices can be found in various field of engineering for example earthquake, structural health monitoring and vibrating machinery. The acceleration signals are often processed traditional algorithms such as Fast Fourier Transform (FFT). According to Stearns (2003) FFT is an algorithm to transform signals from time domain to frequency domain. As mentioned by He and Yi (2013), FFT is more suited to stationary signal processing and feature extraction. The effectiveness of FFT algorithm decreases when processing nonlinear and nonstationary according to He and Yi (2013).

A signal is classified as stationary if its frequency or spectral contents are not changed with respect to time (Non-Stationary Nature of Speech Signal 2011,) and if it can be written as a discrete sum of cosine waves or exponentials (Vlcek 2009). A signal is classified as non-stationary if the statistical structure of the signal (mean, variance, correlation, covariance and etc) changes as a function of time (Hammond and White 1996) or do not exhibit stationary features. According to Smith (1999) and Giron-Sierra (2017), a signal is linear if it has two mathematical properties such as homogeneity and additivity.

According to Huang and Shen (2014) and Huang et al. (1998), in most natural processes, the data is likely to be both nonlinear and nonstationary. Silo discharge under gravity is one of the processes that exhibit both the nonlinearity and nonstationarity. The nonlinearity comes from the fluctuating flow rates which cause the signals to be time varying thus not satisfying the homogeneity and additivity criteria. The nonstationarity comes from the mass fluctuations during discharge and unrepeatable vibration signals. The mass fluctuations cause the natural frequencies and dynamic responses of the structure to change accordingly. Due to the time varying and unrepeatable nature of the signals, traditional signal processing techniques such as FFT are unsuitable as per Park et al. (2008), Zoltan Tuske, Friedhelm R. Drepper, and Schluter (2012), LO et al. (2009), Cardona-Morales, Avendaño, and Castellanos-

Domínguez (2014), and Ditommaso, Mucciarelli, and Ponzio (2012). Furthermore, the discharge process is often associated with strong vibrations commonly named as silo quaking or silo honking.

Huang et al. (1998), a mathematician at the National Aeronautics and Space Administration (NASA), combined the Hilbert Transform (HT) and Empirical Mode Decomposition (EMD) method together to analyse nonlinear and nonstationary signals. The method was subsequently called Hilbert-Huang Transform (HHT). HHT has been further developed and adopted in many research areas (Huang and Shen 2014).

The analysis methods before the development of HHT were, according to Huang et al. (1998), either suitable for linear but non-stationary, or non-linear but stationary and statistically deterministic. However, the data from real-world processes are non-linear, non-stationary and stochastic. Thus HHT was developed to address the need to analyse nonlinear and non-stationary signals that occur in natural processes.

3.6.1 Empirical Mode Decomposition

EMD assumes that any dataset consists of simple but different intrinsic modes of oscillations (Huang et al. 1998). Furthermore, each intrinsic mode represents a simple oscillation. Most importantly, according to Huang et al. (1998), the oscillation is assumed to be symmetric with respect to the local mean and different modes of oscillation are superimposed to form the final complicated data. As such, each mode of oscillation is represented by an intrinsic mode function (IMF). He and Yi (2013) specifies that an IMF has to satisfy the following conditions:

1. The number of extrema and the number of zero-crossings must either equal to differ at most by one.
2. The mean value of the envelopes defined by the local maxima and the local minima is zero.

According to Huang et al. (1998), the first condition is similar to the requirements for stationary Gaussian process whereas the second requirement was invented to filter out the unwanted fluctuations induced by asymmetric wave forms from the instantaneous frequency. The practical implementation of EMD or sifting process outlined by Su and Chuang (2013) for a given signal $x(t)$:

1. Identify the extrema of the signal $x(t)$, and generate the upper and lower envelopes defined by the cubic spline interpolation of the extrema point.
2. Compute the mean, $m(t)$ by averaging the upper and lower envelopes and compute the first component $h(t) = x(t) - m(t)$
3. If the first component is not an IMF, then let $h_1(t)$ be the new data set and repeat steps 1 and 2 until an IMF is found.
4. The first IMF component $h_1(t)$ is called $c_1(t)$. Therefore $r_1(t) = x(t) - c_1(t)$. Repeat steps 1 to 3 until the $r_N(t)$ obtained is monotonic.

The original data $x(t)$ at the end of the sifting process, is decomposed into a set of IMFs satisfying Equation 3-161 which is

$$x(t) = \sum_{j=1}^N c_j + r_N \quad \text{Equation 3-161}$$

Despite the usefulness of EMD, the EMD method suffers a drawback called mode mixing as identified by Wu and Huang (2009). Such drawbacks are apparent when EMD is applied to noisy data as demonstrated by Wang et al. (2012). According to Wang et al. (2012), mode mixing is defined as either a single IMF consisting of signals of disparate scales or signals of the similar scale residing in different IMF. As postulated by Wu and Huang (2009) the presence of mode mixing causes serious

aliasing in the time-frequency distribution. Furthermore, mode mixing also makes the physical meaning of each IMF unclear (Wu and Huang 2009).

Wu and Huang (2009) overcame the scale separation problem by introducing the Ensemble Empirical Mode Decomposition (EEMD). The development of the EEMD algorithm was inspired by the work initiated by Flandrin, Gonçalves, and Rilling (2005) where it was demonstrated that the added artificial noise could help the data analysis. According to Wu and Huang (2009), the EEMD algorithm defines the true IMF components as the mean of an ensemble of trials where each trial consists of the signal plus an artificial white noise of finite amplitude. As demonstrated by Wu and Huang (2009) the added white noise series cancel each other in the final mean of the corresponding IMFs. It was further demonstrated by Wu and Huang (2009), the mean IMFs stay within the natural dyadic filter windows thus reducing the chance of mode mixing. The practical implementation of EEMD as per Wu and Huang (2009):

1. Add a white noise series to the targeted data as shown in Equation 3-162 where $w_i(t)$ is different realisations of Gaussian noise.
2. Decompose the data $x_i(t)$ with added white noise into IMFs.
3. Repeat step 1 and 2 with different white noise series each time.
4. Obtain the means of corresponding IMFs of the decompositions as the final result.

$$x_i(t) = x(t) + w_i(t) \quad \text{Equation 3-162}$$

According to Torres et al. (2011) the resulting decomposition from the EEMD algorithm solves the EMD mode mixing problem, but it also creates some new ones. To address the issue associated with EEMD, Torres et al. (2011) proposed the following modifications to the original EEMD algorithm:

1. Decompose by EMD over I iterations to obtain the first mode and compute

$$\widetilde{IMF}_1(t) = \frac{1}{I} \sum_{i=1}^I IMF_1^i(t) = \overline{IMF}_1(t) \quad \text{Equation 3-163}$$

2. Calculate the first residue $r_1(t)$ where $k = 1$

$$r_1(t) = x(t) - \widetilde{IMF}_1(t) \quad \text{Equation 3-164}$$

3. Decompose realisation $r_1(t) + \varepsilon_1 E_1 w_i(t)$, where ε is the noise standard deviation, I is the ensemble size, E is the mode obtained by EMD and $w_i(t)$ is the noise data, to obtain their first EMD mode and define the second mode

$$\widetilde{IMF}_2(t) = \frac{1}{I} \sum_{i=1}^I E_1 (r_1(t) + \varepsilon_1 E_1 w_i(t)) \quad \text{Equation 3-165}$$

4. Calculate the k residue for $k = 2$ to K

$$r_k(t) = r_{k-1}(t) - \widetilde{IMF}_k(t) \quad \text{Equation 3-166}$$

5. Decompose realisation $r_k(t) + \varepsilon_k E_k w_i(t)$ to obtain their first EMD mode and define the $(k+1)^{\text{th}}$ mode

$$\widetilde{IMF}_{k+1}(t) = \frac{1}{I} \sum_{i=1}^I E_k (r_k(t) + \varepsilon_k E_k w_i(t)) \quad \text{Equation 3-167}$$

6. Repeat step 4 to 5 until the obtained residual can no longer be decomposed

$$R(t) = x(t) - \sum_{k=1}^K \widetilde{IMF}_k(t) \quad \text{Equation 3-168}$$

$$x(t) = \sum_{k=1}^K \widetilde{IMF}_k(t) + R(t) \quad \text{Equation 3-169}$$

Colominas, Schlotthauer, and Torres (2014) proposed further improvements to their Complete Ensemble EMD (CEEMD) with adaptive noise (CEEMDAN) model to eliminate the residual noise in the modes and spurious modes. The residual noise in the modes was determined by subtracting the estimated local mean from the original signal as per Equation 3-170.

$$\tilde{d}_1 = x - \langle M(x_i) \rangle \quad \text{Equation 3-170}$$

$$x^{(i)} = x + w^{(i)} \quad \text{Equation 3-171}$$

Where

- \tilde{d}_1 is the first EEMD or CEEMDAN mode.
- $w^{(i)}$ is the realisation of white Gaussian noise.
- x is the original signal.
- $x^{(i)}$ is the original signal with white Gaussian noise.
- $\langle M(x_i) \rangle$ is the local mean of $x^{(i)}$.

The new algorithm proposed by Colominas, Schlotthauer, and Torres (2014) is:

1. Calculate by EMD the local means of I realisations $x^{(i)} = x + \beta_0 E_1(w^{(i)})$ to obtain the first residue

$$r_1 = \langle M(x^{(i)}) \rangle \quad \text{Equation 3-172}$$

2. Calculate the first mode at $k = 1$ (first stage)

$$\tilde{d}_1 = x - r_1 \quad \text{Equation 3-173}$$

3. Estimate the second residual by averaging the local means of the realisations $r_1 + \beta_1 E_2(w^{(i)})$ and calculate the second mode

$$\tilde{d}_2 = r_1 - r_2 = r_1 - \langle M(r_1 + \beta_1 E_2(w^{(i)})) \rangle \quad \text{Equation 3-174}$$

4. For $k > 2$

$$r_k = \langle M(r_{k-1} + \beta_{k-1} E_k(w^{(i)})) \rangle \quad \text{Equation 3-175}$$

5. Compute k^{th} mode

$$\tilde{d}_k = r_{k-1} - r_k$$

Equation 3-176

6. Repeat step 4 until stoppage criteria are satisfied

3.6.2 Hilbert Transform and Hilbert Marginal Spectrum

The Hilbert Transform (HT) was introduced by David Hilbert over 60 years ago (Feldman 2011) to provide a mechanism to determine instantaneous amplitude and frequency of a signal (Huang and Shen 2014). According to Huang and Shen (2014), the HT method assigns a complementary imaginary to the given real part or vice versa by shifting each component of the signal by a quarter of a period unlike other integral transforms such as Fourier Transform and Laplace Transform. In the HHT algorithm, the HT method is applied to the IMFs obtained from the EMD or EEMD algorithm (Huang and Shen 2014) to determine the instantaneous amplitude and frequency.

The Hilbert transform $c_H(t)$ of any IMF $c(\tau)$ is defined as (Feldman 2011):

$$c_H(t) = \frac{1}{\pi} P \int_{-\infty}^{\infty} \frac{c(\tau)}{t - \tau} d\tau$$

Equation 3-177

Where P is the Cauchy principal value of the singular integral. As such, the analytical signal of the $c(\tau)$ can be defined:

$$z(t) = c(\tau) + jc_H(t) = a(t)e^{j\phi(t)}$$

Equation 3-178

$$a(t) = \sqrt{c(\tau)^2 + c_H(t)^2}$$

Equation 3-179

$$\phi(t) = \tan^{-1} \frac{c_H(t)}{c(\tau)} \quad \text{Equation 3-180}$$

$$w(t) = \frac{d\phi(t)}{dt} \quad \text{Equation 3-181}$$

The value $a(t)$ (Equation 3-179) and $\phi(t)$ (Equation 3-180) is the amplitude of pre-envelope and instantaneous phase respectively. Once the instantaneous phase is determined, the instantaneous frequency of the signal is determined by Equation 3-181. The original signal can be expressed by the Equation 3-182 where R is the real component of the Hilbert transform:

$$X(t) = R \sum_{i=1}^n a_i(t) \exp(j \int w_i(t) dt) \quad \text{Equation 3-182}$$

$$h(w) = \int_0^T H(w, t) dt \quad \text{Equation 3-183}$$

Equation 3-182 illustrate the amplitude and the instantaneous frequency as functions of time and is referred to as Hilbert-Huang Spectrum (HHS), $H(w, t)$. With the HHS defined, one can also define the Hilbert Marginal Spectrum (HMS) $h(w)$ as illustrated in Equation 3-183. According to Huang and Shen (2014), the HMS represents a measure of the total amplitude or energy contribution from each frequency.

3.7 Fundamental Issues with Current Granular Flow Theories

It has been noted in the literature review that researches to date have focused heavily on estimating the pulsating loads generated by the silos during discharge.

Furthermore, research conducted by Tu (2008), identified that silo structures have the

highest rate of failure. As a fellow member of the Institution of Engineers Australia, the author is obligated to uphold the code of ethics thus must alert the public to the two serious fundamental issues with the current approaches aimed at simulating and predicting the silo quaking phenomena. The fundamental issues are, the response of the vibrating silo structure and the effects of the mass loss during discharge are not included in both analytical and numerical methods to date. As such, the analytical and numerical methods are in compliance with fundamentals of physics and Newton's laws of motion, which are the basis of modern engineering.

In accordance to Newton's third law of motion, for every acting force in nature there is an equal and opposite reaction force (Hall 2015). Therefore, if the flowing granular material, at any instance of time during the discharge cycle, exerts a force on the silo structure, the silo structure must exert an equal and opposite reaction force. The equal and opposite reaction force exerting by the silo structure is in the form of vibration. The effects of the vibrating structure have on the properties of the flowing granular material is not adequately included in the current analytical and numerical methods aimed at simulating and predicting the silo quaking phenomena. Simply, from fundamentals of structural dynamics, different structures response differently to the same dynamic force, thus the flowing granular material will be influenced differently depending on the silo structure.

In accordance to Newton's first law of motion, an object at rest stays at rest and an object in motion stays in motion with the same speed and in the same direction unless acted upon by an unbalanced force (Hall 2015). Therefore, in the absence of any mechanically induced force, the only force acting on the granular material inside the silo structure is gravity. As such, it is the earth gravitational force that causes the granular material to flow out of the silo when the gate is opened. However, current granular flow models presented in Chapter 3.3 and Chapter 3.4, state that during granular flow there exist; the formation and collapse of arches, rarefaction waves travelling up the material column, packing density and volumetric changes, changes to shearing direction, unsymmetrical lateral pressures on the silo wall and dilation. Most importantly, these granular flow characteristics are observed when the silo structures quake or vibrate excessively. As per Newton's first law of motion, these

granular flow characteristics cannot happen by themselves given the earth gravitational force is acting down. Therefore, as per Newton's first law of motion, the observed granular flow characteristics are caused by the vibrating silo structure. This can be observed with the kitchen salt dispenser as shown in Figure 3-30 and a box filled with popcorn.



Figure 3-30: Salt dispenser.

If the salt dispenser, Figure 3-30, is turned upside down, it can be observed that the salt particles flow out very slowly. However, if the salt dispenser is shaken, it can be observed that the salt particles flow out quicker and move around inside the salt dispenser. All the flow characteristics observed during silo quaking can be observed by shaking the salt dispenser and the stronger the shaking motion, the more pronounced these effects can be observed. The formation and collapse of the arches inside the hopper can be simulated with the box filled with popcorn. If the box filled with popcorn is pressed and released rapidly, it can be observed that the popcorn inside the box arching up as the box is pressed and collapsing when the box is released.

Furthermore, current granular flow models presented by Roberts (1996), Wensrich (2002b), Wilde, Rucka, and Tejchman (2008), Wilde et al. (2010), Tejchman and Wojcik (2011), Lin and Wu (2016) and Donohue, Wensrich, and Roberts (2016) do not consider the effects of the mass exiting the silo during discharge on the vibrating silo structure. In particular, Wensrich's (2002b) experimental models somewhat overlook the reduction in the mass of the granular inside the silo. Such flow models

are increasingly expected given alignment to the Conservation of Momentum (Spakovszky 2018) towards better representation of the silo quaking phenomena.

3.8 Hazards Associated With Silo Inserts

One of the current methods of reducing and preventing the pulsations loads associated with the flowing granular material from the silo is to place inserts along the silo wall inside the silo (Muite et al. 2004; Roberts 2003; Wilde, Rucka and Tejchman 2008; Hardow, Schulze and Schwedes 1998; Niedostatkiewicz, Wójcik and Tejchman 2014). As a fellow member of the Institution of Engineers Australia, the author is obligated to uphold the code of ethics thus must alert the public to the hazards associated with silo inserts.

Installing insert inside the silo requires personnel to enter confined space and welding inside the confined space. The short term and long term hazards associated with welding inside confined spaces include (Blunt 2002; Mattes 2017; HSE 2016; BOC 2018; Worksafe 2011):

1. Eye, nose and throat irritation, dizziness and nausea.
2. Headache, fever, chills, muscle aches, thirst, nausea, vomiting, chest soreness, fatigue, gastrointestinal pain weakness and tiredness.
3. Pneumoconiosis, damages to the central nervous system, respiratory diseases and cancers.
4. Falls and entrapment.
5. Electrical shocks.
6. Radiation and heat burns.
7. Fire and explosion.

Recently, Work Health and Safety Act 2011 (Government 2017) and Work Health and Safety (Safe Design of Structures) Code of Practice 2015 (Cash 2015), published by the Australian Government, require the designers to integrate risk assessments,

hazards identification and control measures in the design process. In compliance with the laws, the designers have the duty of care and must carry out their due diligence. As such, the hazards associated with silo inserts must be assessed and control measures need to be in place to mitigate or eliminate such hazards.

3.9 Conclusion

Although the field of structural dynamics has advanced significantly over the last few decades. The dynamic structural characteristics of the silo structure during discharge have not been studied in details. This is evident when we consider a silo structure as a structure consisting of both stationary masses such as self-weight of the silo and its supporting beams, columns, braces and foundation and the temporary mass of the granular material stored in the silo. During discharge, the total mass of the silo structure including the stored granular material reduces with respect to time, therefore, the dynamics of the silo structure as a whole also change with respect to time. The current structural dynamic formulations do not take into consideration the time varying mass characteristics of the silo structure during discharge thus requiring modifications for analysing such structures. This forms the basis for work in this thesis.

In this thesis, an equation of motion incorporating time-varying mass to describe the silo quaking phenomena will be presented. The proposed equation does not exclude the pulsating loads generated by the silo during discharge as theorised by other researchers but rather incorporates them with the fundamentals of time varying mass structural dynamics to prevent the silo quaking phenomenon. Thus the proposed equation is called the Equation of Silo Quaking. The Equation of Silo Quaking is formulated by experimental data taken from a 1 to 10 scale of an industrial Train Load Out (TLO) silo containing iron ore and further validated with forces and masses obtained from discrete element analysis and analytical formulae (Roberts 2008).

In addition to the equation of silo quaking, the Hilbert-Huang Transform (HHT) and Hilbert Marginal Spectrum (HMS) algorithms are used to analyse acceleration signals resulting from the experiments and to demonstrate the existence of the silo quaking response spectrum theorised by Tu and Vimonsatit (2013).

4 RESEARCH METHODOLOGY

4.1 Introduction

It has been identified in Chapter 3 that there exists a lack of literature on the structural analysis and design of silo supporting structure subjected to silo quaking. Therefore this chapter addresses the identified shortcomings by employing research methodologies that will identify the silo quake response spectrum and assist in formulating the dynamic response of the silo supporting structure during material discharge. To measure the dynamic response of the silo supporting structure a 1 to 10 scale model of an industrial Train Load Out (TLO) silo was designed and erected. The granular material selected for the research was iron ore from the TLO silo. The TLO silo was chosen because it is known in the industry that these silos suffer excessive vibration during material discharge or commonly known as silo quaking.

This chapter contains the information regarding the design and fabrication of the model silo and its supporting structure, computing architecture used to analyse the data, silo quake response spectrum experimental setup, silo quaking experimental setup and material classification experimental setup.

4.2 Model TLO Silo

A silo and supporting structure, Figure 4-1, capable of storing 2.5 tonnes of iron ore was structurally designed by the author to satisfy the strength requirements outlined in AS3774 (1996), AS4100 (1998), AS/NZS1554.1 (2004), AS/NZS1170.0 (2002) and EN1993-1-6 (2007). The fabricated structure was erected at Curtin University Civil Engineering Laboratory to validate the proposed equation of silo quaking and to confirm the existence of the silo quake response spectrum. The silo is a 1 in 10 scale

model of an actual industrial TLO silo containing iron ore. The iron ore used in the experiments was donated from Rio Tinto.

Figure 4-1 to Figure 4-8 show the design of the model silo support structure. Roberts (1996) believed that the overall stiffness and natural frequencies of the support structure determine whether the silo structure would quake. Furthermore, the author in 2008 structurally designed a 2500 tonne TLO and eliminated the silo quake by modifying the overall stiffness of the supporting structure and its fundamental natural frequencies (Tu and Vimonsatit 2013). Therefore, based on the author's experience, the silo support structure was also structurally designed to ensure that the pulsating loads generated during discharge would cause some quaking. The structure was design and fabricated with X braces. However, during the experiments, the X braces were taken off for accessibility reasons without compromising the structural integrity of the structure.



Figure 4-1: Silo and supporting frame.

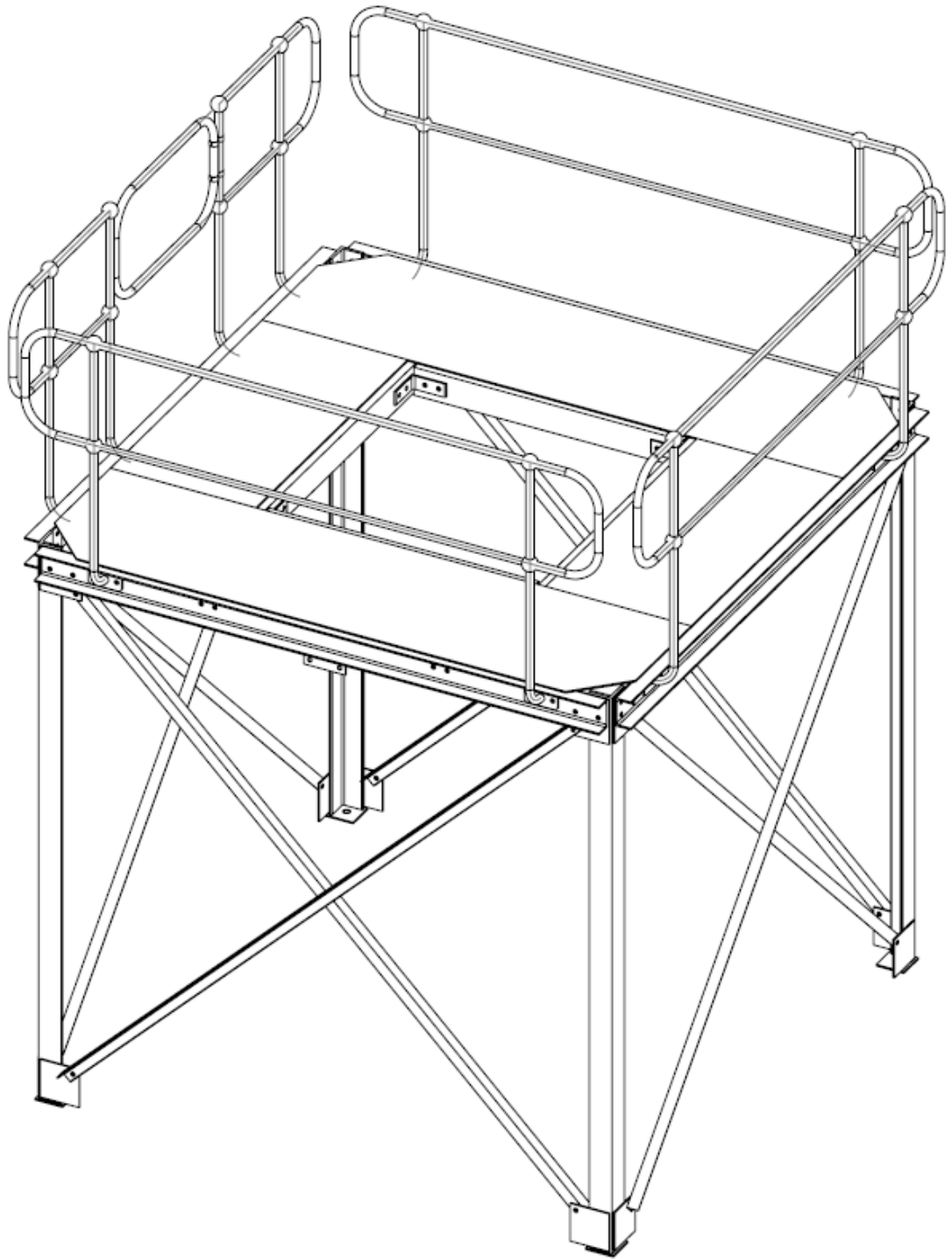


Figure 4-2: 3D isometric view of the silo support structure.

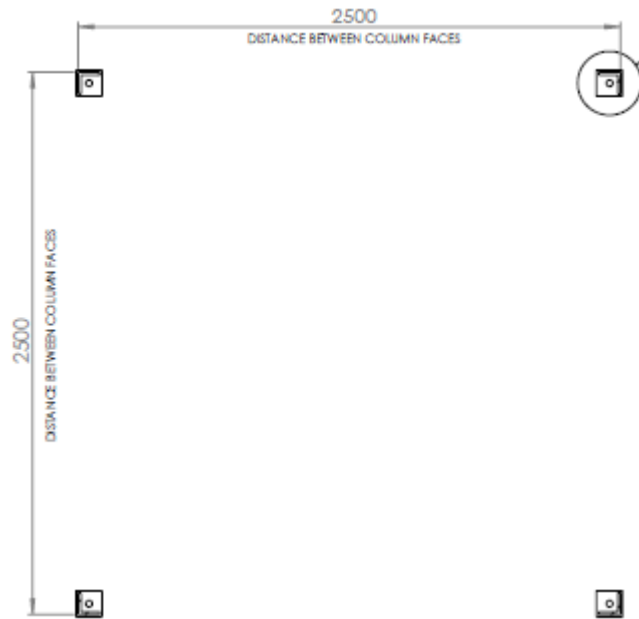


Figure 4-3: Silo support structure – bottom view.

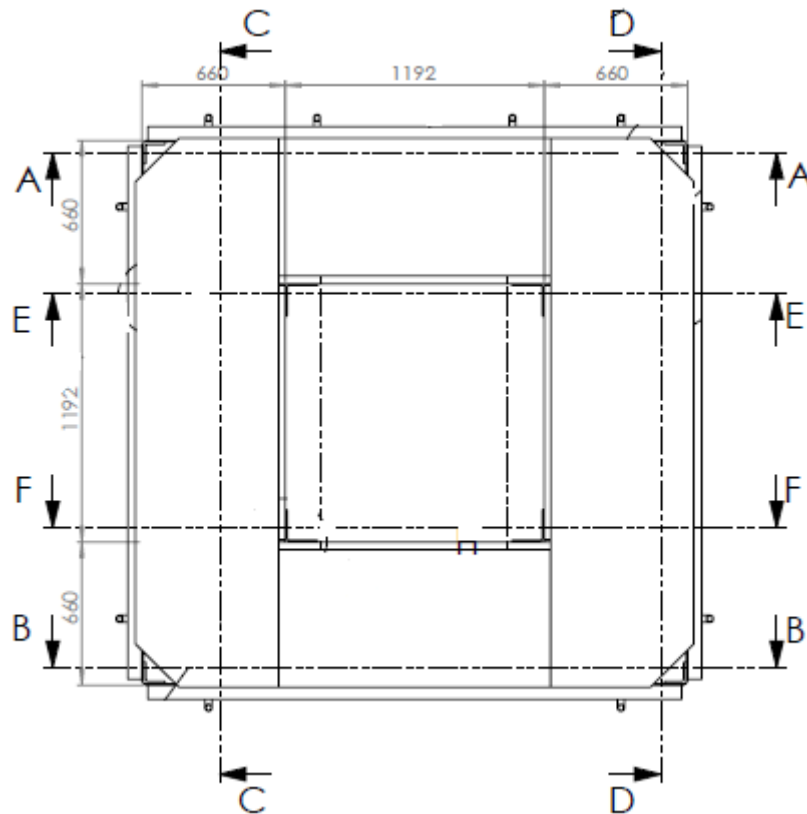


Figure 4-4: Silo support structure – top view.

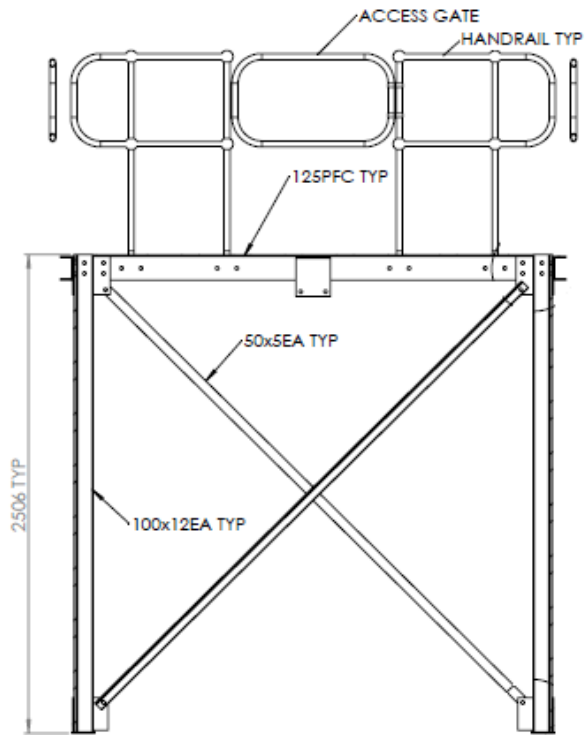


Figure 4-5: Silo support structure – Section A.

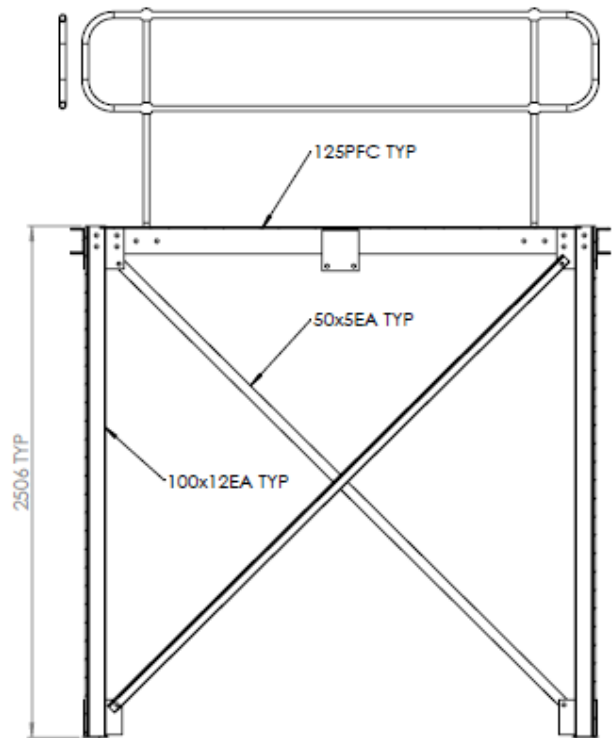


Figure 4-6: Silo support structure – Section B.

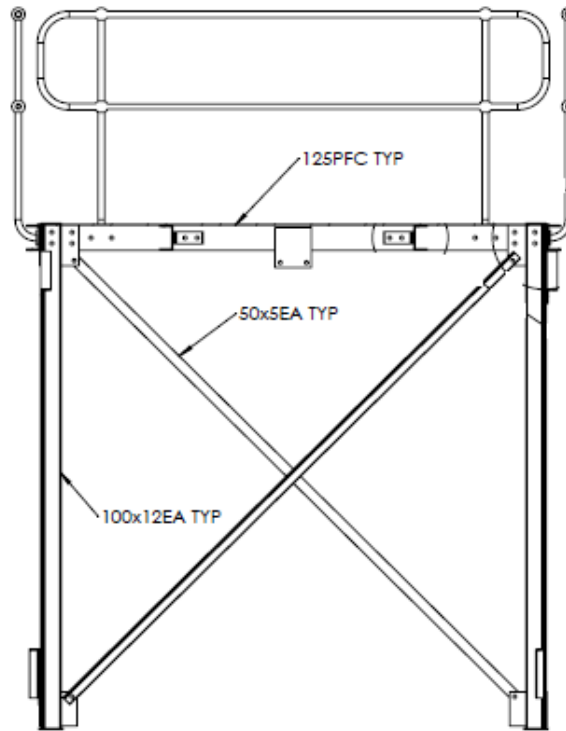


Figure 4-7: Silo support structure – Section C.

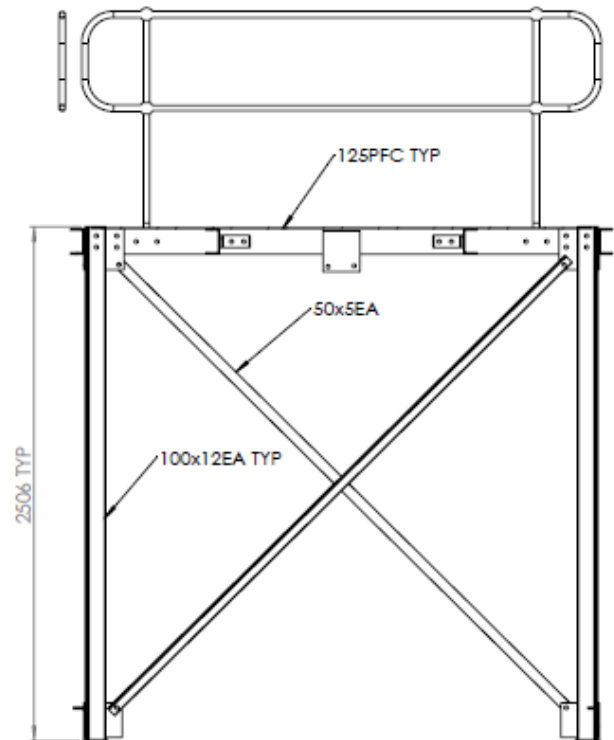


Figure 4-8: Silo support structure – Section D.

The model shown in Figure 4-1 was fabricated from mild steel plates, Grade 250MPa, with thicknesses from 2mm to 5mm. The silo was welded to the supporting structure to prevent lateral movement during discharge and other sources of excitation which may cause lateral movement such as the wind. The hopper openings were fitted with swing gates, as shown in Figure 4-9, designed to hold the iron ore inside the silo. The swing gates were locked by a fabricated steel latch. Once the latch was rotated the pressure acting on the gate automatically opened the gate to allow the iron ore to flow out as shown in Figure 4-10. The design of the silo ensured that the discharge would be concentric to minimise undesired lateral effects that would distort the final results.



Figure 4-9: 200 mm hopper opening with swing gate in locked position.



Figure 4-10: 200 mm hopper opening with swing gate open.

4.3 Computing Facilities for Data Analyses

The amount of data collected during the experiments was impractical to analyse on standard desktop computers. Therefore the parallel computing model adopted for this work and is presented in Figure 4-11.

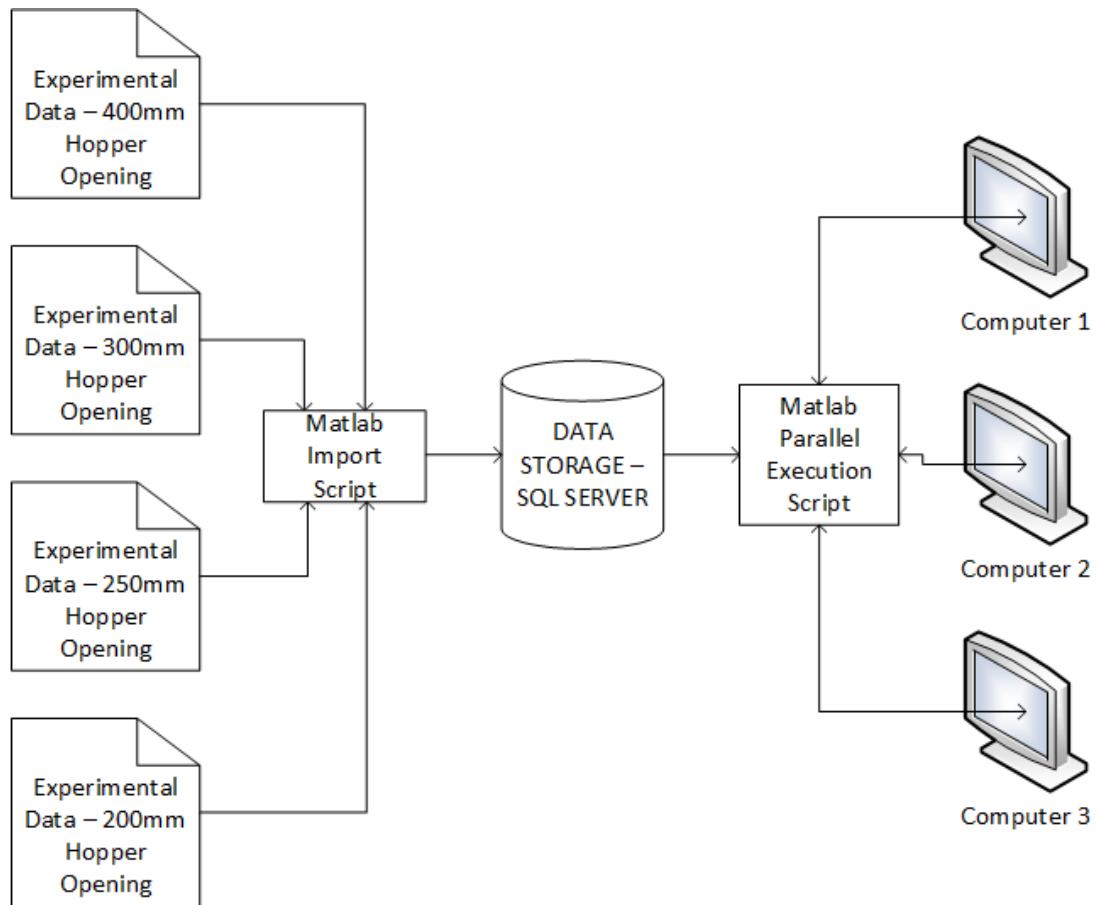


Figure 4-11: Data analysis using parallel computing.

The data collected from the data logger were imported into a relational database (SQL Server) for safe and efficient storage and retrieval purposes. The import script was written in Matlab and was written to execute in parallel. During execution, the parallelised Matlab script would analyse the computer hardware architecture and create compatible threads that would run in parallel based on the type of CPU and available execution cores. Once the threads had been created the computing load

would be distributed accordingly. Furthermore, the computing load was also distributed across to 2 other computers on the network like shown in Figure 4-11.

The specifications for the computers used in analysing the obtained data can be found in Table 4-1. Each of the computer used had two physical CPUs that had at least six execution cores per CPU. Each execution core on the CPU was capable of running two threads simultaneously. In summary, the available computing power was equivalent to approximately 44 desktop computers. Furthermore, it took over three months to completely analyse the available data with the available computing power. Such analyses would take approximately over ten years to compute on an average home computer.

Table 4-1: Computer specifications.

Computer Name	CPU	Total Parallel Execution Cores	Total Parallel Execution Threads	RAM
Computer 1	2 x Intel Xeon E5-2670	16	32	128GB
Computer 2	2 x Intel Xeon E5-2650	16	32	32GB
Computer 3	2 x Intel Xeon E5-2630	12	24	32GB

4.4 Silo Quake Response Spectrum – Experimental Setup

It is documented in the literature that the granular flow rate under gravity is influenced by the size of the hopper opening. To identify the silo quake response spectrum, it was necessary to have different hopper opening sizes to accurately assess the vibrational frequencies associated with the granular flow. It was proven to be expensive to construct many model silos of varying opening sizes. Therefore the

model silo was designed to have the interchangeable lower hopper for economic reasons (refer to Figure 4-12).

In total five different hopper opening sizes, 200mm, 250mm, 300mm, 350mm and 400mm, were fabricated. However, due to time constraints only 200mm, 250mm, 300mm and 400mm were used in the experiments.

Table 4-2 shows the experiments conducted in July 2016. At least six experiments were conducted for each hopper opening to obtain the hypothesised silo quake response spectra. This was primarily due to the unrepeatable nature of the results associated with silo flow experiments. Modal testings of the silo support structure were also conducted to obtain natural frequencies of the support structure and to calibrate the finite element models. However, it was later found that existing structural analysis software was not designed to solve silo quaking problems because these software only allow a single value of the mass of the structure in the analysis whereas the total mass of the silo structure changes with time. Therefore the results of the modal testings are stored for further analyses at a later date when the technology is readily available.

Table 4-2: Experiments – Silo Quake Response Spectrum.

EXPERIMENT N⁰	DESCRIPTION
1	FLOW TESTING – 400MM OPENING
2	MODAL TESTING
3	FLOW TESTING – 400MM OPENING
4	MODAL TESTING
5	FLOW TESTING – 400MM OPENING
6	FLOW TESTING – 400MM OPENING
7	FLOW TESTING – 400MM OPENING
8	FLOW TESTING – 400MM OPENING
9	MODAL TESTING
10	FLOW TESTING – 200MM OPENING
11	FLOW TESTING – 200MM OPENING
12	FLOW TESTING – 200MM OPENING (DATA NOT AVAILABLE)
13	FLOW TESTING – 200MM OPENING

14	FLOW TESTING – 200MM OPENING
15	FLOW TESTING – 200MM OPENING
20	MODAL TESTING
21	FLOW TESTING – 250MM OPENING
22	FLOW TESTING – 250MM OPENING
23	FLOW TESTING – 250MM OPENING
24	FLOW TESTING – 250MM OPENING
25	FLOW TESTING – 250MM OPENING
26	FLOW TESTING – 250MM OPENING
27	FLOW TESTING – 250MM OPENING
28	MODAL TESTING
29	FLOW TESTING – 300MM OPENING
30	FLOW TESTING – 300MM OPENING
31	FLOW TESTING – 300MM OPENING
32	FLOW TESTING – 300MM OPENING (DATA NOT AVAILABLE)
33	FLOW TESTING – 300MM OPENING
34	FLOW TESTING – 300MM OPENING
35	FLOW TESTING – 300MM OPENING
36	FLOW TESTING – 300MM OPENING
37	FLOW TESTING – 300MM OPENING
38	FLOW TESTING – 300MM OPENING
39	FLOW TESTING – 200MM OPENING
40	FLOW TESTING – 200MM OPENING
41	FLOW TESTING – 200MM OPENING
42	FLOW TESTING – 200MM OPENING
43	FLOW TESTING – 200MM OPENING

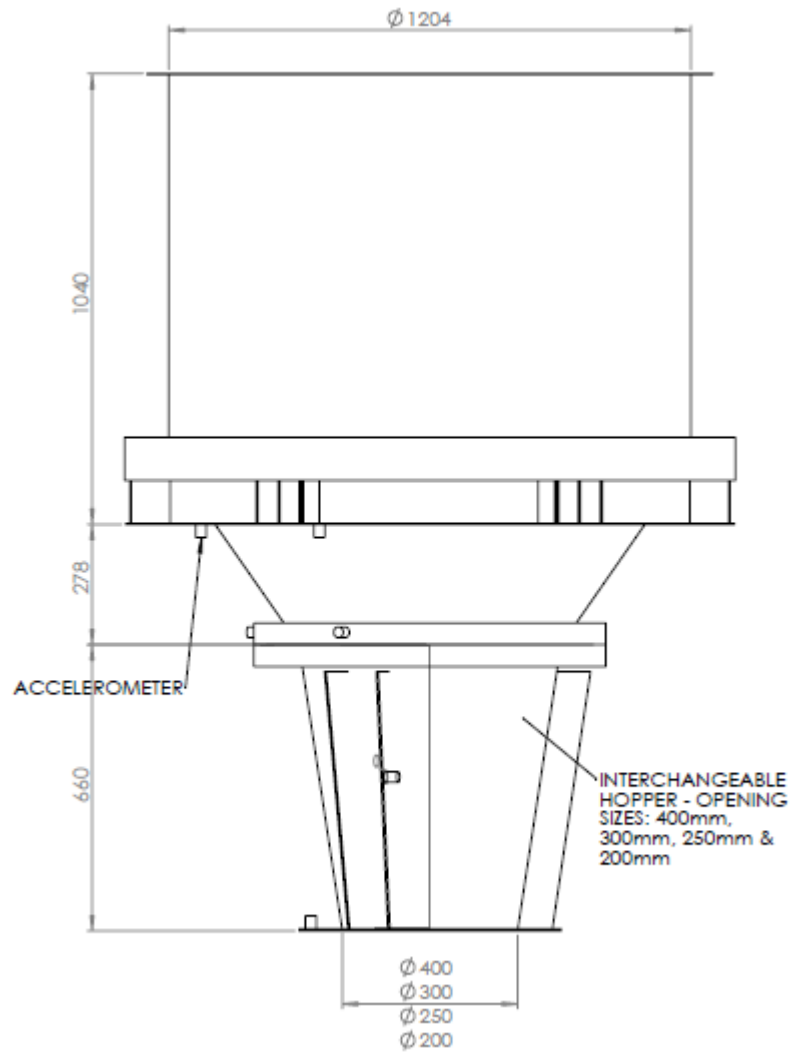


Figure 4-12: Dimensions of test silo (swing gate not shown).

The accelerometers were fastened to the silo and support frame by the screws supplied with the accelerometer kits. The holes in the silo and structure were tapped with the required size drill and taps. The contact surfaces were cleaned to ensure good contacts and readings. The eight white wires shown in Figure 4-9 connect the accelerometers mounted on the silo hopper to the data loggers nearby. Figure 4-13 below shows the accelerometer locations and serial numbers. The other eight accelerometer locations and serial numbers were mounted on the support structure as shown in Figure 4-14, Figure 4-15 and Figure 4-16 to measure the vibrations of the structure during silo discharge.

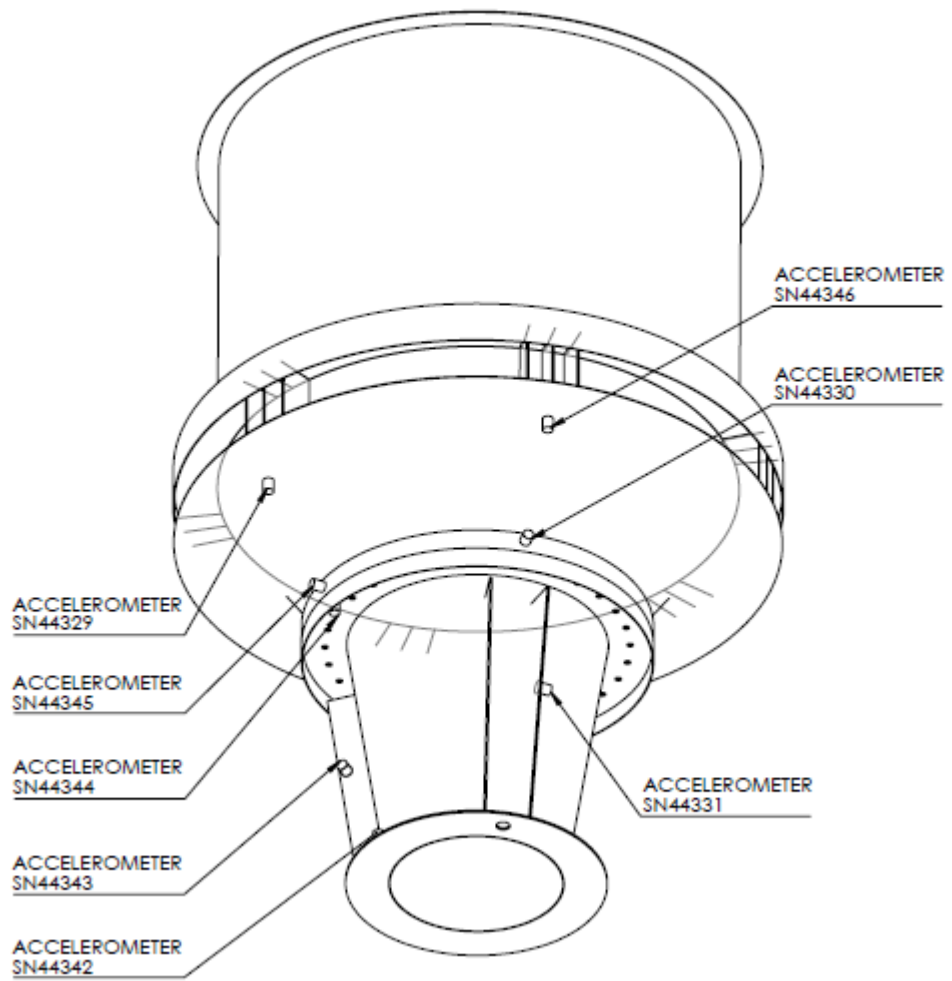


Figure 4-13: Accelerometer locations – Silo.

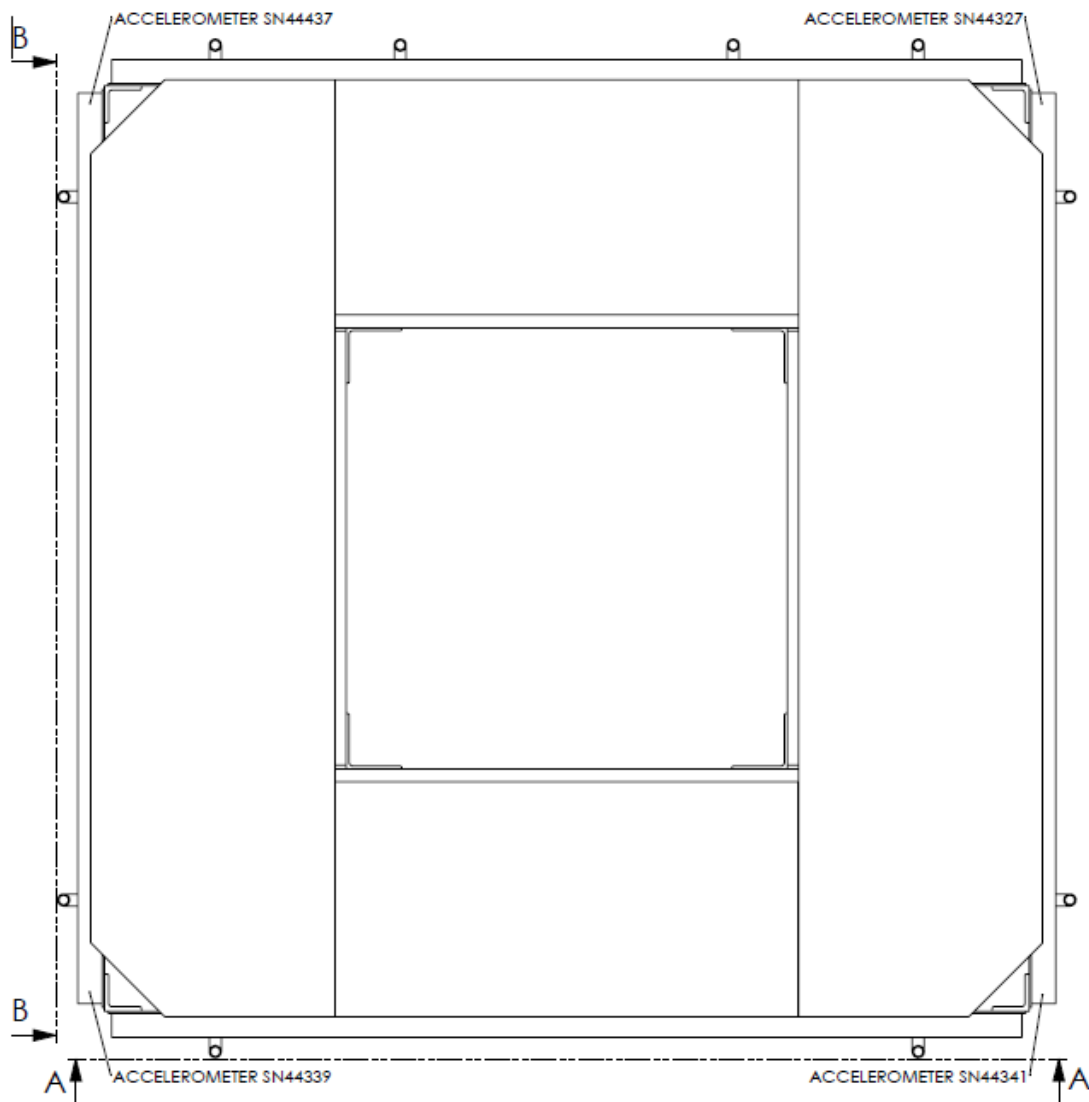


Figure 4-14: Accelerometer locations – platform top view.

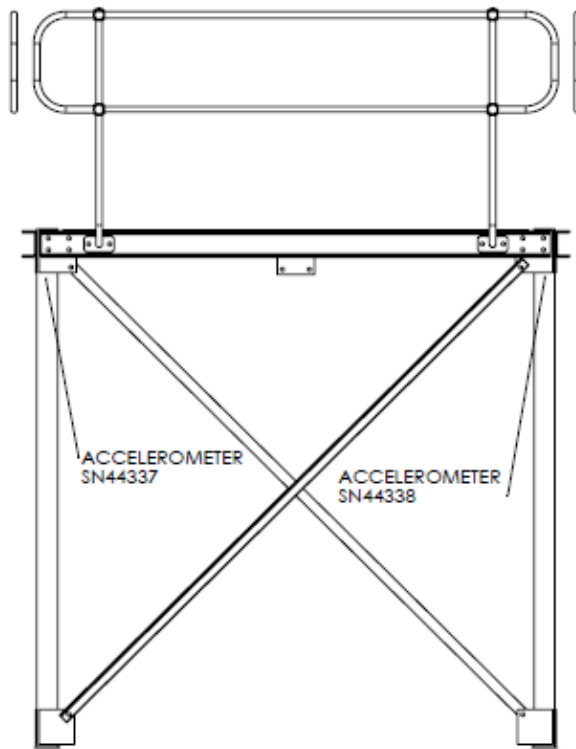


Figure 4-15: Accelerometer locations – Section A.

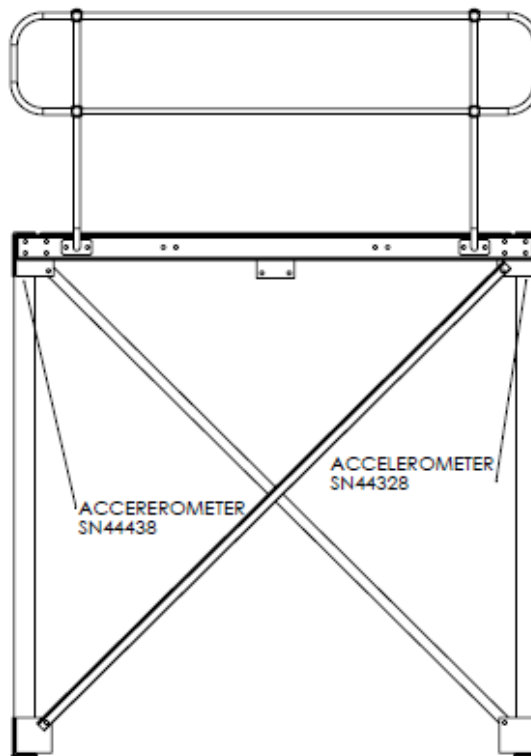


Figure 4-16: Accelerometer locations – Section B.

The accelerometers used in the experiments were seismic ceramic flexural ICP accelerometer model 393B04 made by PCB. They were capable of measuring frequency between 0.06Hz to 450Hz and acceleration up to $\pm 5g$. The accelerometer specifications can be found in Appendix A. The accelerometers were chosen based on their ability to sense frequencies within the expected frequency spectrum generated by the silo during discharge. It was noted by Tu and Vimonsatit (2013) that iron ore train load out silos suffer low frequency quaking of about 2Hz.

The accelerometers were connected to a data logger model NI-9234 and associated software made by National Instruments with the sampling rate set at 2048 samples per second. Each NI-9234 in Figure 4-17 data logger has input four channels, a sampling rate of 51200 per second and input voltage range of ± 5 volts. In total, 4 NI-9234 modules were required to connect 16 accelerometers mounted on the silo and the supporting structure.



Figure 4-17: NI-9234 data logger.

The iron ore discharged from the silo was captured by a tray of the 2.5m square and 0.5m height in dimension placed underneath the hopper opening as shown in Figure

4-19. The tray was designed in accordance to AS3774 (1996), AS4100 (1998), AS/NZS1554.1 (2004), AS/NZS1170.0 (2002), fabricated from steel plates of Grade 250MPa and capable of handling 3 tonnes of iron ore. As shown in Figure 4-1 the tray was resting on top of 2 weighing beams (yellow beams under the steel tray). The weighing beams under the tray contained four AGX-1 load cells capable of recording weight and time at ten samples per second. The load cells inside the yellow weighing beams were connected to the AJIK6 data logger provided by Australian Weighing Equipment Pty Ltd. The measured values were later used to calculate the flow rates for further analyses.

A forklift with a drum rotator attached was used to lift and rotate the drums to load the silo as shown in Figure 4-18. Once the silo was sufficiently filled, the ore at the top of the silo was levelled manually to minimise the dynamic effects due to eccentricities. Upon completion of the filling and preparation processes, the swing gate at the hopper opening was opened like shown in Figure 4-19 to allow the iron ore to flow out into the tray of the 2.5m square and 0.5m height in dimension below. The swing gate was closed after the iron ore had been completely discharged from the silo.

To take the ore out of the tray after each experiment, five bulker bags with a spout at the bottom were placed inside the tray. Each bulker bag had a safe working load (WLL) of 1 tonne. Once the ore was completely discharged from the silo, the bulk bags were lifted out of the tray via the forklift and the spout at the bottom of the bulk bag was opened to fill the drums with the ore. The emptied bulker bags were placed back into the rectangular steel tray. The drums filled with iron ore was lifted by the forklift with drum rotator and discharged into the silo again.



Figure 4-18: Filling test silo with iron ore.

In total, 34 flow experiments were conducted for the silo shown in Figure 4-12 with various opening sizes (refer to Table 4-2). All the parameters were kept the same for all the experiments for each hopper opening size, except moisture content as it was impractical to maintain the moisture content of over 2 tonnes of iron ore. However, the iron ore was kept under cover for the entire duration of the experimental period. The provided roof cover was effective at keeping the rainwater from contaminating the iron ore in the tray and damaging the accelerometers and load cells. After each day of testing, a sample of the ore was taken for moisture content tests.



Figure 4-19: Bulk bags inside the tray filled with iron ore after silo discharge.

The nonlinear nature of the granular flow and time varying mass characteristics associated with the silo had prompted the use of Hilbert Huang Transform (HHT), presented in Chapter 3.6, over the Fast Fourier Transform (FFT) method. Once the signals have been transformed into frequencies and amplitudes, the Hilbert Marginal Spectrum (HMS) method, which represents a measure of the total amplitude or energy contribution from each frequency, was selected to transform the data into graphs to aid the understanding of the silo quake response spectrum.

In total, more than 71500000 data points were collected by the accelerometers during the experiments mentioned in Table 4-2. The acceleration data were used to calculate intrinsic mode functions (IMFs) as outlined by the HHT signal processing

technique. On average one accelerometer generated about 17 to 18 IMFs of the same number of data points. Therefore the total number of data points required to be analysed to find the silo quake response spectrum was more than 1200000000. Due to the amount of data required for analyses was so large that it was deemed necessary to employ parallel computing architectures such as shared memory and distributed memory to assist with the data analysis process as presented in Chapter 4.3.

4.5 Silo Quaking – Experimental Setup

It was witnessed during the experiments described in section 4.1, that the silo structural system was a time varying mass structural dynamic system. This phenomenon has not been documented by previous researches. Further investigations into time varying mass dynamic problems proved that the current structural dynamic formulations assume that the total mass of the structural system remains constant and only consider time varying forces in the solution process. However, it was witnessed that the total mass supported by the silo structure was increasing during filling and reducing with time during discharge thus affecting the overall dynamic response of the structure.

To gain more in depth understanding into the silo quaking phenomenon, a new set of experiments were conducted on the same silo structure and granular material with minor structural modifications. It can be seen in Figure 4-20 and Figure 4-21, four brackets and backing beams were fabricated and welded the existing structure. Further, four support legs were fabricated and welded to the skirt of the silo. Finally, the four load cells, made by HBM (RSCC3/5T), were bolted in between the brackets and the support legs.

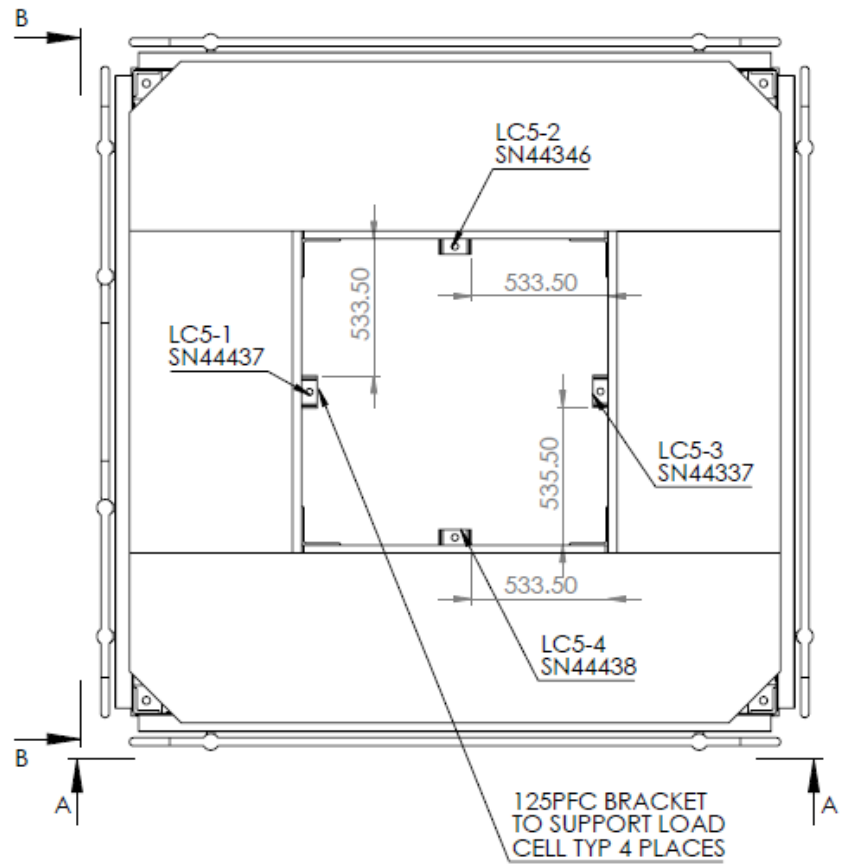


Figure 4-20: Silo support frame modified to carry 4 x load cells – Top View.



Figure 4-21: Silo supported on 4 x load cells – Bottom View.

Adjacent to the four load cells were four PCB 393B04 accelerometers (see Figure 4-21). These accelerometers were necessary to measure the accelerations of the structure due to the forces generated during silo discharge. The measured accelerations adjacent to the load cells would then be used to validate the estimated response of the structure due to the pulsating loads generated from the silo during discharge.

The support frame was also fitted with four accelerometers to measure the lateral movements during silo discharge (refer to Figure 4-22 and Figure 4-23). The lower hopper and the intersection between the lower hopper and upper hopper were also fitted with two accelerometers to measure the difference in amplitudes of vibration during silo discharge as shown in Figure 4-24.

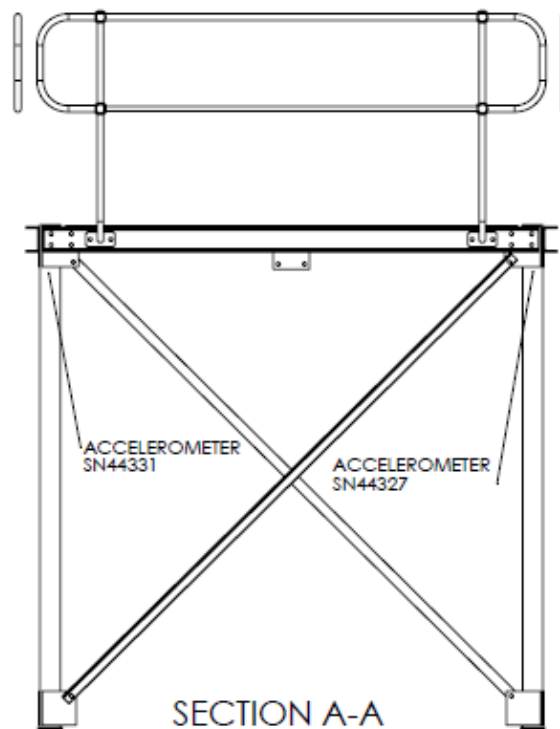


Figure 4-22: Accelerometer locations – Section A.

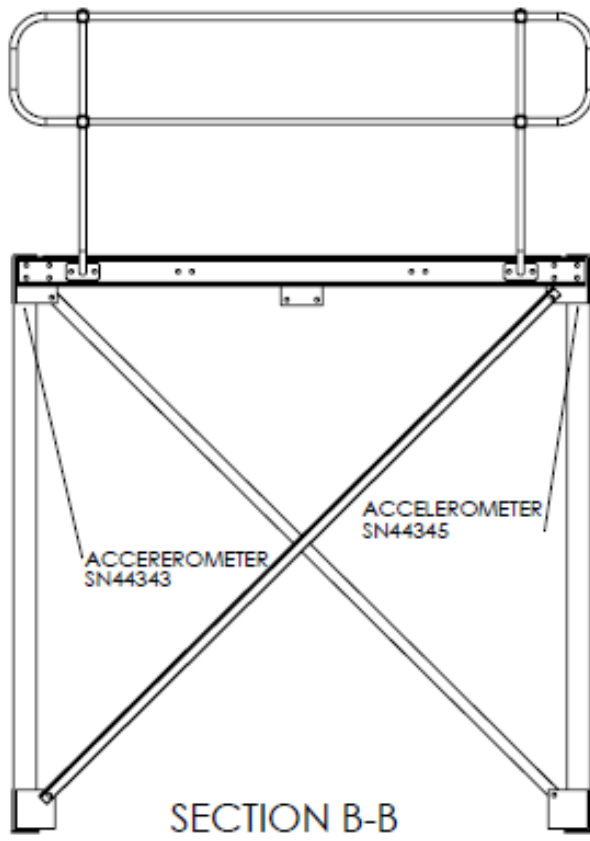


Figure 4-23: Accelerometer locations – Section B.

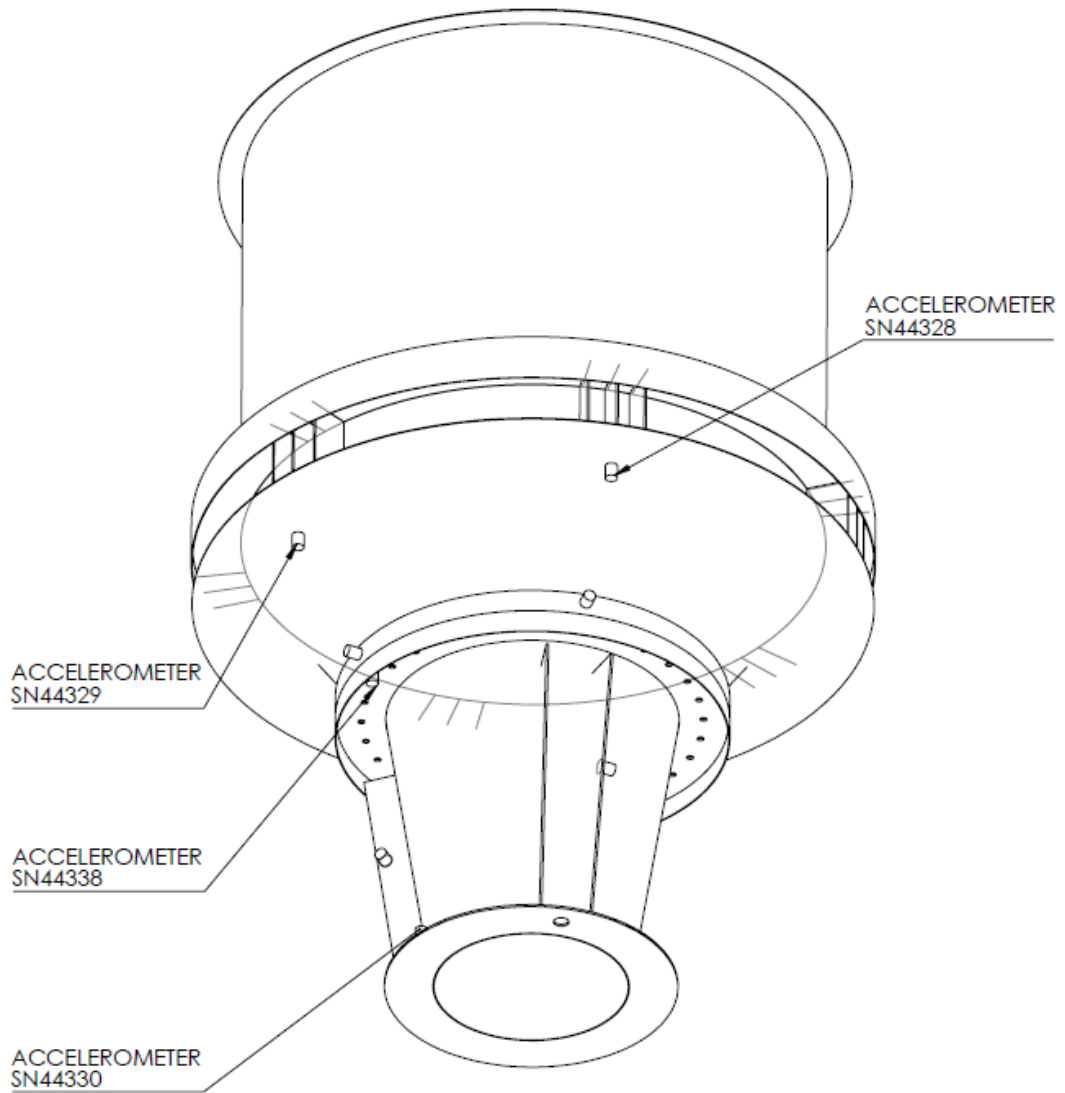


Figure 4-24: Accelerometer locations – Silo.

The load cells, accelerometers and weighing beams were connected to two QuantumX MX840A universal data amplifiers made by HBM (see Figure 4-25). Appropriate calibrations were conducted on all devices connected to the amplifier. The QuantumX MX840A were connected to the computer installed with associated data acquisition software. The main advantage of this configuration was it allowed for synchronisation of captured data across all devices.



Figure 4-25: HBM QuantumX MX840A universal data amplifier.

The accelerometers mounted on the underside of the beams supporting the brackets with load cells attached (Figure 4-21) were connected to the NI 9234 data logger similar to Figure 4-17. All data loggers were set to record at 2400 samples per second.

Apart from the modifications mentioned above, the procedures to load and unload the iron ore from the silo, tray and drums were identical to the procedures mentioned in 4.1. Overall, three hopper size openings were used in the experiment. In total three experiments were conducted (refer to Table 4-3) to check the validity of the Equation of Silo Quaking.

Table 4-3: Experiments – Equation of Silo Quaking.

EXPERIMENT N ⁰	DESCRIPTION
1	FLOW TESTING – 400MM OPENING
2	FLOW TESTING – 350MM OPENING
3	FLOW TESTING – 300MM OPENING

The recorded accelerations were denoised using Wavelet algorithms in Matlab 2017a. The theoretical background into Wavelet denoising can be found in literature

published by Strang (1997), Mertins (1999) and Shukla (2013). The denoised acceleration data were used to find the instantaneous velocities and displacements by applying the fundamentals of calculus as shown in Equation 4-1 and Equation 4-2 below:

$$a = \lim_{\Delta t \rightarrow 0} \frac{\Delta v}{\Delta t} = \frac{dv}{dt} \quad \text{Equation 4-1}$$

$$v = \lim_{\Delta t \rightarrow 0} \frac{\Delta y}{\Delta t} = \frac{dy}{dt} \quad \text{Equation 4-2}$$

The instantaneous forces were calculated based on the following data:

1. Denoised instantaneous accelerations using Wavelet algorithms in Matlab (2017a).
2. Estimated instantaneous velocities from denoised instantaneous accelerations.
3. Estimated instantaneous displacement from instantaneous velocities.
4. Estimated structural stiffness of 4546000 N/m from the SpaceGass structural model. A unit point load was applied at the silo support locations, and the frame was analysed. The stiffness at the location was calculated by dividing the unit load by the deflection obtained from the linear elastic analysis.
5. Estimated critical damping of 2%.
6. Interpolated mass of iron ore remaining in the silo at each time step corresponding to the acceleration data.

4.6 Material Classification

The iron ore supplied by Rio Tinto had particle sizes ranging from microns to less than 6mm. The ore was stored in sixteen 56 gallons drums covered with lids (see Figure 4-26) to maintain its natural moisture content and for ease of transport from the mine site to the laboratory. A representative sample was taken from a drum in accordance with procedures outlined in AS1289.1.1 (2001) for material characterisation.



Figure 4-26: Drums carrying iron ore.

The material was characterised by various established engineering procedures from two engineering disciplines such as Geomechanics and Material Handling. The material classification process included those procedures first introduced by Jenike (1961) and later developed further into ASTM D6128-16 (D6128-16 2016).

However, due to the lack of funding to purchase the Jenike's shear cell, a similar direct shear cell (Figure 4-27) was used to carry out the test procedures as per ASTM D6128-16 to obtain material flow function, material flow factor, major consolidation stress, effective angle of internal wall friction, wall friction angle and unit weight of bulk solid. The shear cell shown in Figure 4-27 below allowed the user to alter consolidation stress which is the primary difference between a direct shear cell and Jenike's shear cell.



Figure 4-27: Automatic direct shear tester.

Liquid Limit (Figure 4-28) as defined in AS1289.3.1.1 (2009) and Plastic Limit (Figure 4-29) as defined in AS1289.3.2.1 (2009) are standard geotechnical laboratory

tests routinely employed to determine the plasticity index of the cohesive soil. Liquid Limit (LL) are defined as the water content where the behaviour of the soil changes from plastic to liquid. The Plastic Limit is defined as the moisture content where the thread of soil as per AS1289.3.2.1 (2009) break apart. These values have proven to be useful in determining whether the soil mass is pre-consolidated qualitatively.



Figure 4-28: Apparatus to test soil liquid limit.



Figure 4-29: Plastic limit test.

The apparatus shown in Figure 4-30, Figure 4-31 and Figure 4-32 are used to determine the density of the soil in accordance with procedures outlined in AS1289.3.5.1 (2006). It is important to distinguish the density obtained here in comparison to the density obtained via the shear cell in accordance to D6128-16 (2016). The density obtained in accordance to AS1289.3.5.1 (2006) is the maximum density of the soil whereas the density values obtained in accordance to D6128-16 (2016) are bulk densities and are dependent on consolidation pressure and moisture content. In any case, the values obtained from AS1289.3.5.1 (2006) are always higher than the ones obtained from D6128-16 (2016).



Figure 4-30: Water bath used for testing soil density.



Figure 4-31: Volumetric flasks used in density measurement.

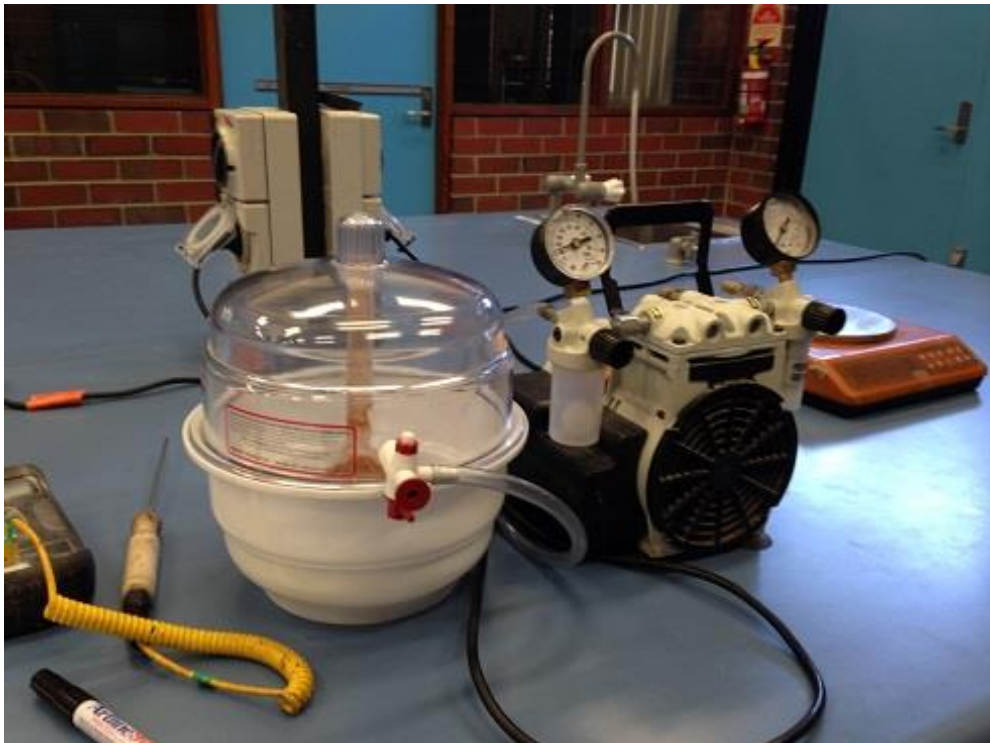


Figure 4-32: Vacuum used for testing soil density.

The particle size distribution of the representative sample of iron ore was carried out in accordance with the procedures outlined in AS1289.3.6.1 (2009) and the apparatus shown in Figure 4-33. In civil engineering, such test provides a quantitative assessment of how the material can be used in practice. In the case of silo design, it provides an assessment of whether the granular material's flow behaviour. Thus critically important to sound operation of the silo and associated equipment.



Figure 4-33: Sieve shaker.

The moisture content of the granular material is one of the most important parameters in the design of silo for flow. It is well documented in the literature that the behaviour of the granular material or soil changes depending on the moisture content. As previously mentioned, the Liquid Limit and Plastic Limit tests seek to determine such limits. In the case of granular material inside a silo, it is rare that the material will reach the Liquid Limit and Plastic Limit. However sufficient changes in moisture content can cause segregation.

Given its importance, the moisture content of the granular material was carried out at the end of each day throughout the experiment period with the oven shown in Figure 4-34 in accordance to AS1289.2.1.1 (2005).



Figure 4-34: Oven used for moisture content tests.

4.7 Conclusion

To identify the silo quake response spectrum and gather sufficient data to formulate the dynamic response of the silo structure during material discharge the following apparatus and experiments were required:

1. Fabrication of the 1 to 10 scale model silo and its supporting structure.
2. Parallel computing architecture used to analyse the data.
3. Silo quake response spectrum experimental setup.
4. Silo quaking experimental setup.
5. Material classification experimental setup.

5 SILO QUAKE RESPONSE SPECTRUM

5.1 Introduction

This chapter presents the results such as flow rates, accelerograms, Hilbert Marginal Spectra (MHS) and silo quake response spectra, obtained from the experiments designed to identify the existence of the silo quake response spectrum. The resulting graphs displaying the MHS have been relocated to Appendix B due to a large number of graphs and importance compared to the graphs presenting the flow rates, pulsation loads and silo quake response spectra.

5.2 Flow Rates and Accelerograms

The recorded flow rates for experiments involving 400mm, 200mm, 250mm and 300mm hopper opening sizes are presented in Figure 5-1, Figure 5-2, Figure 5-3 and Figure 5-4. An analysis of those figures indicate that the flow rates in all the experiments are fluctuating and are very nonlinear. Additionally, it is evident in Figure 5-1, Figure 5-2, Figure 5-3 and Figure 5-4 that the fluctuations in the flow rates coincide with the pulses in the accelerograms shown in Figure 5-9 for the 400mm hopper, Figure 5-10 for the 200mm hopper, Figure 5-11 for the 250mm hopper and Figure 5-12 for the 300mm hopper. Furthermore, it can be concluded that the higher the flow rate, the stronger the pulse in the accelerogram.

The flow rates for the silo with 400mm and 300mm hopper openings are much slower during the first 20 seconds and 40 seconds respectively compared to the last 3 seconds where the flow rates increase rapidly. Such observations are confirmed by inspecting Figure 5-5, Figure 5-6, Figure 5-7 and Figure 5-8 where the total masses of the iron ore remaining inside the model silo are plotted against time. It is evident in Figure 5-5, Figure 5-6, Figure 5-7 and Figure 5-8 that the changes in the total mass of the iron

ore inside the silo are nonlinear across all experiments. The reason for such phenomena may be due to the surcharge acting on top of the flow channel affecting the flow rates.

The accelerograms presented in Section 5.2.2 demonstrate that the flow of the granular material is pulsating thus causing the silo structure to respond accordingly. The accelerations recorded by the accelerometers demonstrate that the pulsations caused by the flow of the granular material occur in all principal directions despite the flow of the granular material is concentric. Thus it can be concluded that the silo and its supporting structure were deflecting in all principal directions and the deflections were caused by the pulsating loads originating from the flow of the granular material.

Furthermore, the accelerometers on the silo (refer to Figure 4-13) recorded higher acceleration values compared to the accelerometers on the silo supporting structure (refer to Figure 4-14, Figure 4-15 and Figure 4-16). Such reductions in the amplitudes of vibration were caused by the damping provided by the supporting beams and columns.

Additionally, it is quite evident that the results are different across all experiments despite all parameters except the moisture content were kept the same during the experiment. Furthermore, the unrepeatable nature of the experimental results is consistent with observations made by Bennett and Kmita (1996) where the measured results from granular flowing out of silos are not repeatable across experiments despite all parameters being kept constant. One immediate cause is the abrasion of the silo wall by the flowing granular particles thus causes the change in friction.

Moreover, it was found to be impractical to maintain a consistent moisture content for over 2 tonnes of iron ore. However, as shown in Table 5-1, that the variations are not large but are not the only contributing factor to the unrepeatable responses recorded by the accelerograms. Other contributing factors include the particle shapes and particle to particle interlocking.

Table 5-1: Moisture content variations for Silo Quake Response Spectrum Experiments.

Experiment N ^o	Hopper Opening Size (mm)	Moisture Content %
1	400	3.98
3	400	4.41
5 & 6	400	4.19
7 & 8	400	4.33
10, 11 & 12	200	4.24
13	200	4.26
14 & 15	200	4.02
21	250	3.72
23 & 23	250	3.73
24, 25, 26 & 27	250	3.51
28, 29 & 30	250	3.46
31, 32 & 33	300	3.39
34 & 35	300	2.67
36, 37 & 38	300	3.66
39 & 40	200	3.37
41, 42 & 43	200	3.27

5.2.1 Flow Rates

The graphs, Figure 5-1 to Figure 5-4, presented in this section illustrate the captured flow rates from the experiments outlined in Table 5-1. Additionally the graphs, Figure 5-5 to Figure 5-8, illustrate the total masses remaining inside the silo in all the experiments. As previously mentioned, the flow rates illustrated in Figure 5-1, Figure 5-2, Figure 5-3 and Figure 5-4 are quite random, nonlinear and pulsating. Figure 5-1 and Figure 5-4 illustrates spikes in the flow rates towards the end of the discharge cycled compared to Figure 5-2 and Figure 5-3. This phenomenon may be caused by the surcharge on top of the flow and the hopper half angle.

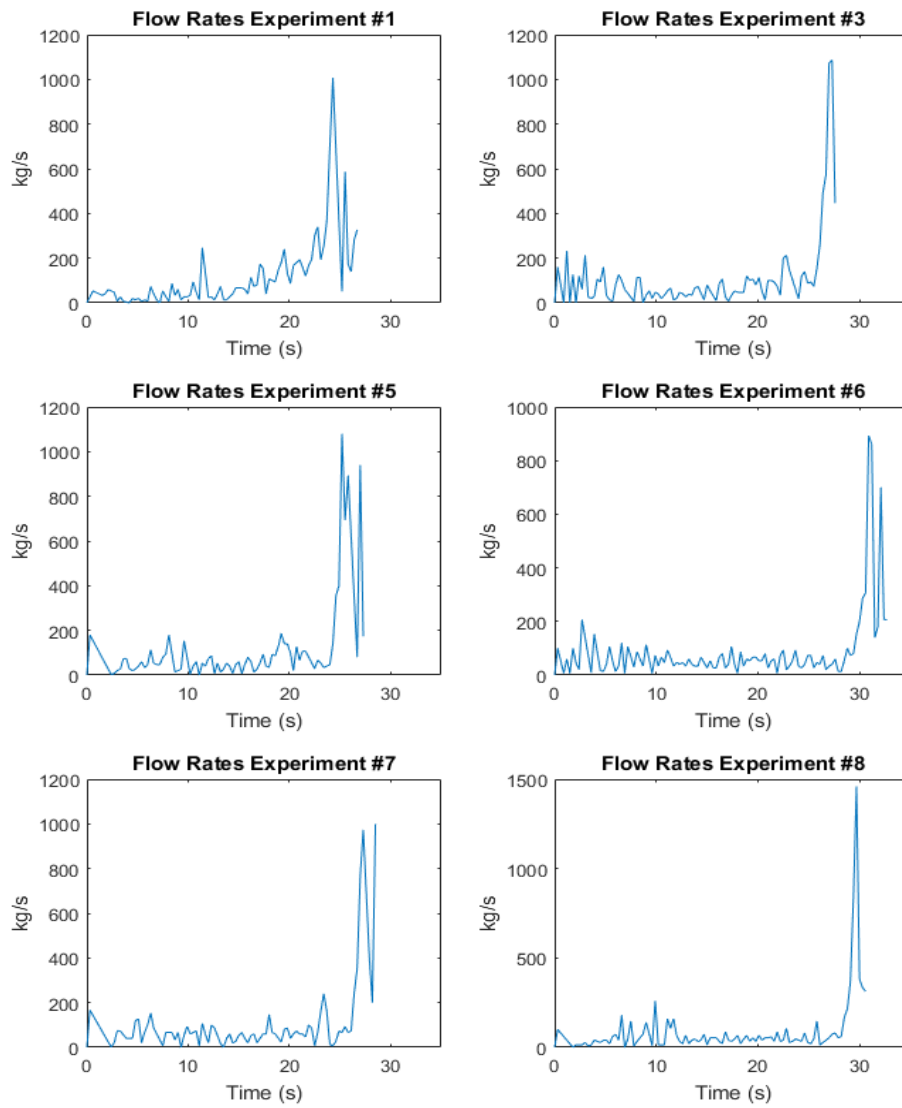


Figure 5-1: Measured flow rates for silo with 400mm hopper opening.

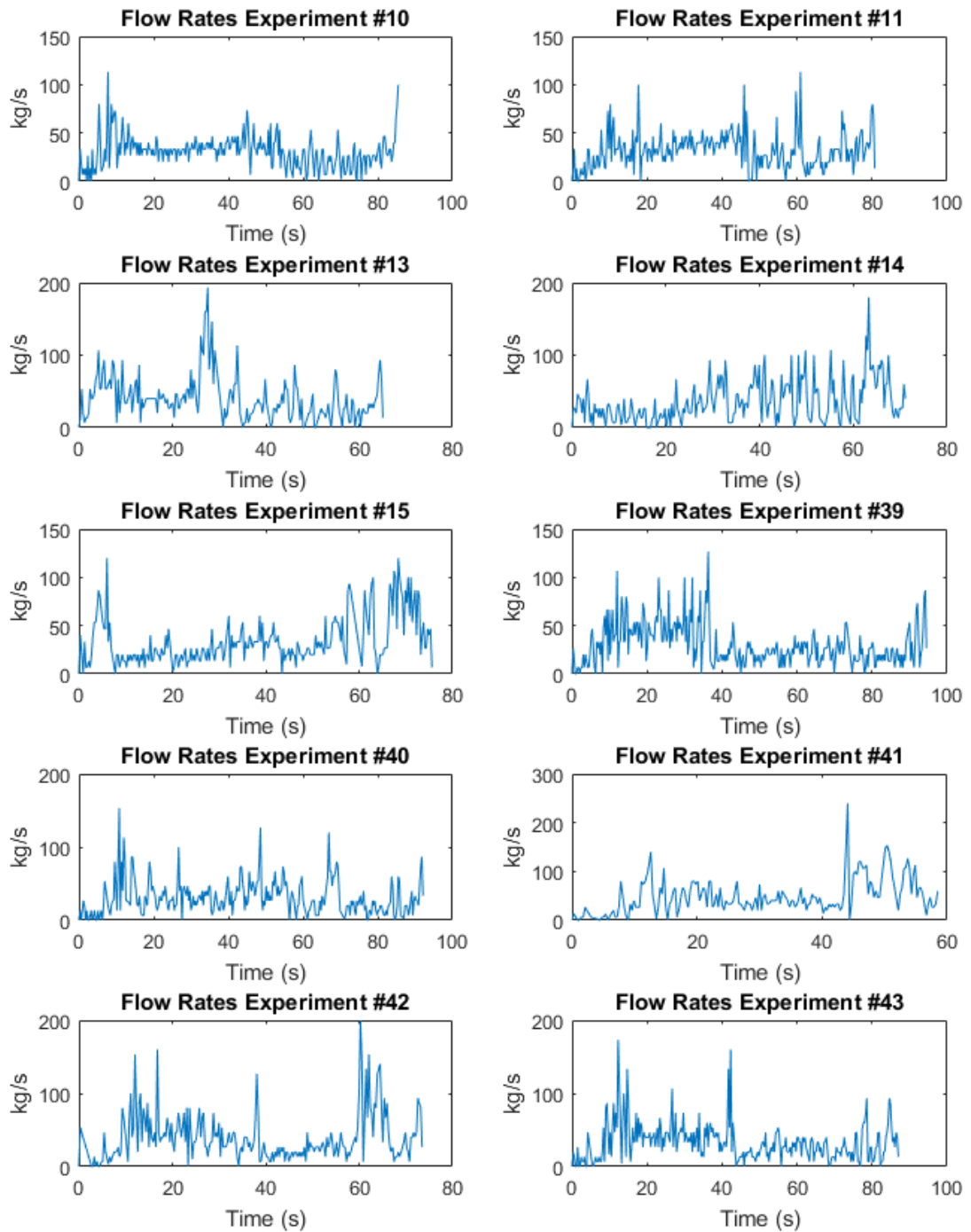


Figure 5-2: Measured flow rates for silo with 200mm hopper opening.

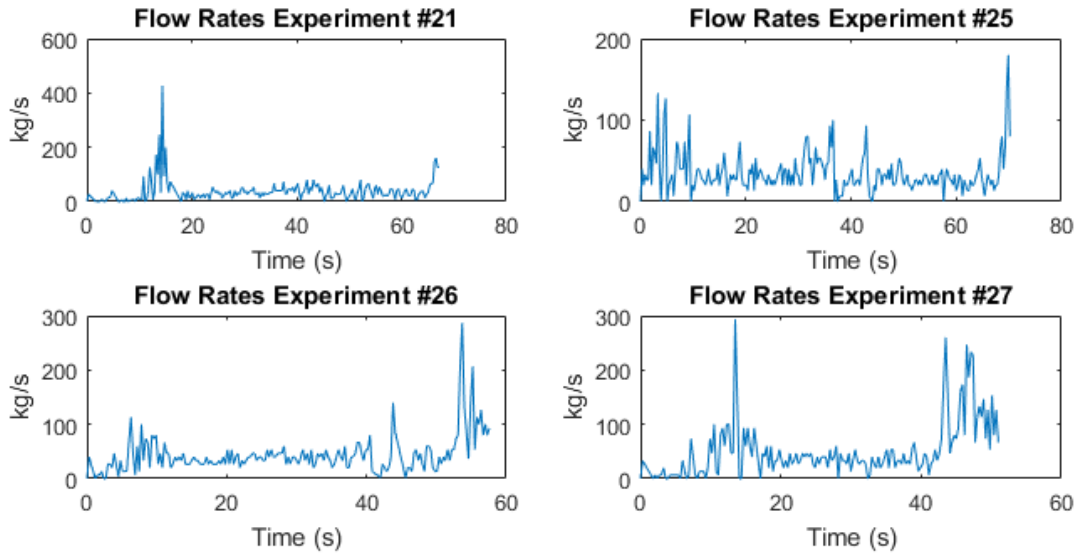


Figure 5-3: Measured flow rates for silo with 250mm hopper opening.

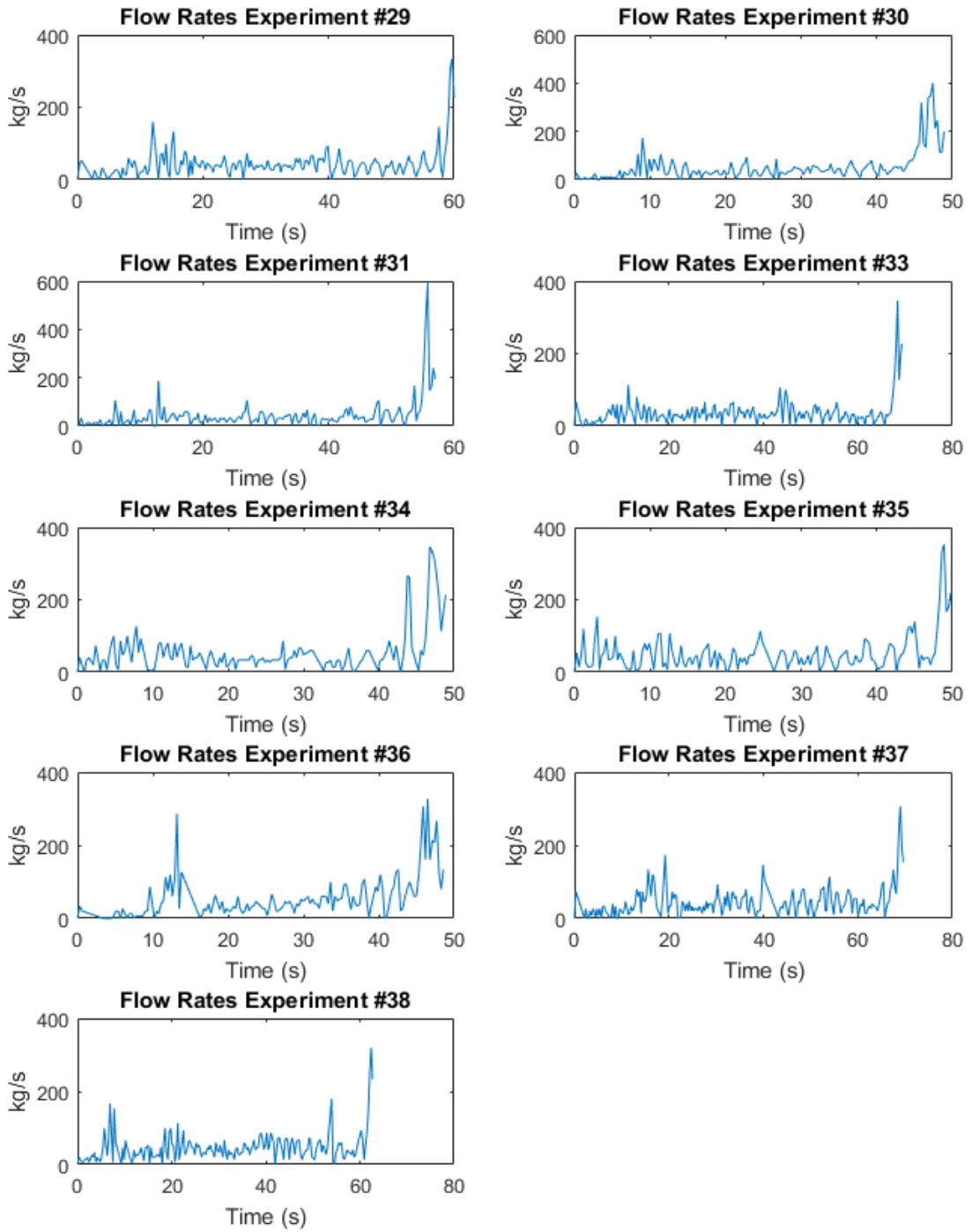


Figure 5-4: Measured flow rates for silo with 300mm hopper opening.

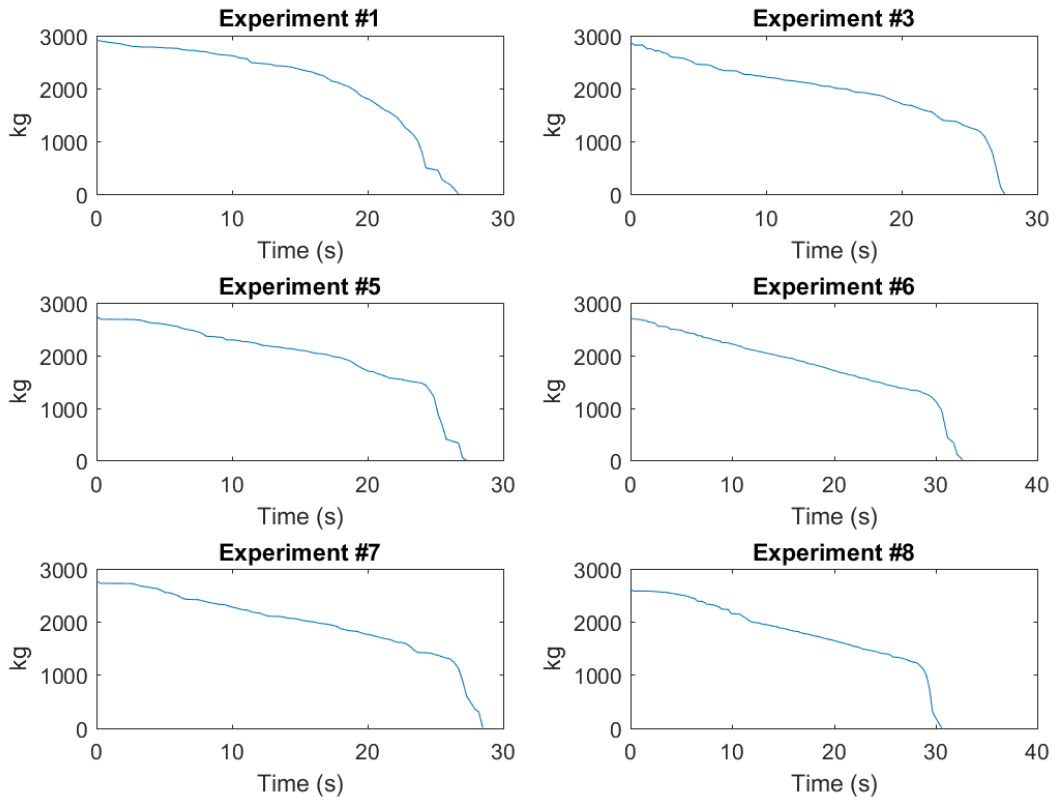


Figure 5-5: Total mass of iron ore remaining inside the silo vs time for 400mm hopper opening.

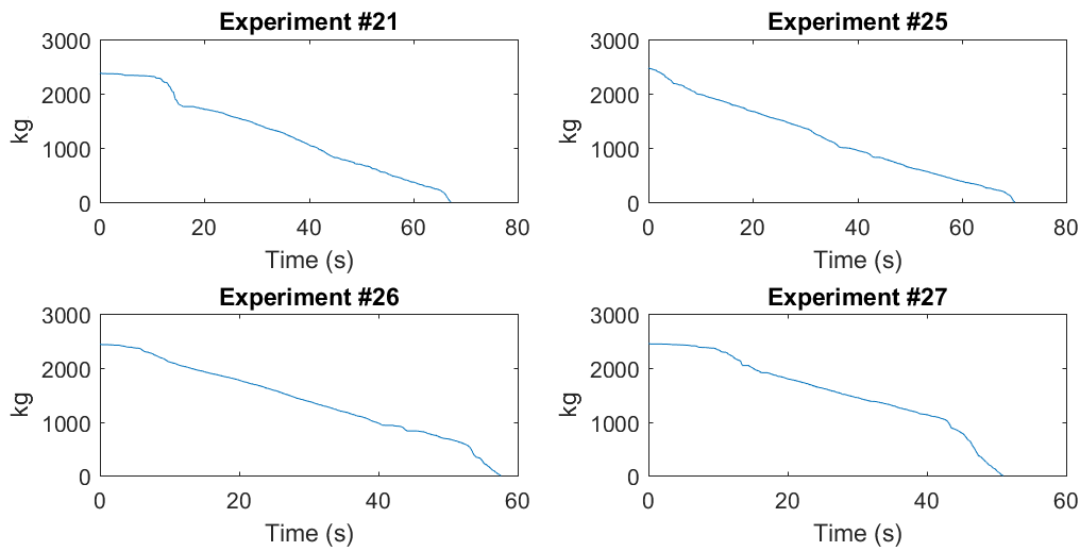


Figure 5-6: Total mass of iron ore remaining inside the silo vs time for 250mm hopper opening.

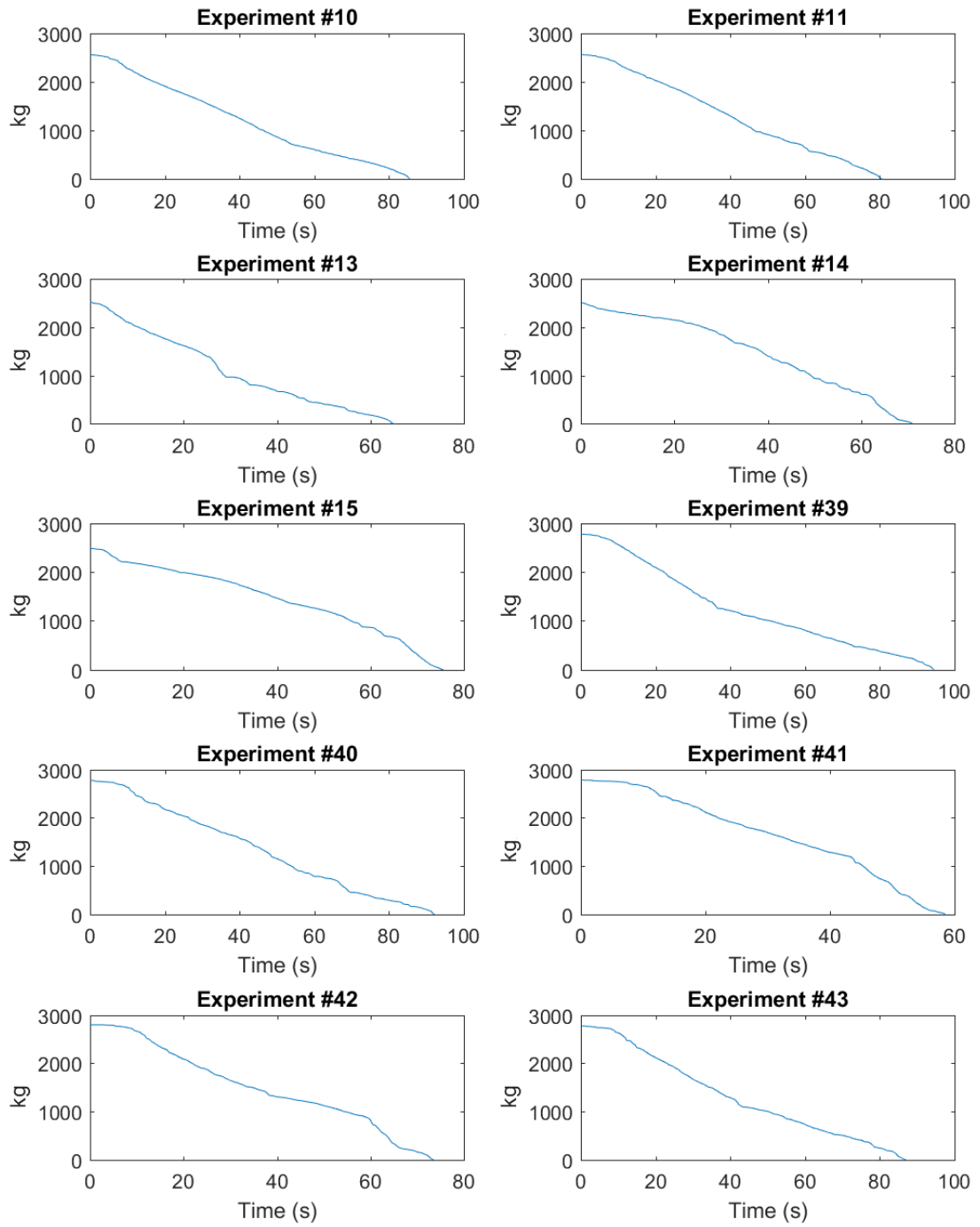


Figure 5-7: Total mass of iron ore remaining inside the silo vs time for 200mm hopper opening.

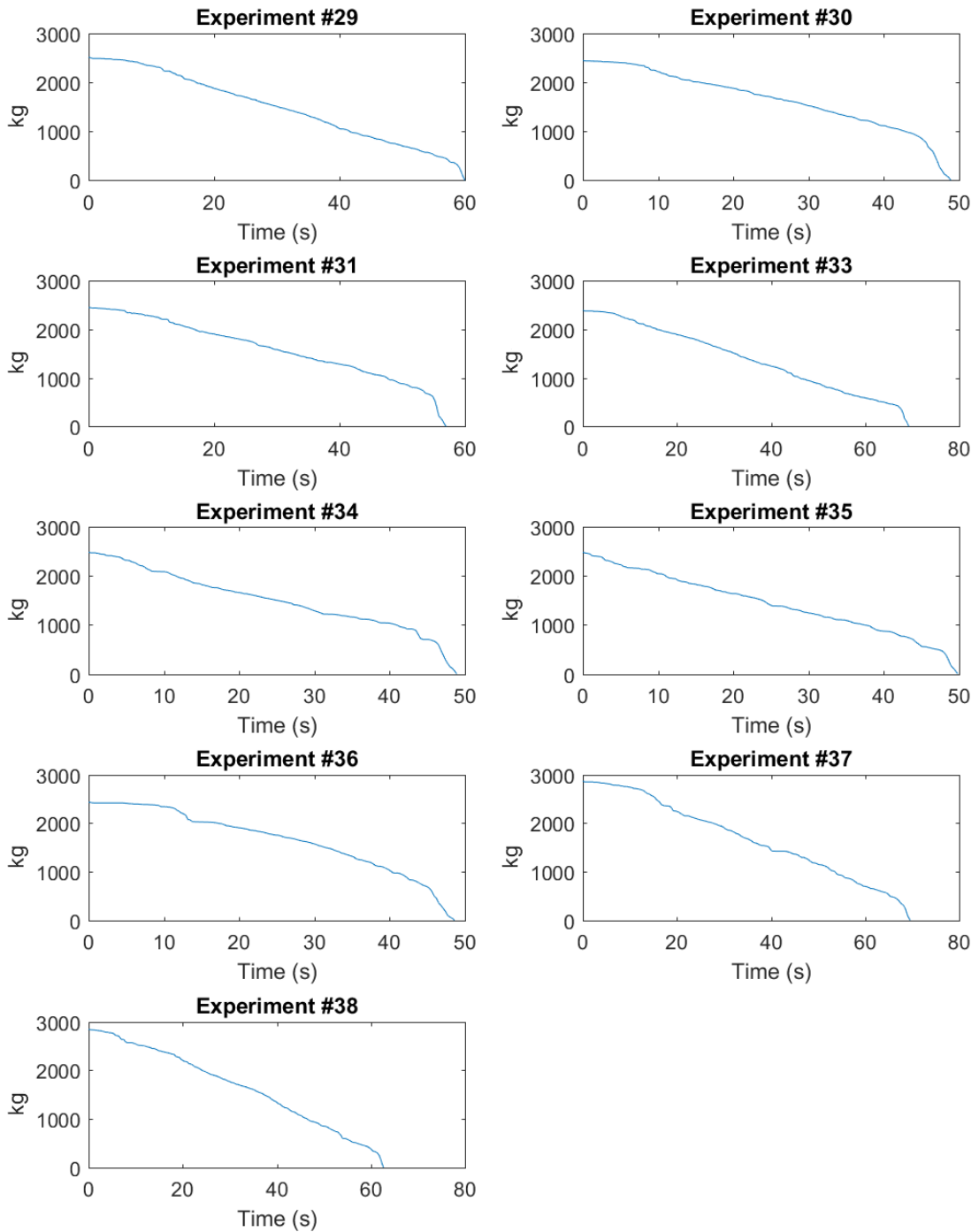


Figure 5-8: Total mass of iron ore remaining inside the silo vs time for 300mm hopper opening.

5.2.2 Accelerograms

The accelerograms, for Experiments 1, 10, 21, and 29, presented in this chapter illustrate the responses of the silo structure, with different hopper opening sizes, during granular discharge. Accelerograms for other experiments can be found in Appendix C.

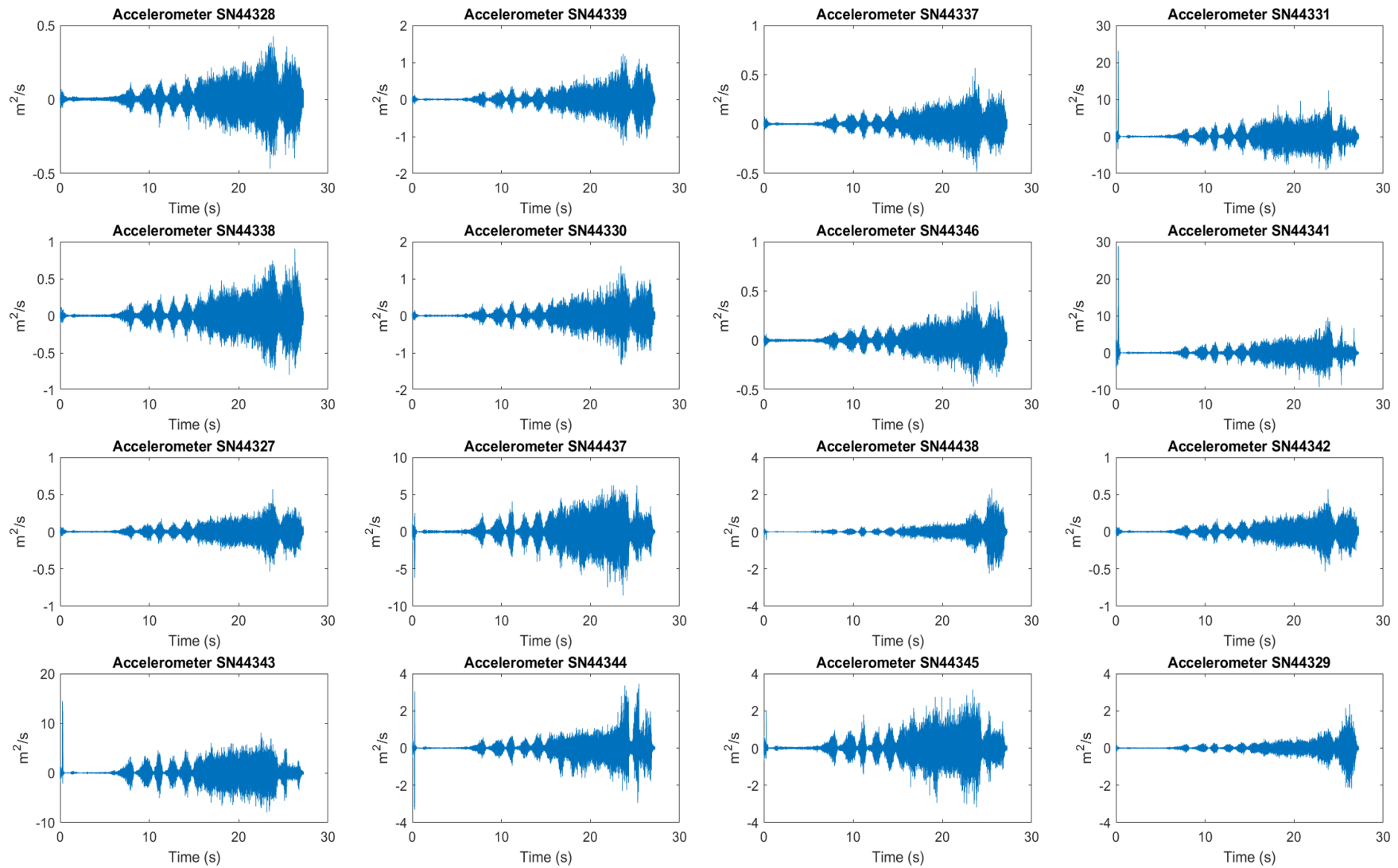


Figure 5-9: Acceleration vs Time for Experiment 1 - 400mm Hopper.

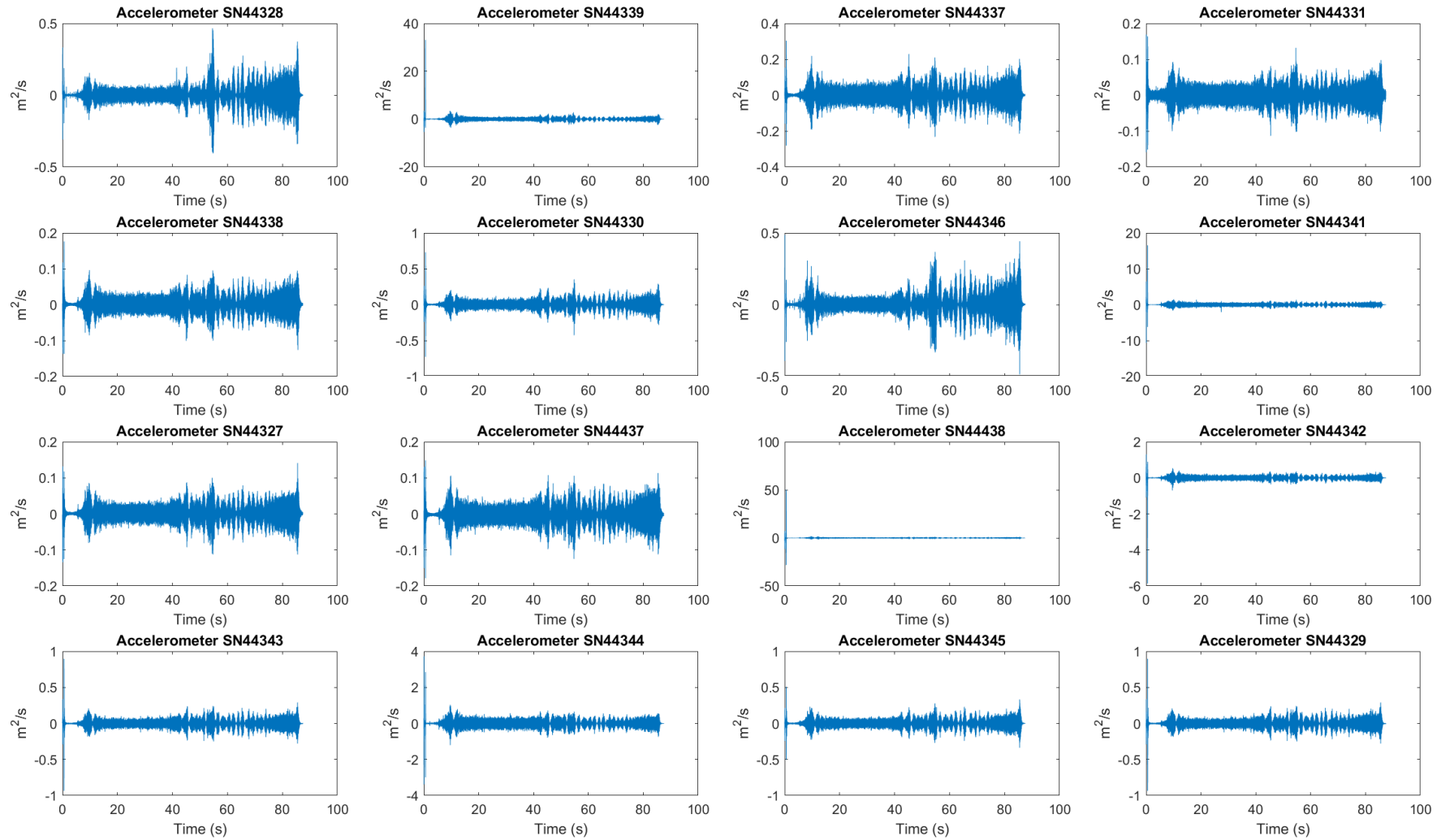


Figure 5-10: Acceleration vs Time for Experiment 10 - 200mm Hopper.

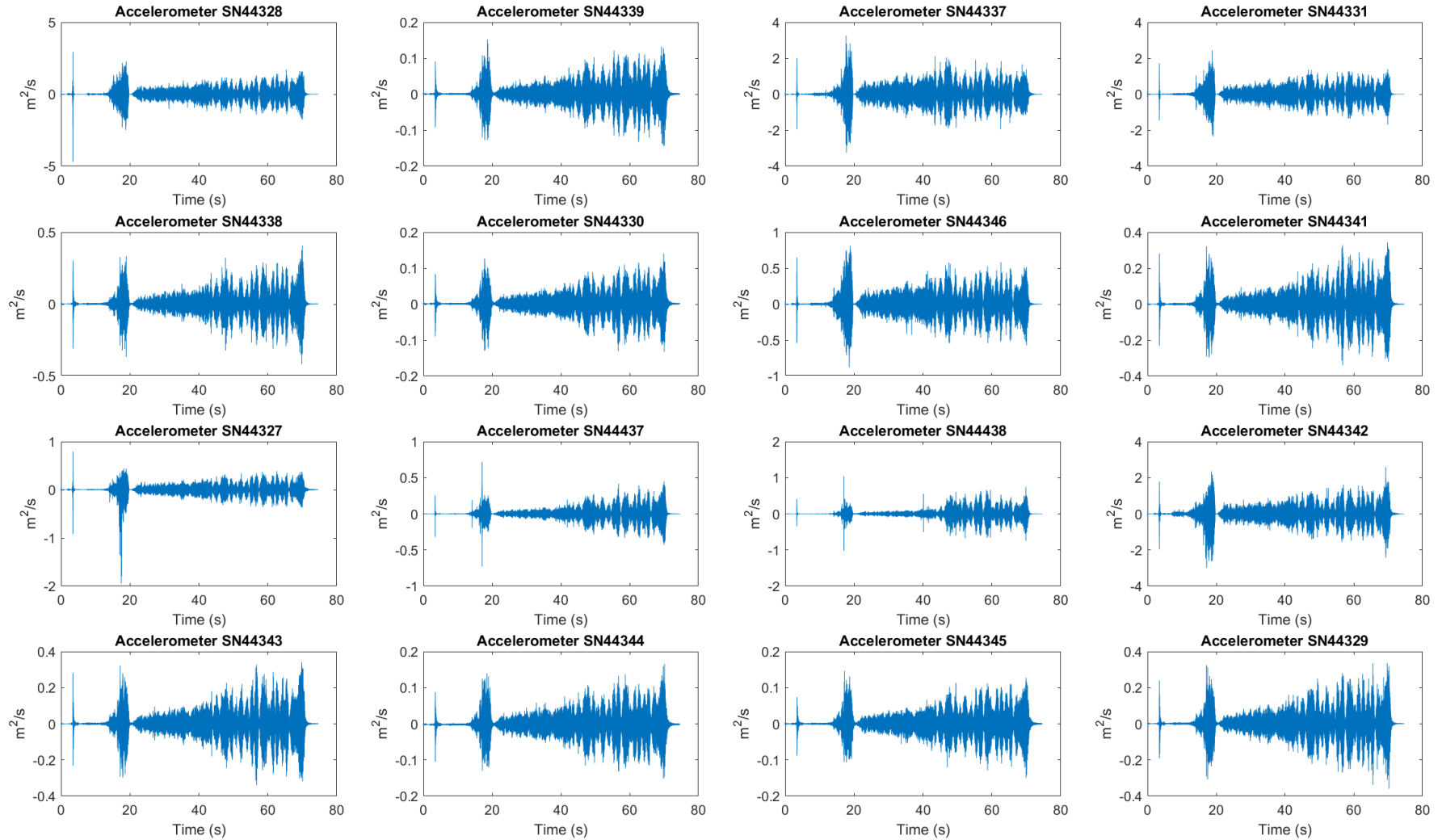


Figure 5-11: Acceleration vs Time for Experiment 21 - 250mm Hopper.

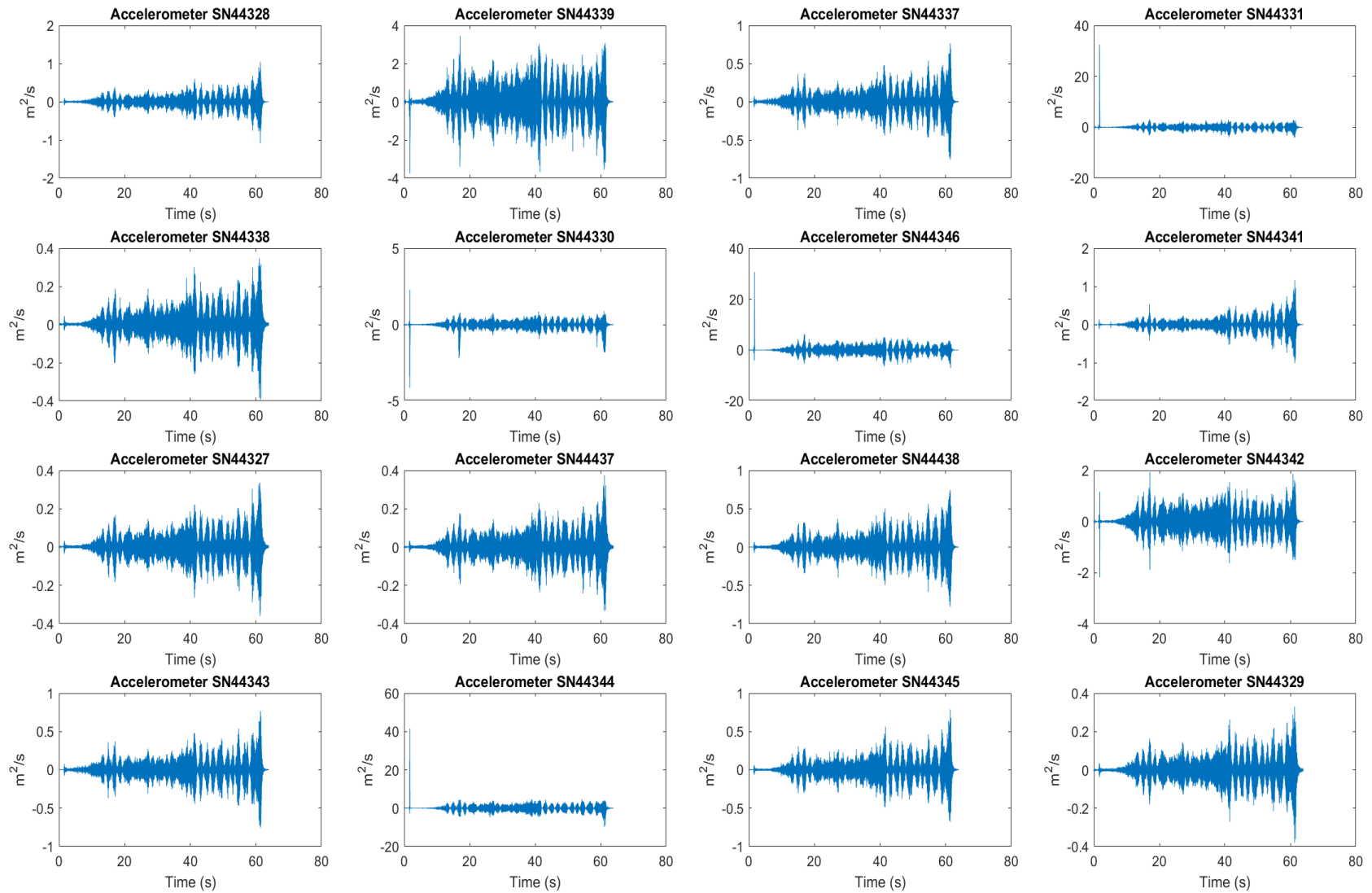


Figure 5-12: Acceleration vs Time for Experiment 29 - 300mm Hopper.

5.3 Silo Quake Response Spectrum

The response spectra shown in Figure 5-13 to Figure 5-16 were calculated from Matlab codes provided by Saa (2010) and Torres et al. (2011) with necessary modifications added for parallel computing. It can be observed that despite the randomness of the signals in the accelerograms shown in Figure 5-9 to Figure 5-12, the spectra shown in Figure 5-13 to Figure 5-16 indicate that most of the vibrational amplitudes are below 2 Hz and decay exponentially as the frequencies increase. This is consistent with observations outlined by Tu and Vimonsatit (2013) and Herral (2012). Figure 5-13 to Figure 5-16 confirm that silo supporting structures with fundamental natural frequencies below 1Hz are more likely to experience large amplitudes of vibration in all principal directions.

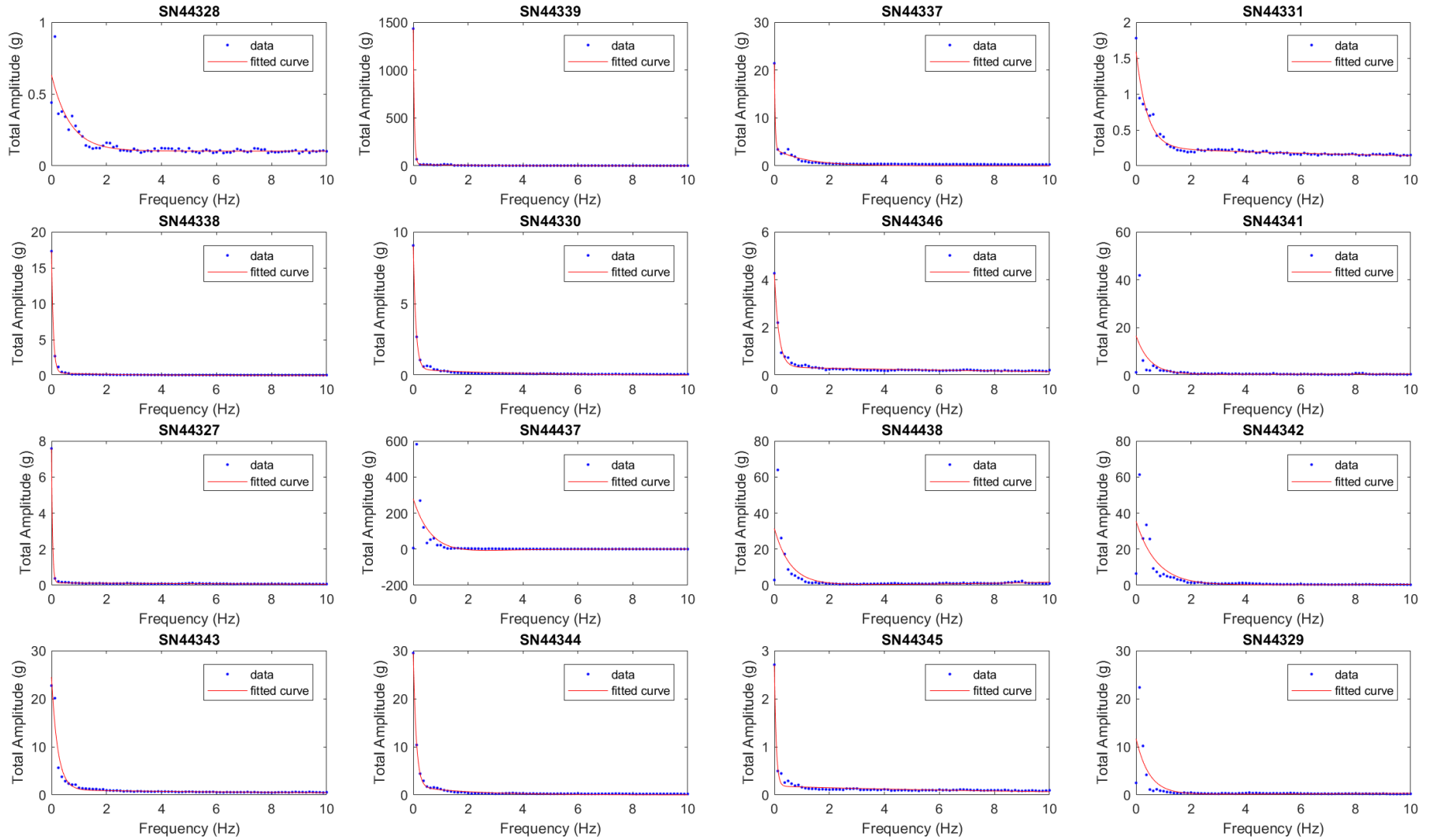


Figure 5-13: Silo Shake Response Spectrum - 200mm Hopper.

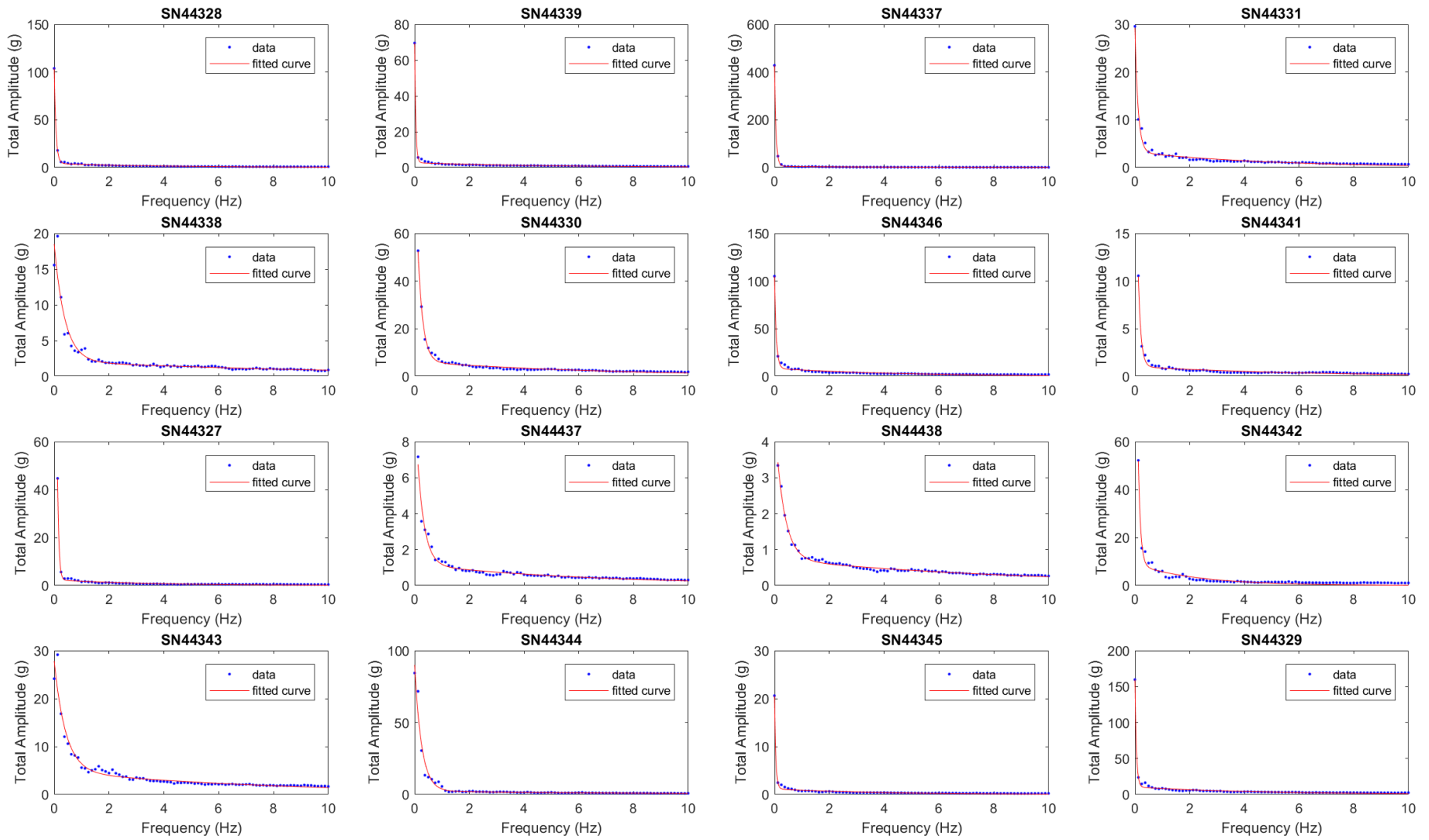


Figure 5-14: Silo Quake Response Spectrum - 250mm Hopper.

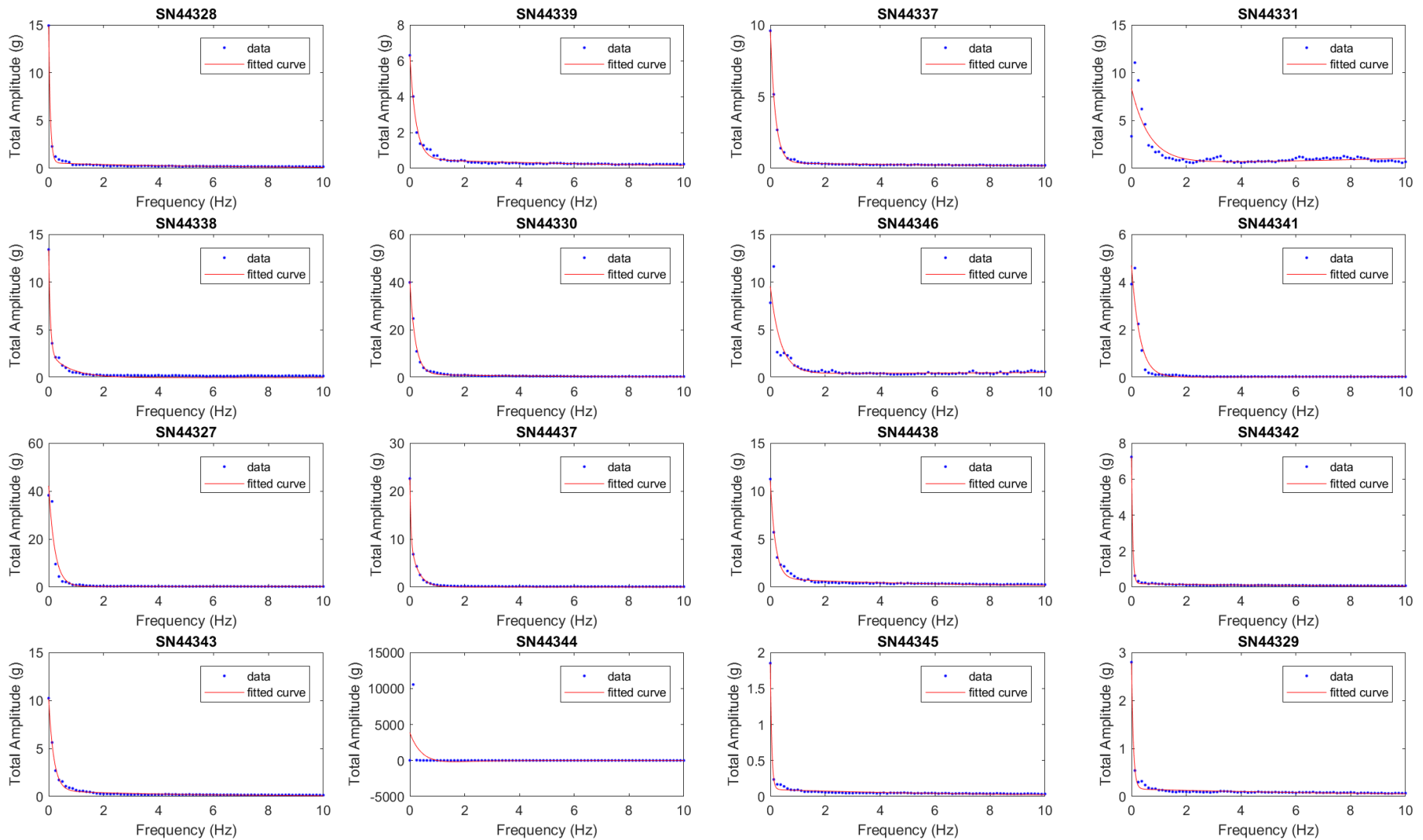


Figure 5-15: Silo Shake Response Spectrum - 300mm Hopper.

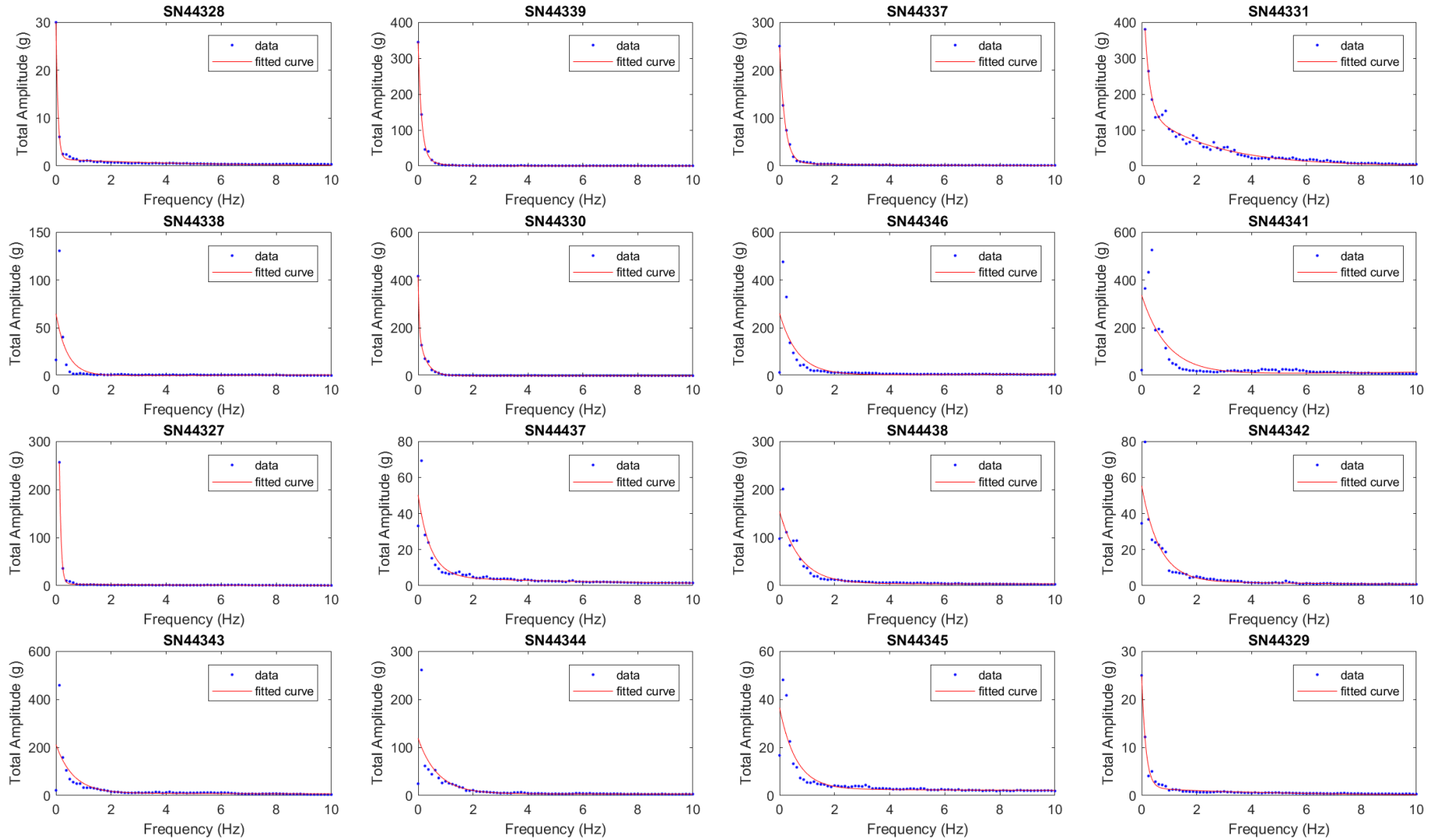


Figure 5-16: Silo Shake Response Spectrum - 400mm Hopper.

Silo Quake Response Spectra, plots of averaged total amplitude vs frequency, shown in Figure 5-13 to Figure 5-16 for the combined data collected from the experiments shown in Table 4-2 further reinforce the hypothesis that silo quake is similar to earthquake, and there exists a vibration spectrum that can be developed into a structural analysis tool. Furthermore, it can be concluded that silo quake is predominantly low frequency and high amplitude similar to that outlined by Buick (2004) and Buick et al. (2005). The Silo Quake Response Spectra indicate the amplitudes decay exponentially as the frequency increases. Such decay can be formulated by curve fitting algorithms to create formula Equation 5-1.

$$\phi(f) = k_1 e^{k_2 f} + k_3 e^{k_4 f} \quad \text{Equation 5-1}$$

Where:

- $\phi(f)$ is the silo quake response spectrum.
- f is the frequency (Hz).
- k_1 calibration factor.
- k_2 calibration factor.
- k_3 calibration factor.
- k_4 calibration factor.

Equation 5-1 is the general equation to generate silo quake response spectra which are the best-fit curves shown in Figure 5-13 to Figure 5-16. The factors k_1 , k_2 , k_3 and k_4 , are calibration factors shown in Table 5-2, are influenced by many factors and are expected to change for different moisture content, wall friction, material lump size, silo geometry, material flow properties, material cohesiveness, filling rate, concentric filling, eccentric filling or radial filling, discharge rate, clamshell gate opening time, eccentricity of the material flow channel during discharge, bin wall liner type, weld bead configuration on bin wall liner and wall roughness.

Table 5-2: Calibration factors for Equation of Silo Quaking Response Spectrum.

Hopper Opening (mm)	Accelerometer	k ₁	k ₂	k ₃	k ₄	SSE	RSQUAR E	DFE	ADJ RSQUARE	RMSE
400mm	SN44328	28.5064	-14.177	1.4531	-0.21414	2.7223	0.99694	77	0.99682	0.18803
400mm	SN44339	318.6769	-7.9986	26.5033	-1.9553	394.48	0.99714	77	0.99703	2.2634
400mm	SN44337	243.3044	-5.2225	5.3271	-0.19719	122.4531	0.99849	77	0.99843	1.2611
400mm	SN44331	471.5285	-5.6378	156.1184	-0.40878	4843.2031	0.98301	76	0.98234	7.9829
400mm	SN44338	64.5849	-2.4368	0.17334	0.17003	9911.0549	0.4558	77	0.4346	11.3453
400mm	SN44330	224.3102	-27.651	191.5356	-3.6946	279.5481	0.99854	77	0.99848	1.9054
400mm	SN44346	258.1444	-1.5232	2.861	0.10236	157729.77	0.52983	77	0.51151	45.2597
400mm	SN44341	330.6097	-1.0749	5.9723	0.095999	244602.60	0.59649	77	0.58077	56.3618
400mm	SN44327	1920.6908	-16.2316	3.8043	-0.24126	57.3286	0.99912	76	0.99909	0.86852
400mm	SN44437	45.4834	-2.2094	4.7619	-0.12169	1289.8969	0.80094	77	0.79319	4.0929
400mm	SN44438	150.5186	-1.3583	3.7846	-	9748.1941	0.87337	77	0.86843	11.2517
400mm	SN44342	53.0405	-1.5477	2.3346	-0.097957	1689.8399	0.82733	77	0.8206	4.6847
400mm	SN44343	202.3485	-1.5915	9.6283	-0.028648	119956.48	0.48225	77	0.46208	39.4699
400mm	SN44344	115.2153	-1.4161	3.7081	-0.013463	36042.421	0.51708	77	0.49827	21.6352
400mm	SN44345	33.8028	-1.6526	2.649	-0.021172	1094.0815	0.73644	77	0.72617	3.7695
400mm	SN44329	23.3417	-6.5954	1.5829	-0.21335	9.2034	0.98767	77	0.98719	0.34572
200mm	SN44328	0.52923	-1.4838	0.10374	-	0.20082	0.79665	77	0.78873	0.051069

200mm	SN44339	1416.4309	-26.1856	15.9096	-0.48793	280.5551	0.99986	77	0.99986	1.9088
200mm	SN44337	17.8787	-34.2306	3.5262	-0.88099	7.5704	0.98363	77	0.983	0.31355
200mm	SN44331	1.3417	-2.4978	0.24618	-0.05605	0.19711	0.9549	77	0.95314	0.050595
200mm	SN44338	16.9338	-15.3092	0.36811	-0.38539	0.42467	0.99858	77	0.99853	0.074265
200mm	SN44330	8.6093	-10.4359	0.43189	-0.26376	0.2938	0.99657	77	0.99644	0.061771
200mm	SN44346	3.9029	-6.1785	0.35823	-0.078515	0.22013	0.98937	77	0.98896	0.053467
200mm	SN44341	16.0998	-2.0361	0.47265	0.027877	1136.276	0.33679	77	0.31095	3.8415
200mm	SN44327	7.451	-27.0028	0.12904	-0.079083	0.022721	0.99959	77	0.99957	0.017178
200mm	SN44437	-	-1.1382	712550.39	-1.1384	220773.34	0.46706	77	0.44629	53.5461
200mm	SN44438	31.2861	-1.7361	0.18682	0.22101	2431.0547	0.49098	77	0.47115	5.6189
200mm	SN44342	35.3242	-1.3494	0.080571	0.19448	2166.181	0.62837	77	0.61389	5.304
200mm	SN44343	23.4562	-4.4175	1.0457	-0.085021	49.0571	0.94378	77	0.94159	0.79819
200mm	SN44344	27.738	-9.0404	1.7192	-0.47462	2.566	0.99731	77	0.9972	0.18255
200mm	SN44345	2.5191	-14.9965	0.18217	-0.099887	0.10202	0.98534	77	0.98477	0.0364
200mm	SN44329	11.5861	-2.0926	0.10275	0.1164	294.4477	0.49669	77	0.47708	1.9555
250mm	SN44328	99.6384	-15.7266	4.217	-0.25047	11.0283	0.99896	77	0.99892	0.37845
250mm	SN44339	66.8908	-24.1999	2.6528	-0.19727	9.1601	0.99804	77	0.99796	0.34491
250mm	SN44337	423.1504	-18.1756	4.9246	-0.251	26.1994	0.99986	77	0.99985	0.58331
250mm	SN44331	26.0144	-8.6491	3.2218	-0.20539	13.6492	0.98556	77	0.985	0.42102
250mm	SN44338	16.4003	-2.5674	2.1156	-0.088183	50.5173	0.92376	77	0.92079	0.80998
250mm	SN44330	92.7837	-5.5552	6.2623	-0.14537	21.1902	0.9938	76	0.99356	0.52803
250mm	SN44346	96.5467	-15.1062	8.4095	-0.21304	78.7631	0.99274	77	0.99245	1.0114
250mm	SN44341	34.4571	-10.3384	1.0423	-0.16636	1.4527	0.98717	76	0.98666	0.13826
250mm	SN44327	513.0647	-19.941	2.3495	-0.28431	5.5191	0.99716	76	0.99705	0.26948

250mm	SN44437	9.2055	-4.0027	1.1768	-0.15358	1.8579	0.97289	76	0.97182	0.15635
250mm	SN44438	3.948	-3.036	0.73459	-0.11051	0.16585	0.99126	76	0.99091	0.046714
250mm	SN44342	190.2477	-11.803	8.9116	-0.44136	79.6617	0.97345	76	0.9724	1.0238
250mm	SN44343	23.0051	-2.3785	4.8419	-0.12205	84.8216	0.946	77	0.94389	1.0496
250mm	SN44344	87.7076	-3.9085	2.3347	-0.11235	410.8796	0.9672	77	0.96592	2.31
250mm	SN44345	19.4193	-20.8191	1.1777	-0.26897	1.8206	0.99559	77	0.99542	0.15377
250mm	SN44329	149.3286	-18.6398	10.3699	-0.22189	114.1045	0.99539	77	0.99521	1.2173
300mm	SN44328	14.3431	-16.3368	0.56884	-0.17581	0.78939	0.99637	77	0.99623	0.10125
300mm	SN44339	5.7781	-4.4644	0.51421	-0.11437	0.6439	0.9881	77	0.98763	0.091446
300mm	SN44337	9.2228	-5.4065	0.37606	-0.077458	0.15569	0.99865	77	0.99859	0.044967
300mm	SN44331	7.8383	-1.5162	0.51622	0.069799	61.7012	0.71213	77	0.70092	0.89516
300mm	SN44338	10.7887	-16.2006	2.6108	-1.3163	2.9035	0.98455	77	0.98395	0.19418
300mm	SN44330	39.141	-4.9662	1.3688	-0.13798	11.6122	0.99468	77	0.99448	0.38834
300mm	SN44346	9.118	-2.7095	0.42396	0.025982	33.7692	0.81921	77	0.81217	0.66224
300mm	SN44341	4.6757	-3.2882	0.018486	0.10708	3.4925	0.91217	77	0.90874	0.21297
300mm	SN44327	41.9739	-4.4123	0.20408	0.040278	186.4477	0.93078	77	0.92808	1.5561
300mm	SN44437	12.6618	-26.539	9.9275	-3.5186	1.3881	0.99751	77	0.99741	0.13426
300mm	SN44438	10.1673	-5.3834	0.8837	-0.15957	1.8683	0.98806	77	0.9876	0.15577
300mm	SN44342	7.0325	-21.9199	0.1932	-0.12428	0.038785	0.99923	77	0.9992	0.022443
300mm	SN44343	9.6139	-5.3798	0.60168	-0.20821	0.79811	0.9941	77	0.99387	0.10181
300mm	SN44344	4512366.7	-1.6215	-	-1.6206	81931167.	0.25302	77	0.22392	1031.5237
300mm	SN44345	1.7512	-19.5778	0.098542	-0.13744	0.01868	0.99428	77	0.99405	0.015575
300mm	SN44329	2.6339	-14.6125	0.15791	-0.10657	0.057933	0.99227	77	0.99197	0.027429

5.4 Structural Connection Failure

After all the experiments were performed, it was noticed that the support structure had minor structural damage. The damages were seen at the end of the 125 PFC primary beams supporting the silo shown in Figure 5-17. The primary beams were bolted in accordance to procedures outlined in AS4100 (1998) onto the secondary beams to transfer the loads to the columns, and their undersides were at the same level at the beginning of the experiments. However, Figure 5-17 shows that one end of the primary beam had sagged by approximately 10mm.



Figure 5-17: Damage to test silo support structure due to silo quaking.

Such failure has been noted in full-scale silo structures that are subjected to quaking. Thus, the failure shown in Figure 5-17 indicates that the supporting structure was

undergoing significant vibration. Fortunately, personnel were not permitted to be on the silo platform during the experiments.

5.5 Conclusion

It can be summarised that the vibration signals resulting from the flow of granular material from the silo are nonlinear and nonstationary, random and contain many frequencies and amplitudes. Thus, traditional methods of signal processing such as FFT and Wavelets are not suitable in decomposing the raw signals into meaningful data thus needing a signal processing technique designed to decompose nonlinear and nonstationary signals.

The application of HHT, designed to analyse nonlinear and nonstationary signals, and HMS were instrumental to the identification of the silo quake response spectrum. The silo quake response spectrum, in its current form, will assist the design engineers in identifying frequencies of vibration that may cause large deflection in the silo structure and serve as the foundation for research and development into an effective structural analysis method similar to earthquake response spectrum method.

6 EQUATION OF SILO QUAKING

6.1 Introduction

This chapter presents the results such as flow rates, accelerograms, dynamic forces, derivation of the Equation of Silo Quaking, Equation of Silo Quaking coupled with Discrete Element Method and how the vibration amplitudes of the support structure can be reduced by applying Equation of Silo Quaking using results obtained from experiments and also Discrete Element Analyses.

6.2 Equation of Silo Quaking

As demonstrated in Section 3, the current methods of dynamic structural analysis are unsuitable for analysing silo structure such as the Train Load Out (TLO) bin. All the structural dynamic formulations to date only consider time varying forces while the mass, stiffness and damping remain constant throughout the solution process. Therefore to accurately represent the time varying mass characteristics of the TLO bin, the equation of motion must be modified.

These TLO bins are often supported on six columns equally spaced around the bin perimeter of the bin ring girder together with cross braces and rigid foundation thus making the centre of gravity of the bin well above the ground level. These iron ore TLO bins usually suffer excessive vibrations in the global directions such as vertical, horizontal and torsional, as shown in Figure 6-1. These modes of vibration could either be independent or combined. A closer examination shows that this frequency range is often related to the global stiffness of the bin supporting structure as a whole. Roberts (1996) recognised that the critical factor in the operation of the silos was the influence of the dynamic characteristics of the overall structure. Furthermore, Roberts (2008)

investigated a 2000 tonnes iron ore TLO bin and concluded that the source of dynamic loading came from the rapid flow of the ore.

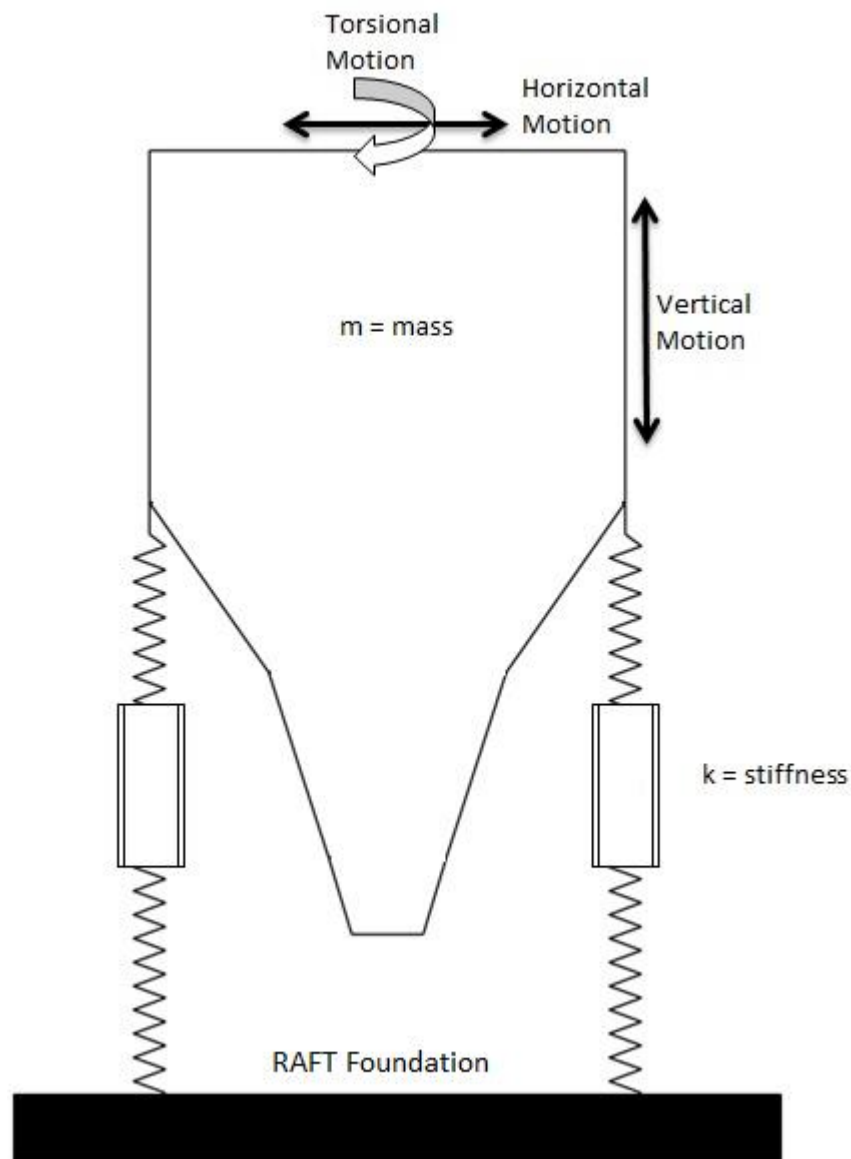


Figure 6-1: A simplified dynamic model of TLO bin (Tu and Vimonsatit 2013).

Figure 6-1 shows three possible global modes of vibration such as vertical, horizontal and torsional. However, for ease of mathematical derivation and explanation of the theory we only considered the vertical mode in our derivation thus effectively reduced the dynamic model down to a single degree of freedom dynamic system as shown in Figure 6-2. It is shown in Figure 6-2 that there are four forces acting on the mass (m) (Hart and Wong 2000). These forces are:

1. Stiffness Force $F_s(t)$: This force acts on the supporting structure when there is a vertical displacement of the mass m . For a linear structural system, this force is proportional to the vertical displacement of the column denoted by y , and the constant stiffness of the column denoted by k . This force is a restoring force thus always act in the opposite direction of the displacement y . Therefore this force can be written as $F_s(t) = -ky$.
2. Damping Force $F_d(t)$: This force acts on the supporting structure when there is a relative vertical velocity between the mass and the ground. For a structural system with linear viscous damping, this force is proportional to the velocity \dot{y} and the damping coefficient c . This force is similar to $F_s(t)$ and always act in the opposite direction of the displacement. Therefore this force can be written as $F_d(t) = -c\dot{y}$.
3. External Force $F_e(t)$: This force is the external force applied to the structural system and varies as a function of time.
4. Inertial Force: This force represents the acceleration of the supporting structure due to the imbalance of the forces above as demonstrated mathematically by Equation 6-1.

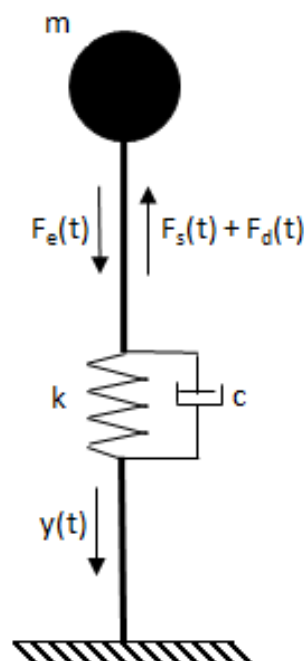


Figure 6-2: Single Degree Of Freedom (SDOF) dynamic model.

$$\sum F = F_s + F_d + F_e = -ky - c\dot{y} + F_e = m\ddot{y} \quad \text{Equation 6-1}$$

$$m\ddot{y}(t) + c\dot{y}(t) + ky(t) = F_e(t) \quad \text{Equation 6-2}$$

Where:

- m is the total mass of the structure.
- c is the damping of the structure.
- k is the stiffness of the structure.
- $\ddot{y}(t)$ is the acceleration of the silo structure at time t .
- $\dot{y}(t)$ is the velocity of the silo structure at time t .
- $y(t)$ is the displacement of the silo structure at time t .
- $F_e(t)$ is the externally applied dynamic force at time t .

Equation 6-2 represents the dynamic equilibrium condition of the structural system and is often called the equation of motion. However, one must appreciate that the mass m , coefficient of damping c , and stiffness k are constant and only the excitation force F_e changes with respect to time in Equation 6-2. In the case of a silo discharging, the total mass of the structural system is reducing with respect to time thus affecting the coefficient of damping c , and depending on the type of structural support may affect the structural stiffness k . Therefore Equation 6-2 needs to be modified to describe the silo discharging phenomenon.

To accurately describe the silo discharging process, one needs to rewrite the mass m , coefficient of damping c , stiffness k , time varying force $F_e(t)$, acceleration $\ddot{y}(t)$, velocity $\dot{y}(t)$ and displacement $y(t)$ as shown in Equation 6-3.

$$M(t)\ddot{y}(t) + c(t)\dot{y}(t) + k(t)y(t) = \sum F(t) \quad \text{Equation 6-3}$$

$$M(t) = m(t) - dm \quad \text{Equation 6-4}$$

$$c(t) = 2(\delta(t))\sqrt{k(t)(m(t) - dm)} \quad \text{Equation 6-5}$$

$$\sum F(t) = \sum (F(t)_{int} + F(t)_{ext}) \quad \text{Equation 6-6}$$

$$(m(t) - dm)\ddot{y}(t) + \left(2(\delta(t))\sqrt{k(t)(m(t) - dm)}\right)\dot{y}(t) + k(t)y(t) = \sum F(t)_{int} \quad \text{Equation 6-7}$$

Where:

- $m(t)$ is the total mass of the silo structure including granular material inside the silo at time t .
- dm is the mass exiting the silo at time t .
- $\delta(t)$ is the critical damping ratio at time t .
- $k(t)$ is the stiffness of the structure at time t .
- $\ddot{y}(t)$ is the acceleration of the silo structure at time t .
- $\dot{y}(t)$ is the velocity of the silo structure at time t .
- $y(t)$ is the displacement of the silo structure at time t .
- $\sum F(t)_{int}$ is the total internal dynamic force generated by the flowing granular material and mass loss time t .
- $\sum F(t)_{ext}$ is the total external dynamic force at time t .

Equation 6-7 represents the instantaneous dynamic equilibrium of a variable mass problem such as the silo vibration during discharge. At any instance during discharge, the summation of the time varying forces $\sum F(t)$, both internal and external, at each time step must equal the restoring forces at the time step for the structure maintain its dynamic equilibrium. For a discharging silo, the dynamic force is self-generated, thus the external force, $\sum F(t)_{ext}$, is taken as zero unless there are other externally imposed dynamic forces.

A general equation of motion with varying m has been proposed by Sommerfeld (1953) and others (Plastino and Muzzio 1992). Based the work of Sommerfeld (1953), the term $\ddot{y}(t)$ in Equation 6-3 is referred to as the acceleration of the centre of mass, and the force term on the right-hand side of the equation is the sum of all the external

forces and the product of the relative velocity of the escaping mass with respect to the centre of the mass of the body. Thus, in the case of isotropical mass loss, the sum of the product of the relative velocity of the escaping mass is zero, and the only remaining term on the right-hand side is the sum of the external forces. However, in the present case, the mass loss cannot be considered isotropic as the flow is subjected to some degree of confinement in the tank, and the whole body of the mass consists of the tank and the flowing iron ore.

During discharge, the mass of the product inside the silo changes with time. The total mass of the system at any instance of time is the difference between the total mass at the previous instance and the mass exiting the system at the current instance of time. Strzałko and Grabski (1995), Holl, Belyaev, and Irschik (1999), Horssen, Abramian, and Hartono (2006), Morrison (2007), Nunez and Torres (2009), Zhu and Wang (2011), Abramian, Horssen, and Vakulenko (2013), Abramian, Horssen, and Vakulenko (2014), investigated the motions of idealised structural systems subjected to time varying mass and demonstrated the vibrational characteristics of dynamic systems subjected to periodically time varying mass.

Based on the studies conducted by Strzałko and Grabski (1995), Holl, Belyaev, and Irschik (1999), Horssen, Abramian, and Hartono (2006), Morrison (2007), Nunez and Torres (2009), Zhu and Wang (2011), Abramian, Horssen, and Vakulenko (2013), Abramian, Horssen, and Vakulenko (2014), we can define the total mass of the system at any instance of time by Equation 6-4.

Equation 6-5 represents the instantaneous value of the coefficient of damping with respect to the time varying mass where $\delta(t)$ is the critical damping ratio at time t valued between 0.6% and 20% for steel structures as defined by Bachmann .H et al. (1995). A critical damping ratio of 2% is commonly used in the structural design office (Papageorgiou and Gantes 2008).

The stiffness factor denoted $k(t)$ in Equation 6-3, and Equation 6-5 represents the instantaneous stiffness of the supporting structure. The value of $k(t)$ is dependent on the supporting structure type and the soil type that the structure is built on. As

identified by Gilbert (2013) and Murray et al. (2016), the stiffness of concrete structural members is also a time varying value. Concrete behaviour is very nonlinear and is subjected to deterioration over time. Furthermore, it is known amongst the geotechnical specialists that the stiffness of the soil can change depending on the soil type and moisture content (Bull 1994). Thus extra considerations must be taken during the design stage to ensure the silo structure is in dynamic equilibrium throughout its design life.

Equation 6-6 represents the sum of the forces acting on the system which can be described as the sum of the external and internal forces. Theoretically, there is no external force acting on the silo structure thus there must exist internal forces generated by the flow of granular from the silo due to particle to particle interaction and particle to silo wall interaction or granular structure interaction. As postulated by Roberts (1996), these forces are associated with the flow rate, angle of internal friction, angle of wall friction, moisture content, cohesion, particle size, particle shape, bulk density, silo opening, silo shape, perimeter of flow channel, surcharge head, type of flow and ratio of lateral to vertical pressure.

Substituting Equation 6-4, Equation 6-5 and Equation 6-6 into Equation 6-3 leads to Equation 6-7, Equation of Silo Quaking, which describes the silo quaking phenomena. An examination of Equation 6-7 shows that the response of the silo and its supporting structure are dependent on the time-varying mass characteristics of the silo. The excitation force is also dependent on the flow rate of the granular material. As the particles flow out of the silo, they cause a reduction in the total mass and generate dynamic forces due to granular structure interaction.

As previously mentioned, it was found to be impractical to maintain a consistent moisture content for over 2 tonnes of iron ore. However, as shown in Table 6-1, that the variations were not large.

Table 6-1: Moisture content variations.

Experiment Number	Hopper Opening Size (mm)	Moisture Content %
1	400	3.98
2	350	4.24
3	300	4.26

6.3 Computation of Dynamic Forces

To compute the accelerations presented in Figure 6-10, Figure 6-13 and Figure 6-16 the weight of iron ore remaining inside the silo and dynamic forces needed to be calculated and separated from the readings captured by the load cells and accelerometers.

The weight of iron ore remaining inside the silo was obtained from the load cells supporting the silo as shown in Figure 4-21. The data obtained from the load cells showed fluctuations due to embedded dynamic loads during the discharge process. However, to obtain the reliable weight iron ore remaining inside the silo (Figure 6-3, Figure 6-4 and Figure 6-5) at any time during the discharge process the following procedure and assumption were used:

1. Smoothen the raw data with a moving average algorithm inside Matlab (2017a).
2. The total weight remaining inside the silo at any time step must be equal or less than the total weight remaining inside the silo at the previous time step.

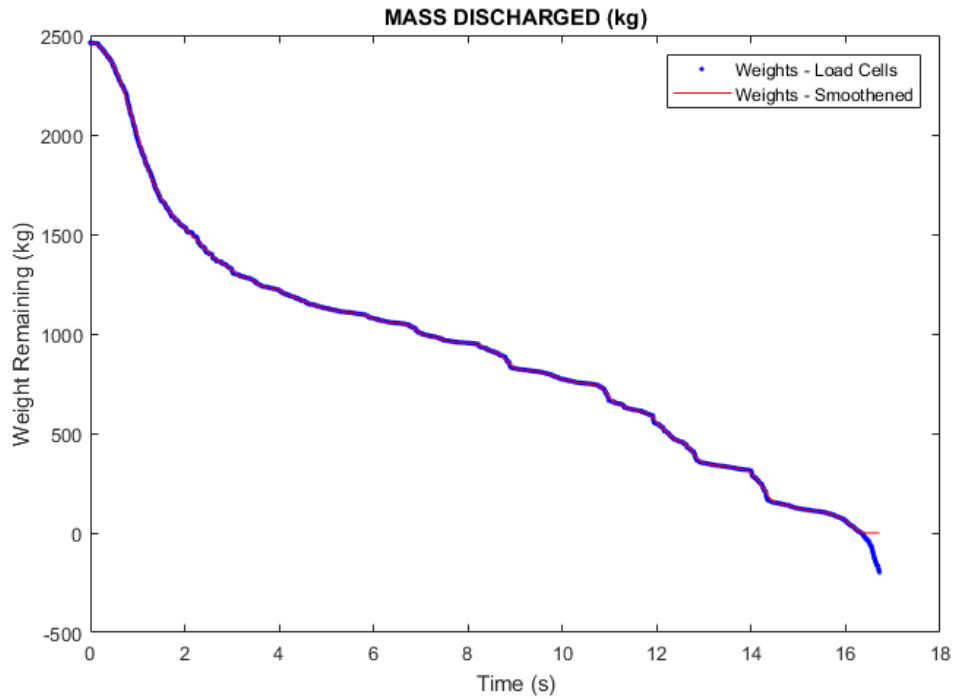


Figure 6-3: Weight of iron ore remaining inside the silo vs time Experiment 1.

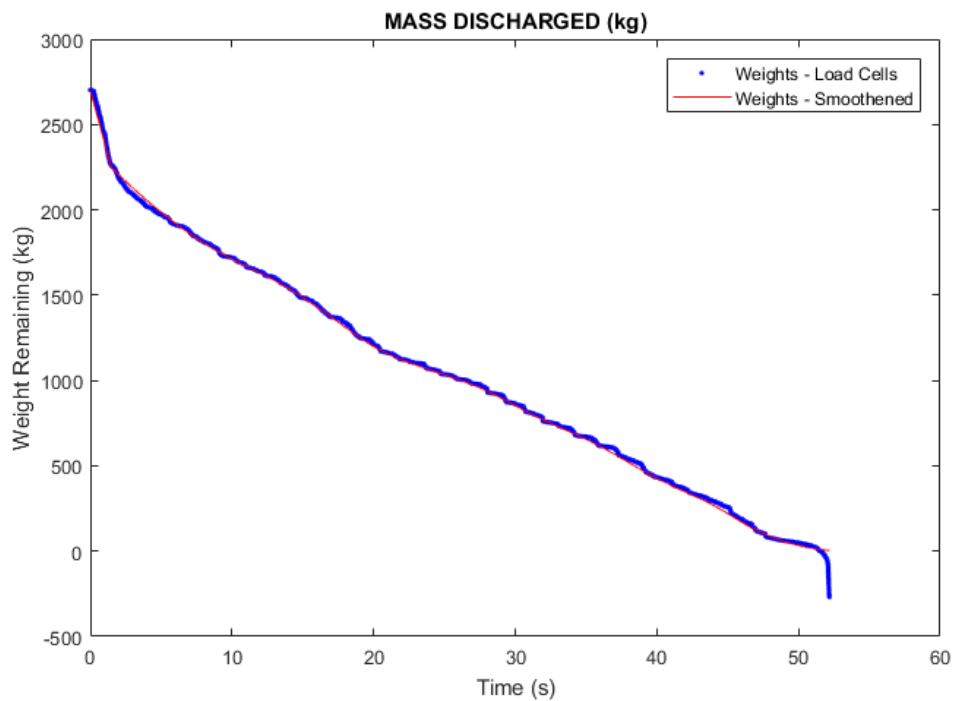


Figure 6-4: Weight of iron ore remaining inside the silo vs time Experiment 2.

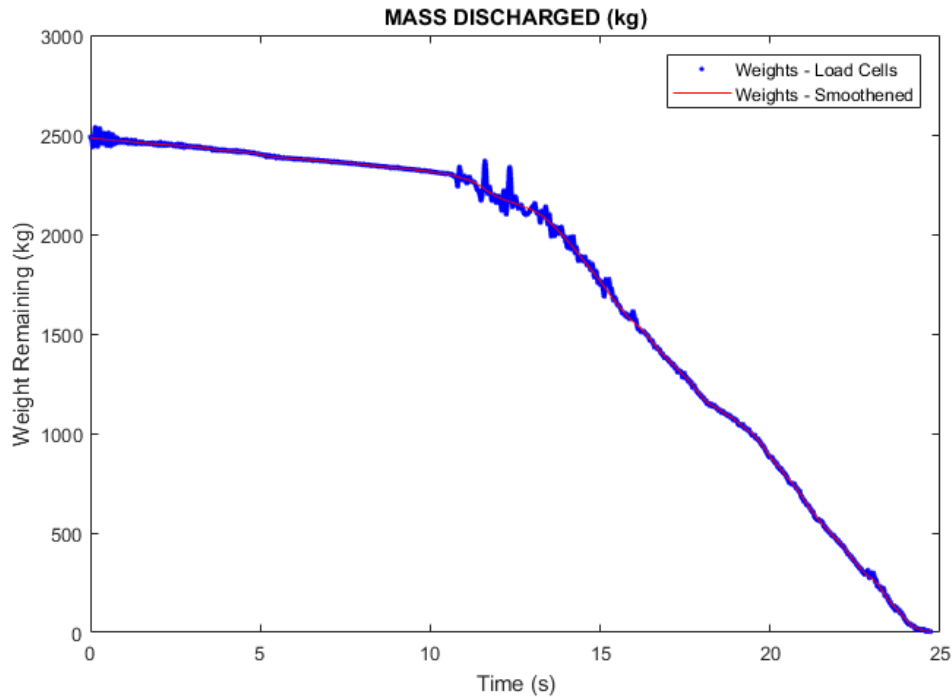


Figure 6-5: Weight of iron ore remaining inside the silo vs time Experiment 3.

Separating the dynamic loads from the load cell readings was proven to be extremely difficult without the accelerometers mounted directly below the brackets supporting the load cells (Figure 4-21). It was assumed that the measured vibrations on the supporting beams were caused by the dynamic loads generated by the flow of the granular and that the dynamic loads were instantaneous thus the measured accelerations were also instantaneous. Due to the instantaneous nature of the captured accelerations, principles of calculus previously described in Chapter 4.5 were used to find the dynamic forces. Furthermore, the forces captured by the four load cells were combined together and the accelerations captured by the four accelerometers (refer to Figure 4-21) were also averaged for reasons of simplicity in calculating the dynamic response. The estimated dynamic forces for Experiment 1, 2 and 3 are shown in Figure 6-6, Figure 6-7 and Figure 6-8. It must be noted that the dynamic forces presented in Figure 6-6, Figure 6-7 and Figure 6-8 are the sums of the forces including those forces generated by the granular to granular, granular to structure and change in momentum.

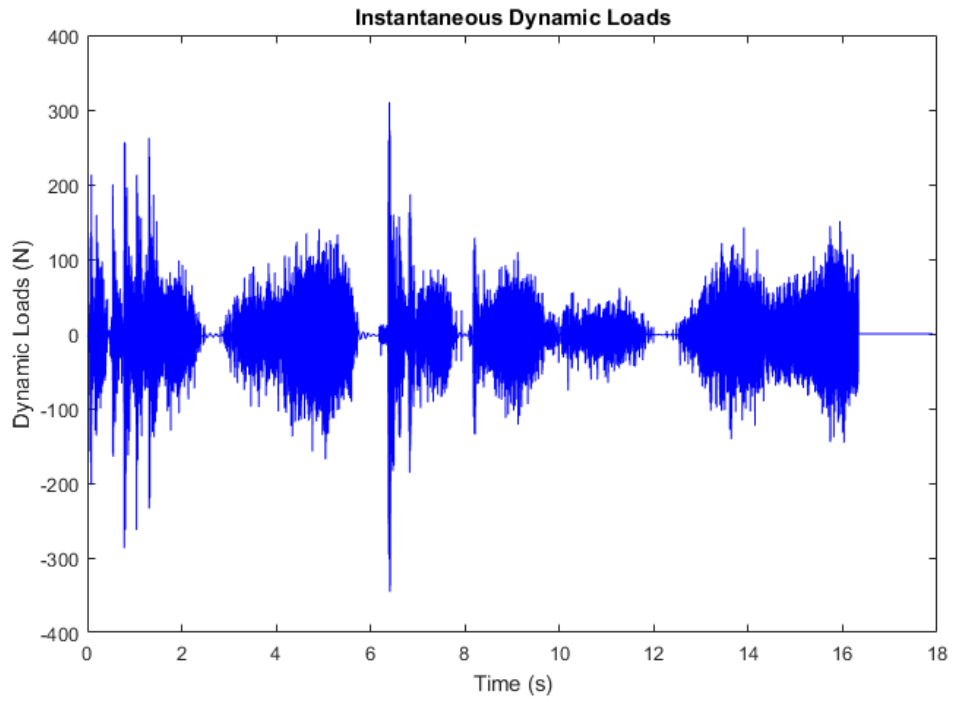


Figure 6-6: Instantaneous dynamic loads for Experiment 1.

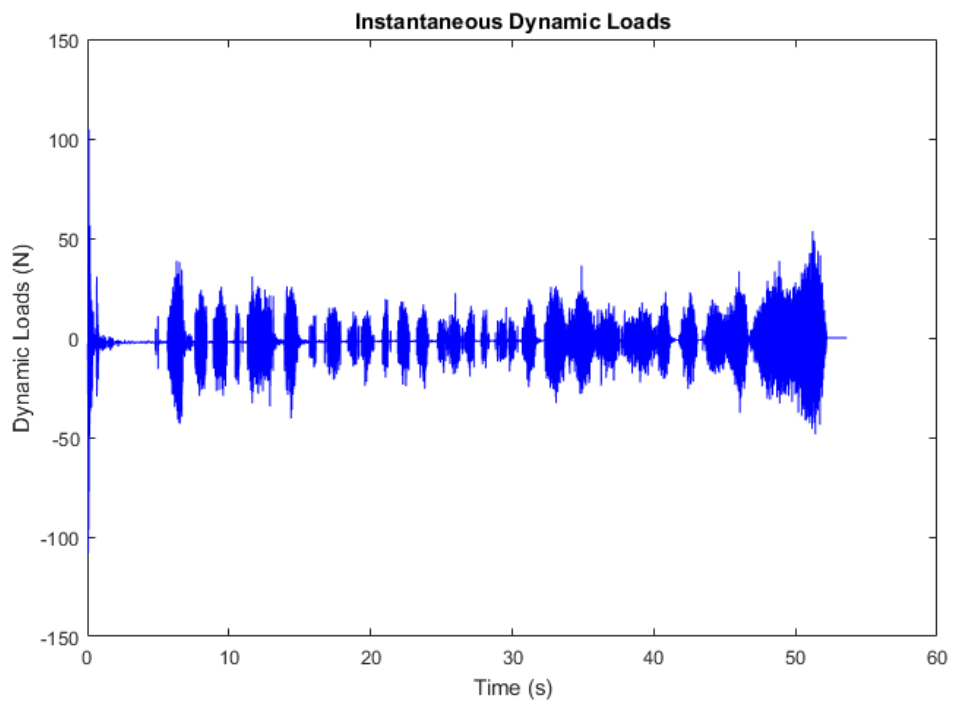


Figure 6-7: Instantaneous dynamic loads for Experiment 2.

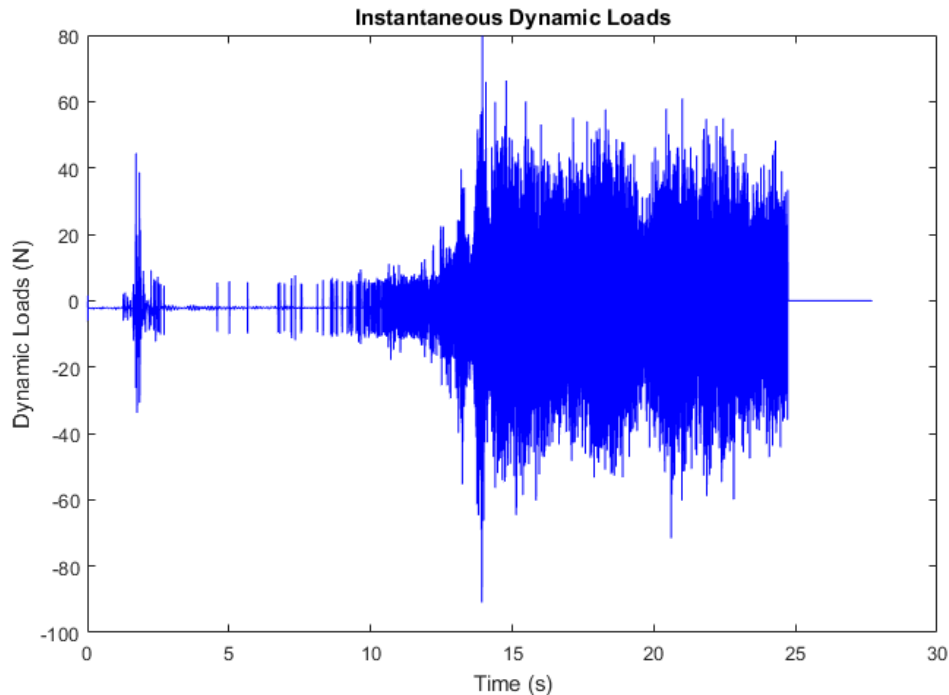


Figure 6-8: Instantaneous dynamic loads for Experiment 3.

The weights remaining inside the silo and the dynamic loads at each time step were input into Equation 6-7 together with the parameters in Table 6-2 to calculate the dynamic responses of the silo during discharge for Experiment 1, 2 and 3. The resulting accelerations vs time for Experiment 1, 2 and 3 are shown in Figure 6-10, Figure 6-13 and Figure 6-16 respectively. It can be concluded that the computed data are in close agreement with the measured data when comparing Figure 6-10 to Figure 6-11, Figure 6-13 to Figure 6-14 and Figure 6-16 and Figure 6-17.

The results of Experiments 1, 2 and 3 shown in Figure 6-9, Figure 6-12 and Figure 6-15 below indicate that the pulsation loads are associated with the fluctuating flow rates. The flow rates, in general, are quite random and pulsating. The flow rates, in general, increased rapidly when the gate first opened, slowed down then rapidly increased towards the end. The flow rates in Experiment 1 and 3 fluctuated a lot more compared to Experiment 2 consequently resulted in higher accelerations and more pronounced periodic pulses. This may be due to the surcharge acting on top of the flow channel affecting the flow rates.

On closer examinations of Figure 6-11, Figure 6-14 and Figure 6-17, one can recognise the randomness of the collected acceleration data. Despite the randomness, the accelerations follow some pulsating patterns which follow the fluctuating flow rates.

The causes of these pulses have been studied by many researchers such as Shinohara et al. (1968), Roberts and Scott (1978), Firewicz (1988), Tejchman and Gudehus (1993a), Roberts (1996), Tejchman (1999), Wensrich (2003), Buick et al. (2004), Muite et al. (2004), Buick et al. (2005), Wilde, Rucka, and Tejchman (2008) and over the years. In summary, at the moment there are two theories explaining the pulses, slip-stick motion as described by Roberts (1996), Wensrich (2002b) and Buick et al. (2005) and dynamic arching proposed by Shinohara et al. (1968) and Firewicz (1988).

6.4 Computed Accelerations vs Measure Accelerations

The slip-stick theory was proposed for tall silos, and the dynamic arching theory was developed to explain the granular flow at the hopper opening. It is evident that such theories exist when inspecting Figure 6-11, Figure 6-14 and Figure 6-17, although it remains unknown whether slip-stick or dynamic arching was present alone or both were acting together to form the fluctuating flows and consequently the pulses observed in the accelerograms.

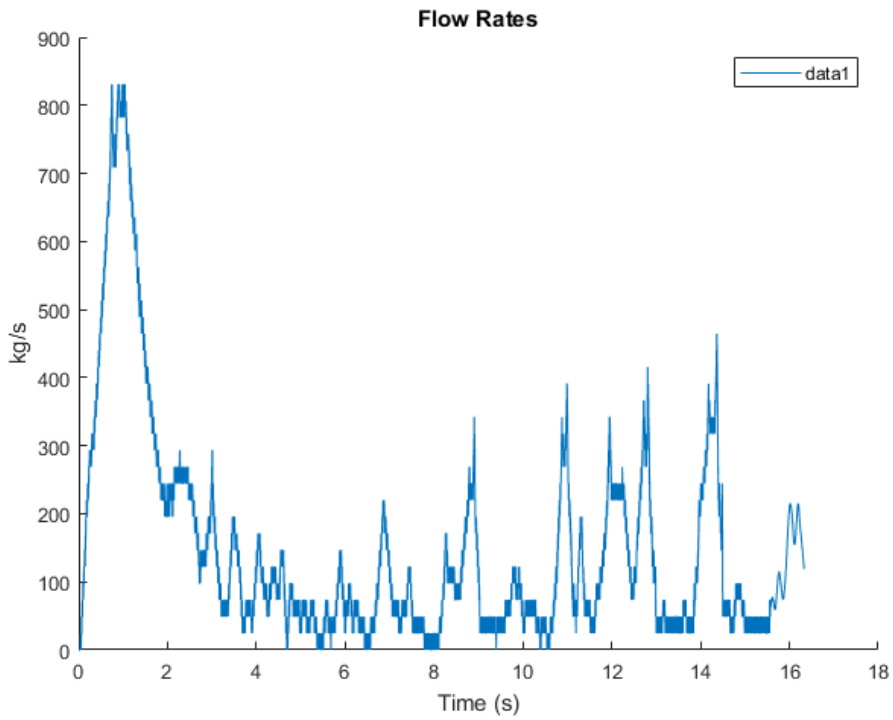


Figure 6-9: Flow rates for Experiment 1.

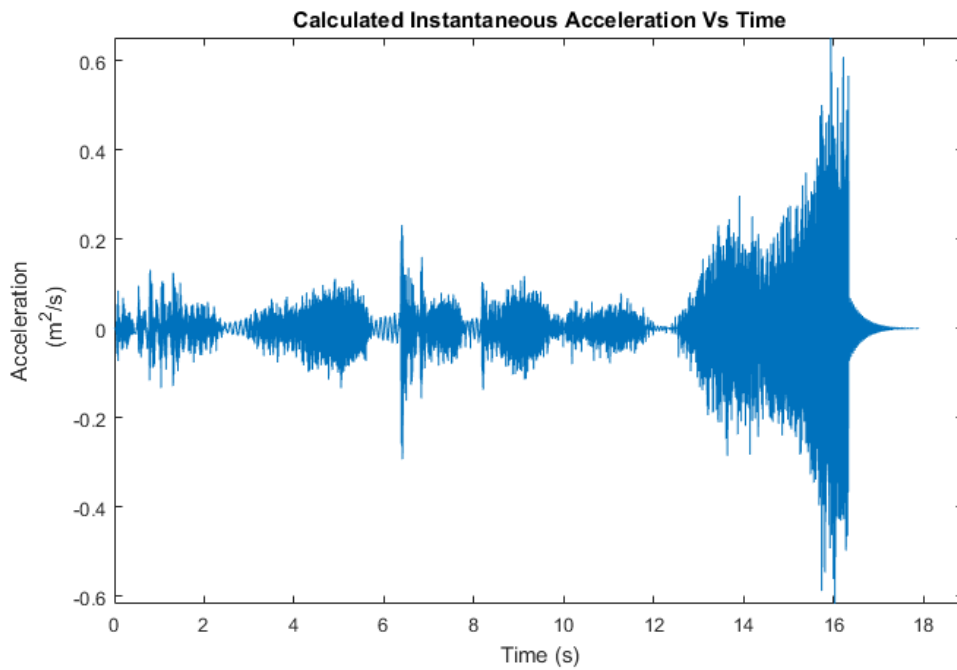


Figure 6-10: Computed accelerations vs time for Experiment 1 – 400mm hopper opening.

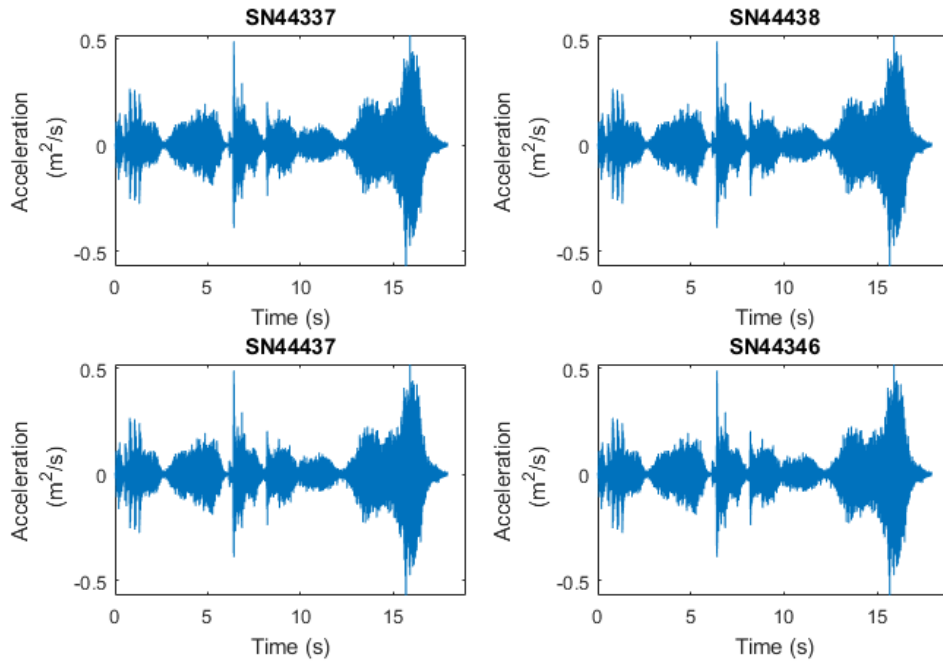


Figure 6-11: Measured accelerations vs time for Experiment 1.

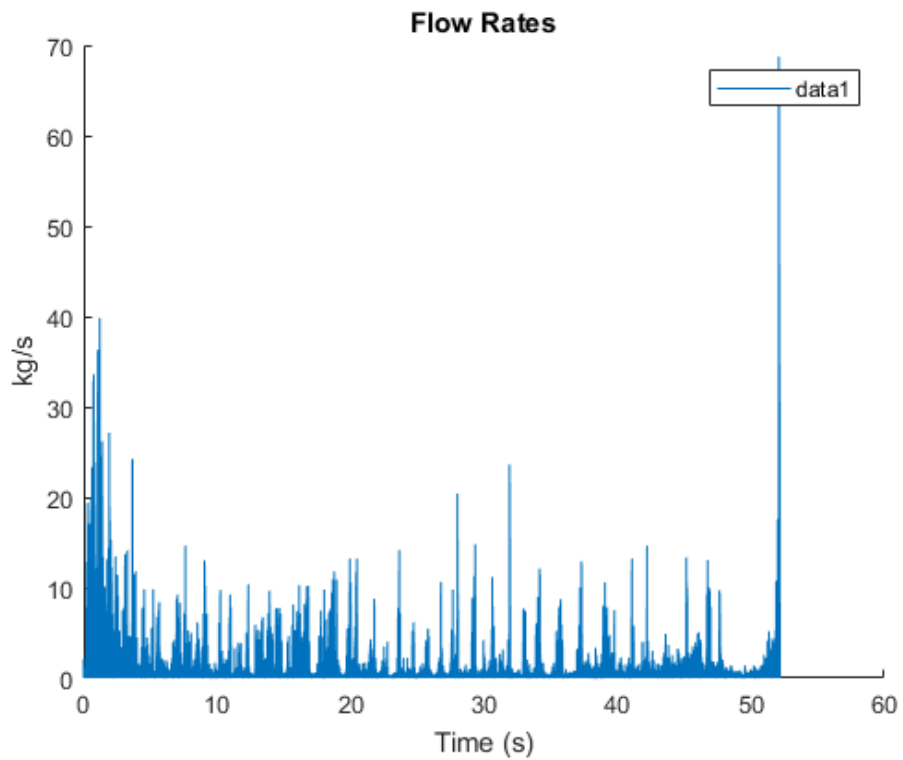


Figure 6-12: Flow rates for Experiment 2.

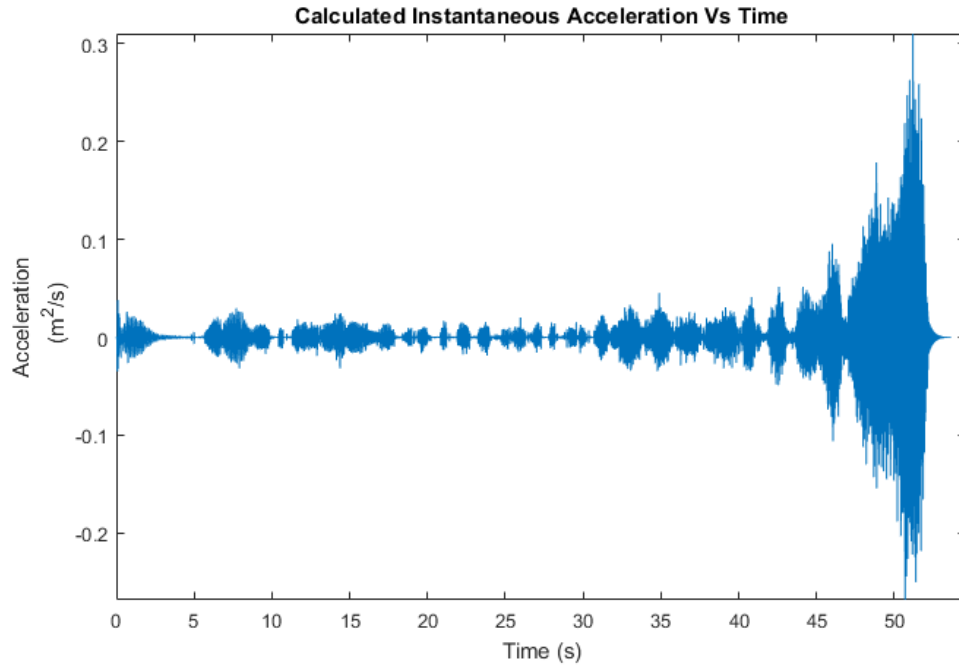


Figure 6-13: Computed accelerations vs time for Experiment 2 – 350mm hopper opening.

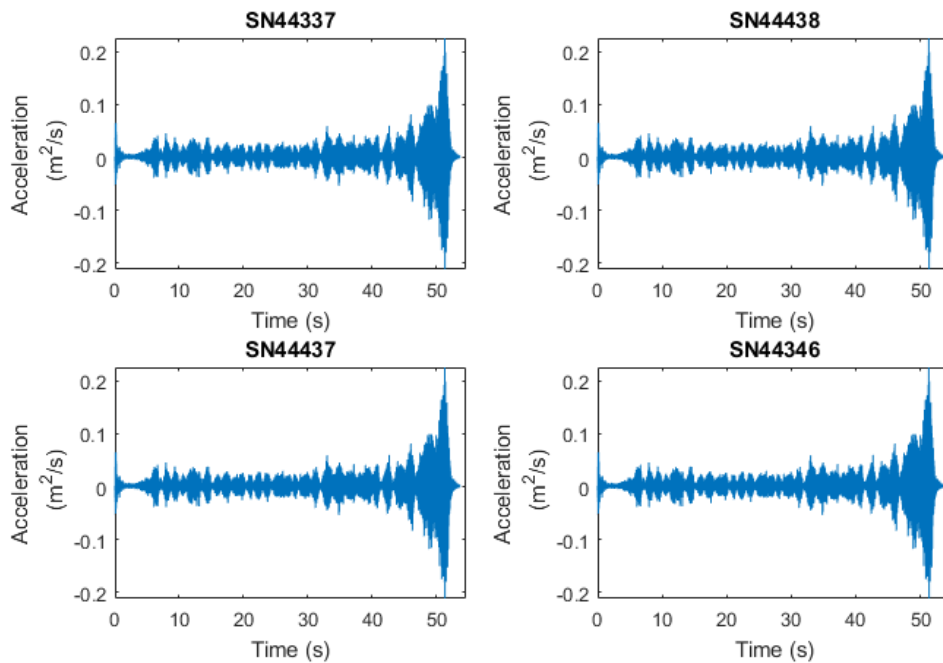


Figure 6-14: Measured accelerations vs time for Experiment 2.

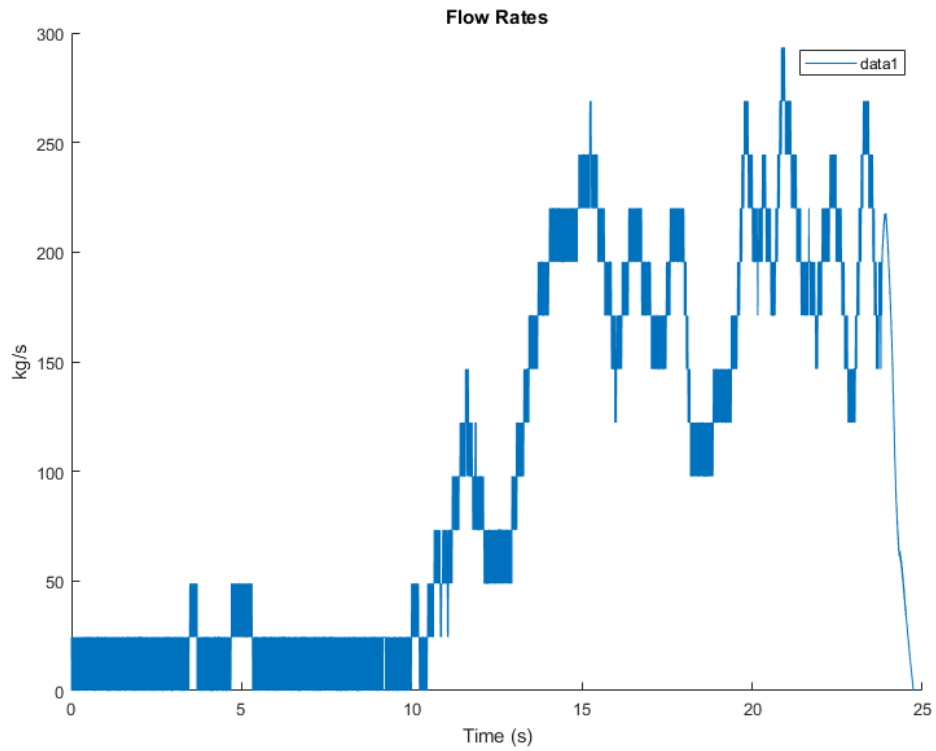


Figure 6-15: Flow rates for Experiment 3.

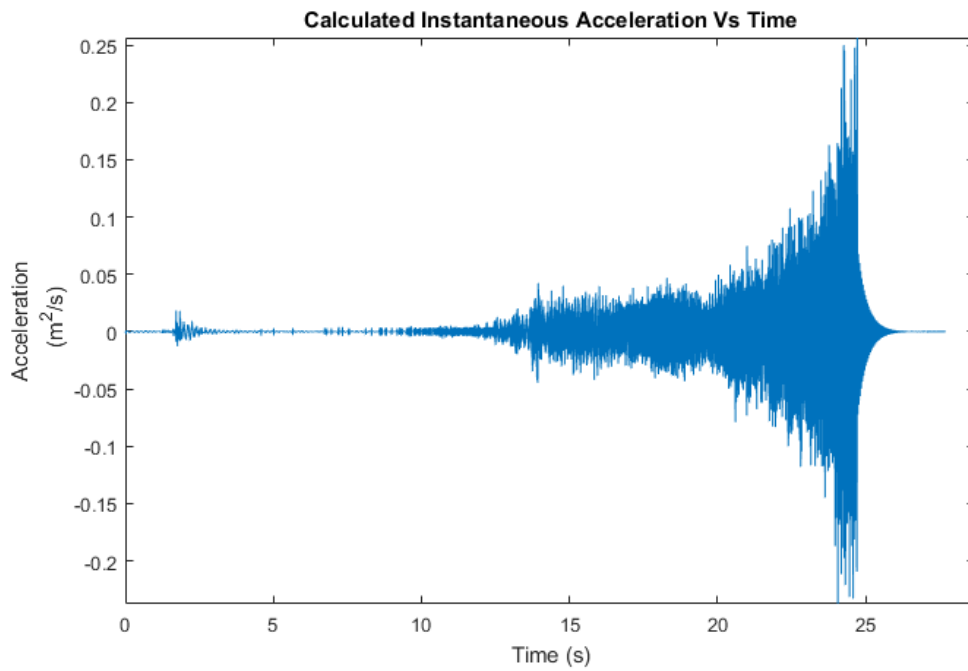


Figure 6-16: Computed accelerations vs time for Experiment 3 – 300mm hopper.

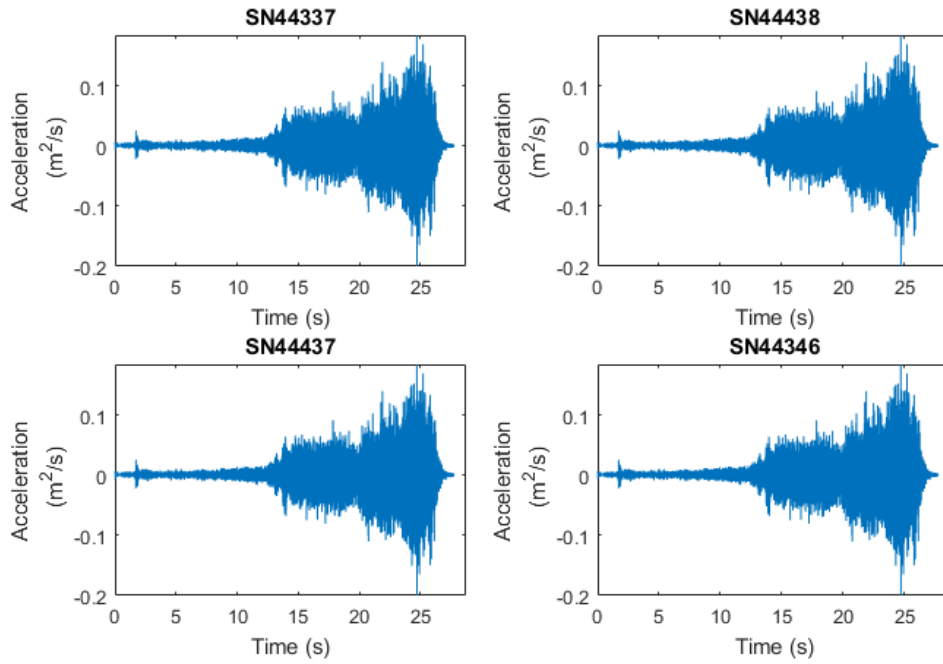


Figure 6-17: Measured accelerations vs time for Experiment 3.

Table 6-2: Stationary mass, critical damping ratio and stiffness for Experiment 1, 2 and 3.

Figure	Mass (kg)	Critical Damping Ratio (%)	Stiffness (N/m)
Figure 6-10	175	2	4550000
Figure 6-13	175	2	4550000
Figure 6-16	175	2	4550000

The stiffness in Table 6-2 was calculated by creating a structural analysis model of the silo structure (Figure 4-1) in structural analysis software SpaceGass. A unit load was applied to the structure at the location supporting the experimental silo to obtain the deflection. The applied load was divided by the associated deflection of the structure to obtain the stiffness.

6.5 Equation of Silo Quaking Coupled with Discrete Element Method

Discrete Element Analysis (DEM) and Ansys Mechanical were used initially to determine the dynamic response of the silo structure using the measured forces and masses. Rocky, a DEM software package, was employed to simulate the granular particles flowing out of the silo with 400mm hopper opening and arbitrary values (refer to Table 6-3) were chosen for the material constants used in the DEM analysis. It was found that Rocky DEM was not able to predict the dynamic response of the silo structure. Furthermore, the coupling of Rocky DEM and Ansys Mechanical also was proven to be futile due to the deficiency in current structural dynamic analysis formulations outlined in Section 3.5. However, when the masses and forces at each time step were extracted from Rocky DEM and input into, Equation of Silo Quaking, Equation 6-7, the dynamic response of the silo structure was able to be calculated using parameters outlined in Table 6-4. The response shown in Figure 6-18 predicts the response of the silo supporting structure and demonstrates the validity of the Equation of Silo Quaking or Equation 6-7.

Table 6-3: Parameters used for Rocky DEM analysis.

Description	400mm Hopper Opening
Hopper Opening (mm)	400
Particle Shape	Spherical
Particle Size (mm)	30
Density (kg/m ³)	2334.45
Young's Modulus (MPa)	100000000
Rolling Resistance	0.1
Particle to Particle Static Friction	0.7
Particle to Particle Dynamic Friction	0.7
Particle to Particle Coefficient of Restitution	0.3
Particle to Particle Adhesive Distance (mm)	1
Particle to Particle Force Fraction	0.1
Particle to Wall Static Friction	0.7
Particle to Wall Dynamic Friction	0.7
Particle to Wall Coefficient of Restitution	0.3

Particle to Wall Adhesive Distance (mm)	1
Particle to Wall Force Fraction	0.1

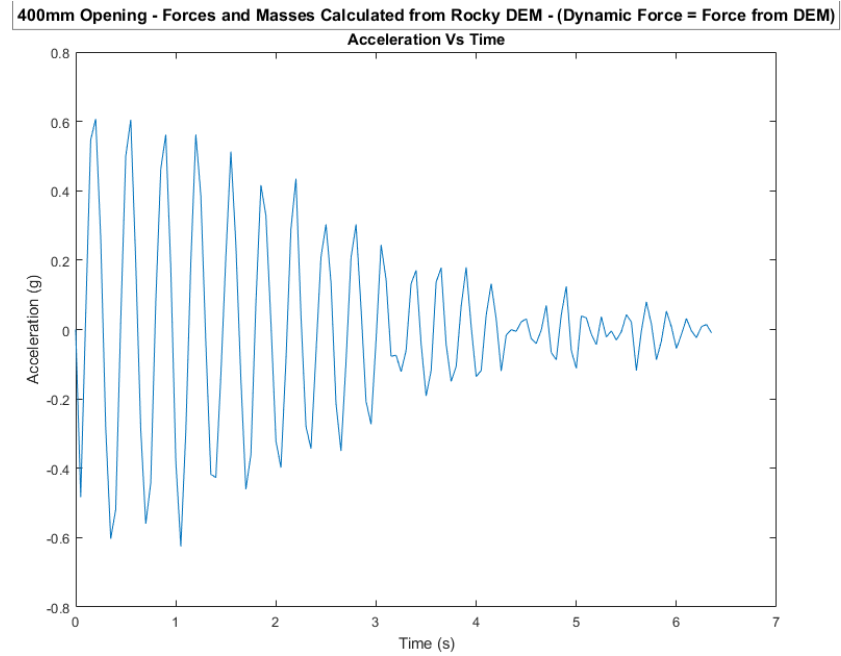


Figure 6-18: Acceleration vs time calculated by Equation 6-7 with forces and masses obtained from Rocky DEM – 400mm hopper opening.

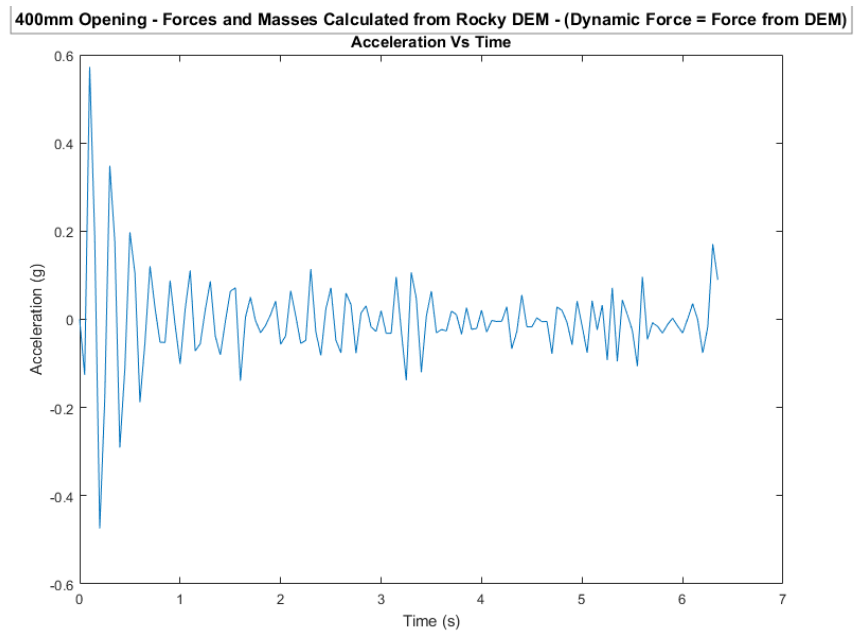


Figure 6-19: Acceleration vs time calculated by Equation 6-7 with forces and masses obtained from Rocky DEM and added stiffness damping– 400mm hopper opening.

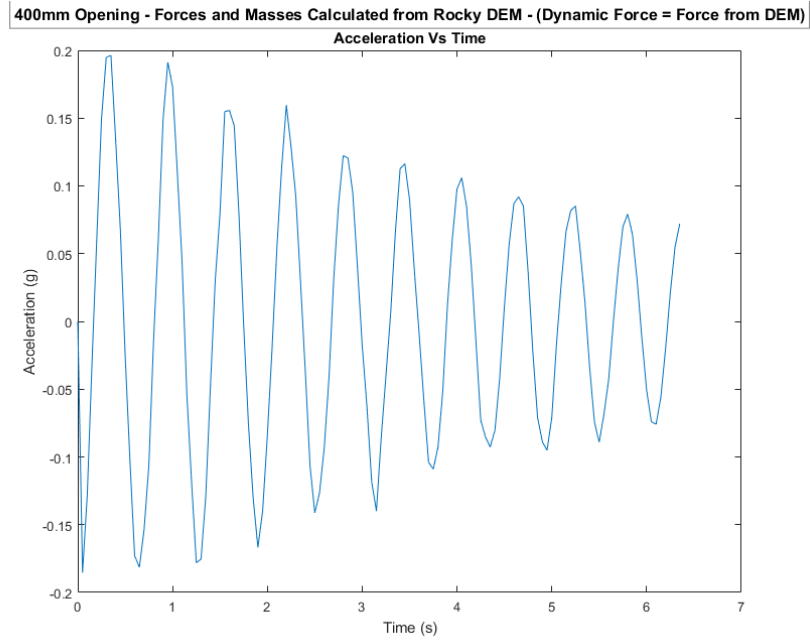


Figure 6-20: Acceleration vs time calculated by Equation 6 7 with forces and masses obtained from Rocky DEM and added mass damping– 400mm hopper opening.

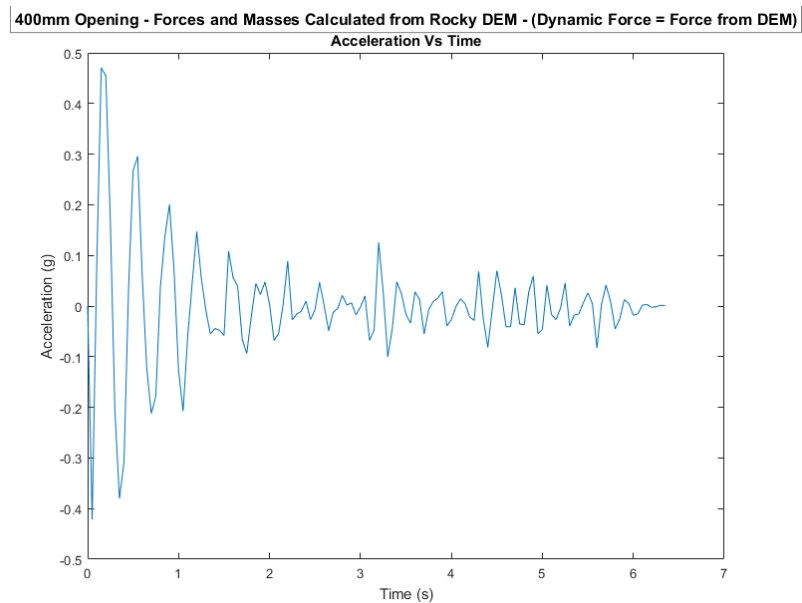


Figure 6-21: Acceleration vs time calculated by Equation 6 7 with forces and masses obtained from Rocky DEM and added critical damping – 400mm hopper opening.

Table 6-4: Stationary mass, critical damping ratio and stiffness for DEM analyses.

Figure	Mass (kg)	Critical Damping (%)	Stiffness (N/m)
Figure 6-18	920	2	1131221
Figure 6-19	920	2	3393663
Figure 6-20	9200	2	1131221
Figure 6-21	920	10	1131221

6.6 Equation of Silo Quaking Coupled with Forces from Analytical Formulae

In a case study on a 2000 tonne iron ore TLO, shown in Figure 6-22 and Figure 6-23, presented by Roberts (2008), it was concluded that the dynamic loads generated by the flowing iron ore induced a perceptible level of swaying motion. Furthermore, Roberts (2008) observed that the level of swaying motion is less when the bin is full. This suggests that the mass of the iron ore inside the silo was providing some damping as demonstrated by Equation 6-7. The data provided by Tu and Vimonsatit (2013) suggested that this particular silo was suffering a combined lateral sway and vertical motions.

Equation 6-7 was further studied by incorporating analytical formulae and data presented by Roberts (2008). For demonstrating the validity of Equation 6-7, only the vertical mode of vibration is studied. Other modes of vibration can be studied by substituting relevant data into Equation 6-7. The dynamic response of the silo supporting structure was calculated by the given structural stiffness, the forces generated by the flow of the iron ore and the masses remaining inside the actual TLO

presented in Figure 6-24. It was assumed that the flow rates illustrated in Figure 6-24 remained constant for different fill level inside the silo and that the filling conveyor on top of the TLO silo could not keep the mass of iron ore inside the silo constant throughout the discharge cycle. Thus the total mass of the iron ore inside the silo fluctuates between each discharge cycle.

The dynamic response of the supporting structure was studied for several fill levels such as 1500 tonnes, 1250 tonnes and 1000 tonnes. The discharge time remained the same at different fill levels. The vertical stiffness was not given by Roberts (2008) and such information was not readily available due to confidentiality agreements. However, from experience, the vertical stiffness of such structure would be approximately ten times the lateral stiffness.

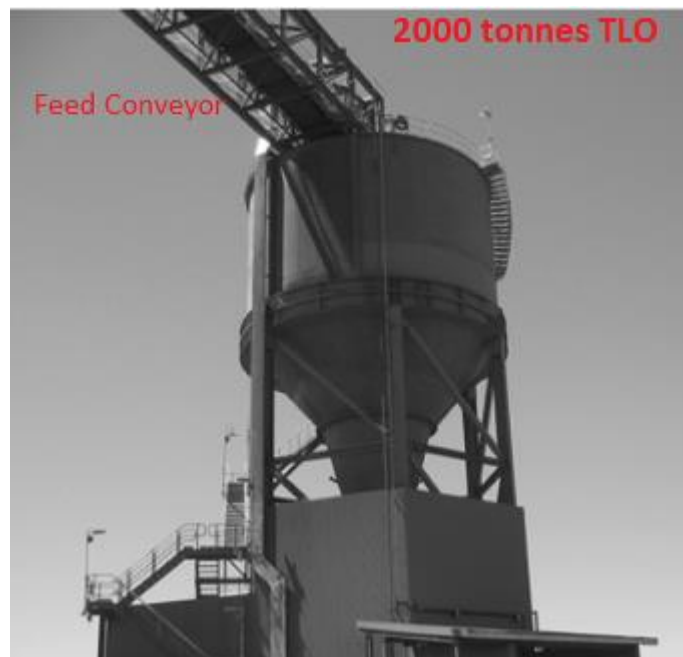
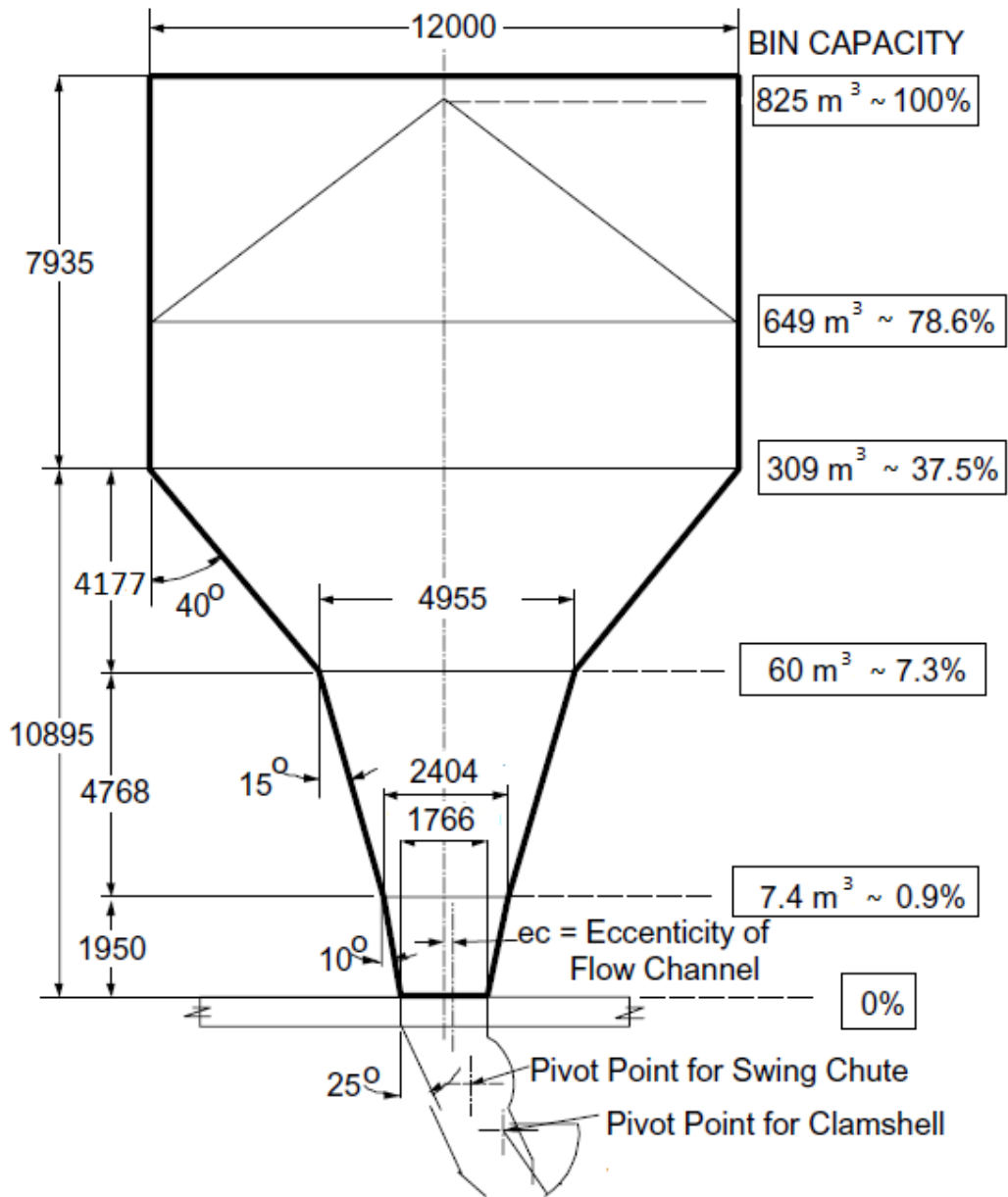


Figure 6-22: Iron ore TLO silo (Roberts 2008).



2000 tonne Iron Ore TLO
All dimensions are in mm UNO

Figure 6-23: 2000 tonne iron ore TLO Silo (Roberts 2008).

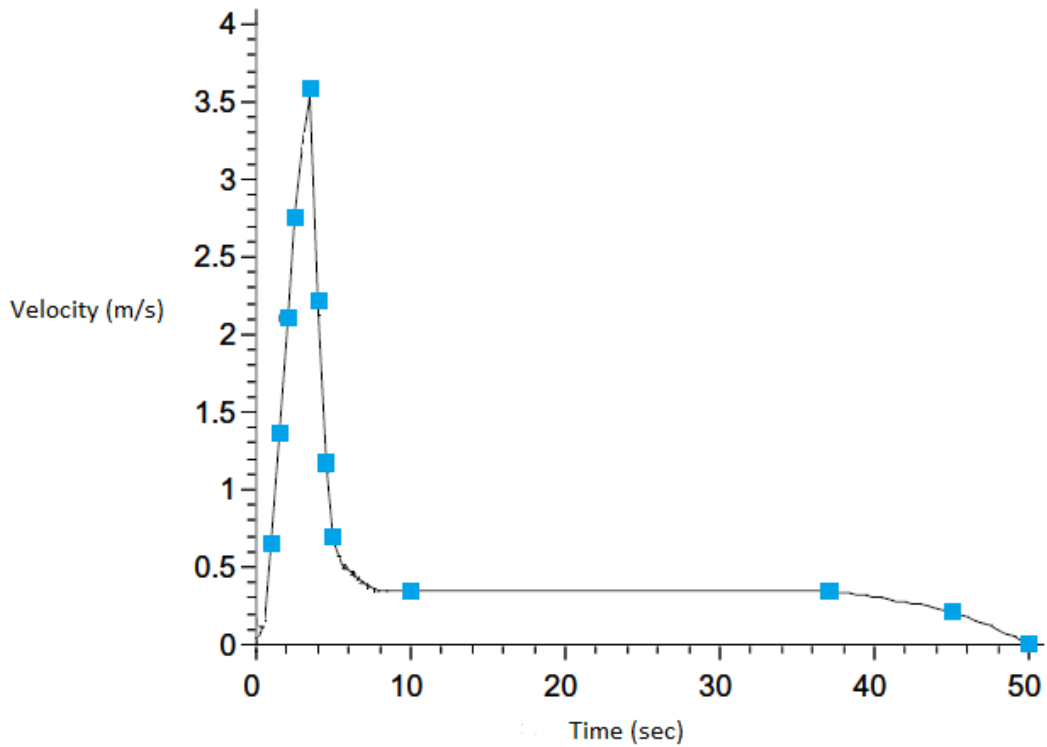


Figure 6-24: Flow rates for 2000 tonne iron ore TLO (Roberts 2008).

The structural properties, illustrated in Table 6-5, used to demonstrate the dynamic response of the supporting structure of the TLO studied by Roberts (2008) are only estimated based on experience for the reasons of confidentiality. The confidentiality agreement prevents necessary data become available to the public.

Table 6-5: Estimated structural properties of the 2000 tonnes TLO.

Description	Value
Self-weight of supporting structure and TLO (kg)	150000
Self-weight mechanical equipment (kg)	25000
Critical damping (%)	2
Stiffness (kN/m)	467290

Figure 6-25, Figure 6-26 and Figure 6-27 demonstrate the response of the silo supporting structure during granular discharge. During the 50-second discharge cycle, the balance of the silo supporting structure was disturbed by the dynamic loads and mass losses caused by the flow. Based on fundamentals of structural dynamics, such disturbances were restored the structural vibrations. The vibrational characteristics of the structure are influenced by the mass, damping and stiffness available in the supporting structure.

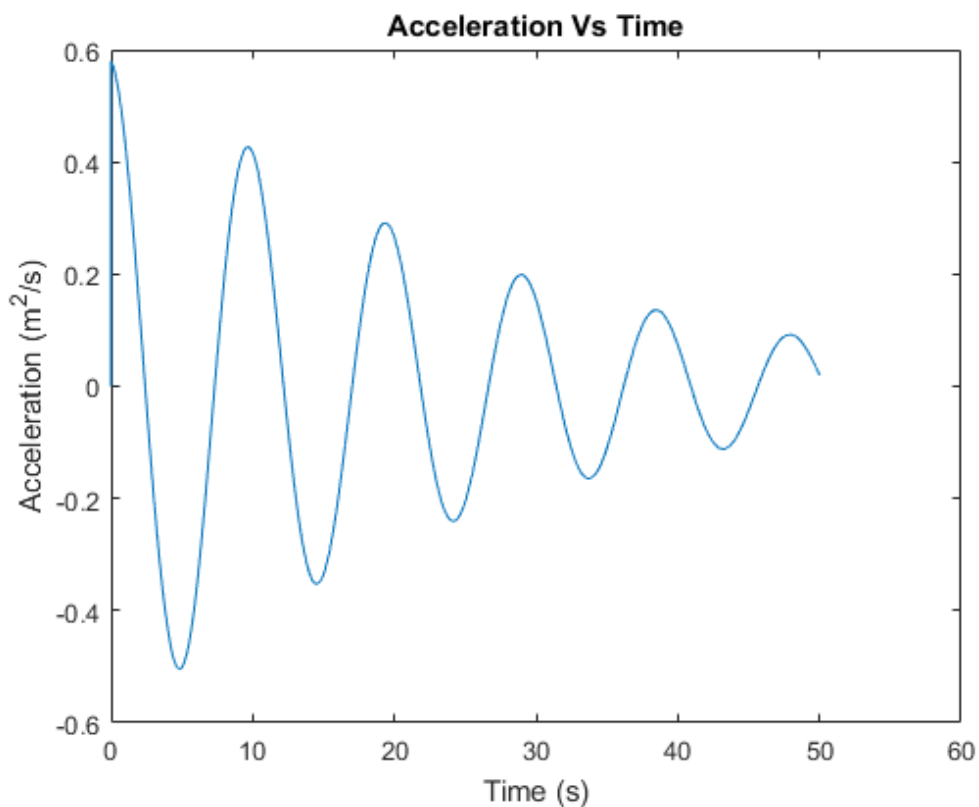


Figure 6-25: Dynamic response of TLO supporting structure with 1000 tonnes of iron ore inside.

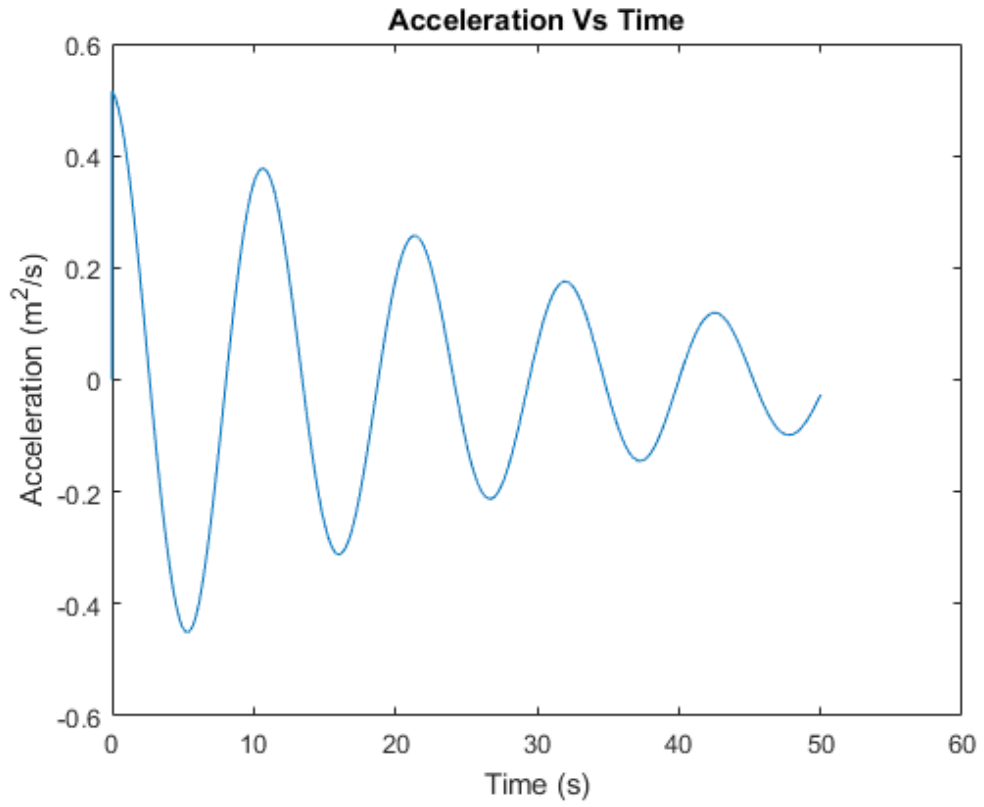


Figure 6-26: Dynamic response of TLO supporting structure with 1250 tonnes of iron ore inside.

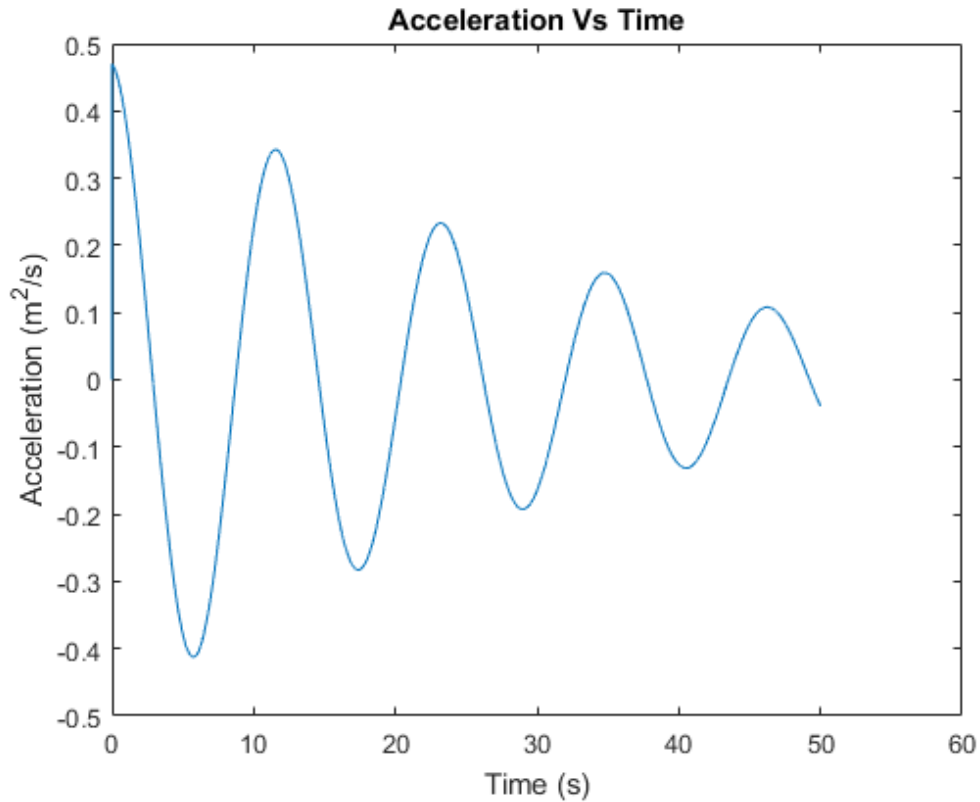


Figure 6-27: Dynamic response of TLO supporting structure with 1500 tonnes of iron ore inside.

6.7 Reduction of Amplitude of Vibration using Equation of Silo Quaking

The validity of the Equation of Silo Quaking, Equation 6-7, was further examined by altering the stationary mass, critical damping and stiffness with values shown in Table 6-4. The reductions in the amplitude of oscillations can be observed in Figure 6-19, Figure 6-20 and Figure 6-21. Furthermore, the calculated dynamic responses for Experiment 1, 2 and 3 were used together with Equation 6-7 to examine effective ways to reduce the vibration amplitude. To study how Equation 6-7 can be used to reduce the amplitude of vibration the stationary mass, critical damping and stiffness were systematically altered with values shown in Table 6-6.

The stiffness, critical damping and stationary mass for Experiment 1, 2 and 3 were increased by 10 times the values used in Table 6-2. The following observations can be drawn from the results:

1. The increase in stiffness in Experiment 1, 2 and 3 shown in Figure 6-28, Figure 6-29 and Figure 6-30 respectively did not alter the amplitude of vibration by significant amounts.
2. The increase in critical damping ratio in Experiment 1, 2 and 3 shown in Figure 6-31, Figure 6-32 and Figure 6-33 respectively did not alter the amplitude of vibration by significant amounts.
3. The increase in stationary mass in Experiment 1, 2 and 3 shown in Figure 6-34, Figure 6-35 and Figure 6-36 respectively altered the amplitude of vibration by a significant amount.

The observations outlined in the preceding paragraphs are different to observations made when using forces obtained from DEM analysis. Masses and forces obtained from DEM analysis coupled with Equation 6-7 show that the amplitude of vibration can be reduced significantly by increasing the stiffness, critical damping ratio and stationary mass whereas the forces and masses obtained from Experiments 1, 2 and 3 only show significant reduction in amplitude when the stationary mass was increased by a notable amount. This may be due to the DEM results did not include forces from granular structure interactions and inertial forces from time varying mass inertial changes.

The results are shown in Figure 6-34, Figure 6-35 and Figure 6-36 demonstrate the effectiveness of damping the amplitudes of vibration by increasing the stationary mass and are consistent with the time-varying mass structural dynamic problem. It has been demonstrated that silo quaking is a time varying mass structural dynamic problem, therefore, it is consistent to increase the stationary mass to reduce the effects of inertial changes. Furthermore, the results shown in Figure 6-28 to Figure 6-36 demonstrate that Equation 6-7 can be used in the analysis and design of silos and most importantly it can be used to repair existing silos that suffer the silo quaking phenomena.

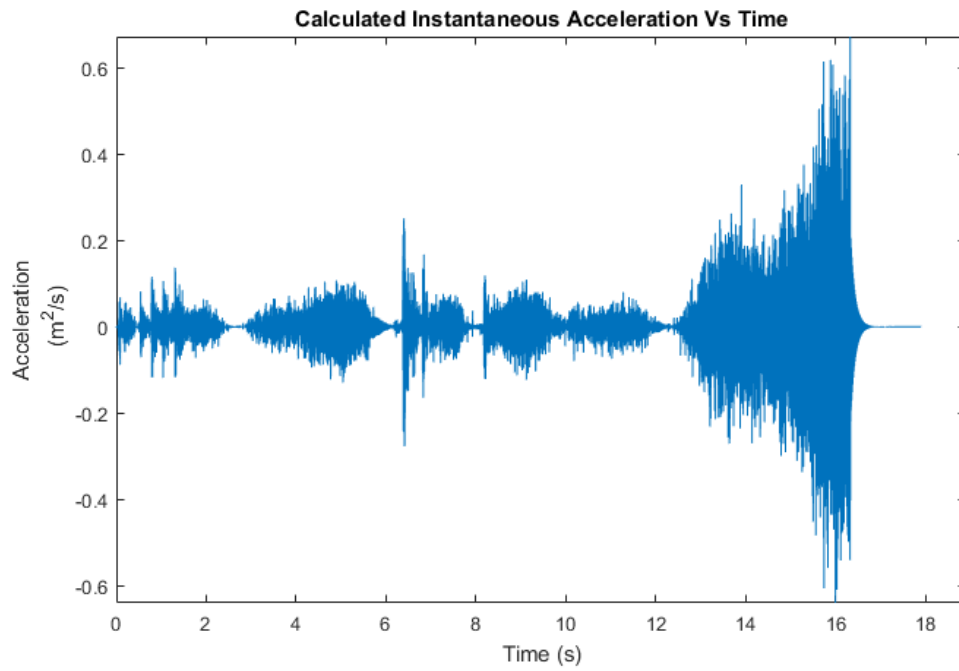


Figure 6-28: Experiment 1 with modified structural stiffness.

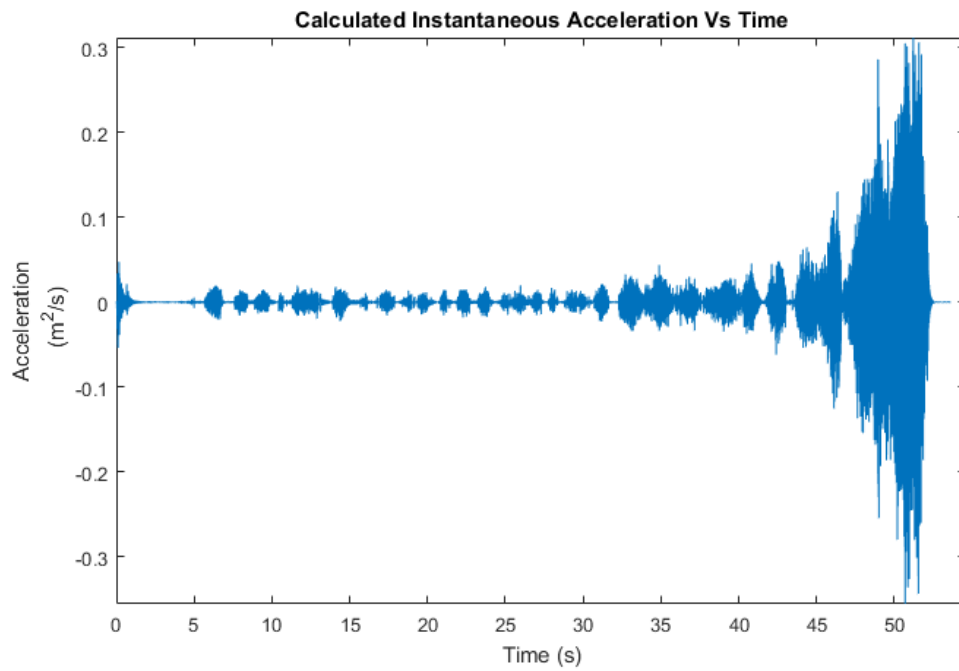


Figure 6-29: Experiment 2 with modified structural stiffness.

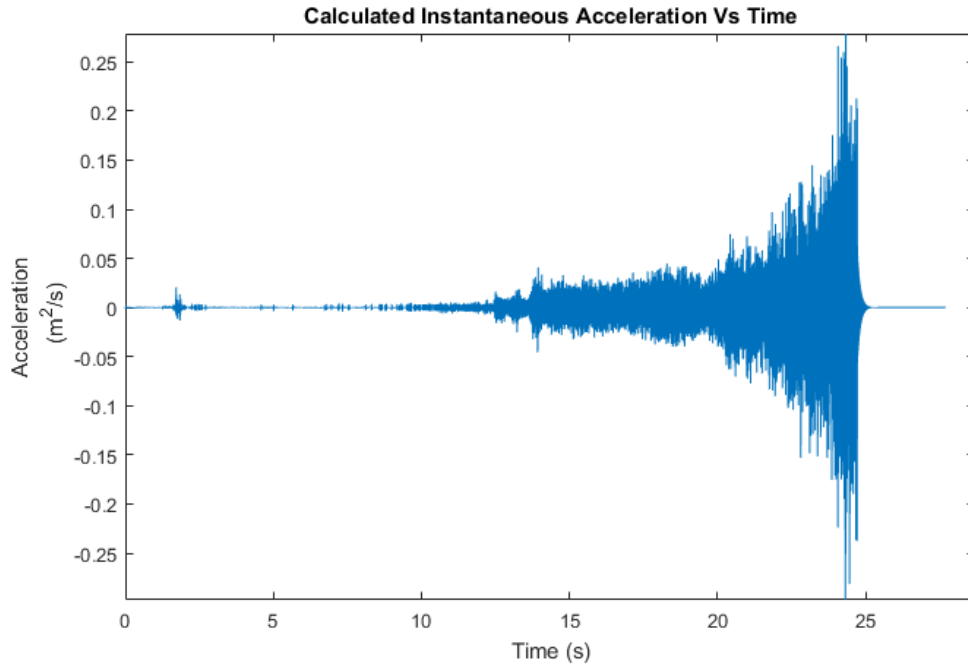


Figure 6-30: Experiment 3 with modified structural stiffness.

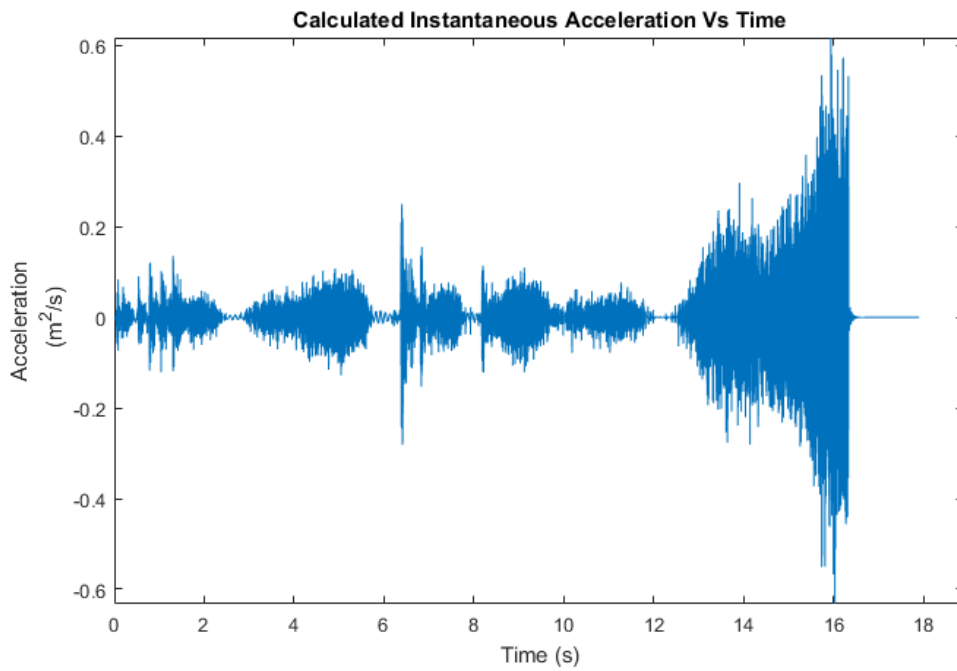


Figure 6-31: Experiment 1 with modified critical damping ratio.

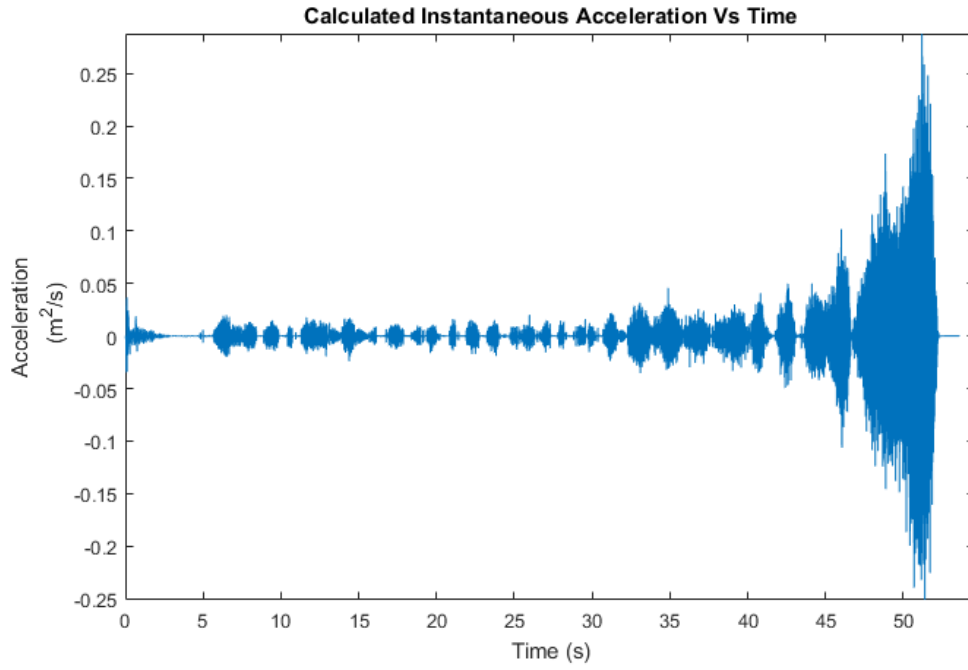


Figure 6-32: Experiment 2 with modified critical damping ratio.

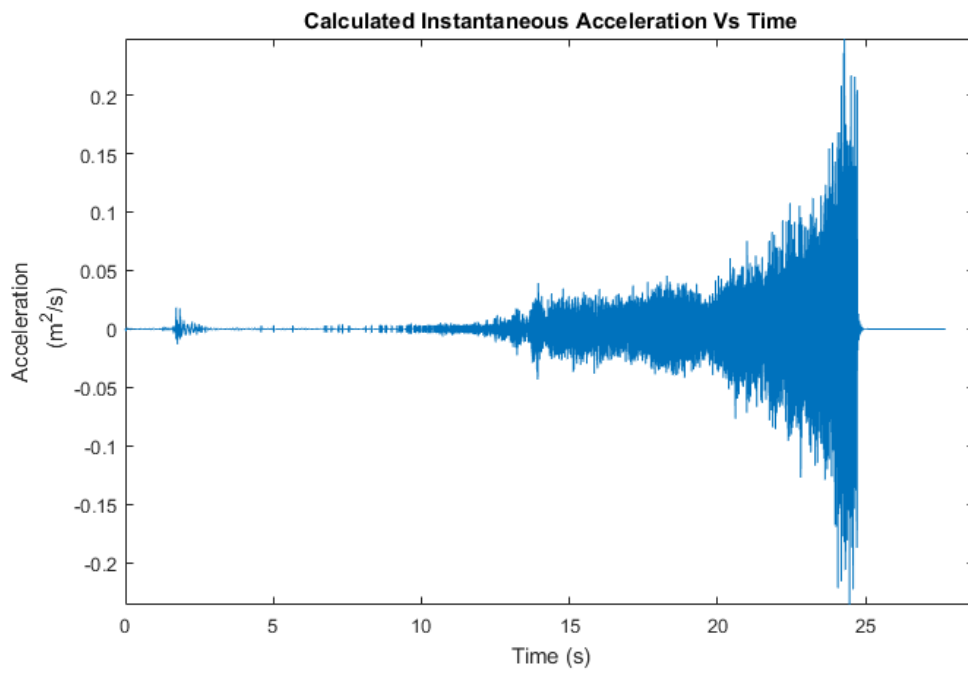


Figure 6-33: Experiment 3 with modified critical damping ratio.

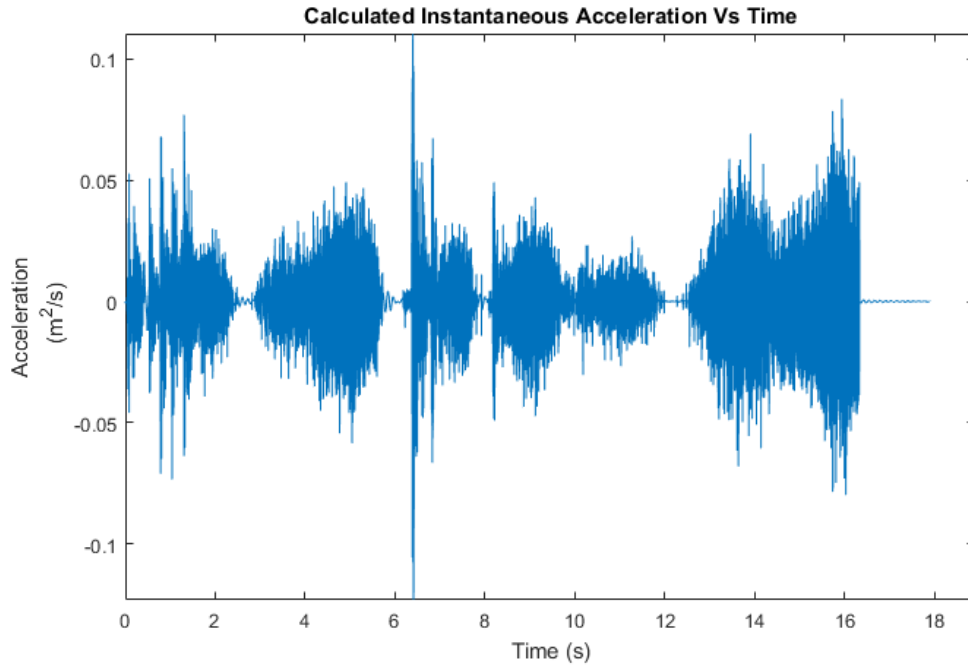


Figure 6-34: Experiment 1 with modified stationary mass.

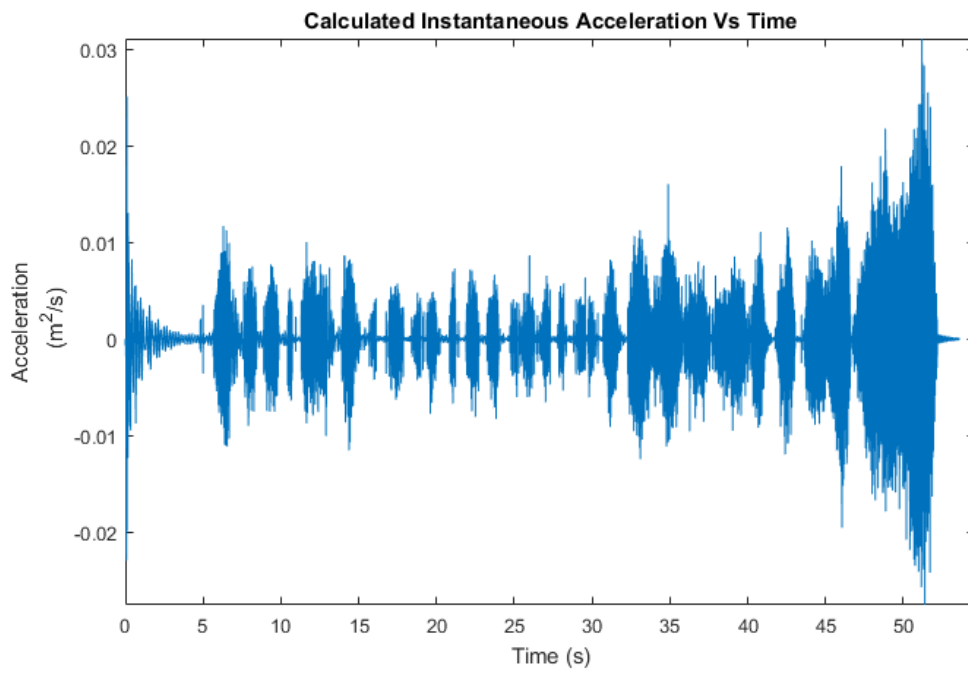


Figure 6-35: Experiment 2 with modified stationary mass.

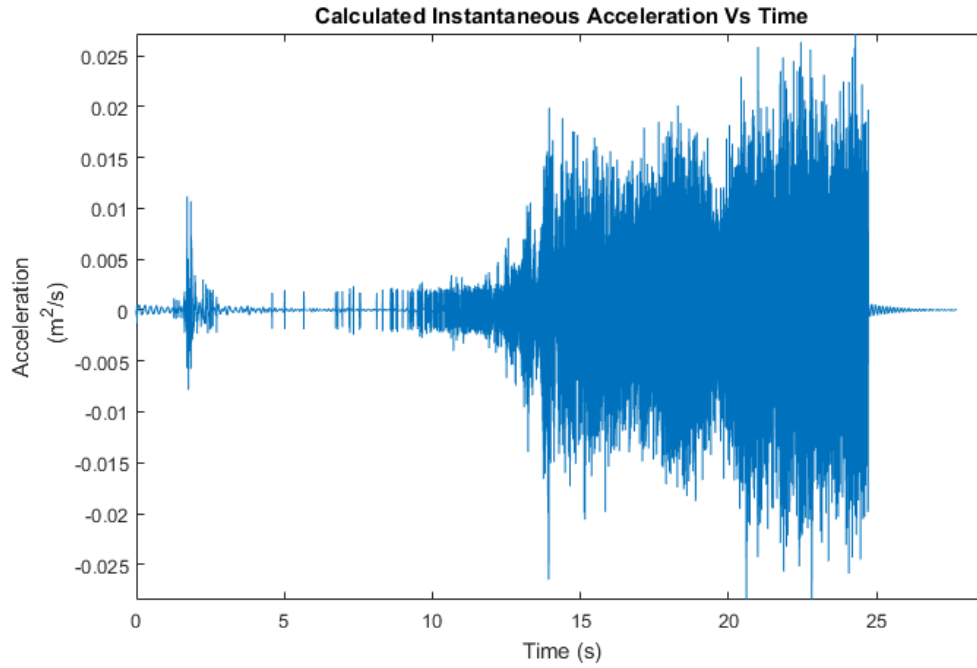


Figure 6-36: Experiment 3 with modified stationary mass.

Table 6-6: Stationary mass, critical damping ratio and stiffness for Experiment 1, 2 and 3.

Figure	Experiment	Stationary Mass (kg)	Critical Damping (%)	Stiffness Damping (N/m)
Figure 6-28	1	175	2	45500000
Figure 6-29	2	175	2	45500000
Figure 6-30	3	175	2	45500000
Figure 6-31	1	175	10	4550000
Figure 6-32	2	175	10	4550000
Figure 6-33	3	175	10	4550000
Figure 6-34	1	1750	2	4550000
Figure 6-35	2	1750	2	4550000
Figure 6-36	3	1750	2	4550000

6.8 Conclusion

During granular discharge, the total mass of the silo structure changes with time similar to a rocket during flight. Furthermore, the flow of the granules is pulsating thus causing time varying dynamic forces. Thus, making the silo structure during discharge a time varying mass structural dynamic problem. Also, it has been demonstrated that the existing dynamic structural analysis methods are not suited for analysing silo structures during granular discharge due to time varying mass effects because they only consider the time varying forces in their solution schemes leaving the mass, stiffness and damping constant.

The fundamental equation of motion was reformulated to account for time varying mass characteristics of silo during discharge and validated with data obtained from experiments, analytical formulae and DEM analyses. It was demonstrated that DEM alone could not predict the silo quaking phenomena because DEM analyses do not consider the response of the structure under time varying mass and pulsating forces. However, the forces and masses obtained from DEM analyses can be input into the Equation of Silo Quaking to assess the dynamic response of the silo supporting structure during granular discharge.

The Equation of Silo Quaking represents the instantaneous dynamic equilibrium of the silo supporting structure and the flowing granular material during discharge for the entire duration of the discharge cycle. At any instance during discharge, the resistance provided by the structure must equate to the force exerted by the granular material. As per Newton's third law of motion, the motion of the silo structure will exert the same force onto the granular material. It is important to note that Equation 6-7 is an extension of the traditional equation of motion and can be extended to multidegrees of freedoms using matrix methods illustrated in Chapter 3.5.

During discharge, the silo supporting structure's dynamic equilibrium is disturbed by the pulsating forces and mass losses. Thus, for the silo structure to maintain its dynamic equilibrium it has to deflect or sway excessively such phenomenon is called

silo quaking at low frequencies and silo honking at frequencies within the auditory spectrum. The Equation of Silo Quaking also demonstrates that the silo quaking phenomena can be prevented by providing sufficient mass, damping and stiffness in the silo supporting structure to counterbalance the disturbances caused by the pulsating forces and mass losses. Furthermore, the Equation of Silo Quaking gives a solid theoretical framework for design engineers to repair existing silos that currently suffer the silo quaking phenomena and a solid foundation to investigate the silo quaking phenomena.

7 MATERIAL CLASSIFICATION

7.1 Introduction

The experiments such as direct shear test, density test, plastic limit, liquid limit and sieve analysis and results described in this chapter was carried out on the iron ore material for completeness. To further quantify the Silo Quake Response Spectrum for structural design, it is imperative that the material must be thoroughly tested and calibrated. Furthermore, all material characterisations techniques were invented for the static design of the silo and its supporting structure without considering the effects of granular structure interaction as described by the Equation of Silo Quaking in Chapter 6 and the Silo Quake Response Spectrum in Chapter 5. Thus it is wise in the author's professional point of view to revisit such techniques, modify and create new laboratory tests to estimate the Silo Quake Response Spectrum and necessary parameters for the Equation of Silo Quaking for the structural design of the silos.

7.2 Direct Shear Test Results to ASTM D6128-16

The iron ore material was tested to the procedures outlined in ASTM D6128-16 with a similar direct shear tester to the Jenike's shear tester for economic reasons as mentioned previously. The iron ore was tested at three moisture contents 0%, 2% and 7.5%. During the experiments, it was found that the moisture content fluctuated between 3% and 4% or in other words, within the boundary limits. Figure 7-1, Figure 7-2 and Figure 7-3 illustrate the importance of the moisture content of the granular material on the behaviour of the material. It can be seen that the stresses deviated significantly over small changes to the moisture content of the granular material. The shear strength of the soil changes with the change in moisture content. The values obtained from such shear tests are used to determine the minimum hopper opening size for flow.

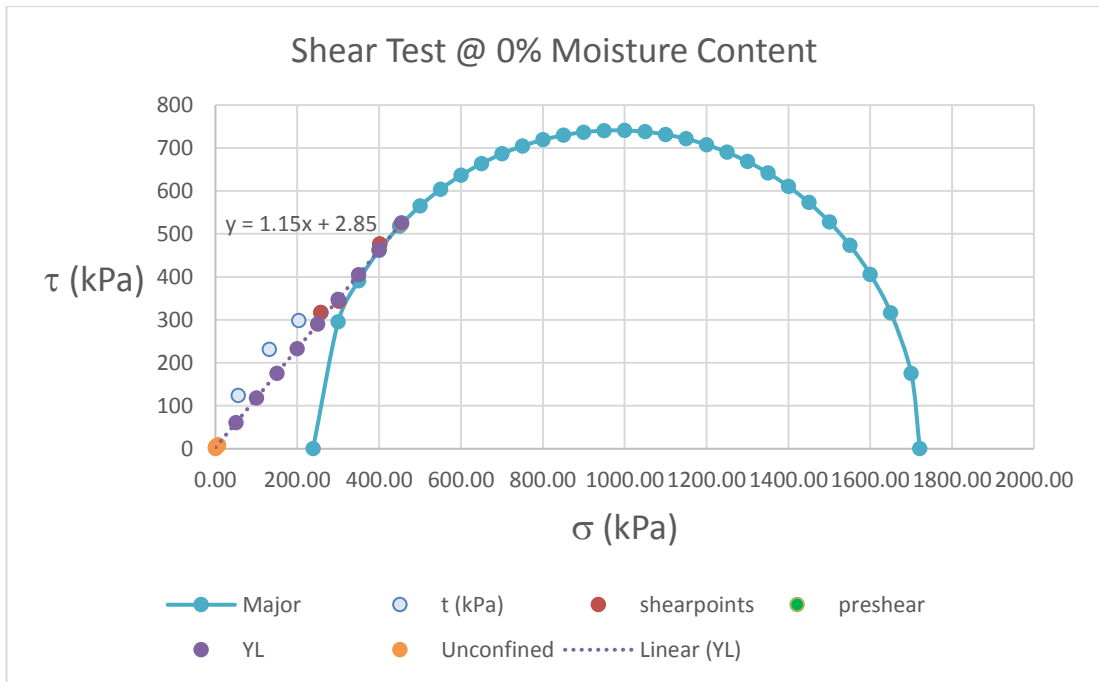


Figure 7-1: Shear experiment at 0% moisture content.

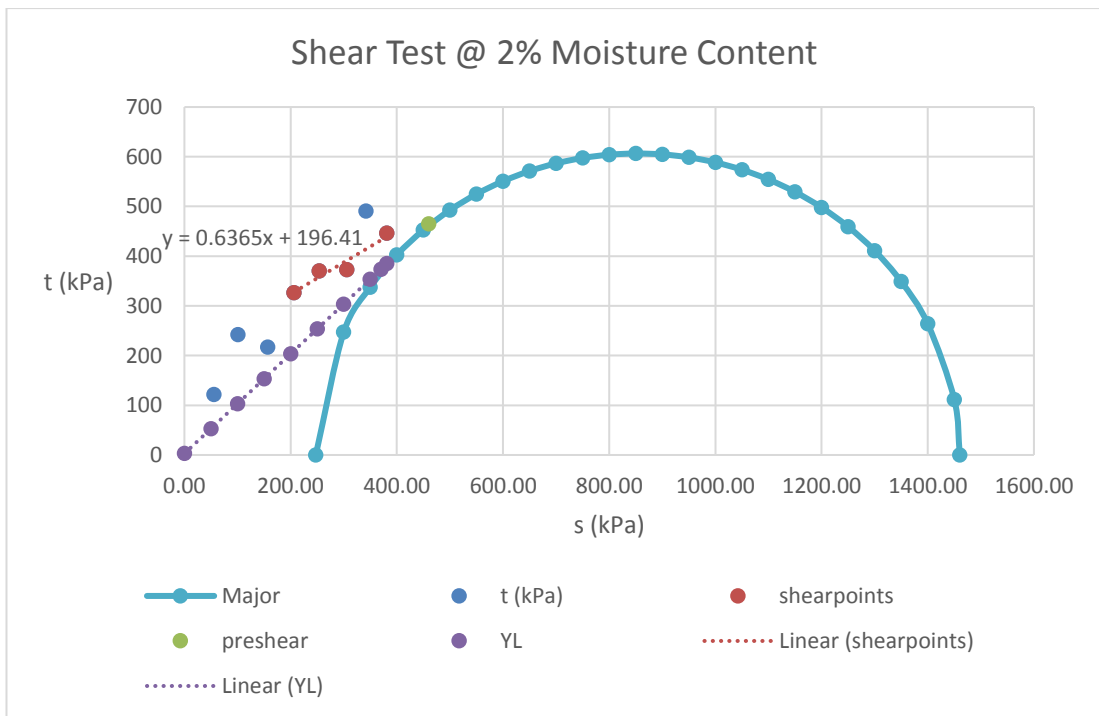


Figure 7-2: Shear experiment at 2% moisture content.

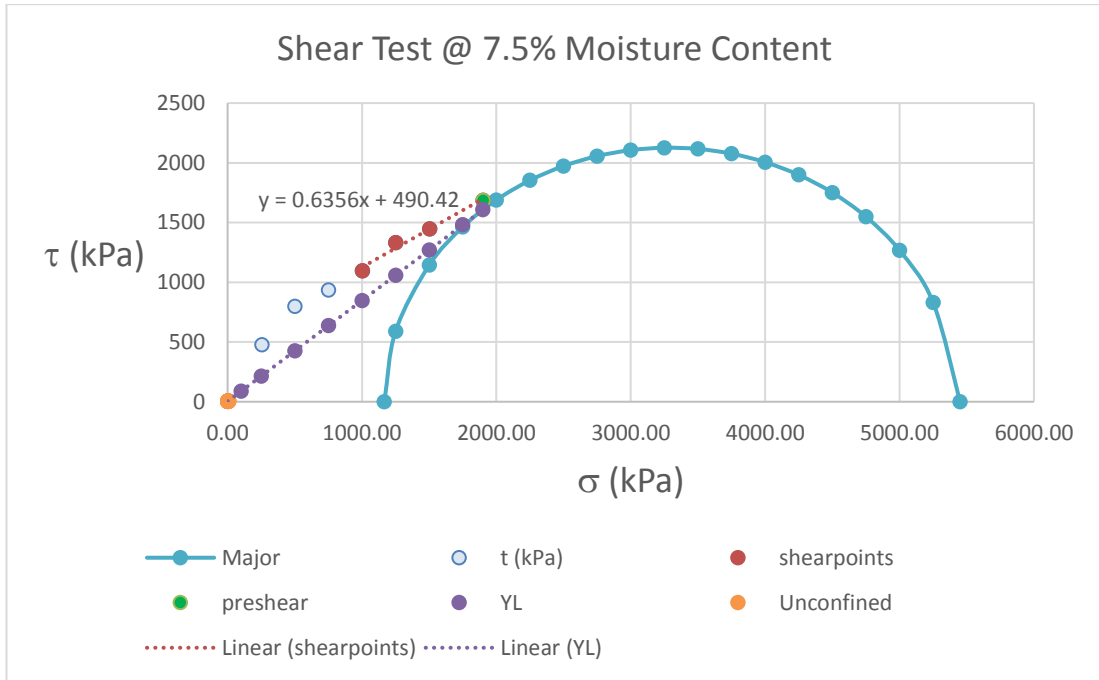


Figure 7-3: Shear experiment at 7.5% moisture content.

Figure 7-1, Figure 7-2 and Figure 7-3 demonstrate how the flow properties of the iron ore changes with the moisture content. The shear strength of the material appears to increase correspondingly with the increase in moisture content. In particular, the angle of internal friction of the material also changes with the moisture content as shown in Table 7-1. Such changes are taken into the design of the minimum hopper opening size to ensure the flow of the granules from the hopper. The methods to calculate the minimum hopper opening sizes can be found in literature such as McGlinchey (2005), Masuda, Higashitani, and Yoshida (2006), Schulze (2007) and Shamlou (1988).

Table 7-1: Angle of Internal Friction vs Moisture Content.

Moisture Content %	Angle of Internal Friction δ
0.0%	49
2.0%	45
7.5%	40.2

Figure 7-4 to Figure 7-6 show the variations in wall friction angle as the moisture content changes. The values obtained from Figure 7-4 to Figure 7-6 are averaged and displayed in Table 7-2. Upon inspection of Table 7-2, it can be concluded that the change in moisture content of the iron ore did not greatly influence the angle of wall friction in comparison to the angle of internal friction in Table 7-1. However this may not be the case for other cohesive materials.

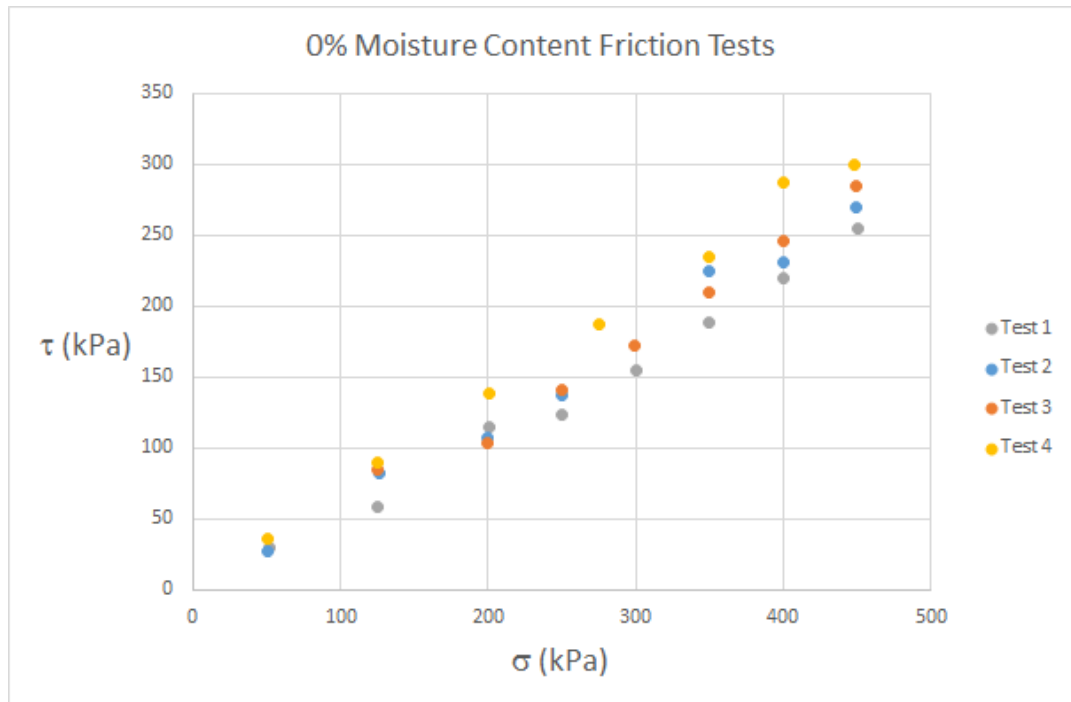


Figure 7-4: Wall friction experiments at 0% moisture content.

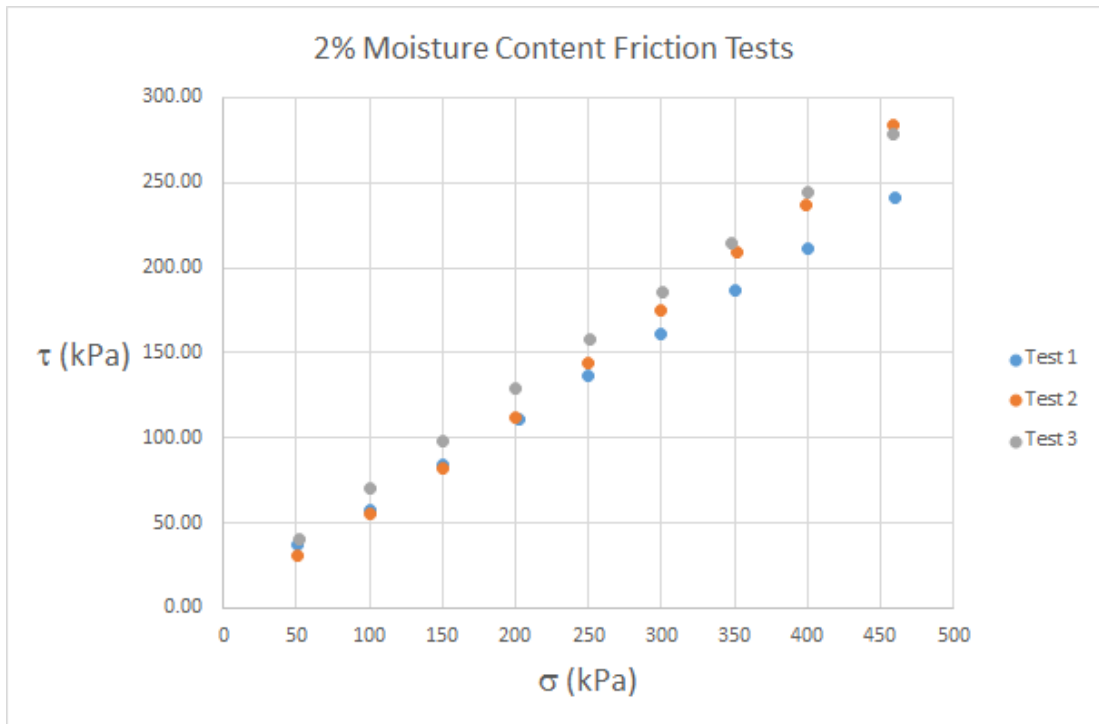


Figure 7-5: Wall friction experiments at 2% moisture content.

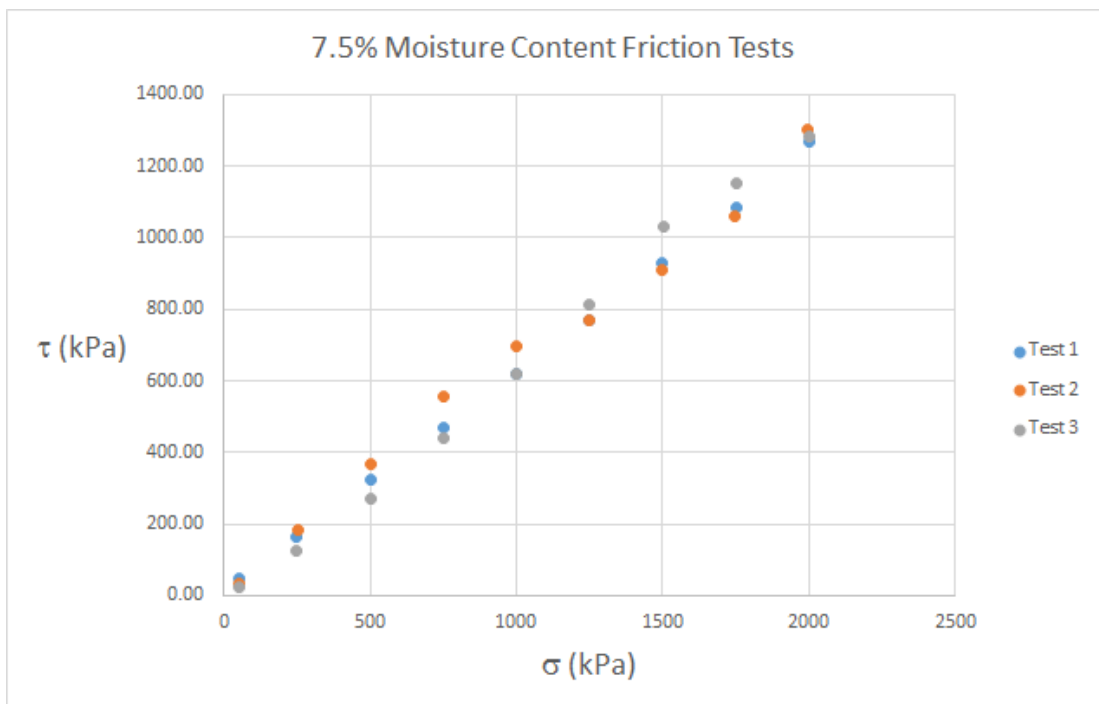


Figure 7-6: Wall friction experiments at 7.5% moisture content.

Table 7-2: Angle of Wall Friction vs Moisture Content.

Moisture Content %	Average Angle of Wall friction ϕ
0.0%	31.88
2.0%	29.6
7.5%	32.45

The bulk density is one of the important parameters in the structural design of the silos as it determines the ultimate weight the silo and its supporting structure needs to carry. The bulk density can change under different consolidation pressure, different mixture of particle sizes and moisture content as shown in Table 7-3. Neither of the international design guides such as AS3774 (1996) and EN1993-4-1 (2007) on silos mention about such changes. Given the importance of the bulk density, the structural design engineers must be made aware of such variations in bulk density with respect to moisture content. Under operating conditions, the moisture content of a granular will change depending on the weather conditions. This was evident during the experiments where it was found to be impractical to maintain the moisture content of 2 tonnes of iron ore.

Table 7-3: Bulk density at various moisture content.

Moisture Content %	Sample	Consolidation Pressure (kPa)	ρ_{\max} (kg/m ³)	ρ_{average} (kg/m ³)
0.0%	1	453	2521.46	2483.31
	2	453	2376.44	
	3	453	2485.51	
	4	453	2472.25	
	5	453	2526.54	
	6	453	2517.64	
2.0%	1	460	2493.35	2485.90
	2	460	2479.61	
	3	460	2441.65	
	4	460	2614.71	
	5	460	2453.89	

	6	460	2432.18	
7.5%	1	2000	2715.71	2685.80
	2	2000	2740.57	
	3	2000	2689.02	
	4	2000	2670.08	
	5	2000	2630.64	
	6	2000	2668.76	

7.3 Density To AS1289.3.5.1 (2006)

The density of the iron ore was determined by two different methods in accordance with the procedures outlined in AS1289.3.5.1 (2006). The material was first separated into a course sample and a fine sample using the sieve shaker. The course sample was tested with the water bath as shown in Figure 4-30 and the fine sample was tested with the volumetric flasks and vacuum as shown in Figure 4-31 and Figure 4-32 respectively. The densities obtained from a series of tests, shown in Table 7-4, were averaged to be 4199 kg/m³. This density value is above that of the bulk density of the iron ore material computed in Section 7.2 and given in various design codes such as AS3774 (1996) and EN1993-4-1 (2007). In practice, the bulk density will always be below that of the actual density due to the presence of air particles in between the bulk particles.

Table 7-4: Density of iron ore.

Material	Sample	ρ_{\max} (kg/m ³)	ρ_{average} (kg/m ³)
Course	1	4249	4199
	2	4229	
	3	4205	
	4	4215	
	5	4181	
Fine	1	4181	4199
	2	4163	
	3	4178	

	4	4188	
--	---	------	--

7.4 Plastic Limit To AS1289.3.2.1 (2009) and Liquid Limit To AS1289.3.1.1 (2009)

The Liquid Limit (LL), Plastic Limit (PL) and Plasticity Index (PI) were experimented in accordance to AS1289.3.2.1 (2009) and AS1289.3.1.1 (2009). The results are shown in Table 7-5, Table 7-6 and Table 7-7. According to Bowles (1996) and Das and Sawicki (2001), the values LL, PL and PI are often used to assess the level of consolidation and behaviour of the soil sample by comparing with the natural moisture content of the soil sample. The moisture contents of the iron in this context are presented in Table 5-1 and Table 6-1. The moisture contents recorded during the experiments were significantly lower than the LL and PL thus suggesting that the iron ore material was under consolidated (Bowles 1996) and behaving like solids (Das and Sawicki 2001).

Table 7-5: Liquid Limit of iron ore.

Container N ⁰	1	2	3	4
Mass of Container + Wet Soil (g)	78.14	88.1	86.8	76.06
Mass of Container + Dry Soil (g)	69.64	77.88	77.17	68.32
Mass of Container (g)	30.31	31.65	34.58	34.92
Actual Moisture Content (%)	17.8%	18.1%	18.4%	18.8%
First Penetration (mm)	15.9	18.5	22.6	23.9
Second Penetration (mm)	16.7	19.2	22.5	24.4
Average Penetration (mm)	16.3	18.9	22.6	24.2

Table 7-6: Plastic Limit of iron ore.

Container N ⁰	1	2	3	4
Mass of Container + Wet Soil (g)	39.35	39.48	39.16	39.73
Mass of Container + Dry Soil (g)	38.52	38.61	38.2	38.87
Mass of Container (g)	33.72	33.55	32.41	33.72
Actual Moisture Content (%)	14.7%	14.7%	14.2%	14.3%

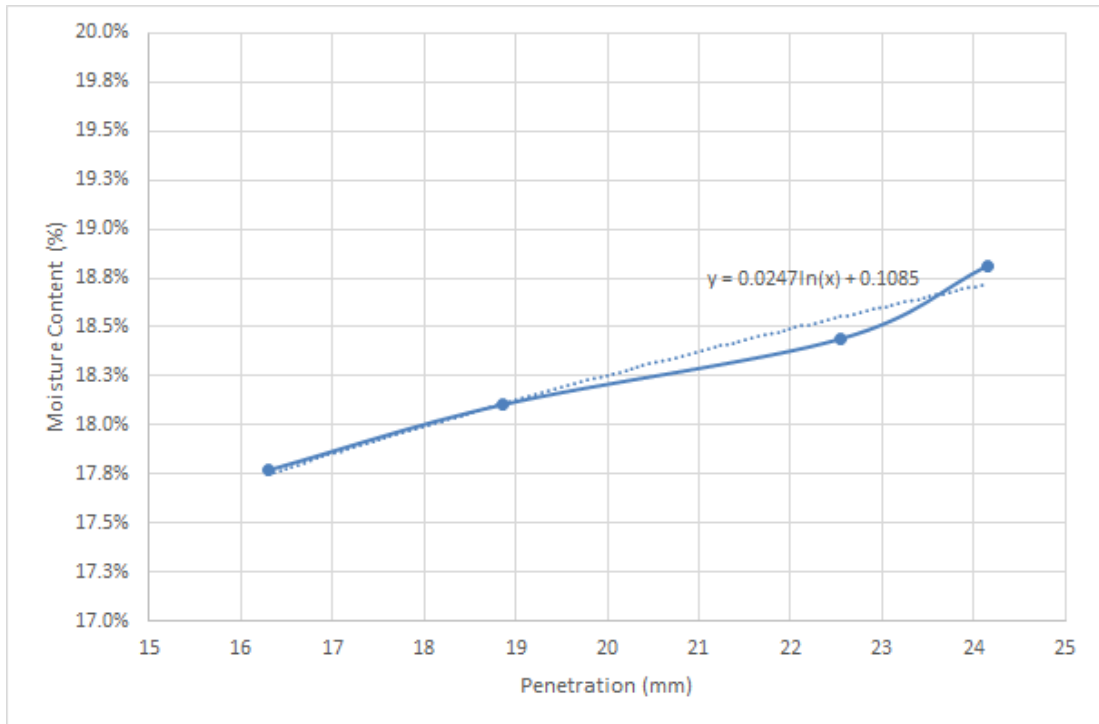


Figure 7-7: Line of best fit for Liquid Limit tests.

Table 7-7: Plasticity Index of iron ore.

Material Test Type	
Liquid Limit (calculated to equation in Figure 7-7)	18.25%
Plastic Limit (average of results in Table 7-6)	14.49%
Plasticity Index = Liquid Limit – Plastic Limit	3.76%

7.5 Sieve Analysis To AS1289.3.6.1 (2009)

The iron ore samples were separated into two samples, raw sample and washed sample. The raw sample was placed in the sieve shaker (Figure 4-33) with opening sizes shown in Table 7-8 while the other samples were thoroughly washed, dried and placed in the same sieve shaker with opening sizes shown in Table 7-9. The sieve shaker was operated in accordance with procedures outlined in AS1289.3.6.1 (2009).

Figure 7-8 presents the graphical details of Table 7-8. It can be summarised from Figure 7-8 that the raw iron ore sample contained mostly fines with over 99% of the particles below 10mm and over 66% of the particles are below 2.36mm. The washed sample of iron ore effectively took out the dust at the micron level. Figure 7-9 presents the results in Table 7-9 in graphical format also reinforces that the iron ore contained mostly fine. It is evident in Figure 7-9 that over 66% of the particles are below 1.18mm in size.

Table 7-8: Sieve Analysis Results of Raw Sample of Iron Ore.

Sieve Opening Size (mm)	Weight (g)	% Weight	Cumulative % Weight	% Fine
9.5	8	0.22%	0.22%	99.78%
6.7	182	5.08%	5.30%	94.70%
4.75	425	11.85%	17.15%	82.85%
2.36	606	16.90%	34.05%	65.95%
0.075	1641	45.76%	79.81%	20.19%
Tray	724	20.19%	100.00%	0.00%
	3586	100%		

Table 7-9: Sieve Analysis Results of Washed Sample of Iron Ore.

Sieve Opening Size (mm)	Weight (g)	% Weight	Cumulative % Weight	% Fine
1.18	208	33.55%	33.55%	66.45%
0.6	159	25.65%	59.19%	40.81%
0.425	63	10.16%	69.35%	30.65%
0.3	30	4.84%	74.19%	25.81%
0.15	84	13.55%	87.74%	12.26%
0.075	76	12.26%	100.00%	0.00%
	620	100%		

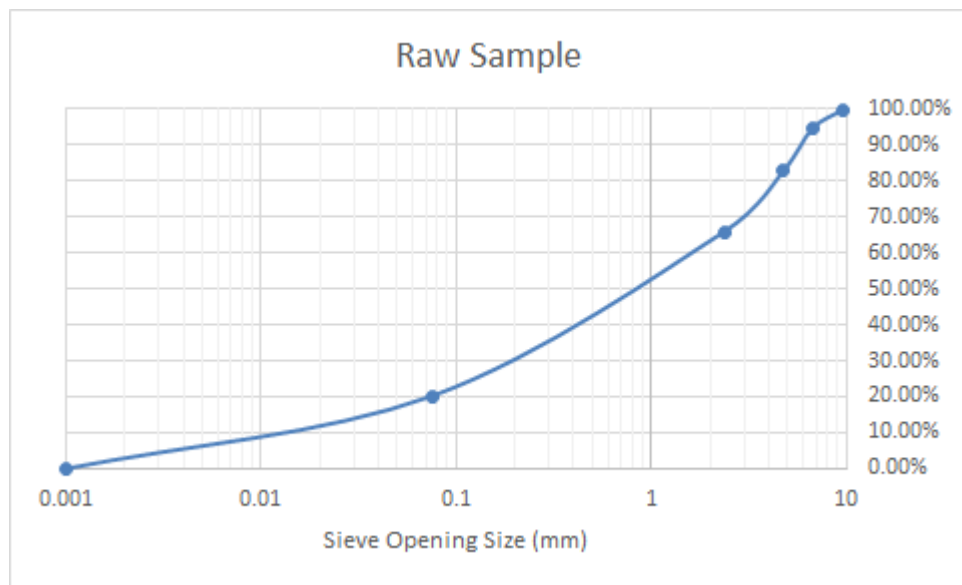


Figure 7-8: A graph of sieve analysis results of raw iron ore sample.

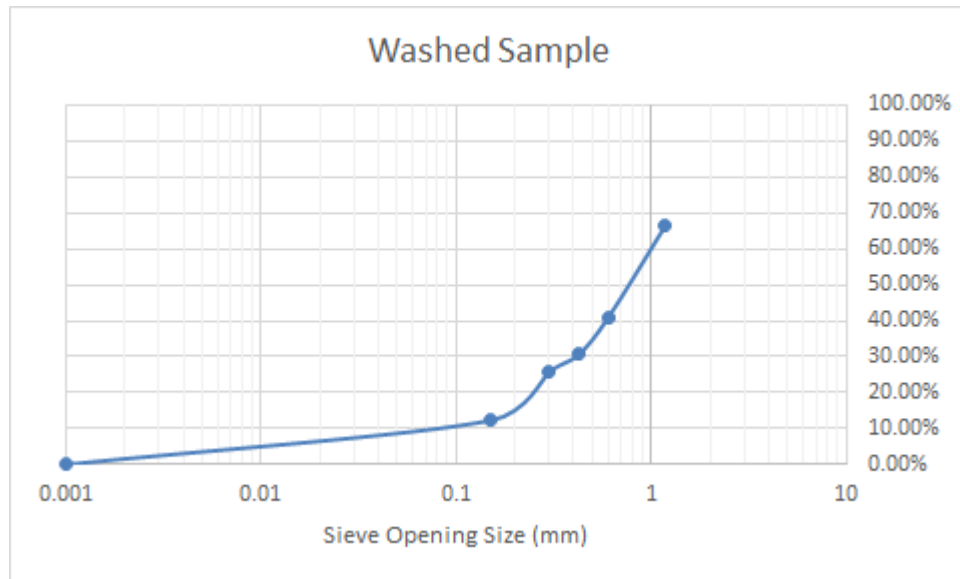


Figure 7-9: A graph of sieve analysis results of washed iron ore sample.

7.6 Conclusion

This chapter demonstrates the results of the experiments used by both material handling and geotechnical engineers to classify the granular material. All material characterisations techniques were invented for the static design of the silo and its supporting structure without considering the effects of granular structure interaction as described by the Equation of Silo Quaking in Chapter 6 and the Silo Quake Response Spectrum in Chapter 5. In light of the Equation of Silo Quaking and the Silo Quake Response Spectrum, it is wise to review the existing material characterisation methods, if necessary create new laboratory tests to estimate the Silo Quake Response Spectrum and necessary parameters for the Equation of Silo Quaking for the structural design of the silos.

8 RELEVANCE OF EQUATION OF SILO QUAKING TO THE SILO HONKING PHENOMENON

8.1 Introduction

This chapter solely discusses the silo honking phenomenon, which is one of the three silo quaking phenomena, and the relevance of the Equation of Silo Quaking derived in Chapter 6 to such phenomenon. All experimental data used in this chapter has been extracted from the literature. The primary reason for the absence of numerical results is due to the lack of structural analysis tools that can incorporate acoustics and time vary mass structural dynamic (Equation 6-7) interactions. Furthermore, such interaction model is not available at the time of writing this thesis.

8.2 Background to Silo Honking

Silo honking is a term used to describe the phenomenon encountered in tall industrial silos during discharge. According to Tejchman (1998b), Tejchman (1999), Buick (2004), Buick et al. (2004), during silo discharge, a loud, intermittent and high-frequency audible sound more than 100dB similar to a truck horn can be heard. Tejchman (1999) observed that silo honking could frequently be encountered in aluminium or steel silos where the walls are not sufficiently stiff. Such loud sound is considered to be environmental pollution.

According to Haskel and Sygoda (1996) and Cutnell and Johnson (2012), the human ear has receptors that can sense sound waves between 20Hz and 20000Hz. Therefore, silo honking must produce sound waves of frequencies between 20Hz and 20000Hz and amplitudes sufficient to be audible to the human ears.

Additionally, movements of the silo walls were observed during experiments conducted by Tejchman (1998b), Tejchman (1999), Buick (2004), Buick et al. (2004), Wilde, Rucka, and Tejchman (2008). The movements detected were both in bending and ovalling modes like shown in Figure 8-1 and Figure 8-2. In particular, Figure 8-2 demonstrates the theoretical mechanism of silo honking. It can be seen that the movement of the mass through the silo causes the wall to deform transversely thus creating the booming sound.

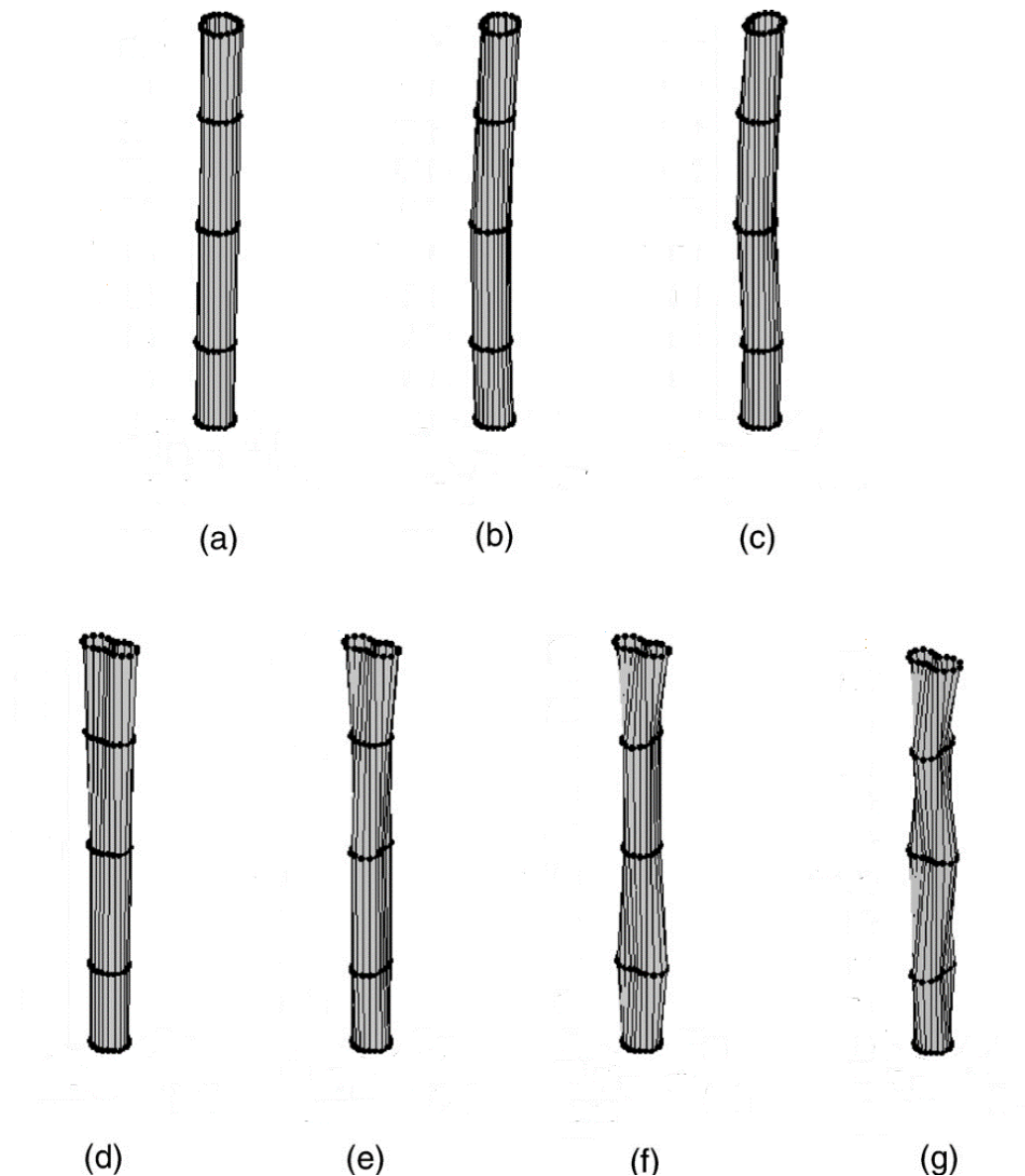


Figure 8-1: Deflected shapes of silo during discharge (Wilde, Rucka and Tejchman 2008).

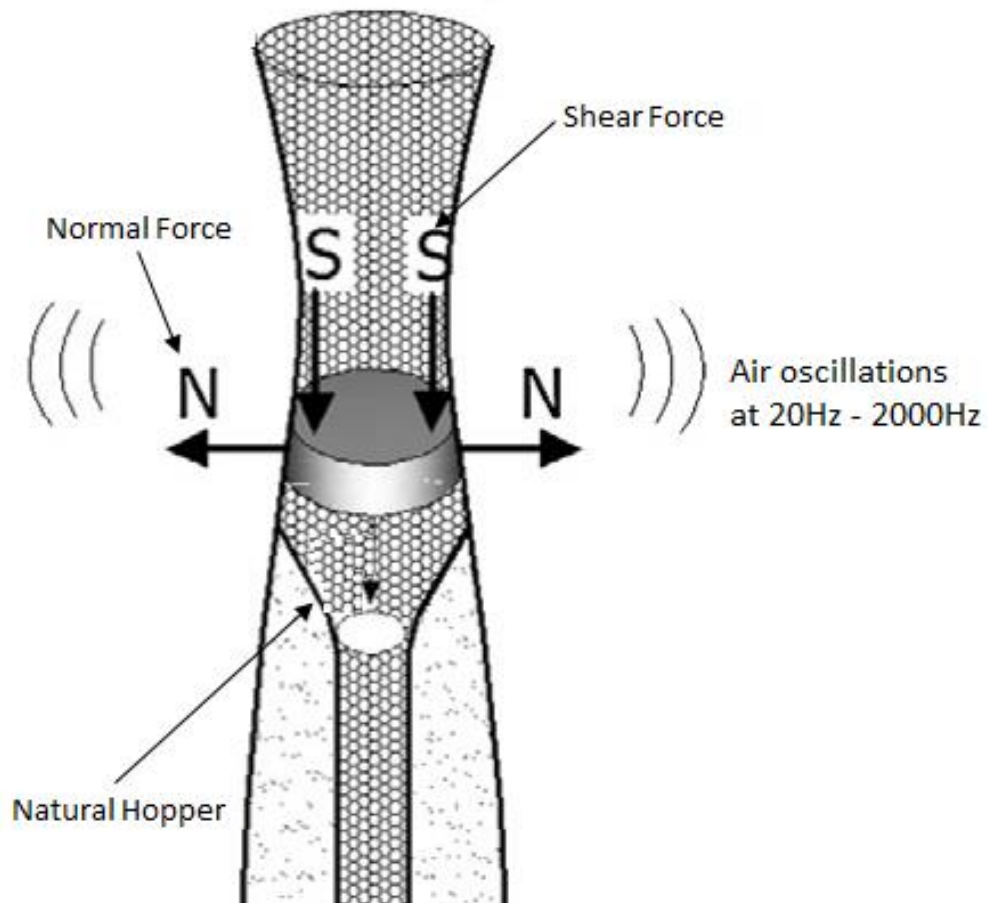


Figure 8-2: Mechanism of silo honking according to (Niedostatkiewicz, Wójcik and Tejchman 2014).

8.3 Background to Acoustics

For ease of explaining the acoustics involved in silo honking and how the Equation of Silo Quaking (Equation 6-7) can be applied, let's first idealise the tall silo as a string in tension similar to that of musical instruments such as a guitar.

Fundamentals of physics state that the sound wave travels faster on a string whose particles have a small mass per unit length (Cutnell and Johnson 2012). Therefore, according to Cutnell and Johnson (2012) the velocity of the wave can be expressed as:

$$v_{wave} = \sqrt{\frac{F}{m/L}}$$

Equation 8-1

Where:

- v_{wave} is the velocity of the wave.
- F is the force applied to the string.
- m is the total mass of the string.
- L is the length of the string.

As the tensioned guitar string is plucked, it vibrates back and forth thus creating condensation and rarefaction waves in the air particles in the process. The sound wave travels through the air and arrives at the ear; they force the eardrum to vibrate at the same frequency as the guitar string. According to Cutnell and Johnson (2012), the vibratory motion of the receptors inside the eardrum, as shown in Figure 8-3, is interpreted by the human brain as sound.

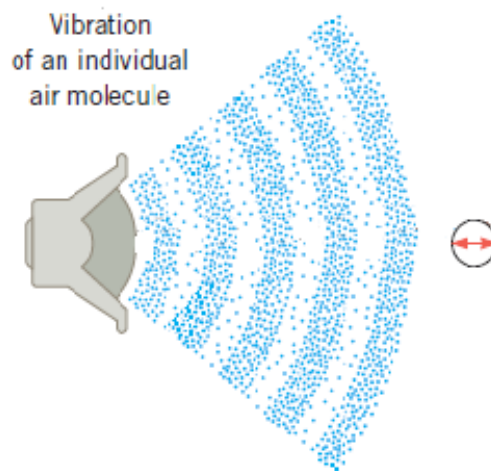


Figure 8-3: Sound waves arrive at the eardrum (Cutnell and Johnson 2012).

The sound waves carry energy capable of forcing the eardrum to vibrate. In extreme cases, the energy can damage windows and buildings (Cutnell and Johnson 2012).

The amount of energy transported by the sound wave per second is called Power (P) and is measured in joules per second J/s or watts (W) Cutnell and Johnson (2012). As such, prolonged exposure to constant high-intensity sound over the long period can cause permanent hearing loss Cutnell and Johnson (2012). The sound intensity I can be defined as:

$$I = \frac{P}{A} \quad \text{Equation 8-2}$$

Where:

- I is the intensity, W/m².
- P is the power, J/s or W, or energy of sound (amplitude squared) per unit time.
- A exposure area, m².

The sound intensities are often compared to the threshold intensity and expressed in decibel (dB) to indicate loudness. The intensity level (β), expressed in decibel (dB) is defined as:

$$\beta = (10dB) \log \left(\frac{I}{I_0} \right) \quad \text{Equation 8-3}$$

Where:

- β is the intensity level in dB.
- I is the intensity of the sound wave.
- I_0 is the reference intensity of the sound wave.

In order for the silo to produce an audible noise of up to 100dB which is 30dB below threshold of pain as outlined in Table 8-1, the wall of the silo under tension load must be vibrating transversely thus producing contraction and rarefaction waves with

sufficient power at frequencies between 20Hz to 20000Hz like a speaker shown in Figure 8-3. Furthermore it was confirmed during experiments conducted by Tejchman (1999), Buick (2004), Buick et al. (2004), Wilde, Rucka, Tejchman (2008) and Niedostatkiewicz, Wójcik, and Tejchman (2014) that the walls of the test silos vibrated transversely. However, no explanations about the acoustics nature of the vibrating silo wall to the sound produced were given and neither any granular-structure-acoustics interaction was formulated.

Table 8-1: Typical sound intensities and intensity levels relative to the threshold of hearing (Cutnell and Johnson 2012)

	Intensity I (W/m ²)	Intensity Level β (dB)
Threshold of hearing	1.0×10^{-12}	0
Rustling leaves	1.0×10^{-11}	10
Whisper	1.0×10^{-10}	20
Normal conversation (1m)	3.2×10^{-6}	65
Inside car in city traffic	1.0×10^{-4}	80
Car without muffler	1.0×10^{-2}	100
Live rock concert	1	120
Threshold of pain	10	130

According to Wang et al. (2015) the basic equations for acoustics problems are:

$$\Delta p - \frac{1}{c^2} \frac{\partial^2 p}{\partial t^2} = 0 \quad \text{Equation 8-4}$$

Where:

- Δ is the Laplace operator.
- p is the acoustic pressure.
- c is the speed of sound travelling in the medium.
- t is time.

The momentum balance required at the structural-acoustic coupling interface (Wang et al. 2015), $\partial\Omega_{sf}$, can be expressed as:

$$\frac{\partial p}{\partial n} = -\rho_f \ddot{u}_f \quad \text{Equation 8-5}$$

Where:

- n is the boundary surface normal vector.
- ρ_f is the density of the fluid.
- \ddot{u}_f is the normal acceleration component of the acoustic fluid at the interface.

Whereas the momentum balance required at the rigid wall boundary (Wang et al. 2015), Γ_f , can be imposed through:

$$\frac{\partial p}{\partial n} = 0 \quad \text{Equation 8-6}$$

As postulated by Wang et al. (2015), the continuity requirement for structural displacements and acoustic pressures at the coupling interface, $\partial\Omega_{sf}$, can be written as:

$$u_s \mathbf{n} = u_f \mathbf{n} \quad \text{Equation 8-7}$$

Where:

- n is the normal vector along the fluid boundary.
- u_s is the displacement of the shell.
- u_f is the displacement of the acoustic fluid.

8.4 Silo Honking a Vibro-Acoustics Problem

Equation 8-1 shows the relationship between the velocity, force, length and mass of the string. The velocity of the string will be different for a given length, applied force but different masses. This is evident on the guitar where the lighter string produces different harmonics to the heavier string for the same tension and plucking force. Equation 8-2, on the other hand, describes the relationship between the sound intensity, power and exposure area. It must be noted that the power (P) is the squared of the vibrational amplitude and frequency of the string. Therefore the stiffer the string, the less amplitude produced by the same plucking force consequently resulting in lower sound intensity.

Equation 6-7 describes the relationship between the generated forces and the time varying mass characteristics of the silo structure by the discharging silo. Similar to the guitar string, the silo wall is subjected to tension before discharge begins. As soon as the silo starts to discharge its content, the mass of the ore inside the silo and associated forces causing tension on the silo wall reduce thus causing a linear elastic structure to vibrate or response to maintain its dynamic equilibrium accordingly as shown in Figure 8-2.

It has been demonstrated that the power of the sound wave is the equal to the amplitude and frequency squared. Therefore the amplitude of vibration of the silo wall must be large enough and within the audible spectrum to be heard by humans. From principles of statics and Equation 6-7, the deflection or amplitude of vibration is directly proportional to the stiffness of the structure. Therefore we can reduce the amplitude of vibration of the silo wall by increasing its stiffness and consequently reducing the sound intensity.

Tejchman (1999) outlined ways to systematically suppress the effects of silo honking such as:

1. Radical decrease of the outflow velocity.

2. Decrease of the filling height.
3. Hanging of a perforated tube in the middle of the silo.
4. Stiffening of the upper part of the silo with steel sheets and steel beams.
5. Mounting of air cannons inside the silo.
6. Use of vibrators along the cylindrical wall.
7. Partitions of silos on small cells with the aid of two very rough cross walls made of aluminium.
8. Construction of circumferential smooth shelf in the middle of the silo.
9. Circumferential filling.
10. Increase the wall roughness.

The methodologies presented by Tejchman (1999) can be summarised, by using principles of structural dynamics, into the following categories:

1. Modifications to the forces generated during silo flow.
2. Modifications to the critical damping ratio.
3. Modifications to the stiffness of the silo.
4. Modifications to the total mass of the silo.

In summary, all of the categories presented in the preceding paragraph are mathematically expressed in Equation 6-7.

8.5 Conclusion

As mentioned previously, there is not an interaction model to account for the Granular – Time-Varying Mass Vibro-acoustics structural dynamics effects at the time of writing this thesis to validate the above hypothesis and equations. Despite the lack of numerical tools, the theoretical explanations above uphold principles of physics, statics and structural dynamics. Moreover, the silo honking is a Vibro-

acoustics problem and can be systematically reduced by reducing the pulsating force, increasing the stiffness, increasing the damping and increasing the mass of the silo structure using the Equation of Silo Quaking.

9 CONCLUSION AND RECOMMENDATION

9.1 Concluding Remarks

Silo quaking phenomenon is a very complex industrial problem, and it has been occurring since the construction of the first silo. It is important to note that all the researches conducted to date have focussed on estimating the pulsating loads but are incomplete without considering the time varying mass dynamic characteristics of the silo supporting structure because silo quake cannot happen if the silo supporting structure has sufficient resistance provided by its mass, damping and stiffness.

The pulsating loads generated by the flow of the granular material coupled with the mass losses disturb the dynamic equilibrium of the supporting structure. As such, causes the supporting structure to vibrate excessively to restore its balance or dynamic equilibrium. This phenomenon is explained by Newton's third law of motion which states that for every action force there is an equal opposite reaction force. Based on Newton's third law of motion, Equation 6-7 demonstrates that the mass losses alone can cause the silo structure to vibrate to maintain its dynamic equilibrium or restoring its balance. The amplitude of vibration of the silo supporting structure is amplified by the pulsating forces and mass losses that occur during discharge.

It can be argued that the understanding of silo quaking has been greatly enhanced by the Silo Quake Response Spectrum and the Equation of Silo Quaking, and that the work here suggests a potential solution to the silo quaking phenomena. It has been demonstrated that silo quaking is a process in which the silo supporting structure maintains its dynamic equilibrium once its dynamic equilibrium is disturbed by the pulsating forces and mass losses. It also has been demonstrated in an industrial application that the pulsating forces cannot cause silo quaking if sufficient mass, damping and stiffness are provided in the supporting structure because the silo supporting structure can maintain its dynamic equilibrium without having to vibrate excessively.

It is important to note that the Equation of Silo Quaking and Silo Quake Response Spectrum are generalised and can be applied to other granular materials and silo structures subjected to further research, material testings and calibrations. In particular, the Equation of Silo Quaking is also applicable to other areas of engineering where the total mass of the dynamic system reduces with time.

9.2 Silo Quake Response Spectrum

The vibration signals generated by the granular flow from the silo are of type nonlinear, nonstationary and instantaneous, primarily due to the time varying mass and pulsating flow characteristics. Thus making traditional signal processing techniques such as Wavelet and Fast Fourier Transform unsuitable. However, the Ensemble Empirical Mode Decomposition (EEMD), Hilbert-Huang Transform (HHT) and Hilbert Marginal Spectrum (HMS) on the other hand have been designed to process nonlinear and nonstationary signals thus is suited to analysing signals generated from silo flow. This is evident in Figure 5-13 to Figure 5-16 where such techniques, when employed, have revealed the existence of the silo quaking response spectrum.

The response spectrum, in its current form, gives the structural engineers the ability to ascertain whether the supporting structure is sufficiently stiff to minimise the effects of the pulsating loads and mass losses associated with silo flow. Moreover, graphical illustrations of the Silo Quake Response Spectrum indicate that it can be expressed by exponential decay mathematics and expressed by Equation 5-1. It is important to note that much more research is needed to further quantify the Silo Quake Response Spectrum and create structural analysis methods to analyse the dynamic response of the silo structure during discharge.

9.3 Equation of Silo Quaking

During granular discharge from the silo, the total mass of the silo structure reduces with time causing the dynamic properties of the silo structure change accordingly. Furthermore, the time varying forces are self-generated due to the fluctuating flow rates, interactions between the granular particles and interactions between the granular particle and the silo wall material. Therefore it can be concluded with confidence that the phenomenon is a time-varying mass dynamic problem and that the vibration is self-induced.

It was also found that the existing dynamic structural analysis methods, based on the fundamental equations of motion, are not suitable in analysing the dynamics of silo structure during material discharge. This is due to the existing dynamic structural analysis methods only consider the time varying forces and leave the mass, damping and stiffness as stationary in their solution schemes. Thus prompted the reformulation of the equation of motion to account for the time varying mass characteristics associated with the silo discharge as expressed by the Equation of Silo Quaking or Equation 6-7.

The Equation of Silo Quaking represents the instantaneous dynamic equilibrium of the silo supporting structure and the flowing granular material during discharge for the entire duration of the discharge cycle. At any instance during discharge, the resistance provided by the structure must equate to the force exerted by the granular material and vice versa as per Newton's third law of motion. During discharge, the silo supporting structure's dynamic equilibrium is disturbed by the pulsating forces and mass losses. Thus, for the silo structure to maintain its dynamic equilibrium it has to deflect or sway excessively such phenomenon is called silo quaking at low frequencies and silo honking at frequencies within the auditory spectrum. The equation of Silo Quaking also demonstrates that the silo quaking phenomena can be prevented by providing sufficient mass, damping and stiffness in the silo supporting structure to counterbalance the disturbances caused by the pulsating forces and mass losses.

The Equation of Silo Quaking gives a solid theoretical framework for design engineers to repair existing silos that currently suffer the silo quaking phenomena and a solid foundation to investigate the silo quaking phenomena. It is important to note that much more research is needed to accurately predict the flow rates and associated dynamic forces. Furthermore, existing commercial structural analysis software needs to be developed to solve the Equation of Silo Quaking expressed in Equation 6-7.

9.4 Recommendations for Future Research

The following possibilities exist for the extension of the work in this thesis:

1. The silo quake response spectrum, similar to the earthquake response spectrum, need to be further researched and formulated into structural analysis methods to predict the dynamic response of the silo structure during material discharge and made readily available in the structural analysis software.
2. It has been identified that the existing dynamic structural analysis methods are unsuitable in analysing the dynamic response of the silo structure during material discharge. The identified deficiencies prompted a reformulation of the equation of motion to account for the time varying mass characteristics of silo flow thus is called Equation of Silo Quaking as expressed in Equation 6-7. Therefore a suitable solution algorithm is required to solve the Equation of Silo Quaking.
3. The Equation of Silo Quaking is also relevant to the case of Silo Honking in Chapter 8. However, at the time of writing this thesis, there is not a suitable formulation to incorporate the Granular – Time-Varying Mass Vibro-acoustics structural dynamics characteristics of silo honking. Therefore such formulation is needed to solve the silo honking phenomenon.
4. The Equation of Silo Quaking demonstrates the dynamic interaction between the pulsating forces and time vary mass during silo flow. The dynamic forces generated during discharge must equate to the response of the structure, and

the dynamic response of the structure will also influence the flow characteristics of the granular material. Therefore it is important to investigate the influence of the dynamic response of the structure on the flow of the granular material.

5. The material characterisation methods to date have not taken into consideration the overall dynamics of the silo structure. Therefore it is recommended that such methods be revised and if necessary create new material characterisation methods to further quantify the Silo Quake Response Spectrum and provide necessary data for the Equation of Silo Quaking to accurately predict the silo quaking phenomena.
6. Suitable numerical integration schemes need to be developed to solve Equation 6-7 and implemented in the structural analysis software.
7. The critical damping ratio was assumed to be constant in this thesis for simplicity. However, in real life it will not be constant thus warrant further investigations.
8. The silo quake spectrum was identified using HHT in this thesis because the signals generated from silo flow are non-linear, non-stationary and instantaneous due to the nature of time varying mass characteristics. Comparisons between the presented spectrum and the spectrum generated by the traditional FFT and wavelets are being made. Practical working experience with actual silo quake problems will help justify which spectrum is more accurate, particularly with the presence of silo honking.

REFERENCES

- 1 Abramian, A., W. Horssen, and S. Vakulenko. 2013. "Nonlinear Vibrations of a Beam with Time-Varying Rigidity and Mass." *An International Journal of Nonlinear Dynamics and Chaos in Engineering Systems* 71 (1): 291-312. doi: 10.1007/s11071-012-0661-2.
- 2 Abramian, A., W. Horssen, and S. Vakulenko. 2014. "On Oscillations of a Beam with a Small Rigidity and a Time-Varying Mass." *An International Journal of Nonlinear Dynamics and Chaos in Engineering Systems* 78 (1): 449-459. doi: 10.1007/s11071-014-1451-9.
- 3 AS1289.1.1. 2001. *Methods of Testing Soils for Engineering Purposes - Sampling and Preparation of Soils - Preparation of Disturbed Soil Samples for Testing*. Standards Australia
- 4 AS1289.2.1.1. 2005. *Methods of Testing Soils for Engineering Purposes - Soil Classification Tests - Determination of the Moisture Content of a Soil – Oven Drying Method*. Standards Australia
- 5 AS1289.3.1.1. 2009. *Methods of Testing Soils for Engineering Purposes - Soil Classification Tests – Determination of the Liquid Limit of a Soil – Four Point Casagrande Method*. Standards Australia
- 6 AS1289.3.2.1. 2009. *Methods of Testing Soils for Engineering Purposes - Soil Classification Tests – Determination of the Plastic Limit of a Soil – Standard Method*. Standards Australia
- 7 AS1289.3.5.1. 2006. *Methods of Testing Soils for Engineering Purposes - Soil Classification Tests - Determination of the Soil Particle Density of a Soil – Standard Method*. Standards Australia
- 8 AS1289.3.6.1. 2009. *Methods of Testing Soils for Engineering Purposes - Soil Classification Tests - Determination of the Particle Size Distribution of a Soil – Standard Method of Analysis by Sieving*. Standards Australia

- 9 AS3774. 1996. *As3774 - Loads on Bulk Solids Containers*. Standards Australia
- 10 AS3990. 1993. *As3990 Mechanical Equipment - Steelwork*. Standards Australia
- 11 AS4100. 1998. *As4100 - Steel Structures*. Standards Australia
- 12 AS/NZS1170.0. 2002. *Structural Design Actions Part 0: General Principles*. Standards Australia
- 13 AS/NZS1170.4. 2007. *Structural Design Actions Part 4: Earthquake Actions in Australia as 1170.4*. Standards Australia
- 14 AS/NZS1554.1. 2004. *Structural Steel Welding Part 1: Welding of Steel Structures*. Standards Australia
- 15 Aschheim, Mark, and Edgar F. Black. 2000. "Yield Point Spectra for Seismic Design and Rehabilitation." *Earthquake Spectra* Vol. 16 (2, pp. 317-335. May).
- 16 Bachmann .H, Ammann J.W, Deischl .F, Eisenmann .J, Floegl .I, Hirsch .G.H, Klein .G.K. et al. 1995. *Vibration Problems in Structures Practical Guidelines*: Birkhäuser Basel.
- 17 Bates, L. 2013. "Silo Honking." In *11th International Conference on Bulk Materials Storage, Handling and Transportation*, edited by P Tu, Newcastle NSW Australia: University of Newcastle.
- 18 Bauer, Erich. 1996. "Calibration of a Comprehensive Hypoplastic Model for Granular Materials." *Soils and Foundations* 36 (1): 13-26.
- 19 Bennett, R M, and J Kmita. 1996. "Static and Dynamic Silo Loads: Experimental Data Comparisons." In *National Conference on Bulk Materials Handling, Melbourne*, 30 September 1996. 321-324.
- 20 Biot, M. A. 1941. "A Mechanical Analyzer for the Prediction of Earthquake Stresses." *Seismological Research Letters* 74 (3): 313-323. doi: 10.1785/gssrl.74.3.313.

- 21 Blunt, J. 2002. *Health and Safety in Welding and Allied Processes / Jane Blunt and Nigel C. Balchin*. Edited by N. C. Balchin. 5th ed.. ed, Woodhead Publishing Series in Welding and Other Joining Technologies: Cambridge, England ; Boca Raton, Florida : Woodhead Publishing : CRC Press.
- 22 BOC. 2018. Confined Spaces. Industrial Gases Australia. Accessed 14 May, <http://www.boc-gas.com.au/en/sheq/welding-cutting-hazards/confined-spaces/confined-space.html>.
- 23 Boon, C. W., G. T. Housby, and S. Utili. 2013. "A New Contact Detection Algorithm for Three-Dimensional Non-Spherical Particles." *Powder Technology* 248: 94-102. doi: 10.1016/j.powtec.2012.12.040.
- 24 Bowles, Joseph E. 1996. *Foundation Analysis and Design / Joseph E. Bowles*. 5th ed.. ed. New York: New York : McGraw-Hill.
- 25 Brown, R.L, and J.C Richards. 1959. "Exploratory Study of the Flow of Granules through Apertures." *Transactions of the Institute of Chemical Engineers* 37: 108-119.
- 26 BS7604. 2015. *Guide to Fatigue Design and Assessment of Steel Products*. British Standards Institution
- 27 Buick, J. M. 2004. "Motion of Granular Particles on the Wall of a Model Silo and the Associated Wall Vibrations." *Journal of Physics D: Applied Physics* 37 (19): 2751-2760. doi: 10.1088/0022-3727/37/19/022.
- 28 Buick, J. M., J. Chavez-Sagarnaga, Z. Zhong, J. Y. Ooi, Pankaj, D.M. Campbell, and C.A. Greated. 2005. "Investigation of Silo Honking: Slip-Stick Excitation and Wall Vibration." *Journal of Engineering Mechanics* 131 (3): 299-307.
- 29 Buick, J.M., J. Chavez-Sagarnaga, J.Y. Ooi, Pankaj, D.M. Campbell, and C.A. Greated. 2004. "Intermittent Particle Motion on the Wall of a Model Silo During Discharge." In *Partec, Germany*, 16 - 18 March.

- 30 Bull, John W. 1994. *Soil Structure Interaction : Numerical Analysis and Modelling*. Edited by John W. Bull. 1st ed.. ed. New York: New York : E & FN Spon.
- 31 Cardona-Morales, O., L. D. Avendaño, and G. Castellanos-Domínguez. 2014. "Nonlinear Model for Condition Monitoring of Non-Stationary Vibration Signals in Ship Driveline Application." *Mechanical Systems and Signal Processing* 44 (1-2): 134-148. doi: 10.1016/j.ymssp.2013.08.029.
- 32 Cash, M. 2015. "Work Health and Safety (Safe Design of Structures) Code of Practice 2015." edited by Australian Government, Australia: Australian Government.
- 33 Chen, Hu, Y. X. Zhang, Mengyan Zang, and Paul J. Hazell. 2015. "An Accurate and Robust Contact Detection Algorithm for Particle-Solid Interaction in Combined Finite-Discrete Element Analysis." *International Journal for Numerical Methods in Engineering* 103 (8): 598-624. doi: 10.1002/nme.4913.
- 34 Chou, C. S., Y. C. Chuang, J. Smid, S. S. Hsiau, and J. T. Kuo. 2002. "Flow Patterns and Stresses on the Wall in a Moving Granular Bed with Eccentric Discharge." *Advanced Powder Technology* 13 (1): 1-23. doi: <http://dx.doi.org/10.1163/15685520252900929>.
- 35 Clough, R.W. 1960. *The Finite Element Method in Plane Stress Analysis*: American Society of Civil Engineers.
- 36 Clough, Ray W. 2010. *Dynamics of Structures / Ray W. Clough, Joseph Penzien*. Edited by Joseph Penzien. 2nd ed., Rev.. ed. Berkeley, Calif.: Berkeley, Calif. : Computers and Structures.
- 37 Colominas, Marcelo A, Gastón Schlotthauer, and María E Torres. 2014. "Improved Complete Ensemble Emd: A Suitable Tool for Biomedical Signal Processing." *Biomedical Signal Processing and Control* 14: 19-29. doi: 10.1016/j.bspc.2014.06.009.
- 38 Cook, Robert D. 1995. *Finite Element Modeling for Stress Analysis / Robert D. Cook*. New York: New York : Wiley.

- 39 Cook, Robert D., David S. Malkus, Michael E. Plesha, and Robert J. Witt. 2002. *Concepts and Applications of Finite Element Analysis*. 4 ed. United States: John Wiley & Sons.
- 40 Cundall, P. A. 1978. "Ball - a Program to Model Granular Media Using the Distinct Element Method." *Technical Note, Advanced Technology Group*.
- 41 Cundall, P. A., and O. D. L. Strack. 1979. "A Discrete Numerical Model for Granular Assemblies." *Géotechnique* 29 (1): 47-65. doi: 10.1680/geot.1979.29.1.47.
- 42 Cundall, P.A. 1971. "A Computer Model for Simulating Progressive Large Scale Movements in Blocky Rock Systems" *Proc. Int. Symp. Rock Fracture, ISRM, Nancy (F)*,
- 43 Cutnell, John D., and Kenneth W. Johnson. 2012. *Physics*. Edited by Kenneth W. Johnson. 9th ed.. ed, *Cutnell & Johnson Physics*. Hoboken, N.J.: Hoboken, N.J. : Wiley.
- 44 D6128-16, ASTM. 2016. *Astm D6128-16 Standard Test Method for Shear Testing of Bulk Solids Using the Jenike Shear Tester*. ASTM International
- 45 Das, B. M., and At Sawicki. 2001. "Fundamentals of Geotechnical Engineering." *Applied Mechanics Reviews* 54 (6): B103. doi: 10.1115/1.1421116.
- 46 DIN18800-3. 2008. *Steel Structures - Part 3: Stability - Buckling of Plates*. Deutsches Institut für Normung e. V.
- 47 DIN18800-4. 2008. *Steel Structures - Part 4: Stability - Safety against Buckling of Shells*. Deutsches Institut für Normung e. V.
- 48 Ditommaso, Rocco, Marco Mucciarelli, and Felice Ponzo. 2012. "Analysis of Non-Stationary Structural Systems by Using a Band-Variable Filter." *Official Publication of the European Association for Earthquake Engineering* 10 (3): 895-911. doi: 10.1007/s10518-012-9338-y.
- 49 Donohue, Timothy J., Christopher M. Wensrich, and Alan W. Roberts. 2016. "Experimental and Numerical Investigation into Silo Quaking." Barton, ACT: Engineers Australia.

- 50 Donohue TJ, Wensrich CM, Roberts AW, Ilic D, and Katterfeld A. 2012. "Analysis of a Train Loud-out Bin Using Combined Continuum Methods and Discrete Element Modelling." In *7th International Conference for Conveying and Handling of Particulate Solids - CHoPS 2012, Friedrichshafen, Germany*. DECHEMA.
- 51 EN1993-1-5. 2006. *En 1993-1-5: Eurocode 3: Design of Steel Structures - Part 1-5: General Rules - Plated Structural Elements*. EN 1993-1-5: Eurocode 3: Design of steel structures - Part 1-5: General rules - Plated structural elements
- 52 EN1993-1-6. 2007. *En 1993-1-6 Eurocode 3 - Design of Steel Structures - Part 1-6: Strength and Stability of Shell Structures*. European Committee for Standardisation
- 53 EN1993-1-9. 2005. *Guide to Fatigue Design and Assessment of Steel Products*. Comite Europeen de Normalisation
- 54 EN1993-4-1. 2007. *En 1993-4-1: Eurocode 3: Design of Steel Structures - Part 4-1: Silos*. European Committee for Standardisation
- 55 Feldman, Michael. 2011. *Hilbert Transform Applications in Mechanical Vibration / by Michael Feldman*. Oxford: Oxford : Wiley.
- 56 Firewicz, H. 1988. "Kinematics of the Gravity Flow of Granules." *Aufbereitungs-Technik 2*: 61-70.
- 57 Flandrin, Patrick, Paulo Gonçalves, and Gabriel Rilling. 2005. "Emd Equivalent Filter Banks, from Interpretation to Applications." In *The Hilbert-Huang Transform and Its Applications*, eds N. E. Huang and S. S. P. Shen. Interdisciplinary Mathematical Sciences.
- 58 Gilardi, G., and I. Sharf. 2002. "Literature Survey of Contact Dynamics Modelling." *Mechanism and Machine Theory 37* (10): 1213-1239. doi: 10.1016/S0094-114X(02)00045-9.

- 59 Gilbert, R. Ian. 2013. "Time-Dependent Stiffness of Cracked Reinforced and Composite Concrete Slabs." *Procedia Engineering* 57: 19-34. doi: <http://dx.doi.org/10.1016/j.proeng.2013.04.006>.
- 60 Giron-Sierra, Jose Maria. 2017. *Digital Signal Processing with Matlab Examples*. 1 ed. Singapore: Springer.
- 61 Gorenc, B. E., A. Abel, I. Bennetts, J. Cottam, G. A. Day, G. Fletcher, M. Frost-Drury et al. 1984. *Design and Construction of Welded Steel Bins*. 7 ed. Milsons Point: Australian Welding Research Council.
- 62 Government, Australian. 2017. "Work Health and Safety Act 2011." Australia: Australian Government.
- 63 Gudehus, G. 1996. "Comprehensive Constitutive Equation for Granular Materials." *Soils and Foundations* 36 (1): 1-12.
- 64 Gupta, Ajaya K. 1992. *Response Spectrum Method in Seismic Analysis and Design of Structures / Ajaya Kumar Gupta Foreword by William J. Hall*. Boca Raton, Fla.: Boca Raton, Fla. : CRC Press.
- 65 Hall, N. Newton's Laws of Motion. National Aeronautics and Space Administration. 05 May 2015 Accessed 14 May, <https://www.grc.nasa.gov/www/k-12/airplane/newton.html>.
- 66 Hammond, J. K., and P. R. White. 1996. "The Analysis of Non-Stationary Signals Using Time-Frequency Methods." *Journal of Sound and Vibration* 190 (3): 419-447. doi: 10.1006/jsvi.1996.0072.
- 67 Hardow, B, D Schulze, and J Schwedes. 1998. "An Experimental Analysis of the "Silo Quaking" Phenomenon." In *World Congress on Particle Technology, Brighton, England*.
- 68 Hart, Garry C, and Kevin Wong. 2000. *Structural Dynamics for Structural Engineers*. United States of America: John Wiley & Sons.
- 69 Haskel, S, and D Sygoda. 1996. *Biology: A Contemporary Approach*. Richmond, TX, USA: Amsco School Pubns Inc.

- 70 Häussler, U, and J Eibl. 1984. "Numerical Investigations on Discharging Silos." *Journal of Engineering Mechanics* 110 (6).
- 71 He, Dhengyun, and Ding Yi. 2013. "Marginal Hilbert Spectrum Based on Emd Reconstruction and Its Application in Fault Diagnosis of Cooling Tower."
- 72 Herle, I., and G. Gudehus. 1999. "Determination of Parameters of a Hypoplastic Constitutive Model from Properties of Grain Assemblies." *Mechanics of Cohesive-frictional Materials* 4 (5): 461-486. doi: 10.1002/(SICI)1099-1484(199909)4:5<461::AID-CFM71>3.0.CO2-P.
- 73 Herrald, Stuart. 2012. "Vibration of Train Load out Bins." edited by P Tu.
- 74 Holl, H. J., A. K. Belyaev, and H. Irschik. 1999. "A Numerical Algorithm for Nonlinear Dynamic Problems Based on Bem." *Engineering Analysis with Boundary Elements* 23 (5): 503-513. doi: 10.1016/S0955-7997(98)00105-2.
- 75 Horssen, W.T. van, A.K Abramian, and Hartono. 2006. "On the Free Vibrations of an Oscillator with a Periodically Time-Varying Mass." *Journal of Sound and Vibration* 298: 1166-1172.
- 76 Housner, G. W., and P. C. Jennings. 1982. *Earthquake Design Criteria*. California: Earthquake Engineering Research Institute.
- 77 Housner, G.W. 1959. "Behavior of Structures During Earthquakes." *Journal of Engineering Mechanics Division, ASCE* 85 (EM4): 109-129.
- 78 HSE. 2016. Lack of Oxygen in Confined Spaces. Health and Safety Executive. Accessed 14 May, <http://www.hse.gov.uk/welding/confined-spaces.htm>.
- 79 Hu, Guoming, Zhenyu Hu, Bin Jian, Liping Liu, and Hui Wan. 2010. "On the Determination of the Damping Coefficient of Non-Linear Spring-Dashpot System to Model Hertz Contact for Simulation by Discrete Element Method."
- 80 Huang, Norden E, and Samuel S Shen. 2014. *Hilbert-Huang Transform and Its Applications / Editors, Norden E. Huang, National Central University, Taiwan, Samuel S.P. Shen*. Edited by Norden E. editor Huang, Samuel S. editor Shen and Corporation Ebooks. 2nd edition.. ed: New Jersey World Scientific.

- 81 Huang, Norden E., Zheng Shen, Steven R. Long, Manli C. Wu, Hsing H. Shih, Quanan Zheng, Nai-Chyuan Yen, Chi Chao Tung, and Henry H. Liu. 1998. "The Empirical Mode Decomposition and the Hilbert Spectrum for Nonlinear and Non-Stationary Time Series Analysis." *Proceedings: Mathematical, Physical and Engineering Sciences* 454 (1971): 903-995.
- 82 Huang, W., K. Nübel, and E. Bauer. 2002. "Polar Extension of a Hypoplastic Model for Granular Materials with Shear Localization." *Mechanics of Materials* 34 (9): 563-576. doi: [http://doi.org/10.1016/S0167-6636\(02\)00163-1](http://doi.org/10.1016/S0167-6636(02)00163-1).
- 83 Huang, Wenxiong, and Erich Bauer. 2003. "Numerical Investigations of Shear Localization in a Micro-Polar Hypoplastic Material." *International Journal for Numerical and Analytical Methods in Geomechanics* 27 (4): 325-352. doi: 10.1002/nag.275.
- 84 Irgens, F. 2008. *Continuum Mechanics* [Book]. Vol. 1st ed. Berlin: Springer-Verlag.
- 85 Jaeger, Heinrich M., Sidney R. Nagel, and Robert P. Behringer. 1996. "Granular Solids, Liquids, and Gases." *Reviews of Modern Physics* 68 (4): 1259-1273. <http://link.aps.org/doi/10.1103/RevModPhys.68.1259>.
- 86 Jenike, A.W. 1961. *Gravity Flow of Bulk Solids*: University of Utah.
- 87 John, F. Peters, Kala Raju, and S. Maier Robert. 2009. "A Hierarchical Search Algorithm for Discrete Element Method of Greatly Differing Particle Sizes." *Engineering Computations: International Journal for Computer-Aided Engineering and Software* 26 (6): 621-634. doi: 10.1108/02644400910975423.
- 88 Kappos, A. J., ed. 2002. *Dynamic Loading and Design of Structures*. 1 ed. London: Spon Press.
- 89 Khennane, Amar. 2013. *Introduction to Finite Element Analysis Using Matlab® and Abaqus, Introduction to Finite Element Analysis Using Matlab® and Abaqus*. Hoboken: Hoboken : Taylor and Francis.

- 90 Kim, Simon, and Enzo D'Amore. 1999. "Push-over Analysis Procedure in Earthquake Engineering." *Earthquake Spectra* Vol. 15 (3, pp. 417-434. Aug.).
- 91 Kobe. 1995. Strong motion virtual data center. Accessed 06 May, <http://www.strongmotioncenter.org/vdc/scripts/plot.plx?stn=4053&evt=1098>.
- 92 Kodam, Madhusudhan, Rahul Bharadwaj, Jennifer Curtis, Bruno Hancock, and Carl Wassgren. 2010. "Cylindrical Object Contact Detection for Use in Discrete Element Method Simulations. Part I – Contact Detection Algorithms." *Chemical Engineering Science* 65 (22): 5852-5862. doi: 10.1016/j.ces.2010.08.006.
- 93 Kolymbas, D. 1977. "A Rate-Dependent Constitutive Equation for Soils." *Mechanics Research Communications* 4 (6): 367-372. doi: 10.1016/0093-6413(77)90056-8.
- 94 Kolymbas, D. 1999. *Introduction to Hypoplasticity (Advances in Geotechnical Engineering and Tunneling)*. Rorrerdam: A.A. Balkema.
- 95 Lin, Jia, and Wei Wu. 2016. "A Comparative Study between Dem and Micropolar Hypoplasticity." *Powder Technology* 293: 121-129. doi: 10.1016/j.powtec.2015.11.033.
- 96 Liu, G. R. 2013. *The Finite Element Method : A Practical Course*. Edited by S. S. Quek. 2nd ed., ed, *Finite Element Method*. Burlington: Burlington : Elsevier Science.
- 97 LO, MEN-TZUNG, PING-HUANG TSAI, PEI-FENG LIN, CHEN LIN, and YUE LOONG HSIN. 2009. "The Nonlinear and Nonstationary Properties in Eeg Signals: Probing the Complex Fluctuations by Hilbert–Huang Transform." *Advances in Adaptive Data Analysis* 1 (3): 461-482.
- 98 Lopez, Oscar A., Julio J. Hernandez, Ricardo Bonilla, and Aura Fernandez. 2006. "Response Spectra for Multicomponent Structural Analysis." *Earthquake Spectra* Vol. 22 (1, pp. 85-113. Feb.).
- 99 Machado, Margarida, Pedro Moreira, Paulo Flores, and Hamid M. Lankarani. 2012. "Compliant Contact Force Models in Multibody Dynamics: Evolution of the

- Hertz Contact Theory." *Mechanism and Machine Theory* 53: 99-121. doi: 10.1016/j.mechmachtheory.2012.02.010.
- 100 Masuda, H, K Higashitani, and H Yoshida, eds. 2006. *Powder Technology Handbook*. 3 ed. Florida: CRC Press.
- 101 Mattes, J. 2017. Hazards of Welding Fumes. Three Sixty Safety. Accessed 14 May, <http://threesixtysafety.com/hazards-of-welding-fumes/>.
- 102 Matuttis, Hans-Georg. 2014. *Understanding the Discrete Element Method : Simulation of Non-Spherical Particles for Granular and Multi-Body Systems*. Edited by J. F. author Chen: Singapore : Wiley.
- 103 McCabe, R. P. 1974. "Flow Patterns in Granular Material in Circular Silos." *Géotechnique* 24 (1): 45-62.
- 104 McGlinchey, D, ed. 2005. *Characterisation of Bulk Solids*. 1 ed. Oxford: Blackwell Publishing.
- 105 Mertins, Alfred. 1999. *Signal Analysis : Wavelets, Filter Banks, Time-Frequency Transforms, and Applications / Alfred Mertins*: Chichester, West Sussex, England New York : Wiley.
- 106 Mindlin, R. D. 1963. "Microstructure in Linear Elasticity." edited by Engineering Columbia Univ New York Dept Of Civil and Mechanics Engineering.
- 107 Moaveni, Saeed. 2008. *Finite Element Analysis : Theory and Application with Ansys / Saeed Moaveni*. 3rd ed.. ed. Upper Saddle River, N.J.: Upper Saddle River, N.J. : Pearson Prentice Hall.
- 108 Mohammadi, S. 2004. "Discontinuum Mechanics Using Finite and Discrete Elements. (Cd-Rom Included)." Portland: Ringgold Inc.
- 109 Morrison, Richard A. 2007. "Stability Analysis of the Helmholtz Oscillator with Time Varying Mass."

- 110 Mühlhaus, H. 1989. "Application of Cosserat Theory in Numerical Solutions of Limit Load Problems." *Ingenieur-Archiv* 59 (2): 124-137. doi: 10.1007/BF00538366.
- 111 Muite, Benson K, Shandon F Quinn, Sankaran Sundaresan, and K Kesava Rao. 2004. "Silo Music and Silo Quake: Granular Flow-Induced Vibration." *Powder Technology* 145: 190–202.
- 112 Munjiza, Ante. 2004. *The Combined Finite-Discrete Element Method*. Chichester, West Sussex, England: Chichester, West Sussex, England : John Wiley Sons.
- 113 Murray, Angus, Arnaud Castel, Raymond Ian Gilbert, and Zhen-Tian Chang. 2016. "Time-Dependent Changes in the Instantaneous Stiffness of Reinforced Concrete Beams." *Engineering Structures* 126: 641-651. doi: <http://dx.doi.org/10.1016/j.engstruct.2016.08.025>.
- 114 Nassauer, Benjamin, and Meinhard Kuna. 2013. "Contact Forces of Polyhedral Particles in Discrete Element Method." *Granular Matter* 15 (3): 349-355. doi: 10.1007/s10035-013-0417-9.
- 115 Newmark, Nathan M. (Nathan Mortimore), and W. J. (William Joel) Hall. 1982. *Earthquake Spectra and Design*: Earthquake Engineering Research Institute.
- 116 Nezami, Erfan G., Youssef M. A. Hashash, Dawei Zhao, and Jamshid Ghaboussi. 2004. "A Fast Contact Detection Algorithm for 3-D Discrete Element Method." *Computers and Geotechnics* 31 (7): 575-587. doi: 10.1016/j.compgeo.2004.08.002.
- 117 Niedostatkiewicz, M., M. Wójcik, and J. Tejchman. 2014. "Application of Inserts for Suppression of Coupled Dynamic–Acoustic Effects During Confined Granular Flow in Silos." *Advanced Powder Technology* 25 (1): 398-407. doi: 10.1016/j.appt.2013.06.005.
- 118 Non-Stationary Nature of Speech Signal. 2011. Sakshat Virtual Labs. Accessed 23 April, <http://iitg.vlab.co.in/?sub=59&brch=164&sim=371&cnt=1104>.

- 119 Nunez, Daniel, and Pedro J Torres. 2009. "On the Motion of an Oscillator with a Periodically Time-Varying Mass." *Nonlinear Analysis: Real World Applications* 10: 1976-1983.
- 120 O'Sullivan, Catherine. 2014. *Particulate Discrete Element Modelling : A Geomechanics Perspective*. 1. ed. Hoboken: Hoboken : Taylor and Francis.
- 121 Papageorgiou, A.V, and C.J Gantes. 2008. "Equivalent Uniform Damping Ratios for Irregular in Height Concrete / Steel Structural Systems." In *Eurosteel 2008, Brussels*, 2008. edited by R Ofner, D Beg, J Fink, R Greiner and H Unterwegger, 1485-1490. European Convention for Constructional Steelwork.
- 122 Park, Sang-Gil, Hyoun-Jin Sim, Hae-Jin Lee, and Jae-Eung Oh. 2008. "Application of Non-Stationary Signal Characteristics Using Wavelet Packet Transformation." *Journal of Mechanical Science and Technology* 22 (11): 2122-2133. doi: 10.1007/s12206-007-1218-z.
- 123 Paz, Mario. 2004. *Structural Dynamics : Theory and Computation / by Mario Paz, William Leigh*. Edited by William Leigh. Fifth Edition.. ed: Boston, MA : Springer US : Imprint: Springer.
- 124 Pcb Piezotronics. 2017. Accessed 22 April 2017, <http://www.pcb.com/Products/model/393B04>.
- 125 Phillips, C.E.S. 1910. "Electrical and Other Properties of Sand." *Nature* 84 (2130): 255-261.
- 126 Plastino, Angel, and Juan Muzzio. 1992. "On the Use and Abuse of Newton's Second Law for Variable Mass Problems." *Celestial Mechanics and Dynamical Astronomy* 53 (3): 227-232. doi: 10.1007/BF00052611.
- 127 Quinn, Victor. 2012. *Continuum Mechanics [Book]*. Vol. 1st ed. Delhi: Orange Apple.
- 128 Rao, S. S. 2011. *The Finite Element Method in Engineering / Singiresu S. Rao*. 5th ed.. ed. Boston, MA: Elsevier/Butterworth Heinemann.

- 129 Remias, Michael G. 1998. "Discrete Dynamic Modelling of Granular Flows in Silos." Master's thesis, School of Mathematics and Statistics, Curtin University of Technology, Perth.
- 130 Roberts, A. 1996. "Pulsating Loads in Silos During Discharge - a Review." In *1996 National Conference on Bulk Materials Handling, Melbourne Australia*, 30 September - 2 October 1996. 13.
- 131 Roberts, A. 2008. "Shock Loads in an Iron Ore Train Loading Bin." In *Structures and Granular Solids*, 67-76. Taylor & Francis.
- 132 Roberts, A.W, and O.J Scott. 1978. "An Investigation into the Effects of Sinusoidal and Random Vibrations on the Strength and Flow Properties of Bulk Solids." *Powder Technology* 21: 45 - 53.
- 133 Roberts, Alan W, and Christopher M Wensrich. 2002. "Flow Dynamics or 'Quaking' in Gravity Discharge from Silos." *Chemical Engineering Science* 57: 295-305.
- 134 Roberts, Alan W. 2003. "Review of the "Silo Quaking" Problems in Bins of Various Geometrical Shapes and Flow Patterns." *TASK Quarterly : Scientific Bulletin of Academic Computer Centre in Gdansk* 7 (4): 623-641.
- 135 Saa, J.D. 2010. Marginal Hilbert Spectrum. (1). Mathworks. Accessed 10 Feb 2017, <http://au.mathworks.com/matlabcentral/fileexchange/27531-marginal-hilbert-spectrum>.
- 136 Sarhosis, Vasilis, Katalin Bagi, José V Lemos, and Gabriele Milani, eds. 2016. *Computational Modeling of Masonry Structures Using the Discrete Element Method*. Hershey, Pennsylvania: IGI Global.
- 137 Schulze, D. 2007. *Powders and Bulk Solids Behavior, Characterization, Storage and Flow*. 1 ed. New York: Springer.
- 138 Shamlou, P. A. 1988. *Handling of Bulk Solids : Theory and Practice / P.A. Shamlou*. London,Boston: Butterworths.

- 139 Shinohara, K, Y Idemitsu, K Gotoh, and Tatsuo Tanaka. 1968. "Mechanism of Gravity Flow of Particles from a Hopper." *I & EC Process Design and Development* 7 (6): 378-383.
- 140 Shukla, K. K. 2013. *Efficient Algorithms for Discrete Wavelet Transform : With Applications to Denoising and Fuzzy Inference Systems / by K. K. Shukla, Arvind K. Tiwari*. Edited by Arvind K. Tiwari and SpringerLink. London: London : Springer London : Imprint: Springer.
- 141 Smith, I. M. 2004. *Programming the Finite Element Method / I.M. Smith, D.V. Griffiths*. Edited by D. V. Griffiths. 4th ed.. ed. Hoboken, NJ: Hoboken, NJ : Wiley.
- 142 Smith, W S. 1999. *The Scientist and Engineer's Guide to Digital Signal Processing*. San Diego: California Technical Publishing.
- 143 Sommerfeld, Arnold. 1953. "Mechanics, Lectures on Theoretical Physics." *American Journal of Physics* 21 (5): 399-399. doi: 10.1119/1.1933476.
- 144 Spakovszky, ZS. The Rocket Equation. MIT. Accessed 13 May 2018, <http://web.mit.edu/16.unified/www/SPRING/propulsion/notes/node103.html>.
- 145 Stearns, Samuel D. 2003. *Digital Signal Processing with Examples in Matlab / Samuel D. Stearns*. Boca Raton, Fla.: Boca Raton, Fla. : CRC Press.
- 146 Strang, Gilbert. 1997. *Wavelets and Filter Banks / Gilbert Strang, Truong Nguyen*. Edited by Truong Nguyen. Rev. ed.. ed. Wellesley, MA: Wellesley, MA : Wellesley-Cambridge Press.
- 147 Strzałko, J., and J. Grabski. 1995. "Dynamic Analysis of a Machine Model with Time-Varying Mass." *Acta Mechanica* 112 (1): 173-186. doi: 10.1007/BF01177487.
- 148 Su, Mei-Lin, and Keh-Shih Chuang. 2013. "An Ecg Signal Enhancement Based on Improved Emd" *PIERS Proceedings, Taipei: Progress In Electromagnetics Research Symposium*.

- 149 Tano, E, L Godoy, and M Diez. 1994. "Numerical Modelling of the Flow of Solids Stored in Silos." *Computer Methods and Advances in Geomechanics 2*: 1281-1291.
- 150 Tejchman, J. 1995. "Silo-Quake-Experiments and a Polar Hypoplastic Model." In *Proceedings of the 3rd European Symposium on Storage and Flow of Particulate Solids, Nuremberg*, 151-163. Institute of Soil Mechanics and Rock Mechanics.
- 151 Tejchman, J. 1996. "Dynamic Effects During Silo Flow." In *National Conference on Bulk Materials Handling, Melbourne, 25-29*. Institution of Engineers Australia.
- 152 Tejchman, J. 1998a. "Fe-Simulations of Rapid Silo Flow with a Polar Elasto-Plastic Constitutive Model." *TASK Quarterly : Scientific Bulletin of Academic Computer Centre in Gdansk 2 (3)*: 473-501.
- 153 Tejchman, J. 1998b. "Silo-Quake—Measurements, a Numerical Approach and a Way for Its Suppression." *Thin-Walled Structures 31 (1-3)*: 137-158.
- 154 Tejchman, J. 1999. "Technical Concept to Prevent the Silo Honking." *Powder Technology 106*: 7-22.
- 155 Tejchman, J. 2005. *Finite Element Modeling of Shear Localization in Granular Bodies in Hypoplasticity with Enhancements*. Gdansk: Gdansk University.
- 156 Tejchman, J, and G Gudehus. 1993a. "Silo-Music and Silo-Quake Experiments and a Numerical Cosserat Approach." *Powder Technology 76* (201-212).
- 157 Tejchman, J, and M Wojcik. 2011. *Experimental and Theoretical Investigations of Some Characteristic Silo Phenomena*. Gdansk: Gdansk University.
- 158 Tejchman, J. 1998c. "Numerical Simulation of Filling in Silos with a Polar Hypoplastic Constitutive Model." *Powder Technology 96 (3)*: 227-239. doi: 10.1016/S0032-5910(97)03378-0.

- 159 Tejchman, J. 2002. "Patterns of Shear Zones in Granular Bodies within a Polar Hypoplastic Continuum." *Acta Mechanica* 155 (1): 71-94. doi: 10.1007/BF01170841.
- 160 Tejchman, J., and E. Bauer. 2005. "Fe-Simulations of a Direct and a True Simple Shear Test within a Polar Hypoplasticity." *Computers and Geotechnics* 32 (1): 1-16. doi: <http://doi.org/10.1016/j.compgeo.2004.11.004>.
- 161 Tejchman, J., and J. Górski. 2008. "Computations of Size Effects in Granular Bodies within Micro-Polar Hypoplasticity During Plane Strain Compression." *International Journal of Solids and Structures* 45 (6): 1546-1569. doi: <http://doi.org/10.1016/j.ijsolstr.2007.10.007>.
- 162 Tejchman, J., and G. Gudehus. 1993b. "Silo-Music and Silo-Quake Experiments and a Numerical Cosserat Approach." *Powder Technology* 76 (2): 201-212. doi: 10.1016/S0032-5910(05)80028-2.
- 163 Tejchman, J., and G. Gudehus. 2001. "Shearing of a Narrow Granular Layer with Polar Quantities." *International Journal for Numerical and Analytical Methods in Geomechanics* 25 (1): 1-28. doi: 10.1002/1096-9853(200101)25:1<1::AID-NAG115>3.0.CO 2-8.
- 164 Tejchman, J., and T. Ummenhofer. 2000. "Bedding Effects in Bulk Solids in Silos: Experiments and a Polar Hypoplastic Approach." *Thin-Walled Structures* 37 (4): 333-361. doi: [http://doi.org/10.1016/S0263-8231\(00\)00026-4](http://doi.org/10.1016/S0263-8231(00)00026-4).
- 165 Tejchman, Jacek. 2004. "Comparative Fe-Studies of Shear Localizations in Granular Bodies within a Polar and Non-Local Hypoplasticity." *Mechanics Research Communications* 31 (3): 341-354. doi: <http://doi.org/10.1016/j.mechrescom.2003.11.009>.
- 166 Tejchman, Jacek. 2013. *Confined Granular Flow in Silos : Experimental and Numerical Investigations / by Jacek Tejchman*. Edited by SpringerLink. Heidelberg: Heidelberg : Springer International Publishing : Imprint: Springer.
- 167 Tejchman, Jacek, and Wei Wu. 2007. "Modeling of Textural Anisotropy in Granular Materials with Stochastic Micro-Polar Hypoplasticity." *International*

Journal of Non-Linear Mechanics 42 (6): 882-894. doi:

<http://doi.org/10.1016/j.ijnonlinmec.2007.03.015>.

168 To, Kiwing. 2005. "Jamming Patterns in a Two-Dimensional Hopper." *Pramana* 64 (6): 963-969.

169 Torres, M. E., M. A. Colominas, G. Schlotthauer, and P. Flandrin. 2011. "A Complete Ensemble Empirical Mode Decomposition with Adaptive Noise" *2011 IEEE International Conference on Acoustics, Speech and Signal Processing (ICASSP)*, doi: 10.1109/ICASSP.2011.5947265.

170 Tu, P. 2008. "Risk Management of Silos at Mine Sites in Western Australia." Civil Engineering, Curtin University of Technology, Perth.

171 Tu, P, and V Vimonsatit. 2013. "The Effect of Structural Stiffness on Iron Ore Train Load out Bin." In *11th International Conference on Bulk Materials Storage, Handling and Transportation, Newcastle NSW Australia*, edited by Jan-Dirk Prigge and Mark Jones. University of Newcastle.

172 Vlcek, Miroslav. 2009. Stationary and Non-Stationary Signals. Department of applied mathematics, Faculty of Transportation Sciences CTU. Accessed 23 April, <http://euler.fd.cvut.cz/predmety/mathtools/files/nestacionarni2.pdf>.

173 Walizer, Laura E., and John F. Peters. 2011. "A Bounding Box Search Algorithm for Dem Simulation." *Computer Physics Communications* 182 (2): 281-288. doi: 10.1016/j.cpc.2010.09.008.

174 Wang, G., X. Y. Cui, Z. M. Liang, and G. Y. Li. 2015. "A Coupled Smoothed Finite Element Method (S-Fem) for Structural-Acoustic Analysis of Shells." *Engineering Analysis with Boundary Elements* 61: 207-217. doi: 10.1016/j.enganabound.2015.07.017.

175 Wang, Tong, Mingcai Zhang, Qihao Yu, and Huyuan Zhang. 2012. "Comparing the Applications of Emd and Eemd on Time-Frequency Analysis of Seismic Signal." *Journal of Applied Geophysics* 83: 29-34. doi: 10.1016/j.jappgeo.2012.05.002.

- 176 Wensrich. 2002a. "Analytical and Numerical Modelling of Quaking in Tall Silos." Department of Mechanical Engineering, University of Newcastle, Newcastle.
- 177 Wensrich, Christopher M. 2002b. "Experimental Behaviour of Quaking in Tall Silos." *Powder Technology* 127: 87-94.
- 178 Wensrich, Christopher M. 2003. "Numerical Modelling of Quaking in Tall Silos." *International Journal of Mechanical Sciences* 45: 541-551.
- 179 Wilde, K, M Rucka, and J Tejchman. 2008. "Silo Music — Mechanism of Dynamic Flow and Structure Interaction." *Powder Technology* 186 (2): 113-129.
- 180 Wilde, K, J Tejchman, M Rucka, and M Niedostatkiewicz. 2010. "Experimental and Theoretical Investigations of Silo Music." *Powder Technology* 198 (1): 38-48.
- 181 Wilson, E. 2002. *Three Dimensional Static and Dynamic Analysis of Structures: A Physical Approach with Emphasis on Earthquake Engineering*. 3 ed. Berkeley, California, USA: Computers and Structures, Inc.
- 182 Worksafe. 2011. Explosive Conditions: Grinding, Cutting and Welding (Including Pre-Heating) from the inside or Outside of Confined Spaces. Work Cover Queensland. Accessed 14 May, <https://www.worksafe.qld.gov.au/injury-prevention-safety/alerts/whsq/2011/explosive-conditions-grinding,-cutting-and-welding-including-pre-heating-from-the-inside-or-outside-of-confined-spaces>.
- 183 Wu, Wei, Erich Bauer, and Dimitrios Kolymbas. 1996. "Hypoplastic Constitutive Model with Critical State for Granular Materials." *Mechanics of Materials* 23 (1): 45-69. doi: 10.1016/0167-6636(96)00006-3.
- 184 Wu, Wei, and Andrzej Niemunis. 1996. "Failure Criterion, Flow Rule and Dissipation Function Derived from Hypoplasticity." *Mechanics of Cohesive-frictional Materials* 1 (2): 145-163. doi: 10.1002/(SICI)1099-1484(199604)1:2<145::AID-CFM8>3.0.CO2-9.
- 185 Wu, Wei, and Andrzej Niemunis. 1997. "Beyond Failure in Granular Materials." *International Journal for Numerical and Analytical Methods in*

Geomechanics 21 (3): 153-174. doi: 10.1002/(SICI)1096-9853(199703)21:3<153::AID-NAG863>3.0.CO2-D.

186 Wu, Zhaohua, and Norden E. Huang. 2009. "Ensemble Empirical Mode Decomposition: A Noise-Assisted Data Analysis Method." *Advances in Adaptive Data Analysis* 01 (01): 1-41. doi: 10.1142/s1793536909000047.

187 Zhao, G.F. 2015. *High Performance Computing and the Discrete Element Model*. United States: Elsevier.

188 Zhu, Yan, and Shulin Wang. 2011. "Analysing the Vibration System with Time-Varying Mass." *Applied Mechanics and Materials Vols 50-51*: 160-165.

189 Zoltan Tuske, Friedhelm R. Drepper, and Ralf Schluter. 2012. "Non-Stationary Signal Processing and Its Application in Speech Recognition." In *SAPA - SCALE Conference 2012, Portland USA, 7-8 September 2012*.

APPENDIX A – ACCELEROMETER SPECIFICATIONS

Table A-1: PCB 393B04 performance specifications (Pcb Piezotronics 2017).

PERFORMANCE	SI
Sensitivity ($\pm 10\%$)	102 mV/(m/s ²)
Measurement Range	± 49 m/s ² pk
Frequency Range ($\pm 5\%$)	0.06 to 450 Hz
Frequency Range ($\pm 10\%$)	0.05 to 750 Hz
Frequency Range (± 3 dB)	0.02 to 1,700 Hz
Resonant Frequency	$\geq 2,500$ Hz
Broadband Resolution (1 to 10000 Hz) Typical	0.00003 m/s ² RMS
Non-Linearity Zero-based, least-squares, straight line method.	$\leq 1\%$
Transverse Sensitivity Transverse sensitivity is typically $\leq 3\%$.	$\leq 5\%$

Table A-2: PCB 393B04 environmental specifications (Pcb Piezotronics 2017).

ENVIRONMENTAL	SI
Overload Limit (Shock)	$\pm 2,950$ m/s ² pk
Temperature Range	-18 to 80 °C
Temperature Response	See Graph %/°F
Base Strain Sensitivity Typical	≤ 0.005 (m/s ²)/ $\mu\epsilon$

Table A-3: PCB 393B04 electrical specifications (Pcb Piezotronics 2017).

ELECTRICAL	SI
Excitation Voltage	18 to 30 VDC
Constant Current Excitation	2 to 10 mA
Output Impedance	<500 Ohm
Output Bias Voltage	7 to 12 VDC
Discharge Time Constant	5 to 15 sec
Settling Time	<100 sec
Spectral Noise (1 Hz) Typical	2.9 ($\mu\text{m}/\text{sec}^2$)/ $\sqrt{\text{Hz}}$
Spectral Noise (10 Hz) Typical	1 ($\mu\text{m}/\text{sec}^2$)/ $\sqrt{\text{Hz}}$
Spectral Noise (100 Hz) Typical	0.4 ($\mu\text{m}/\text{sec}^2$)/ $\sqrt{\text{Hz}}$
Spectral Noise (1 kHz) Typical	0.4 ($\mu\text{m}/\text{sec}^2$)/ $\sqrt{\text{Hz}}$

Table A-4: PCB 393B04 physical specifications (Pcb Piezotronics 2017).

PHYSICAL	SI
Sensing Element	Ceramic
Sensing Geometry	Flexural
Housing Material	Titanium
Sealing	Hermetic
Size - Diameter	25 mm
Size - Height	31 mm
Weight Typical	50 gm

Electrical Connector	10-32 Coaxial Jack
Electrical Connection Position	Top
Mounting Thread	10-32 Female

**APPENDIX B – MARGINAL SPECTRUM (MS) – SILO QUAKE RESPONSE
SPECTRUM**

Data available online.

APPENDIX C – ACCELEROGRAMS

Data available online.


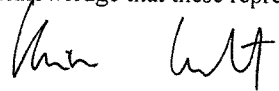
APPENDIX D – IMFS

Data available online.



APPENDIX E – ATTRIBUTION OF RESEARCH OUTPUTS

Refer to next page.



Tu, P, and V Vimonsatit. 2013. "The Effect of Structural Stiffness on Iron Ore Train Load out Bin." In 11th International Conference on Bulk Materials Storage, Handling and Transportation, Newcastle NSW Australia, edited by Jan-Dirk Prigge and Mark Jones. University of Newcastle.

	Conception and design	Acquisition of data & method	Data conditioning & manipulation	Analysis & statistical method	Intepretation & discussion	Final approval
Phung Tu	X	X	X	X	X	X
I acknowledge that these represent my contribution to the above research output						
 31/10/18						
Dr Vimonsatit						X
I acknowledge that these represent my contribution to the above research output						
 31/10/18						

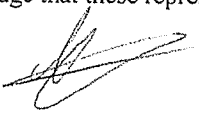
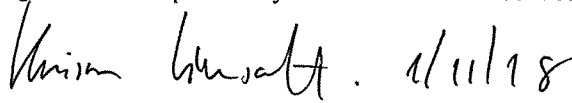
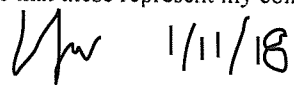
Tu, P and Vimonsatit, V. 2013. Structural Design of Iron Ore Train Load Out Bin. Australian Bulk Handling Review. 18 (6): pp. 24-28.

	Conception and design	Acquisition of data & method	Data conditioning & manipulation	Analysis & statistical method	Intepretation & discussion	Final approval
Phung Tu	X	X	X	X	X	X
I acknowledge that these represent my contribution to the above research output						
 31/10/18						
Dr Vimonsatit						X
I acknowledge that these represent my contribution to the above research output						
 31/10/18						

Tu, P and Vimonsatit, V. 2017. Silo Quaking of Iron Ore Train Load Out Bin - A Time-Varying Mass Structural Dynamic Problem. Advanced Powder Technology. 2017;28(11):3014-25.

	Conception and design	Acquisition of data & method	Data conditioning & manipulation	Analysis & statistical method	Intepretation & discussion	Final approval
Phung Tu	X	X	X	X	X	X
I acknowledge that these represent my contribution to the above research output						
 31/10/18						
Dr Vimonsatit						X
I acknowledge that these represent my contribution to the above research output						
 1/11/18						

Tu, P, Vimonsatit, V, Li, J. 2018. Silo Quake Response Spectrum of Iron Ore Train Load Out Bin. Advanced Powder Technology. 2018, 29(11): 2775-2784.

	Conception and design	Acquisition of data & method	Data conditioning & manipulation	Analysis & statistical method	Intepretation & discussion	Final approval
Phung Tu	X	X	X	X	X	X
I acknowledge that these represent my contribution to the above research output						
 31/10/18						
Dr Vimonsatit						X
I acknowledge that these represent my contribution to the above research output						
 1/11/18						
Dr Li						X
I acknowledge that these represent my contribution to the above research output						
 1/11/18						

I warrant that I have obtained, where necessary, permission from the copyright owners to use any third-party copyright material reproduced in the thesis (e.g. questionnaires, artwork, unpublished letters), or to use any of my own published work (e.g. journal articles) in which the copyright is held by another party (e.g. publisher, co-author).